Mathematical modelling and imaging of asthmatic airways

Jonathan E. Hiorns

Thesis submitted to The University of Nottingham
for the degree of Doctor of Philosophy

July 2014

Abstract

The hyper-responsiveness of airway smooth muscle to certain external stimuli, and the associated remodelling of the airway wall, is central to the development of asthma, making it of widespread clinical significance.

In this thesis, mathematical models for the asthmatic airway embedded in parenchymal tissue are presented. The stiffening due to recruitment of collagen fibres and force generation by smooth muscle is taken into account, to develop a nonlinear elastic model for the airway wall. The contractile force of the muscle is governed by the dynamically changing subcellular crossbridge populations. A nonlinear elastic and, to take into account the viscoelasticity of the lung, a linear viscoelastic model for the parenchyma are developed.

Consistent with experimental findings, deforming the airway passively, the model predicts strain-stiffening on inflation and deflation. The displacements predicted within the parenchyma are much smaller when the airway is inflated internally than externally, due to the airway wall shielding the parenchyma. Stress heterogeneities are predicted within the thickened airway wall when active contractile forcing is applied, which may contribute to further remodelling of the wall. If tidal stretching is applied to a contracted airway, the model predicts that the contractile force reduces, resulting in a reversal of bronchoconstriction. This is more exaggerated when the parenchyma is viscoelastic.

Image analysis techniques are also developed to investigate data from lung-slice experiments, whereby pharmacological stimuli can be added to segments of lung tissue to stimulate smooth muscle contraction. By tracking the lumen area and fitting to exponential functions, two timescales of contraction are found to exist, consistent with the mathematical model predictions, and that the ratio of the timescales is robust. Methods are also developed and tested to find the displacement field of the tissue surrounding the airway lumen and it is shown that there are important heterogeneities within the tissue.

Acknowledgements

I would like to thank my supervisors Oliver Jensen, Bindi Brook and Ian Hall. Special thanks to Oliver and Bindi for helpful insights as I developed the mathematical models and for reading through my work when it was at various stages of completeness.

Special thanks to Jane Fox for directing me to useful asthma literature and for the videos from the lung slice experiments. Also to Andrew French for helping me to get started with the image analysis.

I would also like to acknowledge all the support staff in the maths school, who have helped with computing and administrative needs, and the Medical Research Council for funding me.

My thanks to everyone in Boston, and especially to Jeff Fredberg and Rama Krishnan, for enabling me to experience life in a laboratory and in America.

Finally, many thanks to my family and friends, who have supported and encouraged me.

Contents

Chapter 1

Motivation for modelling asthmatic airways

1.1 Asthma

Asthma is a chronic inflammatory disease of the lungs characterised by repeated episodes of wheezing, breathlessness, chest tightness and coughing [54]. Asthma affects around 300 million individuals of all ages and ethnic groups and it is estimated that around 250,000 people die prematurely each year as a result [15] and is the most common chronic disease among children [181]. There are large costs associated with asthma. Some of the costs come from the drugs used to treat the diseases but a large proportion of the costs comes as a result of poorly controlled asthma, which can result in the need for emergency treatment and a loss of productivity due to time off work [6].

For many people, symptoms follow exposure to particular triggers. Common triggers include exposure to allergens (such as those from house dust mites, furry animals, cockroaches, pollens and moulds), occupational irritants, tobacco smoke, respiratory (viral) infections, exercise, chemical irritants and drugs (such as aspirin and beta blockers) [48]. Asthma may be classified by the trigger, yielding for example occupational asthma, exercise-induced asthma or aspirin-induced asthma [177]. In contrast there are some patients who are thought to be genetically susceptible to developing symptoms [81].

1.2 The respiratory system

The lungs are responsible for the oxygenation of the blood and for the removal of carbon dioxide. During breathing, air enters through the nose or mouth and passes the epiglottis into the trachea, which splits into the left and right bronchi that lead to the lungs. The lungs are split into sections called lobes, with three lobes in the right lung and two in the left lung of a human. The airways continue to divide and become smaller yielding a branching structure of bronchi and bronchioles, which terminate in the alveoli (Fig. 1.1). Within human lungs there are 23 generations of airways. The first 16 generations consist of the conducting airways, responsible for warming and moistening the air and removing any foreign objects in the air. The remaining generations consist of the transitional and respiratory airways. Within these, and especially within the alveoli, gas exchange occurs [139]. There are approximately 300 million alveoli in the normal lung [117], which are tiny air sacs enveloped by a network of blood vessels containing deoxygenated blood.

There are a number of muscles that contribute to breathing (Fig. 1.1). For normal tidal breathing, the main muscle is the diaphragm. The diaphragm flattens from its natural curved form to increase the lung volume so that air is inhaled, before relaxing so that air is exhaled as the lung recoils. For deeper or more forceful breathing (e.g. during exercise) other muscles are recruited. The external intercostal muscles can be recruited to lift the ribcage up, to help with inspiration, while the internal intercostal muscles can be recruited to force the ribcage back down, to help with expiration. The abdominal muscles may also be recruited to push the diaphragm up, increasing the force of the expiration [139]. The lungs and the chest wall are covered by pleural membranes, between which is a space called the pleural cavity containing lubricating fluid. This allows the membranes to slide past each other, while the pleural cavity provides a surface pressure that ensures the lungs adhere to the chest wall as it moves during breathing.

1.2.1 Airway wall anatomy and histology

The main features of lung airways are shown in Fig. 1.2.

Lining the airway are epithelial cells, which have hair-like cilia protruding into the lumen. Interspersed between these cells are goblet cells, which secrete mucus [147]. The mucus traps inhaled particles and is transported back up the airway by cilia, thus cleansing the air that is inhaled.

The basement membrane separates the epithelial cells from the region of the wall

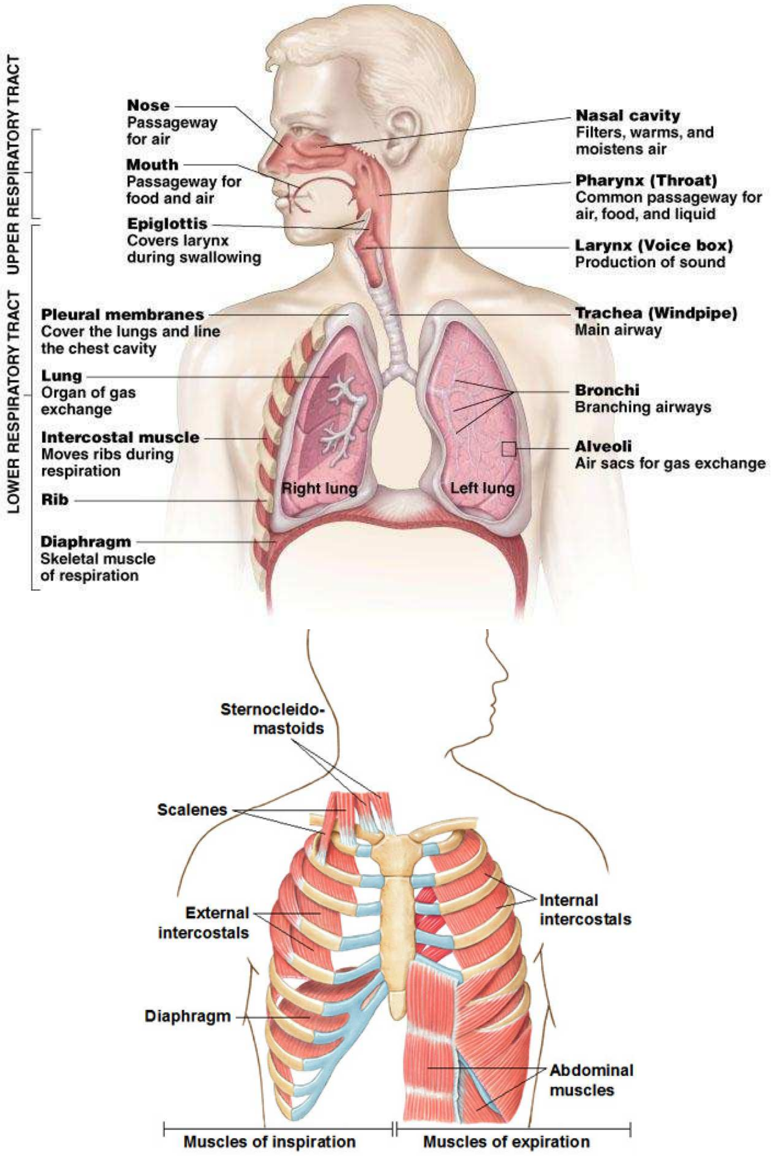

Figure 1.1: Top: The respiratory system. (http://upanya.blogspot.co.uk/2011/06/human-body-structure.html).
Bottom: Muscles for breathing. (http://www.colorado.edu/intphys/Class/IPHY3430-200/image/17-1.jpg).

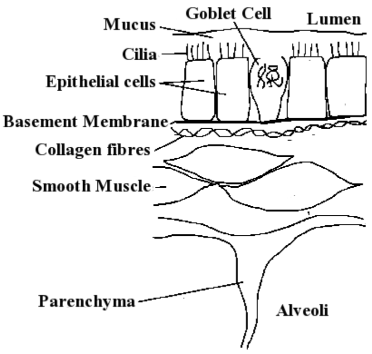

Figure 1.2: A representation of the structure of the airway wall. Adapted from [78]. For an image of a section of a constricted rabbit bronchial see [86].

largely responsible for the control of the calibre of the airway and its mechanical stability [31]. The following types of tissue are found in this region:

- Cartilage provides the support for the trachea, encircling 70-80% of the circumference [163]. As the airways get smaller the pieces of cartilage become smaller and less regular, with no cartilage present in the bronchioles [31].
- Elastin fibres form both concentric and axial bands [31] and are responsible for the elastic recoil within the lungs [162].
- Collagen fibres group together to form wavy bands [75]. As they are stretched they straighten and stiffen the airway [115], protecting the lung from over expansion.
- Airway smooth muscle (ASM) cells are spindle-shaped [86] and grouped together to form bundles of cells. The orientation of a bundle depends on its location within the lung. For large proximal airways they are mainly circumferential, while further into the lung the muscle cells are arranged in a helical formation, with the angle of the fibres changing so that they are oriented more to the longitudinal direction and less to the circumferential direction [31]. ASM contraction narrows the airway. There have been a number of suggestions for a necessary physiological function of the ASM, including to help with exhalation, mucus transport or the development of the lung, while others believe it does not have any essential function [10].

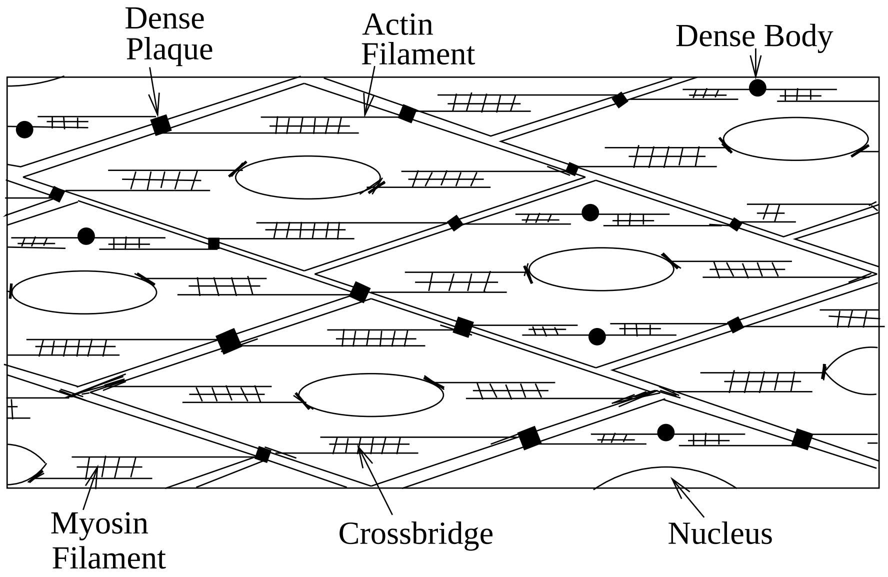

Figure 1.3: Airway smooth muscle. A schematic representation of the contractile filament structure within the ASM cells. In practice there are many more myosin filaments in each of the cells and there are more than two actin filaments for every myosin filament. Adapted from [87]. For an image of the staining of ASM in a mouse, that shows the helical nature of the fibres, see [154].

1.2.2 Parenchyma

Surrounding the airway there are a number of different types of tissues, including other airways, alveoli, connective tissue, blood vessels, that bring oxygenated blood to cells or deoxygenated blood for gas exchange, and partitions between the lobes. Collectively these may be known as the lung parenchyma, although in strictest sense only the alveoli tissue is parenchyma. The parenchyma makes up ninety percent of the lung, resembling a sponge with a honeycomb structure [70].

By transmitting the stresses on the pleura throughtout the lung, the parenchyma is responsible for the majority of the lung recoil, which is the ability of the lung to return to its original deformation [64]. Lung recoil is lower during deflation than during inflation, since energy is lost during inflation through heat dissipation, thus resulting in hysteresis. Experiments have shown that the energy loses are independent of the frequency of the pressure oscillations applied to the lung [64]. Hysteresis is one phenomena of a viscoelastic material; others include stress adaptation and creep which have also been observed in lung tissue [28, 112, 135]. One of the main reasons for these features is due to surfactant, which sits at the air-liquid interface on the surface of the alveoli, with lower surface tension during deflation, due to a more compact layer of surfactant molecules at the interface [168]. In comparison, experiments with a saline-filled lung, where there is no air-liquid interface, show much smaller differences between inflation and deflation [73].

1.2.3 Smooth muscle contraction

ASM cells are able to produce contractile forces along their length, due to the presence in the cytoplasm of myofilaments that run parallel to the longitudinal axis of the cell [87]. Actin (thin) filaments, that are attached to dense bodies and the nuclear envelope, surround myosin (thick) filaments, forming the scaffold for the cytoskeleton (Fig. 1.3). Protruding from the backbone of the myosin filaments are long α-helical coiled tails, each of which has a globular head [51]. These heads attach to binding sites on the actin filaments to form crossbridges. Crossbridges are repetitively formed and perform a power stroke before detaching, causing the actin filament to slide relative to the myosin filament. This is known as crossbridge cycling and is responsible for the generation of a contractile force [175]. There is also evidence that the filaments can deform, flow or remodel [88, 114, 152]. It is even thought that the small length changes that occur during breathing profoundly perturb the binding of myosin to actin leading to remodelling of the cytoskeletal lattice [40].

Calcium signalling within the cell, and particularly an increase in the intracellular calcium (Ca^{2+}) concentration [74], is essential for ASM to generate contractile force. Initially, following the exposure of ASM cells to contractile agonists, there is a sharp rise in the intracellular calcium concentration followed by a reduction to some sustained steady state greater than the initial concentration [74]. The rise occurs as calcium is released from internal stores in the endoplasmic reticulum and crosses the plasma membrane [13]. Within the cytoplasm the calcium binds to calmodulin, leading to the activation of myosin light chain kinase (MLCK), which phosphorylates the myosin light chains [77]. Once phosphorylation has occurred, crossbridges can be formed [71] and adenosine triphosphate (ATP) is hydrolysed, producing energy so that a force can be applied to bend the crossbridge and slide the actin filament past the myosin filament [51]. This process of sliding the filaments relative to one another is called the power stoke. If the level of phosphorylation drops, there is evidence that the crossbridges can remain attached and are capable of maintaining a force, in which case they are called latch bridges [37]. Further discussion about calcium regulation and the various pathways involved are beyond the scope of this thesis, with interested readers directed to [35, 74].

1.3 The asthmatic lung

There are a number of features of the asthmatic lung that are different from a normal lung. During an asthmatic exacerbation short-term airway inflammation occurs, while remodelling of the airway wall can occur over longer periods of time, which can lead to worsening symptoms [17, 178]. There is also evidence that remodelling is observed early in the development of the disease and is possibly required for the onset of persistent inflammation [32].

1.3.1 Inflammation in human allergic asthma

As described previously, mucus is continuously produced to trap particles that are inhaled and thereby protects the airways. However, on occasions inhaled allergens may disrupt the epithelial-cell barrier and cause damage to the airway wall [54]. Upon initial contact with an antigen, T helper cells, a type of white blood cell, produce Immunoglobulin E (IgE) antibodies specific to the allergen, which attach to mast cells. Upon subsequent contact, the antigen binds to the IgE antibodies and the mast cell releases proinflammatory mediators such as histamine, cysteinyl leukotrienes and cytokines. This leads to an early allergic response.

The release of the proinflammatory mediators characterises the early allergic response and results in mucus secretion, ASM contraction and elevated vascular permeability, which allows cells of the immune system to leave blood vessels [60]. In asthma the airways may be over-sensitised, which can result in chronic inflammation [144], mucus hypersecretion and airway hyperresponsiveness. Mucus hypersecretion refers to an excessive production and secretion of mucus. This can contribute towards airway hyperresponsiveness [148] and plugging of the airways. Airway hyperresponsiveness refers to smooth muscle cells contracting more readily to a given dose of agonist. These responses restrict air flow [126] and contribute to a decrease in lung function. Deterioration in lung function can begin within a few minutes, and reach its worst by 30 minutes before improving over several hours [7].

Some individuals who have allergic asthma can also experience a late response between 6 to 9 hours later. This occurs due to the elevated vascular permeability of the blood vessels, which dilate and transport a large number of eosinophils to the airway wall [34]. Eosinophils are a type of white blood cell that are normally absent or low in number [169]. On arrival, the eosinophils release further proinflammatory mediators, cytotoxic mediators and cytokines, which results in further vascular leakage, mucus hypersecretion, smooth muscle contraction plus epithelial shedding [14].

1.3.2 Airway wall remodelling

Damage to the epithelial surface reduces its protective barrier effect and so increases the likelihood for allergic insult on the airway [11]. In a healthy lung the original structure of the epithelial cells is restored following damage [143]. However, if the repair of the damaged epithelium is incomplete this can lead to persistent asthma. Due to the incomplete repair process, the epithelium produces various growth factors such as epithelial growth factors, fibroblast growth factors and insulin-like growth factors, that can contribute towards tissue remodelling [59]. Greater volumes of these factors can be released in the presence of mechanical stress, chemical and physical injury, virus infection and interactions with inflammatory cells [59, 137]. There are various ways in which airway remodelling may occur, leading to a progressive reduction in lung function [133]. They include the following:

- Goblet cell hyperplasia is the process where goblet cells proliferate abnormally, not only in the proximal airways, where they are usually found, but also in the smallest conducting airways (<2mm in diameter), where they are normally scarce or absent (here the proliferation is known as metaplasia) [147]. As a result more mucus can be secreted, increasing the likelihood that the airways will be blocked, or collapse due to elevated surface tension [14].

- Subepithelial fibrosis leads to a thickened basement membrane, due to extracellular matrix including collagen and fibronectin being deposited [11, 145]. This thickening persists even in patients with well-controlled mild asthma [72].

- ASM cells can increase both in number and size as they undergo hyperplasia and/or hypertrophy [58]. Usually this mainly affects the large airways, but in some cases the whole network is affected [14].

- As a damaged airway is repaired, new blood vessels sprout from the existing vessels, a process called angiogenesis. These airways have been found to be hyperpermeable and lead to an increase of oedema [14].

- The layer between the airway smooth muscle and the parenchyma can also thicken, which may enhance the ability of the ASM to contract by reducing the effect of lung recoil [165].

1.3.3 Diagnosis and treatment

There is no all-encompassing test for asthma with symptoms common to a range of disorders. For example, some of the diseases, whose symptoms can be mistaken for asthma include chronic obstructive pulmonary disease, cystic fibrosis and vocal cord dysfunction [164]. There are various tests that are used to determine the performance of the lung, including measuring the forced expiratory volume in one second (FEV1) and the peak flow in a forced expiration [19]. The results are used to help diagnose for asthma by comparing with normal values for a person of a particular height, gender, ethnicity and age [161], with lung function tending to improve for the first 18-20 years of life before plateauing and then slowly declining [25]. Readings are likely to be lower in those with asthma, since episodes of inflammation and remodelling can lead to persistent airflow obstruction [23]. A reduction in lung function has been seen in large studies for all people suffering from asthma, with greater reduction in those with more severe asthma [136, 142]. The natural decline with ageing is also seen to be accelerated, although many asthmatics can retain a near normal level of lung function throughout life with some reversible acute deterioration [151]. Lung function tests can also be used periodically to highlight any variations and indicate the effectiveness of treatment.

There is also no cure or definitive treatment for asthma. Due to some types of asthma being allergen-induced, it is possible to reduce the likelihood of attacks by avoiding contact with the allergen. However, since this is not always possible, or avoidance alone may not be sufficient, medicines are also required. These can take the form of preventers or relievers [18, 60]. A common treatment for reducing asthma symptoms is the use of bronchodilators, which act as relievers. β_2-adrenoceptor agonists are inhaled, either once asthma symptoms appear or shortly before they are expected, with the agonists attaching to the β_2-adrenoceptor on the airway smooth muscle cell, which leads to ASM relaxation and bronchodilation. Salbutamol and terbutaline are examples of quick-acting relievers, which restore normal breathing within five to ten minutes and are effective for about four hours [60]. Formoterol and salmeterol are examples of long-acting relievers, which act more slowly but can induce bronchodilation for at least 12 hours [131]. Indacaterol is an example of an ultra-long acting reliever, which need only be taken once every 24 hours [149]. Rather than relieving symptoms, corticosteroids inhibit the expression of cytokines, chemokines and adhesion molecules, reducing the inflammation of the airways, thus preventing the onset of asthma symptoms [5].

Bronchial thermoplasty is a more recently developed treatment for severe asthmatics, that involves transmitting radiofrequency energy to the airway wall to reduce the ASM mass [30]. Following treatment it has been observed that the frequency of severe exacerbations reduced, but lung function tests and hyperresponsiveness measures showed no significant difference [9].

1.3.4 Experiments on ASM

There has been a large amount of experimental research to understand the processes behind asthma better. Since the hyper-responsiveness of ASM to certain external stimuli, and the associated remodelling of the airway wall, is central to the development of asthma, research into ASM in particular has widespread clinical significance [82]. One approach that has aided understanding has been an experimental one, involving the addition of agonists that are known to cause smooth muscle contraction. The resulting isometric force or contraction can be found, so that dose response curves can be plotted [12, 33, 42, 132, 182]. However, *in vivo* the length of the ASM within the airway will vary continuously due to tidal breathing and periodic deep inspirations. It has also long been known that a deep inspiration (DI) has a bronchodilatory effect on constricted airways of normal subjects [122], while for asthmatics a DI may have a reduced bronchodilatory effect, may do nothing, or may even result in additional contraction [107]. Due to the importance of understanding the difference between asthmatics and non-asthmatics, many experiments have been designed to investigate how dynamic stretching affects the level of bronchocontraction.

A number of experiments have been carried out on tracheal tissue strips, dissected from a variety of different species, with most of the extracellular matrix removed [8, 43, 174]. Agonist is applied to the strips, which are stretched and clamped at each end and allowed to reach maximum isometric force. Length oscillations are then prescribed with the resulting force along the strip being recorded, from which force-length loops can be plotted [8, 43]. These studies showed that the introduction of length oscillations reduces the mean contractile force, with the size of the reduction proportional to the amplitude of the oscillations. Similar experiments were carried out on airways dissected from the parenchyma by applying volume oscillations [50], for which increased oscillation amplitude again resulted in reduced contractile force. Due to the questions over the relevance of length/volume oscillations of ASM *in vivo*, further experiments have been carried out on tissue strips, where force rather than length was prescribed [104, 129]. The size of the force exerted on the strip was chosen to try to mimic the force that a ring of ASM would experience when physiological transpulmonary pressures are applied to the lung. The Young Laplace approximation and the semi-empirical expressions of Lambert *et al.* [96, 98] were used to approximate the force. Results showed that increasing the amplitude of the transpulmonary pressure led to a reduction in the mean force along the strip and an increase in the mean length of the strip.

In the last few years, experiments have also been developed to prescribe physiological transmural pressures to airways dissected from the parenchyma [103, 125]. In contrast to the strip experiments, initial results on bovine airways demonstrated little reduction in contraction when tidally oscillated compared to when static [103]. Having initially questioned whether the result was species specific [124], Noble *et al.* went on to show that similar results are found with human airways [125]. A number of editorials were published that discussed questions raised by these differences [100, 102, 124]. LaPrad *et al.* [103] pose the following questions: are appropriate loading conditions being applied to the ASM strips, which are based on static airway wall models, while the experiments on the airway are dynamic; how do the oscillatory strains measured in the airway compare to the actual strain in the ASM; do the geometry and structure of the airway wall provide a unique mechanical environment, thus producing the differences observed?

In a recent paper, Noble *et al.* [101] obtained a number of surgically removed bronchial segments from subjects with or without known asthma. They found some evidence that ASM mass was a key reason for the greater contraction in segments from asthmatics and, independent of diagnosis for asthma, if segments were initially equally contracted, they would respond in the same way to deep inspirations. They therefore concluded that the maximum contraction and the reduced bronchodilatory response to deep inspirations in asthma are independent, and that there does not exist some impairment in asthmatic tissue that reduces the effectiveness of deep inspirations.

Another way to study the ASM is through the use of precision-cut lung slices [12], which allows contacted airways embedded in parenchyma to be studied. Recently Lavoie *et al.* [105] developed a technique that allows for oscillatory stretching of the surrounding parenchyma, to simulate breathing. They also found that the amount of stretch experienced by the ASM was important in determining the level of reversal of bronchoconstriction, with both the amplitude of the oscillations and the severity of the initial contraction being important factors.

1.3.5 Summary

The airways are integral in the transport of oxygenated air into the lung and the removal of carbon dioxide. In asthma these processes can be hindered as the airways narrow, due to an exaggerated response to inhaled allergens, characterised by extra mucus secretion and ASM contraction. The contractile force produced by the ASM depends on calcium signalling and the attachment of cycling crossbridges between myosin and actin filaments within the ASM cells. Another important feature is the long-term remodelling of the airway wall, including increased ASM mass, which can lead to the persistence of inflammation and asthma symptoms. Due to the nature of asthma — with contributions ranging from calcium signalling right up to the deformation of the lung as a whole — there is a wide spectrum of length scales that are important. Due to the importance of both inflammation and airway remodelling there are also multiple timescales involved.

Between asthma sufferers there are large variations in the triggers and symptoms and there is no definitive treatment or cure. In order to try to understand ASM more fully, a range of experiments have been carried out with various geometries and protocols, but the results from the different experiments have not been consistent. Experiments have been carried out on tissue strips, dissected airways and lung slices, where length oscillations or pressure oscillations have been prescribed. The results are very difficult to compare given the potentially different strains being imposed, existence (or lack) of parenchymal tethering and changes in geometry of the ASM. A mathematical model will enable us to understand how different factors contribute. Some of the things that could be taken into account by the model include:

- the thickness of the airway wall due to remodelling;
- the level of agonist applied to the airway;
- the effect collagen has on the airway;
- how passive forcing alters the level of contraction;
- how ASM responds differently in a strip compared to in an airway.

In the following sections we shall review existing mathematical models, indicating areas for us to further investigate, before going on to review some of the mathematical techniques that will be required to carry out the modelling.

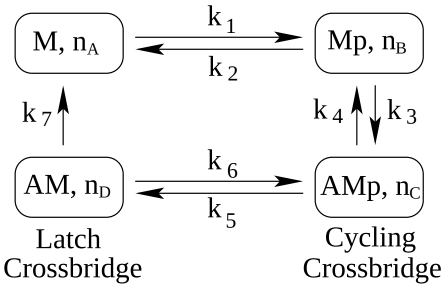

Figure 1.4: Four state crossbridge model by Hai and Murphy [52]. *M* refers to the myosin filament. *A* refers to the actin filament, which a crossbridge has attached to. *p* indicates that a crossbridge has been phosphorylated. The *n*s refer to the fraction of crossbridges in each of the states.

1.4 Review of mathematical models

We begin by considering models that describe the crossbridge dynamics before moving on to previous models of asthmatic airways.

1.4.1 Crossbridge mechanics

In the 1980s a model for crossbridge dynamics of smooth muscle was introduced by Hai and Murphy [52] consisting of four states. Myosin crossbridges can be detached and unphosphorylated, M, detached and phosphorylated, Mp, attached and phosphorylated, AMp, or attached and dephosphorylated, AM. The phosphorylated crossbridges are called cycling crossbridges due to the fact that they are rapidly attaching and detaching. The attached-dephosphorylated crossbridges detach more slowly and are known as latch bridges. The possible reactions from the Hai-Murphy model are shown in figure 1.4. The rates at which unattached crossbridges are phosphorylated and dephosphorylated are k_1 and k_2, respectively. k_1 is related to the calcium concentration, while k_2 is related to the level of agonist. Similarly the attached crossbridges are phosphorylated and dephosphorylated at rates k_6 and k_5. Phosphorylated crossbridges attach at a rate k_3 and detach at a rate k_4. Dephosphorylated crossbridges detach at a rate k_7 (experiments have shown that the crossbridges must be phosphorylated in order to attach).

By considering n_A, n_B, n_C and n_D, representing the fraction of crossbridges in states M, Mp, AMp and AM, respectively, in the chemical kinetic scheme (Fig. 1.4), Hai and Murphy [52] derive four coupled ordinary differential equations, which in vector form become

$$\frac{\mathrm{d}\mathbf{n}(t)}{\mathrm{d}t} = \mathsf{Q}(t)\mathbf{n}(t), \tag{1.4.1}$$

where **n** is a vector of the crossbridge state fractions and Q is the transition matrix given by

$$\mathrm{Q} = \begin{pmatrix} -k_1 & k_2 & 0 & k_7 \\ k_1 & -k_2 - k_3 & k_4 & 0 \\ 0 & k_3 & -k_5 - k_4 & k_6 \\ 0 & 0 & k_5 & -k_6 - k_7 \end{pmatrix}. \tag{1.4.2}$$

In order to take into account load fluctuations on the rates of attachment and detachment, Mijailovich *et al.* [116] and Fredberg *et al.* [44] integrated the four-state model of Hai and Murphy [52] with the sliding filament theory of muscle contraction developed by Huxley [68]. The adapted model is referred to as HHM theory. The rates of phosphorylation and dephosphorylation are unchanged, but now phosphorylated crossbridges attach at a rate $f_p(x)$ and detach at a rate $g_p(x)$, and dephosphorylated crossbridges detach at a rate $g(x)$. These rates depend on x, where x is the distance along the actin filament to the binding site (Fig. 1.5). Attachment is assumed only to be possible if the actin binding site is in the interval $0 < x < h$, where h is the power-stroke length. Detachment can occur at any x. If $x < 0$, the rate of detachment is assumed to be much more likely, so that the crossbridges do not stay attached and resist further contraction. If $x > h$, the rate of detachment is assumed to increase as x increases, to take into account the fact that the crossbridges are more likely to snap off, the more they are stretched. The attachment and detachment rates may be described as follows [116]:

$$f_p(x) = \begin{cases} 0, & x < 0 \\ f_{p1} x/h, & 0 \le x \le h \\ 0, & x > h, \end{cases} \tag{1.4.3a}$$

$$g_p(x) = \begin{cases} g_{p2}, & x < 0 \\ g_{p1} x/h, & 0 \le x \le h \\ (g_{p1} + g_{p3}) x/h, & x > h, \end{cases} \tag{1.4.3b}$$

$$g(x) = \begin{cases} g_2, & x < 0 \\ g_1 x/h, & 0 \le x \le h \\ (g_1 + g_3) x/h, & x > h. \end{cases} \tag{1.4.3c}$$

The way that the HHM model is solved depends on what is assumed about the distribution of the actin binding sites. Firstly, it may be assumed that the distance between the actin binding sites is much larger than the region within which the crossbridges can attach, meaning that there is only ever one binding site that a crossbridge can attach to.

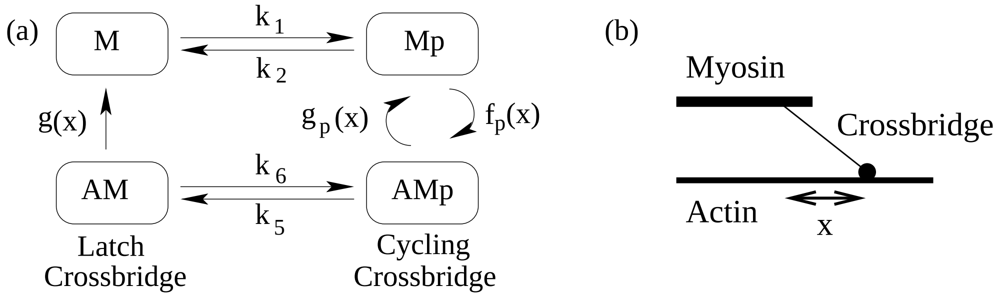

Figure 1.5: (a) The four-state crossbridge HHM model. The rate of attachment and detachment now depend on x. (b) x is the distance reached by a crossbridge to an actin binding site.

In this case there is the following conservation law:

$$n_A(x,t) + n_B(x,t) + n_C(x,t) + n_D(x,t) = 1. \tag{1.4.4}$$

There is the following system of partial differential equations:

$$\frac{\partial \mathbf{n}}{\partial t} - v\frac{\partial \mathbf{n}}{\partial x} = \mathsf{Q}\mathbf{n}, \tag{1.4.5}$$

where v is the velocity of the actin relative to the myosin and is taken to be positive during contraction, $\mathbf{n}$ is a vector of the crossbridge state fractions and Q is the transition matrix given by

$$\mathsf{Q}(x,t) = \begin{pmatrix} -k_1 & k_2 & 0 & g(x) \\ k_1 & -k_2 - f_p(x) & g_p(x) & 0 \\ 0 & f_p(x) & -k_5 - g_p(x) & k_6 \\ 0 & 0 & k_5 & -k_6 - g(x) \end{pmatrix}. \tag{1.4.6}$$

Secondly, it can again be assumed that the distance between binding sites Δx is greater than h, but that as the actin filament slides occupied binding sites can enter the region of attachment. The displacement associated with unattached crossbridges is the distance to the binding site with which it could bind, and the density of unattached crossbridges is defined only in the region $0 < x < \Delta x$. While it is only possible for crossbridges to attach in the region $0 < x < h$, due to contraction and extension of the muscle, it is possible that there exist attached crossbridges in the region $-\infty < x < \infty$. Whenever an attached crossbridge detaches, it is assumed that it immediately becomes an unattached crossbridge with position $x + i\Delta x$, where i is the smallest integer for which $x + i\Delta x > 0$. The evolution equations for the densities of each of the four types of crossbridges are [80]

$$\frac{\partial n_A}{\partial t} - v(t)\frac{\partial n_A}{\partial x} = k_2 n_B - k_1 n_A + \sum_{i=-\infty}^{\infty} g(x - i\Delta x) n_D(x - i\Delta x, t), \tag{1.4.7a}$$

$$\frac{\partial n_B}{\partial t} - v(t)\frac{\partial n_B}{\partial x} = k_1 n_A - (k_2 + f_p(x)) n_C + \sum_{i=-\infty}^{\infty} g_p(x - i\Delta x) n_C(x - i\Delta x, t), \tag{1.4.7b}$$

$$\frac{\partial n_C}{\partial t} - v(t)\frac{\partial n_C}{\partial x} = k_6 n_D + f_p(x) n_B - (k_5 + g_p(x)) n_C, \tag{1.4.7c}$$

$$\frac{\partial n_D}{\partial t} - v(t)\frac{\partial n_D}{\partial x} = k_5 n_C - (k_6 + g(x)) n_D. \tag{1.4.7d}$$

It is also required that as the muscle contracts or lengthens, the flux of unattached crossbridges at $x = 0$ and at $x = \Delta x$ are equal, so that [80]

$$\frac{\partial n_A(0,t)}{\partial x} = \frac{\partial n_A(\Delta x, t)}{\partial x}, \quad \frac{\partial n_B(0,t)}{\partial x} = \frac{\partial n_B(\Delta x, t)}{\partial x}. \tag{1.4.8}$$

Now if (1.4.7a)-(1.4.7b) are evaluated at $x + i\Delta x$ and summed over all i and then also add (1.4.7c) and (1.4.7d) the following conservation law is found [116]:

$$n_A(x,t) + n_B(x,t) + \sum_{i=-\infty}^{\infty} \left[n_C(x + i\Delta x, t) + n_D(x + i\Delta x, t) \right] = 1, \tag{1.4.9}$$

for $0 < x < \Delta x$. More complex models could also be derived, for which $\Delta x < h$ or there is a continuous distribution of binding sites.

An alternative to using the Huxley model [68], to adapt the Hai-Murphy model [53], would be to use a variation of the model of Marcucci and Truskinovsky [110, 111]. Rather than considering the kinetics of the power stroke in terms of jump processes, the energy of the crossbridges is considered and is assumed to evolve stochastically. In brief, they modelled a crossbridge as a spring and a bistable element in series (Fig. 1.6). An attached crossbridge starts off with the end of the spring in the well of the bistable element with the greater potential energy. When the crossbridge performs a power-stroke, the spring stretches and its end moves into the second well. Given a sufficient stimulus the crossbridge can also step along a ratchet, that represents the actin filament. The system cycles spontaneously between the different states, driven by external noise, so that over long timescales (and on average) the behaviour is similar to the deterministic Hai-Murphy model. An advantage of the stochastic system is that arrays of wells and ratchets can be studied to understand force-length-velocity relationships arising from different spatial arrangements of sarcomeres in the cell.

1.4.2 Existing models for asthmatic airways

An overview of relevant previous models of the asthmatic airway are now presented.

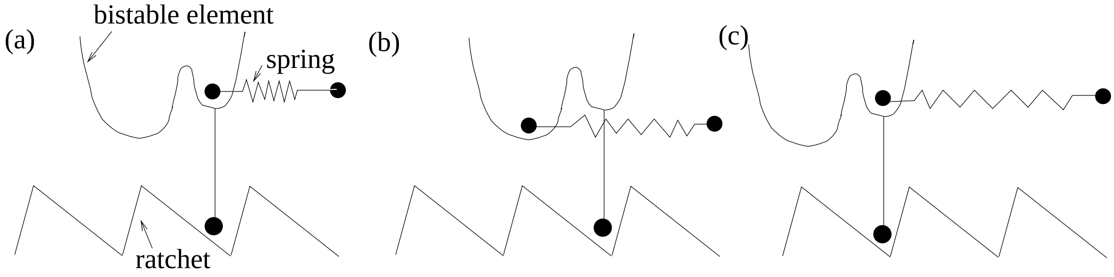

Figure 1.6: Diagram of the setup used by Marcucci and Truskinovsky [111] to model crossbridge mechanics in skeletal muscle. The model consists of a spring, a bistable element and a Brownian ratchet. (a) The spring starts off in the higher potential well of the bistable element. (b) Following a power stroke, the spring moves to the lower potential well. (c) The crossbridge can step along the ratchet, with the spring returning to the higher potential well of the bistable element. The process can repeat.

While considering expiratory flow, Lambert *et al.* [98] developed a model for human airways, to describe the relationship between α, the airway area normalised by the maximum airway area, and P, the transmural pressure. The model was based on the data of Weibel [176] and Hyatt *et al.* [69] and consisted of two rectangular hyperbolae, so that

$$\alpha = \begin{cases} \alpha_0 \left(1 - \frac{P\alpha_0'}{\alpha_0 n_1}\right)^{-n_1} & \text{if } P \leq 0 \\ 1 - (1-\alpha_0)\left(1 + \frac{P\alpha_0'}{(1-\alpha_0)n_2}\right)^{-n_2} & \text{if } P > 0. \end{cases} \tag{1.4.10}$$

There are five parameters, the maximum airway area, α_0 and α_0', the normalised area and slope when $P = 0$, and n_1 and n_2. The value of these parameters are set for each airway generation. Lambert and Wilson [97] extended this work to take into account smooth muscle contraction. They expressed the transmural pressure as the sum of three terms: the elastic recoil pressure due to the distortion of the airway wall given by (1.4.10); a recoil pressure due to distortion of the parenchyma; and a pressure due to the contraction of ASM. The Laplace law for thin cylinders is used to assume that the pressure due to the muscle is of the form

$$P_m = \frac{F}{r_m}, \tag{1.4.11}$$

where r_m is the radius to the muscle and F is active force, that can be modelled to take into account the level of muscle activation, muscle length and length history.

In recent years a number of further models of the asthmatic airway have been published. Wang *et al.* [173] assumed the ASM cells formed a ring that was embedded in a linearly elastic, isotropic, homogeneous sheet. Assuming axisymmetry they found that the radial displacement u_r satisfies

$$u_r = -\frac{N_c F}{2\mu}, \tag{1.4.12}$$

where μ is the shear modulus of the sheet and N_c is the number of ASM cells arranged serially around the airway, each of which exert the tangential force F. F is proportional to the first moment of the attached crossbridge distribution [173],

$$F = \kappa \int_{-\infty}^{\infty} x(n_C + n_D)\mathrm{d}x, \tag{1.4.13}$$

where κ takes into account the stiffness of the crossbridges. The number of attached crossbridges is found by solving the HHM model, accounting specifically for calcium dependent changes in the rates of phosphorylation and dephosphorylation of the crossbridges. The model is able to predict contractions due to an agonist.

A further multiscale model is presented by Politi *et al.* [140]. The model not only takes into account the crossbridge mechanics and the airway, but also the branching structure of the airway tree and the conditions on the lung as a whole due to breathing and gravity. For the model of the airway itself, Politi *et al.* [140] assume a three-layered axisymmetric cylinder under plane strain. The layers represent passive tissue, a muscle layer and the parenchyma. In order to determine the relationship between the airway radius and the pressure difference across the inner layer, the model of Lambert *et al.* [98] as shown in (1.4.10) is assumed. Within the muscle layer there is a circumferential contractile force, which is calculated by solving HHM theory. Finally, the parenchyma local to the airway is modelled as a homogeneous, linearly elastic layer that provides a tethering force. Results indicate that tidal breathing reduces the size of the contractile force.

Rather than simply having a ring of muscle, Brook *et al.* [22] considered the structural aspects of the airway wall, by considering a thickened wall, as observed in asthmatics [58], and by taking into account the ratio of connective tissue to muscle. They developed a linearly elastic model of the airway wall embedded in parenchyma. Within the airway wall, a uniform contractile force was prescribed along fibres in the circumferential direction. The model predicts that for a thickened wall, significant stress heterogeneities can exist; at some points the wall is under compression, while at others it is under tension. Brook *et al.* [22] also investigated how muscle and extra-cellular matrix growth affect the heterogeneities predicted, with the model predicting that the heterogeneities are more pronounced when muscle growth is dominant. The average hoop stress was found to be close to the stress calculated using the Young-Laplace approximation. However, the Young-Laplace approximation, that has often been used to model narrowing airways (e.g. (1.4.11)), averages out the heterogeneity that is predicted to exist.

An alternative to the elastic models would be viscoelastic models. In order to model the hysteresis observed when length oscillations are applied to an unactivated strip of ASM, Bates *et al.* [8] assumed that the passive component of the material could be described using a spring parallel to a spring and dashpot in series. A similar arrangement of springs and dashpots that were in series with the force generator, was assumed to describe the active component of the material. With such a model they were able to get a reasonable fit to the data from the strip experiment. While this model is for a strip of ASM, a similar model could be used for an airway.

1.4.3 Other relevant models

Various techniques have also been used to model the lung parenchyma. A number of strain-energy functions have been proposed including those of Lai-Fook *et al.* [90, 92], Stamenovic and Wilson [159] and Fung *et al.* [45]. However, each of these are quite complex, depending on six, six and four parameters respectively. Alternatively, Mead *et al.* [113] and Takishima and Mead [167] assumed a network of hexagonally arranged springs. However, it has been shown that predictions differ when the parenchyma is modelled as a network of hexagonally arranged springs or as an elastic continuum [108], and by comparing the model predictions to the displacement observed in a contracting lung slice, Ma *et al.* [109] showed that the continuum approach is superior. When modelling lung ventilation, further models were developed consisting of an elastic or viscoelastic porous material [99, 130, 153].

Buckling of airways is also an important feature, although beyond the scope of this thesis. For models of mucosal folding the reader is pointed to the work of Wiggs *et al.* [179] and the simplified model of Donovan and Tawhai [38]. A model that takes into account growth, by increasing the mass in the radial or circumferential direction, or a combination of the two, is presented by Moulton and Goriely [119]. For a model taking into account the surface-tension-driven instabilities due to the surfactant and liquid that lines the airways, see the work of Heil *et al.* [56].

1.4.4 Extending the current models

In this thesis we will extend the existing models for the asthmatic airway. Given the interesting model predictions of Brook *et al.* [22] for a thickened airway wall as it contracts, we will extend this work to allow for finite deformations. This will be possible by implementing nonlinear elasticity with fibre-reinforcement within the airway wall. The model of Brook *et al.* [22] will also be extended by using HHM to determine the contractile force as in [140, 173], so that time-dependent solutions can be investigated. By applying oscillatory boundary conditions, in order to mimic breathing, comparisons will be made to experimental data that investigates the effect of tidal breathing on bronchoconstriction. To take into account that the lung parenchyma is strongly viscoelastic, a simple viscoelastic model will also be developed that can be compared to the elastic model.

1.5 Review of mathematical techniques

A review is now presented of some of the mathematical techniques required to develop the model of the airway wall embedded in parenchymal tissue. Nonlinear elasticity is introduced in section 1.5.1, including a discussion on strain energy functions and an introduction to the incorporation of anisotropy and active force within fibres. Some simple models for a linear viscoelastic material are reviewed in Sec. 1.5.2.

1.5.1 Nonlinear elasticity

If $\mathbf{X}$ and $\mathbf{x}$ denote the position vector of a material point in the reference and deformed configurations, the deformation gradient tensor F, defined by

$$\mathsf{F} = \text{Grad}\mathbf{x} \quad \text{or} \quad F_{ij} = \frac{\partial x_i}{\partial X_j}, \tag{1.5.1}$$

maps the deformation from the reference to the current configuration. The deformation gradient tensor can split in the following ways [36]:

$$\mathsf{F} = \mathsf{RU}, \quad \mathsf{F} = \mathsf{VR}, \tag{1.5.2}$$

where R is a proper orthogonal rotation tensor, and U and V are positive definite symmetric tensors known as the right and left stretch tensors. Two other important symmetric tensors are the right and left Cauchy-Green deformation tensors that are related to the square of the stretch and are respectively defined as

$$\mathsf{C} = \mathsf{F}^T\mathsf{F} = \mathsf{U}^2, \quad \mathsf{B} = \mathsf{F}\mathsf{F}^T = \mathsf{V}^2. \tag{1.5.3}$$

B and C depend on the coordinate system that is used; however, stress invariants are independent of the coordinate system that is used. The isotropic invariants of C are given by

$$I_1 = \text{tr}(\mathsf{C}), \quad I_2 = \frac{1}{2}\left[\text{tr}(\mathsf{C})^2 - \text{tr}\left(\mathsf{C}^2\right)\right], \quad I_3 = \det(\mathsf{C}). \tag{1.5.4}$$

The isotropic invariants of B are defined analogously.

Now while isotropic materials have the same material properties in all directions, in order to include extensible fibres to model the collagen and ASM, an anisotropic material is required. Assuming that there are two sets of densely-distributed fibres with preferred directions $\mathbf{M}_1$ and $\mathbf{M}_2$, there are the following additional strain invariants [128]:

$$\begin{aligned} I_4 &= \mathbf{M}_1 \cdot (\mathsf{C}\mathbf{M}_1), \quad I_5 = \mathbf{M}_1 \cdot (\mathsf{C}^2\mathbf{M}_1), \quad I_6 = \mathbf{M}_2 \cdot (\mathsf{C}\mathbf{M}_2), \\ & I_7 = \mathbf{M}_2 \cdot (\mathsf{C}^2\mathbf{M}_2) \quad \text{and} \quad I_8 = \mathbf{M}_1 \cdot (\mathsf{C}\mathbf{M}_2). \end{aligned} \tag{1.5.5}$$

I_4 and I_6 represent the square of the stretch in the directions $\mathbf{M}_1$ and $\mathbf{M}_2$, respectively [63]. The other invariants have no simple physical interpretation.

The second Piola-Kirchoff stress is given by [66]

$$\mathsf{S} = 2\frac{\partial W}{\partial \mathsf{C}} = 2\sum_{i=1}^{3} W_i \frac{\partial I_i}{\partial \mathsf{C}} \tag{1.5.6}$$

where W is the strain-energy function for the material and $W_i \equiv \partial W/\partial I_i$. Therefore [128], S is given by

$$\begin{aligned} \mathsf{S} =& 2\Bigg[W_1\mathsf{I} + W_2\left(I_1\mathsf{I} - \mathsf{C}\right) + W_3 I_3 \mathsf{C}^{-1} + W_4\mathbf{M}_1 \otimes \mathbf{M}_1 + W_5(\mathbf{M}_1 \otimes \mathsf{C}\mathbf{M}_1 + \mathsf{C}\mathbf{M}_1 \otimes \mathbf{M}_1) \\ & + W_6\mathbf{M}_2 \otimes \mathbf{M}_2 + W_7(\mathbf{M}_2 \otimes \mathsf{C}\mathbf{M}_2 + \mathsf{C}\mathbf{M}_2 \otimes \mathbf{M}_2) \\ & + \frac{W_8}{2}(\mathbf{M}_1 \otimes \mathbf{M}_2 + \mathbf{M}_2 \otimes \mathbf{M}_1)\Bigg], \end{aligned} \tag{1.5.7}$$

where I is the identity tensor and $\mathsf{C}^{-1} = \mathsf{F}^{-1}\mathsf{F}^{-T}$ is the inverse of C.

It is necessary to find the Cauchy stress tensor, $\boldsymbol{\tau}$, which is given in terms of the second Piola-Kirchoff stress tensor S as follows:

$$\boldsymbol{\tau} = \frac{\mathsf{F}\mathsf{S}\mathsf{F}^T}{J}, \tag{1.5.8}$$

where

$$J = \det(\mathsf{F}) = \sqrt{I_3} \tag{1.5.9}$$

is the ratio between the current volume and the undeformed volume. Using (1.5.7) and (1.5.8), the Cauchy stress tensor is

$$\begin{aligned} \boldsymbol{\tau} = \frac{2}{J}\Bigg[& W_1\mathsf{B} + W_2\left(I_1\mathsf{B} - \mathsf{B}^2\right) + I_3W_3\mathsf{I} + W_4\mathbf{m}_1 \otimes \mathbf{m}_1 + W_5(\mathbf{m}_1 \otimes \mathsf{B}\mathbf{m}_1 + \mathsf{B}\mathbf{m}_1 \otimes \mathbf{m}_1) \\ & + W_6\mathbf{m}_2 \otimes \mathbf{m}_2 + W_7(\mathbf{m}_2 \otimes \mathsf{B}\mathbf{m}_2 + \mathsf{B}\mathbf{m}_2 \otimes \mathbf{m}_2) \\ & + \frac{W_8}{2}(\mathbf{m}_1 \otimes \mathbf{m}_2 + \mathbf{m}_2 \otimes \mathbf{m}_1)\Bigg], \end{aligned} \tag{1.5.10}$$

where $\mathbf{m}_1 = \mathsf{F}\mathbf{M}_1$ and $\mathbf{m}_2 = \mathsf{F}\mathbf{M}_2$ are the directions of the two sets of fibres in the current configuration. Conservation of momentum requires $\nabla \cdot \boldsymbol{\tau} = 0$, where differentiation is with respect to the deformed configuration [155].

1.5.1.1 Strain-energy functions

Strain-energy functions relate the energy put into the material with the resulting strain. So that the function is independent of the coordinate system used, the function depends on the stress invariants. There is a lot of freedom in the choice of the function, but for the stress to vanish in the reference configuration it is required that

$$\left(\frac{\partial W}{\partial I_1}+2\frac{\partial W}{\partial I_2}+\frac{\partial W}{\partial I_3}\right)\bigg|_{I_1=I_2=3,I_3=1}=0. \tag{1.5.11}$$

Some commonly used strain energy functions are now briefly described.

A simple strain-energy function for incompressible materials is the neo-Hookean function that depends only on I_1 and the shear modulus μ so that

$$W=\frac{\mu}{2}(I_1-3). \tag{1.5.12}$$

A slightly more complicated version is that of a Mooney-Rivlin material, which satisfies

$$W=c_1(I_1-3)+c_2(I_2-3), \tag{1.5.13}$$

where c_1 and c_2 are material constants.

The following extension of the Mooney-Rivlin model is given in [62], to allow for the material to be compressible:

$$W=\alpha\frac{\mu}{2}(I_1-3)+(1-\alpha)\frac{\mu}{2}(I_2-3)+c(J-1)^2-d\log J, \tag{1.5.14}$$

where $\alpha\in[0,1]$ is an interpolation parameter and the terms containing J were proposed by Ciarlet and Geymonat [26]. c is a material parameter and d is a parameter that, assuming the reference configuration is stress free, using (1.5.11) yields $d=\mu(2-\alpha)/2$. This is an example of a strain-energy function where the isochoric component, that deals with volume preserving deformations, and the volumetric component, that deals with volume changes, are coupled. An alternative is split the function into separate volumetric and isochoric components, W_{vol} and W_{iso} respectively, such that

$$W(J,\overline{I}_1,\overline{I}_2)=W_{vol}(J)+W_{iso}(\overline{I}_1,\overline{I}_2), \tag{1.5.15}$$

where $\overline{I}_i=I_i/I_3$ for $i=1,2$. An example of an equation for W_{vol} is the Ogden model for compressible (rubber-like) materials, where

$$W_{vol}=\kappa\beta^{-2}\left(\beta\log J+\frac{1}{J^{\beta}}-1\right). \tag{1.5.16}$$

κ is the bulk modulus and β is a positive material parameter.

As neo-Hookean and Mooney-Rivlin materials are stretched, smaller increases in force are required to stretch the material further. An example of an isotropic strain-energy function that can produce strain-stiffening (so that as the material stretches, larger increases in force are required to stretch the material further) is the Ogden strain-energy function. This depends on the principal stretches, λ_1, λ_2 and λ_3, of F rather than the strain invariants and is given by

$$W = 2\mu \frac{\lambda_1^{\beta} + \lambda_2^{\beta} + \lambda_3^{\beta} - 3}{\beta}, \tag{1.5.17}$$

where μ and β are positive constants [127]. This function is used when modelling incompressible rubber. Holzapfel *et al.* [61] discussed other examples, before developing a new model. Instead of simply assuming an isotropic material, they based their model on the theory of the mechanics of fiber-reinforced composites [157] and assumed that the underlying material is isotropic but there are also anisotropic fibres. The strain-energy function is split into an isotropic part, W_i and an anisotropic part, W_{ani} so that

$$W = W_i(I_1, I_2, I_3) + W_{ani}(I_1, I_2, I_3, I_4, I_5, I_6, I_7, I_8). \tag{1.5.18}$$

For simplicity when considering an incompressible material, Holzapfel *et al.* [61] describe the isotropy by I_1 alone and the anisotropy by I_4 and I_6 so that

$$W(I_1, I_4, I_6) = W_i(I_1) + W_{ani}(I_4, I_6). \tag{1.5.19}$$

For the isotropic component they assume a neo-Hookean material, while modelling W_{ani} as

$$W_{ani}(I_4, I_6) = \frac{k_1}{2k_2} \sum_{i=4,6} H(I_i - 1) \left\{ \exp\left[k_2 (I_i - 1)^2\right] - 1 \right\}, \tag{1.5.20}$$

where $k_1 > 0$ is a stress-like parameter while $k_2 > 0$ is a dimensionless parameter, that can be used to alter the amount of strain-stiffening. $H(I_i - 1)$ is the Heaviside function so that the fibres only contribute when stretched. According to this model, for small stretches the fibres provide little resistance, however, as the fibres stretch the amount of energy required to stretch them further increases exponentially. Gasser *et al.* [47] extended (1.5.20) to also allow for some dispersion of the fibre directions.

1.5.1.2 Including active fibres

In order to take into account the contractile forces produced by the ASM, active forcing can be applied along fibres. As described by Ambrosi and Pezzuto [3], there are two ways in which active stress can be included into a continuum body; either a multiplicative decomposition of the deformation gradient tensor is used or an active component is added to the stress. In the multiplicative setup

$$\mathsf{F} = \mathsf{F}_a \mathsf{F}_e, \tag{1.5.21}$$

where F_a is the active contribution and F_e is the elastic deformation that ensures that the material remains compatible [3], meaning that no gaps or overlaps develop in the deformation. To take into account the orientation of fibres, F_a can take the form

$$\mathsf{F}_a = \mathsf{I} - \gamma \mathbf{m_1} \otimes \mathbf{m_1}, \tag{1.5.22}$$

where $\gamma \in (0, 1)$ and $\mathbf{m_1}$ is the current orientation of the fibres [3]. Examples where the multiplicative method is used are [123, 166].

Using the additive setup the Cauchy stress tensor and the strain-energy function can be split into passive and active components, so for example

$$\boldsymbol{\tau} = \boldsymbol{\tau}_p + \boldsymbol{\tau}_a, \tag{1.5.23}$$

where $\boldsymbol{\tau}_p$ gives the passive stress and $\boldsymbol{\tau}_a$ gives the active stress. The general form for the active component, in the case that the orientation of the fibres is taken into account, is [3]

$$\boldsymbol{\tau}_a = \frac{f(I_4)}{J} \left(\mathbf{m}_1 \otimes \mathbf{m}_1 \right). \tag{1.5.24}$$

There have been a number of suggestions for the form of $f(I_4)$, each of which include a function A, to take into account the level of activation, and the fibre stretch λ. When modelling vascular smooth muscle Rachev and Hayashi [141] used the following form:

$$f(I_4) = A\lambda \left(1 - \left(\frac{\lambda_m - \lambda}{\lambda_m - \lambda_0} \right)^2 \right), \tag{1.5.25}$$

where λ_m is the stretch at maximum activation and λ_0 is the stretch when activation ceases. Alternatively, when modelling contracting myocytes, Tracqui and Ohayon [172] let

$$f(I_4) = A(Ca^{2+}) \exp\left(\frac{(\lambda_m - \lambda)^2}{a} \right), \tag{1.5.26}$$

where a is a positive parameter and λ_m again represents the stretch at maximum activation. Here, a Hill function is used to describe the contribution of the calcium concentrations to A. Again, in modelling vascular smooth muscle, Zulliger *et al.* [185] let

$$f(I_4) = A\left(\lambda - 1\right). \tag{1.5.27}$$

Further models have coupled the chemical state model of Hai and Murphy [52] (Sec. 1.4.1) with a mechanical model. Models for smooth muscle cells and vessels in arteries were introduced by Yang *et al.* [183, 184]. Stålhand *et al.* [158] developed these models to enable the coupling of the crossbridge mechanics to a continuum mechanics model. Two further models coupled to the model of Hai Murphy [52] are those of Kroon [83] and Murtada *et al.* [120].

Kroon [83] considers that the strain energy function can be split into an active component, W_a, and a passive component, W_p, modelling the active component by considering a spring in series with a dashpot. This takes into account the relative sliding of the myosin and actin filaments, which are assumed to be rigid, and the elastic stretching of the attached crossbridges. The stretch of the contractile unit is given by

$$\lambda_f = \lambda_s \lambda_e, \tag{1.5.28}$$

where λ_s is the stretch due to the sliding of the filaments and λ_e is the stretch due to the elastic stretching of the crossbridges (Fig. 1.7). Kroon assumes the active component to the strain-energy function satisfies

$$W_a = \frac{\mu_f}{2}(n_C + n_D)\left(\frac{\lambda_f^2}{\lambda_s^2} - 1\right)^2, \tag{1.5.29}$$

where μ_f is related to the stiffness of the crossbridges and the number of contractile units per unit area. The following evolution equation is used to update λ_s, taking into account T_e, the active stress caused by the attached crossbridges, and $\frac{\partial W_a}{\partial \lambda_s}$, the resistance to filament sliding:

$$\varpi \dot{\lambda}_s = T_e - \frac{\partial W_a}{\partial \lambda_s}, \tag{1.5.30}$$

where ϖ is a viscous damping parameter. Since contraction relates to $\dot{\lambda}_s < 0$, $T_e < 0$. In prescribing T_e it was assumed that there are three possibilities: the cycling crossbridges (n_C) provide a force that is greater than the resistance to sliding so the muscle contracts; the cycling crossbridges are not strong enough to lead to contraction, but with the latch bridges (n_D) they resist backsliding; the crossbridges are unable to resist backsliding and the latch bridges detach. T_e is thus prescribed as follows [83]:

$$T_e = \begin{cases} -v_C n_C, & \text{if } -\frac{\partial W_a}{\partial \lambda_s} < v_C n_C, \\ \frac{\partial W_a}{\partial \lambda_s}, & \text{if } v_C n_C \leq -\frac{\partial W_a}{\partial \lambda_s} \leq v_C n_C + v_D n_D, \\ -v_C n_C, & \text{if } v_C n_C + v_D n_D < -\frac{\partial W_a}{\partial \lambda_s}, \end{cases} \tag{1.5.31}$$

where v_C and v_D are material parameters relating to the driving force of the phosphorylated crossbridges and passive resistive strength of the latch bridges. In a follow-up paper Kroon [84] developed the model to include dispersion of the orientation of the filaments.

A similar model was developed by Murtada *et al.* [120]. They first found an expression for the (averaged) first Piola-Kirchoff stress acting on the contractile units T_f, motivated

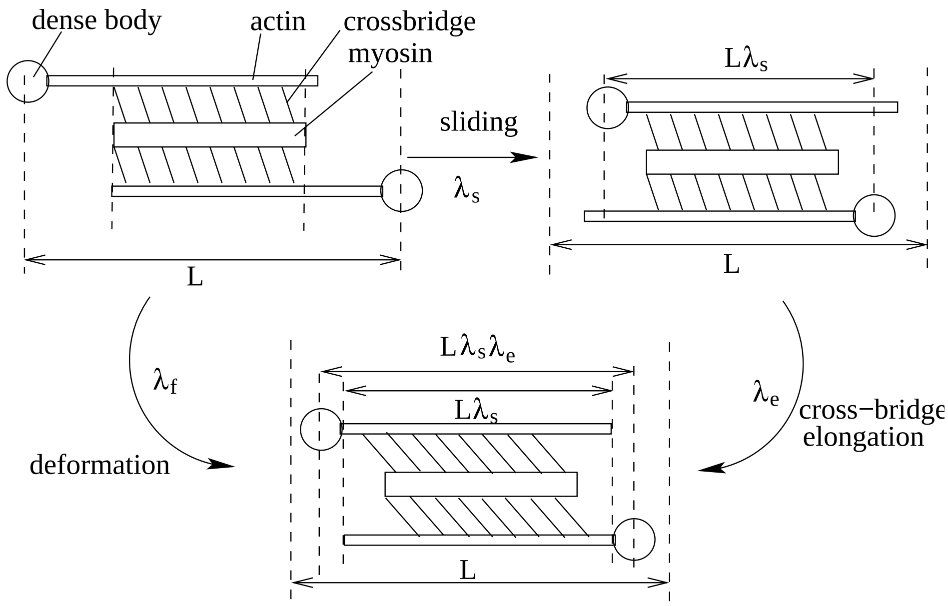

Figure 1.7: Diagram of the deformation of the contractile unit. The deformation is composed of a stretch, λ_s caused by the actin filaments sliding past the myosin during contraction and a stretch, λ_e caused by the crossbridges stretching. In the reference configuration the unit has length L, while in the deformed state it has length $L\lambda_s\lambda_e$. Adapted from [120].

by considering the attached crossbridges. The total number of attached crossbridges within a contractile unit is $(n_C + n_D)\rho$, where ρ is the number of available crossbridges, which is assumed to remain constant. Considering the change of length parallel to the filaments, each of the crossbridges have stiffness E_f, while the actin and myosin filaments are assumed to be rigid. If there are N_f contractile units per unit area, summing over all the attached crossbridges, the resulting stretch of the crossbridges is given by

$$\lambda_e = 1 + \frac{T_f}{L\lambda_s(n_C + n_D)E_f\rho N_f}, \tag{1.5.32}$$

where L is the reference length of a contractile unit. From (1.5.28) and (1.5.32)

$$T_f = \mu_a(n_C + n_D)\lambda_s(\lambda_e - 1) = \mu_a(n_C + n_D)(\lambda_f - \lambda_s), \tag{1.5.33}$$

where $\mu_a = L\rho E_f N_f$.

The following strain-energy function is found by integrating (1.5.33) with respect to λ_f:

$$W_a = \frac{\mu_a}{2}(n_C + n_D)(\lambda_f - \lambda_s)^2. \tag{1.5.34}$$

Murtada *et al.* [120] also assume a slightly different form for the evolution equation to Kroon [83], letting $v_C = v_D$ and assume that the latch bridges are able to resist elongation, so that

$$T_e = -v_C(n_C + n_D), \quad \text{if } v_C(n_C + n_D) < -\frac{\partial W_a}{\partial \lambda_s}. \tag{1.5.35}$$

Once again this work was extended to allow for the dispersion of filaments [121].

Instead of using the Hai-Murphy model [52], the HHM model could be used ([140, 173] use the HHM model but assume linear elasticity). Whereas with the Hai-Murphy model [52] the number of attached crossbridges will tend towards a steady state unless the rate parameters are altered, with the HHM model passive forcing can alter the distribution, due to the x dependence in the rate parameters. The HHM model also takes into account the velocity of the relative sliding of the myosin and actin filaments, so there is no need for a separate evolution equation, and the number and position of each of the attached crossbridges are updated at each timestep.

While many of these models assume that the number of crossbridges available for binding is constant, for finite displacements the number available will vary. There have been a number of approaches to try to overcome this. One approach is to match up to data by using producing a phenomenological model as used by Schmitz and Böl [150] or Politi *et al.* [140] to enable a certain stretch at which the active forcing is greatest. Politi *et al.* multiply the force given by (1.4.13) by the following factor:

$$f_l = \sin\left(\frac{\pi r}{2 r_{max}}\right)^3, \tag{1.5.36}$$

where r_{max} is the lumen radius at which the force is greatest. Alternatively Kroon [85] considers how the overlap length of the myosin and actin filaments varies and so the number of crossbridges available. The model of Brook and Jensen [21] also considers the change in the number of crossbridges available. They do so by considering both the overlap length and how the filaments are able to remodel as the length of the smooth muscle cells changes.

1.5.2 Linear Viscoelasticity

Elastic materials deform instantaneously to a new equilibrium state when stresses are applied to them, returning to the initial state when the stresses are removed, while viscous materials deform indefinitely under an applied load. Viscoelastic materials exhibit a mixture of these properties. Viscoelastic materials will be referred to as viscoelastic solids or liquids depending on how they act at long timescales. In a solid the elastic properties dominate at large time, while in a fluid the viscous properties dominate.

When stress is increased on a viscoelastic material there will be an immediate change in the strain followed by a time-dependent increase in strain, known as creep. At large times the strain of viscoelastic solids will tend to some equilibrium, however viscoelastic fluids will strain indefinitely [138].

Increasing the strain will initially cause the stress to increase but then it will reduce over some time scale. This is known as stress relaxation [138]. The stress in a viscoelastic solid will reach an equilibrium greater than zero, while the stress in a viscoelastic fluid will tend to zero.

Hysteresis is observed in viscoelastic materials when a sinusoidal force is applied to the material. For an elastic material the strain curve is in phase with the forcing curve, while the curves are out of phase by $\pi/2$ in a viscous material. For a viscoelastic material the strain lags behind by a phase angle between zero and $\pi/2$ [93].

1.5.2.1 Standard Linear solid model

Some simple one-dimensional viscoelastic models, which incorporate springs and dashpots so that both elastic and viscous properties can be accounted for, are now considered. The relationship between stress, σ, and strain, ϵ, in a linear spring is $\sigma = E\epsilon$, where E is the elastic modulus. In a dashpot, $\sigma = \eta\frac{\mathrm{d}\epsilon}{\mathrm{d}t}$, where η is a viscosity. Two elements in parallel experience the same strain, while the total stress is the sum of the stresses in the two elements. Two elements in series experience the same stress, while the total strain is the sum of the strains of the elements.

Some simple configurations are the Maxwell model, consisting of a spring and a dashpot in series; the Kelvin-Voigt model, consisting of a spring and dashpot in parallel; and the Standard Linear solid model, consisting of a spring and a Maxwell model in parallel. The Standard Linear model with parameters as shown in Fig. 1.8 reduces to the Maxwell model in the limit $E_0 \to 0$, or the Kelvin-Voigt model in the limit $E_1 \to \infty$. The limit $E_0 \to \infty$, would result in a rigid material, while the limit $E_1 \to 0$, would result in a single spring with elastic modulus E_0. Taking the limits $\eta \to 0$ or $\eta \to \infty$ would reduce to springs with elastic moduli E_0 or $E_0 + E_1$, respectively.

The constitutive equation for the Standard Linear solid is

$$\frac{\eta}{E_1}\frac{\mathrm{d}\sigma}{\mathrm{d}t} + \sigma = E_0\left(\left(\frac{1}{E_0} + \frac{1}{E_1}\right)\eta\frac{\mathrm{d}\epsilon}{\mathrm{d}t} + \epsilon\right). \tag{1.5.37}$$

resulting in the constitutive equation

$$t_r\frac{\mathrm{d}\sigma}{\mathrm{d}t} + \sigma = E_0\left(t_c\frac{\mathrm{d}\epsilon}{\mathrm{d}t} + \epsilon\right), \tag{1.5.38}$$

where

$$t_r = \frac{\eta}{E_1}, \quad t_c = \frac{\eta}{E_0} + \frac{\eta}{E_1} = t_r\left(1 + \frac{E_1}{E_0}\right) \tag{1.5.39}$$

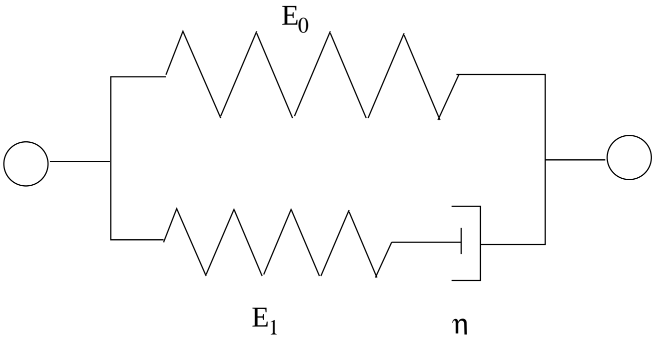

Figure 1.8: The Standard Linear solid model consists of a spring in parallel with a Maxwell model, consisting of a spring and a dashpot in series. The elastic moduli of the springs are E_0 and E_1 and the viscosity of the dashpot is μ.

are the relaxation and creep timescales.

Introducing an instantaneous stress $\sigma(0)$ at time $t = 0$, assuming zero stresses previously, yields the strain

$$\epsilon(t) = \frac{\sigma(0^+)}{E_0} \left\{ 1 - \left(1 - \frac{t_r}{t_c} \right) \exp\left(-\frac{t}{t_c} \right) \right\}, \quad t \geq 0. \tag{1.5.40}$$

An instantaneous elastic response is observed and at large times the strain tends to some equilibrium. Taking the limit $E_1 \to \infty$,

$$\epsilon(t) = \frac{\sigma(0^+)}{E_0} \left\{ 1 - \exp\left(-\frac{E_0 t}{\eta} \right) \right\}, \quad t \geq 0. \tag{1.5.41}$$

Hence with the Kelvin-Voigt model, an instantaneous response is not seen. Taking the limit $E_0 \to 0$,

$$\epsilon(t) = \sigma(0^+) \left\{ \frac{1}{E_1} + \frac{t}{\eta} \right\}, \quad t \geq 0, \tag{1.5.42}$$

hence with the Maxwell model no equilibrium is reached, signifying that at large times it acts as a fluid. This indicates that the standard linear solid model is superior to the other two models.

Introducing an instantaneous strain $\epsilon(0)$ at time $t = 0$, assuming zero stresses previously, yields the stress

$$\sigma(t) = E_0 \left\{ 1 + \left(\frac{t_c}{t_r} - 1 \right) \exp\left(-\frac{t}{t_r} \right) \right\} \epsilon(0). \tag{1.5.43}$$

There is an instantaneous change in stress that will relax to some equilibrium greater than zero.

Stressing a material sinusoidally with frequency f, so the angular frequency satisfies $\omega = 2\pi f$, and amplitude $\bar{\sigma}$,

$$\sigma(t) = \bar{\sigma} \sin(\omega t) = \mathrm{Im}\left(\bar{\sigma} \exp(i\omega t) \right). \tag{1.5.44}$$

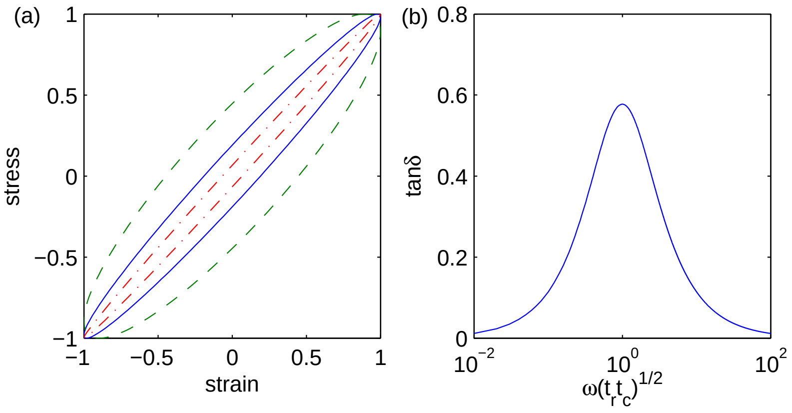

Figure 1.9: (a) Plots of the hysteresis curve from the standard linear solid model when $\omega = 0.1$ (solid), 1 (dashed) and 10 (dot-dashed). The area inside the curves increases and then decreases again, which relates to there being a peak in the loss tangent as shown in (b). The maximum occurs when $t_r t_c \omega^2 = 1$. For these plot $E_0 = 1$, $E_1 = 2$, $\eta = 2$, $\bar{\epsilon} = \bar{\sigma} = 1$.

where Im indicates the imaginary part. The resulting strain satisfies

$$\epsilon(t) = \bar{\epsilon}\sin(\omega t - \delta) = \mathrm{Im}\left(\bar{\epsilon}\exp(i(\omega t - \delta))\right), \tag{1.5.45}$$

where $\bar{\epsilon}$ is the amplitude and δ is the phase angle relating to the lag of the strain. The dynamic modulus E, for the Standard Linear solid, satisfying

$$\frac{\sigma}{\epsilon} = E = E' + iE'', \tag{1.5.46}$$

where E' and E'' are the storage and loss moduli, can be found by substituting the exponential forms into (1.5.37). They have values

$$E' = \frac{\bar{\epsilon}}{\bar{\sigma}}\left(E_0 + E_1\frac{\omega^2 t_r^2}{1+\omega^2 t_r^2}\right), \quad E'' = \frac{\bar{\epsilon}}{\bar{\sigma}}E_1\frac{\omega t_r}{1+\omega^2 t_r^2}. \tag{1.5.47}$$

The loss tangent or hysteresivity is

$$\tan\delta \equiv \frac{E''}{E'} = \frac{\omega(t_c - t_r)}{1+\omega^2 t_r t_c}. \tag{1.5.48}$$

This is a measure of the “internal friction” [46]. The loss tangent is dependent on the angular frequency (Fig. 1.9). As $\omega \to 0$ or ∞, $\delta \to 0$ and $\tan\delta$ is maximum when

$$t_r t_c \omega^2 = 1. \tag{1.5.49}$$

For lung tissue the hysteresis loop is in fact independent of the strain rate within several decades [46], which shows that the standard linear solid model may not be appropriate in some circumstances. This problem can be overcome by adding additional Maxwell models in parallel, each of which have a different timescale [76]. When a graph of $\tan\delta$ against ω is then plotted, the bell shaped graphs from each of the timescales add up to produce a plateau. Alternatively Fung [46] considered introducing a continuous spectrum of relaxation times, although this then leads to additional parameters.

In three dimensions the constitutive equation for a linear elastic material is of the form

$$\sigma_{ij} = \lambda \epsilon_{kk} \delta_{ij} + 2\mu \epsilon_{ij}, \tag{1.5.50}$$

where λ and μ are the Lamé coefficients. Using (1.5.38), (1.5.50) can be transformed into a three-dimensional linear viscoelastic material, based on the standard linear model, by letting

$$\sigma_{ij} \to t_r \frac{\mathrm{d}\sigma_{ij}}{\mathrm{d}t} + \sigma_{ij}, \quad \epsilon_{ij} \to t_c \frac{\mathrm{d}\epsilon_{ij}}{\mathrm{d}t} + \epsilon_{ij}. \tag{1.5.51}$$

Appropriate material derivatives are required when modelling finite deformations.

1.6 Thesis structure

The full mathematical model, that couples the tissue-level mechanics with those of the sub-cellular crossbridges, is outlined in Chapter 2. The tissue-level model consists of two layers to represent the airway wall and surrounding parenchymal tissue. To account for large deformations, nonlinear elasticity is used. To take into account the contribution of the collagen, fibre-reinforcement is included within the airway wall, where it is assumed there are two sets of helically-oriented fibres. These fibres are also used to exert the contractile forces generated by the ASM. The level of force generation is modelled by coupling the tissue model to the HHM model.

The model presented in Chapter 2 is solved in Chapters 3 and 4. Results are shown in Chapter 3 when there is no active forcing. Firstly, the airway wall is considered in isolation and appropriate model parameters are selected. The numerical techniques used to couple the airway wall to the parenchyma are described. Results are shown when passive stresses or displacements are applied to the boundaries, and method of inflation of the airway is investigated. The differences when the parenchyma is elastic or viscoelastic are also investigated.

The effect of active forcing is considered in Chapter 4. By considering the steady-state solutions, the effect of airway wall thickening and the level of activation on the level of contraction and the stress distributions are investigated. Time-dependent forcing is then considered. Initially the force is simply prescribed by solving HHM for the isometric case. Results are then shown when the continuum model is fully coupled to HHM. Comparisons are made between the cases when the parenchyma is elastic or viscoelastic, and the displacement and stress distributions are investigated when the airway contracts or when tidal stretching is applied to the parenchyma. Further validation of the model is shown by making comparisons to the experimental results of LaPrad *et al.* [103]. Finally, comparisons are made between an airway and a tissue strip.

The focus in Chapter 5 shifts from modelling to imaging. Techniques are developed to analyse images of contracting airways from precision-cut lung slice experiments. The area of the lumen is tracked and the rates of contraction are found by fitting to an exponential function with two timescales. In particular it is shown that the contraction depends on multiple timescales and that the mathematical model also predicts this. Techniques are also developed to find an estimate of the displacement field of the tissue surrounding an airway. The level of heterogeneity in the lung slice is investigated and comparisons are made to the mathematical model.

Finally, in Chapter 6 the results and areas for further investigation are discussed.

Chapter 2

Two-layer multi-scale model of an asthmatic airway

In the previous chapter the need for mathematical models of airways was motivated to help improve the understanding of asthma. In this chapter we present our biomechanical model for an asthmatic airway embedded in parenchyma. When modelling the asthmatic airway we want to

- allow for finite deformations and thus use nonlinear elasticity;
- take account of airway wall thickening due to airway remodelling and thus assume a thick walled airway;
- let the subcellular crossbridge mechanics determine the size of the contractile force produced by the airway smooth muscle (ASM) and thus use the Huxley-Hai-Murphy (HHM) model;
- allow for the viscoelastic nature of the lung and thus present a viscoelastic model for the parenchyma.

The geometry of the airway wall and surrounding parenchyma is described in Sec. 2.1, and we discuss how the geometry may be simplified if a plane strain or plane stress approximation is assumed. In Sec. 2.2 the tissue mechanics are considered. By introducing the relevant strain-energy functions, we find the nonzero components of the Cauchy stress tensor. We describe the equilibrium and compatibility equations and the relevant boundary and initial conditions. We end the section by nondimensionalising the governing equations. In Sec. 2.3 we consider the sub-cellular crossbridge mechanics and how it is coupled to the tissue mechanics. We present the governing equations

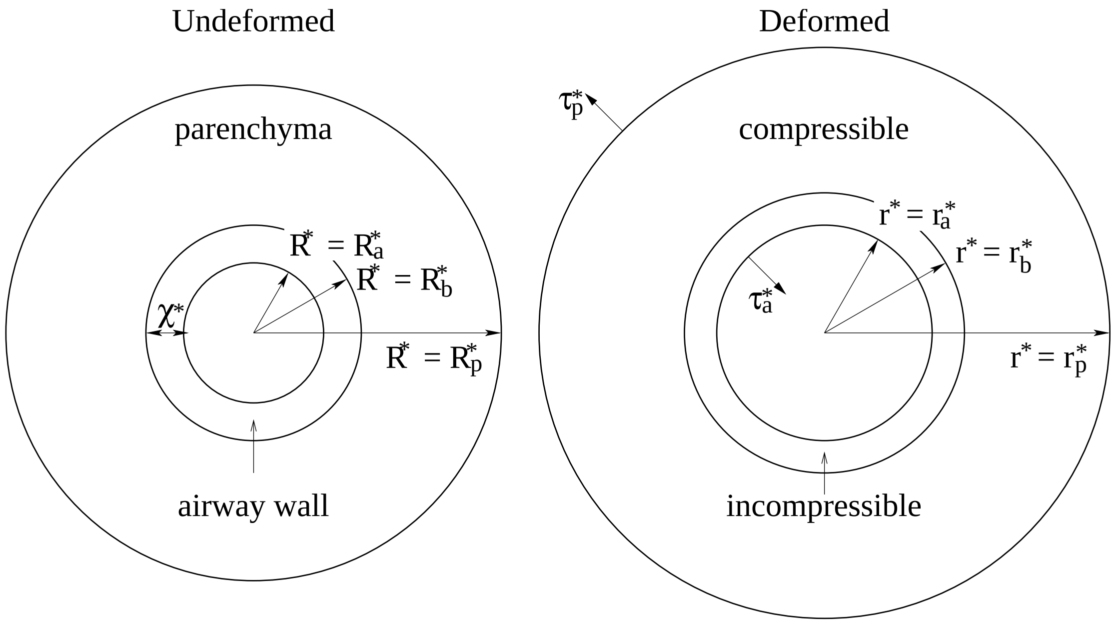

Figure 2.1: The airway is modelled as a thin incompressible layer embedded in a compressible layer with stress $\tau^*_{rr}(R^*_a, t^*) = \tau^*_a(t^*)$ and $\tau^*_{rr}(R^*_p, t^*) = \tau^*_p(t^*)$.

and the initial condition for the crossbridge mechanics, before nondimensionalising the governing equations. We conclude the chapter by summarising the model and briefly describing our approach to solving the model.

2.1 Geometry

We model the airway as a two-layer axisymmetric material, consisting of the airway wall embedded in parenchymal tissue (see Fig. 2.1). Using cylindrical polar coordinates, R^*, Θ, Z^* are Lagrangian coordinates and r^*, θ^*, z^* are coordinates in the deformed configuration. The undeformed airway wall occupies $R^*_a \leq R^* \leq R^*_b \equiv R^*_a + \chi^*$, where χ^* is its undeformed thickness. The parenchyma occupies $R^*_b \leq R^* \leq R^*_p$. It is assumed that the airway wall is much thinner than the surrounding parenchyma, hence $R^*_p - R^*_b \gg \chi^*$. The subscripts a, b and p are used to refer to the inner boundary of the airway wall, the boundary between the airway wall and the parenchyma, and the outer boundary of the parenchyma. Asterisks denote dimensional quantities.

Assuming that deformations are axisymmetric (i.e. there is no buckling) and do not undergo torsion,

$$r^* = r^*(R^*), \quad \theta = \Theta, \quad z^* = \lambda_z Z^*, \tag{2.1.1}$$

where λ_z is the stretch in the axial direction, which is assumed to be equal in the two layers. Hence, the deformation gradient tensor F and the left and right Cauchy Green

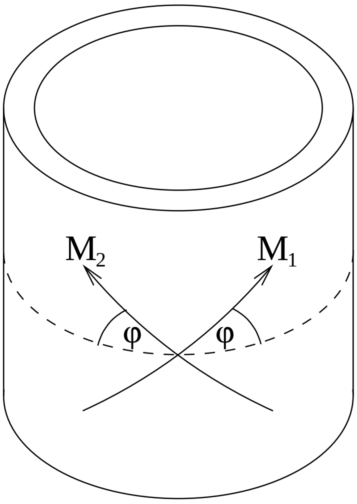

Figure 2.2: The airway wall is embedded with with two sets of fibres, which are symmetrically disposed about the circumferential direction.

stress tensors, B and C, are given by

$$[\mathsf{F}] = \begin{pmatrix} r^{*'} & 0 & 0 \\ 0 & \frac{r^*}{R^*} & 0 \\ 0 & 0 & \lambda_z \end{pmatrix}, \quad [\mathsf{B}] = [\mathsf{C}] = \begin{pmatrix} r^{*'2} & 0 & 0 \\ 0 & \frac{r^{*2}}{R^{*2}} & 0 \\ 0 & 0 & \lambda_z^2 \end{pmatrix} \tag{2.1.2}$$

where $r^{*'} = \partial r^* / \partial R^*$.

Within the airway wall we assume there are two sets of helical fibres that are symmetrically disposed about the circumferential direction and have no radial component (Fig. 2.2). In the undeformed state, they have directions

$$\mathbf{M}_1 = \cos\varphi \mathbf{e}_\theta + \sin\varphi \mathbf{e}_z, \qquad \mathbf{M}_2 = -\cos\varphi \mathbf{e}_\theta + \sin\varphi \mathbf{e}_z, \tag{2.1.3}$$

while in the deformed state, they have directions

$$\mathbf{m}_1 = \mathsf{F}\mathbf{M}_1 = \frac{r^*}{R^*}\cos\varphi \mathbf{e}_\theta + \lambda_z \sin\varphi \mathbf{e}_z, \tag{2.1.4a}$$

$$\mathbf{m}_2 = \mathsf{F}\mathbf{M}_2 = -\frac{r^*}{R^*}\cos\varphi \mathbf{e}_\theta + \lambda_z \sin\varphi \mathbf{e}_z. \tag{2.1.4b}$$

These fibres are endowed with two functions: they stiffen the airway when inflated to mimic collagen and they produce a contractile force due to activated ASM.

The three dimensional problem can be reduced to a two dimensional problem by making one of the following approximations [4]:

- Plane strain is a special case of the three dimensional problem, that may be applied if the length of the cylinder is very long. It requires that the two ends are frictionless and that any boundary conditions are independent of z and have no z-component. The material is thus prevented from stretching axially so $\lambda_z = 1$.

- Plane stress is an approximate solution and requires that the material forms a thin sheet, with a thickness very small compared to the other dimensions. The dominant stresses act in the plane of the material so it is possible to neglect the forces in the z-direction. These forces may be neglected by simply setting $\tau_{zz} = 0$ everywhere or by ensuring that the mean force in the z-direction is zero.

For an airway *in-vivo*, if pre-stretch is neglected, the deformation is primarily in the radial and circumferential directions and the plane strain approximation can be used [67]. We will therefore concentrate on the plane strain case. For a lung slice, however, which consists of a thin slice of tissue about an airway, with the stresses act in the plane, a plane stress approximation would be more appropriate. However, there are a number of issues with solving for the plane stress. Firstly, as the airway inflates, the thickness of the airway wall reduces, becoming closer to that of the thickness of the slice. Secondly, ensuring there is no forcing in the z-direction adds complexity to the model and it is hard to match the change in thickness of the two layers at the boundary.

2.2 Tissue-level mechanics

2.2.1 Strain-energy functions

First we introduce the strain-energy functions used. Different functions are used for the two layers. For the parenchyma a simple model is used. For the airway wall, where most of the remodelling associated with asthma takes place, the model is developed more fully. In particular, fibres are taken into account to represent the ASM and collagen.

2.2.1.1 Parenchyma

The parenchyma is modelled as an isotropic, homogeneous, compressible material. An adaption of the Neo-Hookean constitutive law that allows for compressibility is used [26, 62]. This model is favourable since the strain-energy function,

$$W^* = \frac{\mu^{(p)*}}{2}(I_1 - 3) + \frac{\lambda^{(p)*}}{2}(J-1)^2 - \mu^{(p)*}\log J, \tag{2.2.1}$$

only depends on $\lambda^{(p)*}$ and $\mu^{(p)*}$, which are Lamé's first and second parameters. $\mu^{(p)*}$ is also known as the shear modulus. $\lambda^{(p)*}$ may also be written in terms of the Poisson ratio $\nu^{(p)}$, such that $\lambda^{(p)*} \equiv 2\mu^{(p)*}\nu^{(p)}/(1-2\nu^{(p)})$. The (p) superscripts are used to show that these are parameters for the parenchyma. $I_1 \equiv \mathrm{tr}(\mathsf{C})$ is the first strain invariant of C and

$$J \equiv \sqrt{\det(\mathsf{C})} = \sqrt{I_3} \tag{2.2.2}$$

is the square root of the third invariant of C.

2.2.1.2 Airway Wall

To model the matrix of the airway wall, the isotropic strain-energy function developed for the parenchyma, (2.2.1), is used, but with the parameters $\mu^{(w)*}$ and $\lambda^{(w)*}$, where the (w) superscripts indicate that the parameters are for the wall. In order to take into account the fibres embedded in the matrix, anisotropic components are added to the strain-energy function.

In order to introduce stiffening when the airway is inflated, we include the following passive anisotropic component developed by Holzapfel *et al.* [61]:

$$W^*_{pas}(I_4, I_6) = \frac{C_1^*}{2C_2} \sum_{f=4,6} H(I_f - 1)\left\{\exp\left[C_2(I_f-1)^2\right] - 1\right\}. \tag{2.2.3}$$

$C_1^* > 0$ is a stress-like parameter taking into account the density of the fibres in the matrix and their stiffness when a small stretch is applied, while $C_2 > 0$ is a dimensionless parameter that controls the nonlinear increase in stiffness of each fibre as it is stretched. The Heaviside function $H(I_f - 1)$ is included so that the collagen fibres are recruited only when stretched. The additional strain invariants are defined as $I_4 \equiv \mathbf{M}_1 \cdot (\mathsf{C}\mathbf{M}_1)$ and $I_6 \equiv \mathbf{M}_2 \cdot (\mathsf{C}\mathbf{M}_2)$, so that

$$I_4 = I_6 = \frac{r^{*2}}{R^{*2}}\cos^2\varphi + \sin^2\varphi = \left(\frac{r^{*2} - R^{*2}}{R^{*2}}\right)\cos^2\varphi + 1. \tag{2.2.4}$$

I_4 and I_6 are the square of the stretches of the fibres, which due to the symmetry are equal.

In order to introduce contractile forces, A^*, along the fibres, an active anisotropic component is added to the strain-energy function. We want to ensure that the active component of the Cauchy stress tensor matches the general form described by Ambrosi and Pezzuto [3], namely

$$\boldsymbol{\tau}^*_{act} = \frac{A^*}{J}\left(\mathbf{m}_1 \otimes \mathbf{m}_1 + \mathbf{m}_2 \otimes \mathbf{m}_2\right). \tag{2.2.5}$$

Assuming that the contractile force produced by the fibres is independent of I_4 and I_6, using (1.5.10), the active anisotropic component to the strain-energy function takes the following form:

$$W^*_{act} = \frac{A^*}{2}(I_4 + I_6). \tag{2.2.6}$$

The strain-energy function for the airway wall is thus the sum of (2.2.1), (2.2.3) and (2.2.6), namely

$$\begin{aligned} W^* =&\frac{\mu^{(w)*}}{2}(I_1-3)+\frac{\lambda^{(w)*}}{2}(J-1)^2-\mu^{(w)*}\log J+\frac{A^*}{2}(I_4+I_6)\\ &+\frac{C_1^*}{2C_2}\sum_{f=4,6}H(I_f-1)\left\{\exp\left[C_2(I_f-1)^2\right]-1\right\}. \end{aligned} \tag{2.2.7}$$

The strain-energy function thus depends on I_1, I_4 and I_6 as in (1.5.19), plus $J=\sqrt{I_3}$ to allow for compressibility.

2.2.2 Cauchy stress tensor

The Cauchy stress tensor satisfies [128]

$$\boldsymbol{\tau}^* = \frac{1}{J}\left[2W_1^*\mathsf{B}+2I_3W_3^*\mathsf{I}+2W_4^*\mathbf{m}_1\otimes\mathbf{m}_1+2W_6^*\mathbf{m}_2\otimes\mathbf{m}_2\right], \tag{2.2.8}$$

where $W_i^* = \partial W^*/\partial I_i$ for $i=1,3,4,6$. Using (2.2.2),

$$W_3^* = \frac{\partial W^*}{\partial J}\frac{\partial J}{\partial I_3} = -\frac{1}{2J}p^*, \tag{2.2.9}$$

where

$$p^* \equiv -\frac{\partial W^*}{\partial J} = \frac{\mu^*}{J}-\lambda^*(J-1). \tag{2.2.10}$$

Now for the airway wall, using (2.2.8) with (2.2.7) yields

$$\begin{aligned} \boldsymbol{\tau}^* = -p^*\mathsf{I}+\frac{1}{J}\Bigg\{&\mu^*\mathsf{B}+2A^*\mathsf{M}+4C_1^*H(r^*-R^*)\left(\frac{r^{*2}-R^{*2}}{R^{*2}}\right)\cos^2\varphi\\ &\exp\left[C_2\left(\frac{r^{*2}-R^{*2}}{R^{*2}}\right)^2\cos^4\varphi\right]\mathsf{M}\Bigg\}, \end{aligned} \tag{2.2.11}$$

where

$$\mathsf{M} = \frac{\mathbf{m}_1\otimes\mathbf{m}_1+\mathbf{m}_2\otimes\mathbf{m}_2}{2} = \begin{pmatrix} 0 & 0 & 0\\ 0 & \frac{r^{*2}}{R^{*2}}\cos^2\varphi & 0\\ 0 & 0 & \sin^2\varphi \end{pmatrix}. \tag{2.2.12}$$

Due to the symmetry of the fibres, the anisotropic strain invariants are equal, so M is diagonal and the shear forces produced by the fibres cancel each other out. Since $0 \geq \varphi \geq \pi/2$ and both r^* and R^* are non-negative, the Heaviside function has been simplified as follows:

$$H\left(\left(\frac{r^{*2}-R^{*2}}{R^{*2}}\right)\cos^2\varphi\right) = H\left(r^*-R^*\right). \tag{2.2.13}$$

The nonzero components of the Cauchy stress tensor are therefore

$$\tau^*_{rr} = -\,p^* + \frac{\mu^* r^{*'2}}{J}, \tag{2.2.14a}$$

$$\begin{aligned}\tau^*_{\theta\theta} = &-\,p^* + \frac{1}{J}\Bigg\{\mu^*\frac{r^{*2}}{R^{*2}} + 4C_1^* H(r^* - R^*)\left(\frac{r^{*2}-R^{*2}}{R^{*2}}\right)\frac{r^{*2}}{R^{*2}}\\ &\exp\left[C_2\left(\frac{r^{*2}-R^{*2}}{R^{*2}}\right)^2\cos^4\varphi\right]\cos^4\varphi + 2A^*\frac{r^{*2}}{R^{*2}}\cos^2\varphi\Bigg\},\end{aligned} \tag{2.2.14b}$$

$$\begin{aligned}\tau^*_{zz} = &-\,p^* + \frac{1}{J}\Bigg\{\mu^* + C_1^* H(r^* - R^*)\left(\frac{r^{*2}-R^{*2}}{R^{*2}}\right)\\ &\exp\left[C_2\left(\frac{r^{*2}-R^{*2}}{R^{*2}}\right)^2\cos^4\varphi\right]\sin^2 2\varphi + 2A^*\sin^2\varphi\Bigg\}.\end{aligned} \tag{2.2.14c}$$

For the airway wall, the incompressible limit is taken, which is determined by considering the limits $\nu \to 1/2$ or $\lambda^{(w)*}/\mu^{(w)*} \to \infty$. In order that $p^{(w)*}$ remains $O(1)$ in (2.2.38), it is required that $J \to 1$, so J can be expanded as follows:

$$J = 1 + \frac{\mu^{(w)*}J_1}{\lambda^{(w)*}} + O\left(\frac{\mu^{*(w)2}}{\lambda^{*(w)2}}\right), \tag{2.2.15}$$

where $\lambda^{(w)*}/\mu^{(w)*} \gg 1$ and J_1 is $O(1)$. Likewise

$$\boldsymbol{\tau}^* = \boldsymbol{\tau}_0^* + \frac{\mu^{(w)*}\boldsymbol{\tau}_1}{\lambda^{(w)*}} + O\left(\frac{\mu^{*(w)2}}{\lambda^{*(w)2}}\right), \tag{2.2.16a}$$

$$r^* = r_0^* + \frac{\mu^{(w)*}r_1^*}{\lambda^{(w)*}} + O\left(\frac{\mu^{*(w)2}}{\lambda^{*(w)2}}\right), \tag{2.2.16b}$$

$$p^* = p_0^* + \frac{\mu^{(w)*}p_1^*}{\lambda^{(w)*}} + O\left(\frac{\mu^{*(w)2}}{\lambda^{*(w)2}}\right). \tag{2.2.16c}$$

Now $J = \det(\mathsf{F}) = r^{*'}r^*/R^*$, so expanding and using (2.2.15) and (2.2.16b) we recover

$$\frac{r_0^{*'}r_0^*}{R^*} = 1, \quad \frac{r_0^* r_1^{*'} + r_0^{*'} r_1^*}{R^*} = J_1. \tag{2.2.17}$$

Integrating and using the definition that $r_0^*(1) = r_{a0}^*$ gives

$$r_0^{*2} = r_{a0}^{*2} + R^{*2} - R_a^{*2}. \tag{2.2.18}$$

Therefore, given knowledge of r_0^* at one point in the airway wall, this equation may be used to find r_0^* for the other points in the wall.

At leading order, the nonzero components of the Cauchy stress tensor, (2.2.14), are

$$\tau^*_{rr0} = -\, p^*_0 + \mu^{(w)*}\frac{R^{*2}}{r_0^{*2}}, \tag{2.2.19a}$$

$$\begin{aligned}\tau^*_{\theta\theta 0} = &-\, p^*_0 + \mu^{(w)*}\frac{r_0^{*2}}{R^{*2}} + 4C_1^* H(r^*_{a0} - R^*_a)\left(\frac{r^2_{a0} - R_a^{*2}}{R^2}\right)\frac{r_0^{*2}}{R^{*2}} \\ &\exp\left[C_2\left(\frac{r_{a0}^{*2} - R_a^{*2}}{R^{*2}}\right)^2 \cos^4\varphi\right]\cos^4\varphi + 2A_0^*\frac{r_0^{*2}}{R^{*2}}\cos^2\varphi,\end{aligned} \tag{2.2.19b}$$

$$\begin{aligned}\tau^*_{zz0} = &-\, p^*_0 + \mu^{(w)*} + C_1^* H(r^*_{a0} - R^*_a)\left(\frac{r_{a0}^{*2} - R_a^{*2}}{R^{*2}}\right) \\ &\exp\left[C_2\left(\frac{r_{a0}^{*2} - R_a^{*2}}{R^{*2}}\right)^2 \cos^4\varphi\right]\sin^2 2\varphi + 2A_0^*\sin^2\varphi,\end{aligned} \tag{2.2.19c}$$

where

$$p^*_0 = \mu^{(w)*}\left(1 - J_1\right). \tag{2.2.20}$$

At present both p^*_0 and J_1 are unknown.

Assuming the elastic model of the parenchyma, the nonzero components of the parenchyma are found by inserting (2.2.1) into (2.2.8), yielding

$$\tau^*_{rr} = \frac{\mu^{(p)*}}{J}\left(r^{*\prime 2} - 1\right) + \lambda^{(p)*}(J - 1), \tag{2.2.21a}$$

$$\tau^*_{\theta\theta} = \frac{\mu^{(p)*}}{J}\left(\frac{r^{*2}}{R^{*2}} - 1\right) + \lambda^{(p)*}(J - 1), \tag{2.2.21b}$$

$$\tau^*_{zz} = \lambda^{(p)*}(J - 1). \tag{2.2.21c}$$

2.2.3 Viscoelastic alternative for the parenchyma

As an alternative to the elastic model for the parenchyma, we introduce a linear viscoelastic model. We base the model on the Standard linear solid model (Sec. 1.5.2).

To find the nonzero components of the Cauchy stress tensor, first we linearise (2.2.14) by letting

$$r^* = R^* + \epsilon\hat{r}^*, \quad \boldsymbol{\tau}^* = \epsilon\hat{\boldsymbol{\tau}}^*, \tag{2.2.22}$$

where $\epsilon \ll 0$. We also use that from (2.2.2), $J = r'^* r^*/R^*$. Taking the leading order terms,

$$\tau^*_{rr} = \lambda^{(p)*}\left(r^{*\prime} + \frac{r^*}{R^*} - 2\right) + 2\left(r^{*\prime} - 1\right), \tag{2.2.23a}$$

$$\tau^*_{\theta\theta} = \lambda^{(p)*}\left(r^{*\prime} + \frac{r^*}{R^*} - 2\right) + 2\left(\frac{r^*}{R^*} - 1\right), \tag{2.2.23b}$$

$$\tau^*_{zz} = \lambda^{(p)*}\left(r^{*\prime} + \frac{r^*}{R^*} - 2\right). \tag{2.2.23c}$$

This is the linear elastic case. From (1.5.51) we make the transformation

$$\boldsymbol{\tau}^* \to t_r^* \frac{\mathrm{d}\boldsymbol{\tau}^*}{\mathrm{d}t^*} + \boldsymbol{\tau}^*, \quad r^* \to t_c^* \frac{\mathrm{d}r^*}{\mathrm{d}t^*} + r^*, \tag{2.2.24}$$

so the nonzero components of the Cauchy stress tensor satisfy

$$\left[t_r^* \frac{\mathrm{d}}{\mathrm{d}t^*} + 1\right] \tau_{rr}^* = \left[t_c^* \frac{\mathrm{d}}{\mathrm{d}t^*} + 1\right] \left\{\lambda^{(p)*}\left(r^{*\prime} + \frac{r^*}{R^*} - 2\right) + 2\left(r^{*\prime} - 1\right)\right\}, \tag{2.2.25a}$$

$$\left[t_r^* \frac{\mathrm{d}}{\mathrm{d}t^*} + 1\right] \tau_{\theta\theta}^* = \left[t_c^* \frac{\mathrm{d}}{\mathrm{d}t^*} + 1\right] \left\{\lambda^{(p)*}\left(r^{*\prime} + \frac{r^*}{R^*} - 2\right) + 2\left(\frac{r^*}{R^*} - 1\right)\right\}, \tag{2.2.25b}$$

$$\left[t_r^* \frac{\mathrm{d}}{\mathrm{d}t^*} + 1\right] \tau_{zz}^* = \left[t_c^* \frac{\mathrm{d}}{\mathrm{d}t^*} + 1\right] \left\{\lambda^{(p)*}\left(r^{*\prime} + \frac{r^*}{R^*} - 2\right)\right\}, \tag{2.2.25c}$$

where t_r^* is the relaxation timescale and t_c^* is the creep timescale.

2.2.4 Equilibrium and compatibility equations

Conservation of momentum requires that $\nabla \cdot \boldsymbol{\tau}^* = 0$, which yields the linear momentum balance equations

$$\frac{\partial \tau_{rr}^*}{\partial r^*} + \frac{1}{r^*}\frac{\partial \tau_{r\theta}^*}{\partial \theta} + \frac{\partial \tau_{zr}^*}{\partial z^*} + \frac{\tau_{rr}^* - \tau_{\theta\theta}^*}{r^*} = 0, \tag{2.2.26a}$$

$$\frac{\partial \tau_{r\theta}^*}{\partial r^*} + \frac{1}{r^*}\frac{\partial \tau_{\theta\theta}^*}{\partial \theta} + \frac{\partial \tau_{z\theta}^*}{\partial z^*} + \frac{2}{r^*}\tau_{r\theta}^* = 0, \tag{2.2.26b}$$

$$\frac{\partial \tau_{zr}^*}{\partial r^*} + \frac{1}{r^*}\frac{\partial \tau_{\theta z}^*}{\partial \theta} + \frac{\partial \tau_{zz}^*}{\partial z^*} + \frac{1}{r^*}\tau_{zr}^* = 0. \tag{2.2.26c}$$

From (2.2.14), the only nonzero components of the Cauchy stress tensor are the diagonal terms, which are independent of both θ and z^*. Therefore $\partial \tau_{\theta\theta}^* / \partial \theta = \partial \tau_{zz}^* / \partial z^* = 0$ and $\tau_{r\theta}^* = \tau_{zr}^* = \tau_{\theta z}^* = 0$, which implies that (2.2.26) reduces to the single equation

$$\frac{\partial \tau_{rr}^*}{\partial r^*} + \frac{\tau_{rr}^* - \tau_{\theta\theta}^*}{r^*} = 0. \tag{2.2.27}$$

Applying the chain rule this becomes

$$\frac{\partial \tau_{rr}^*}{\partial R^*} + \frac{r^{*\prime}}{r^*}(\tau_{rr}^* - \tau_{\theta\theta}^*) = 0. \tag{2.2.28}$$

Considering the airway wall, where we expand using (2.2.16) to take the incompressible limit, the conservation of momentum equation is identical to (2.2.28), except that for the addition of zero subscripts, so that

$$\frac{\partial \tau_{rr0}^*}{\partial R^*} + \frac{r_0^{*\prime}}{r_0^*}(\tau_{rr0}^* - \tau_{\theta\theta 0}^*) = 0. \tag{2.2.29}$$

Finally in the case where we consider a linear mechanical model, expanding using (2.2.22), the conservation of momentum equation becomes

$$\frac{\partial \tau_{rr}^*}{\partial R^*} + \frac{\tau_{rr}^* - \tau_{\theta\theta}^*}{R^*} = 0. \tag{2.2.30}$$

In continuum mechanics, compatibility equations are used to ensure that no gaps form in the material as it deforms. These require that the curl of the deformation gradient tensor is zero, such that

$$\nabla \times \mathsf{F} = 0. \tag{2.2.31}$$

Now given that, by definition, $\mathsf{F} = \mathrm{grad}\mathbf{x}^*$, where $\mathbf{x}^*$ is the coordinates in the deformed configuration, (2.2.31) is automatically satisfied.

2.2.5 Boundary conditions

We now introduce the boundary conditions that are used. Since we are applying a plane strain approximation, we assume that there is no displacement in the z-direction at the two ends. We now describe the conditions that are applied to the other boundaries, which must be independent of z and have no z-component, due to the plane strain approximation. Two conditions ensure that the displacement and radial stress are continuous at $R^* = R_b^*$, so that the two layers are coupled. Since displacements are purely radial, we only need to ensure continuity of the radial displacement. Further conditions are given at $R^* = R_a^*$ and $R^* = R_b^*$. A radial stress is prescribed at $R^* = R_a^*$ and either a radial stress or a displacement is prescribed at $R^* = R_p^*$. Hence, there are the following boundary conditions:

$$\tau_{rr}^{(w)*}(R_a^*, t^*) = \tau_a^*(t^*), \tag{2.2.32a}$$

$$r^{(w)*}(R_b^*, t^*) = r^{(p)*}(R_b^*, t^*) \equiv r_b^*(t^*), \tag{2.2.32b}$$

$$\tau_{rr}^{(w)*}(R_b^*, t^*) = \tau_{rr}^{(p)*}(R_b^*, t^*) \equiv \tau_b^*(t^*), \tag{2.2.32c}$$

$$\tau_{rr}^{(p)*}(R_p^*, t^*) = \tau_p^*(t^*) \quad \text{or} \quad r^*(R_p^*, t^*) = r_p^*(t^*). \tag{2.2.32d}$$

It should be noted that r_b^* and τ_b^* can not be known prior to solving. If we were to expand these boundary conditions using (2.2.16), there would only be leading order terms, so these equations are unchanged for the incompressible case and could be rewritten with additional zero subscripts.

2.2.6 Nondimensionalisation of the tissue mechanics

We finish this section by nondimensionalising the nonzero components of the Cauchy stress tensor for the various cases, (2.2.19), (2.2.21) and (2.2.25), the expression for the deformed radius in the airway wall, (2.2.18), and the boundary conditions, (2.2.32), using

$$(R^*, R_a^*, R_b^*, R_p^*, \chi^*, r^*, r_a^*, r_b^*, r_p^*) = R_a^*(R, 1, R_b, R_p, \chi, r, r_a, r_b, r_p), \tag{2.2.33}$$

$$(\boldsymbol{\tau}^*, \tau_a^*, \tau_b^*, \tau_p^*, C_1^*, \lambda^{(w)*}, A^*, p^{(w)*}) = \mu^{(w)*}(\boldsymbol{\tau}, \tau_a, \tau_b, \tau_p, C_1, \lambda^{(w)}, A, p^{(w)}), \tag{2.2.34}$$

$$(t^*, t_r^*, t_c^*) = T^*(t, t_r, t_c). \tag{2.2.35}$$

Lengths are nondimensionalised with respect to R_a^*, the inner undeformed radius, stresses are nondimensionalised with respect to $\mu^{(w)*}$, the shear modulus of the matrix of the airway wall, and times are nondimensionalised with respect to a reference time T^*, which shall be selected later.

The airway wall occupies $R_a \leq R \leq R_b \equiv R_a + \chi$, while the parenchyma occupies $R_b \leq R \leq R_p \equiv R_b + \chi$, with $R_p - R_b \gg \chi$.

Having seen that both the conservation of momentum equation and the boundary conditions are only changed by the addition of zero subscripts in the incompressible case, for convenience these subscripts are dropped. Within the airway wall from (2.2.18) there is the following expression for the radius,

$$r^2 = r_a^2 + R^2 - 1. \tag{2.2.36}$$

The dimensionless nonzero components of the Cauchy stress tensor, (2.2.19), are

$$\tau_{rr} = -p^{(w)} + \frac{R^2}{r^2}, \tag{2.2.37a}$$

$$\begin{aligned}\tau_{\theta\theta} = & -p^{(w)} + \frac{r^2}{R^2} + 4C_1 H(r_a - 1)\left(\frac{r_a^2 - 1}{R^2}\right)\frac{r^2}{R^2}\exp\left[C_2\left(\frac{r_a^2 - 1}{R^2}\right)^2 \cos^4\varphi\right]\cos^4\varphi \\ & + 2A\frac{r^2}{R^2}\cos^2\varphi,\end{aligned} \tag{2.2.37b}$$

$$\begin{aligned}\tau_{zz} = & -p^{(w)} + 1 + C_1 H(r_a - 1)\left(\frac{r_a^2 - 1}{R^2}\right)\exp\left[C_2\left(\frac{r_a^2 - 1}{R^2}\right)^2 \cos^4\varphi\right]\sin^2 2\varphi \\ & + 2A\sin^2\varphi,\end{aligned} \tag{2.2.37c}$$

where

$$p^{(w)} = 1 - J_1. \tag{2.2.38}$$

Within the parenchyma, using that $J = r'r/R$, the dimensionless nonzero components of the Cauchy stress tensor, (2.2.21), are

$$\tau_{rr} = \varrho\left\{\lambda^{(p)}\left(\frac{r'r}{R} - 1\right) - \frac{R}{r'r} + \frac{r'R}{r}\right\}, \tag{2.2.39a}$$

$$\tau_{\theta\theta} = \tau_{rr} + \varrho\left(\frac{r}{Rr'} - \frac{r'R}{r}\right), \tag{2.2.39b}$$

$$\tau_{zz} = \tau_{rr} + \varrho\left(\frac{R}{r'r} - \frac{r'R}{r}\right), \tag{2.2.39c}$$

where $\lambda^{(p)} = \lambda^{(p)*}/\mu^{(p)*}$, $\varrho = \mu^{(p)*}/\mu^{(w)*}$.

If instead the viscoelastic model is used, within the parenchyma the dimensionless nonzero components of the Cauchy stress tensor, (2.2.25), are

$$\left[t_r \frac{\mathrm{d}}{\mathrm{d}t} + 1\right] \tau_{rr} = \varrho \left[t_c \frac{\mathrm{d}}{\mathrm{d}t} + 1\right] \left\{\lambda^{(p)} \left(r' + \frac{r}{R} - 2\right) + 2\left(r' - 1\right)\right\}, \tag{2.2.40a}$$

$$\left[t_r \frac{\mathrm{d}}{\mathrm{d}t} + 1\right] \tau_{\theta\theta} = \varrho \left[t_c \frac{\mathrm{d}}{\mathrm{d}t} + 1\right] \left\{\lambda^{(p)} \left(r' + \frac{r}{R} - 2\right) + 2\left(\frac{r}{R} - 1\right)\right\}, \tag{2.2.40b}$$

$$\left[t_r \frac{\mathrm{d}}{\mathrm{d}t} + 1\right] \tau_{zz} = \varrho \left[t_c \frac{\mathrm{d}}{\mathrm{d}t} + 1\right] \left\{\lambda^{(p)} \left(r' + \frac{r}{R} - 2\right)\right\}. \tag{2.2.40c}$$

In particular if time is nondimesionalised with respect to the relaxation timescale, so that $T^* = t_r^*$, t_r can be removed from the above equations and $t_c = t_c^*/t_r^*$ is the ratio of the creep and relaxation timescales.

The dimensionless equation for the conservation of momentum, (2.2.28), is

$$\frac{\partial \tau_{rr}}{\partial R} + \frac{r'}{r}(\tau_{rr} - \tau_{\theta\theta}) = 0, \tag{2.2.41}$$

or in the case of linear mechanics, (2.2.30),

$$\frac{\partial \tau_{rr}}{\partial R} + \frac{\tau_{rr} - \tau_{\theta\theta}}{R} = 0. \tag{2.2.42}$$

The boundary conditions, (2.2.32), are

$$\tau_{rr}^{(w)}(1,t) = \tau_a(t), \tag{2.2.43a}$$

$$r^{(w)}(R_b) = r^{(p)}(R_b,t) = r_b(t), \tag{2.2.43b}$$

$$\tau_{rr}^{(w)}(R_b,t) = \tau_{rr}^{(p)}(R_b,t) = \tau_b(t), \tag{2.2.43c}$$

$$\tau_{rr}^{(p)}(R_p,t) = \tau_p(t) \quad \text{or} \quad r(R_p,t) = r_p(t). \tag{2.2.43d}$$

2.3 Crossbridge mechanics

We have introduced a general contractile force A^* into the strain-energy function for the airway wall, (2.2.7), that could vary with time or across the thickness of the wall. In order to include the sub-cellular crossbridge mechanics we couple A^* to the HHM model developed by Mijailovich *et al.* [116].

2.3.1 Huxley-Hai-Murphy theory

Huxley-Hai-Murphy theory [44, 116] was introduced in Sec. 1.4.1. The model assumes that there are four states that the crossbridges can be in: unattached and not phosphorylated, unattached but phosphorylated, attached and phosphorylated, or attached and dephosphorylated (Fig. 1.5). As was assumed in [21, 140, 173], we assume that the distance between the actin binding sites is much greater than the region within which the crossbridges can attach. The vector of the fraction of crossbridges in the four states, $\mathbf{n} \equiv (n_A, n_B, n_C, n_D)$ are thus governed by the following system of differential equations:

$$\frac{\partial \mathbf{n}}{\partial t^*} - v^* \frac{\partial \mathbf{n}}{\partial x^*} = \mathsf{Q}^* \mathbf{n}, \tag{2.3.1}$$

where v^* is the velocity of the actin relative to the myosin and is taken to be positive during contraction. Q^* is the transition matrix given by

$$\mathsf{Q}^*(x^*, t^*) = \begin{pmatrix} -k_1^* & k_2^* & 0 & g^*(x^*) \\ k_1^* & -k_2^* - f_p^*(x^*) & g_p^*(x^*) & 0 \\ 0 & f_p^*(x^*) & -k_5^* - g_p^*(x^*) & k_6^* \\ 0 & 0 & k_5^* & -k_6^* - g^*(x^*) \end{pmatrix}. \tag{2.3.2}$$

The attachment and detachment rates may be described as follows [116]:

$$f_p^*(x^*) = \begin{cases} 0, & x^* < 0 \\ f_{p1}^* x^*/h^*, & 0 \le x^* \le h^* \\ 0, & x^* > h^*, \end{cases} \tag{2.3.3a}$$

$$g_p^*(x^*) = \begin{cases} g_{p2}^*, & x^* < 0 \\ g_{p1}^* x^*/h^*, & 0 \le x^* \le h^* \\ (g_{p1}^* + g_{p3}^*) x^*/h^*, & x^* > h^*, \end{cases} \tag{2.3.3b}$$

$$g^*(x^*) = \begin{cases} g_2^*, & x^* < 0 \\ g_1^* x^*/h^*, & 0 \le x^* \le h^* \\ (g_1^* + g_3^*) x^*/h^*, & x^* > h^*. \end{cases} \tag{2.3.3c}$$

2.3.2 Coupling the crossbridge and tissue mechanics

Using HHM theory we predict the number of attached crossbridges and how much they are stretched. Assuming that the two sets of attached crossbridges are linearly elastic and contribute equally to the contractile force, then the active force per unit area, in each set of fibres, can be calculated using

$$A^*(t^*; R^*) = \beta^* \int_{-\infty}^{\infty} x^* (n_C(x^*, t^*; R^*) + n_D(x^*, t^*; R^*)) \mathrm{d}x^*. \tag{2.3.4}$$

The notation $A^*(t^*; R^*)$ is used to show that t^* is an independent variable and R^* is a parameter. Here the integral gives the sum of the stretch of the attached crossbridges onto one actin filament. The parameter β^* is the product of the following factors:

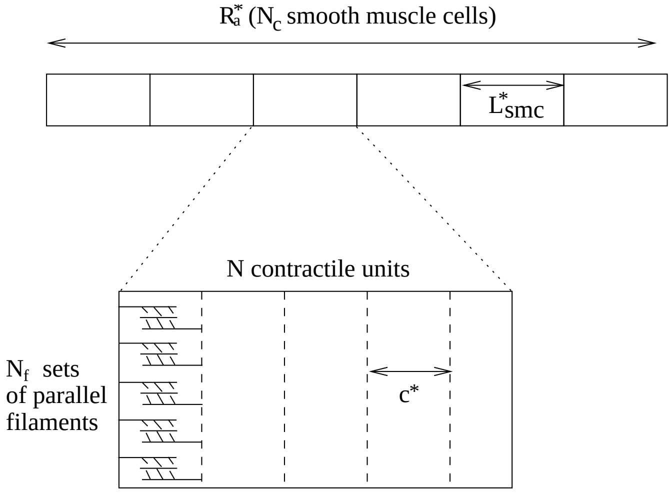

Figure 2.3: The reference length is made up of smooth muscle cells in series (solid lines). Each smooth muscle cell is formed of N contractile units (dashed lines). Within each contractile unit there are N_f sets of myosin filaments with parallel actin filaments.

- the stiffness of a crossbridge,
- the number of crossbridges per myosin filament,
- N_f (see Fig. 2.3), the number of myosin filaments in parallel in a contractile unit,
- the number of parallel cells in a muscle fibre,
- the area fraction of muscle layer made up of ASM fibres.

In order to solve (2.3.1), v^* is found in terms of V^*, the local tissue velocity, by considering the relative length scales. Firstly, we consider the tissue velocity, and take a length of fibre R_a^* (say) in the reference configuration (Fig. 2.3). Since the square of the stretch of the two sets of fibres is equal, (2.2.4), they each have the deformed length $L_{def}^* \equiv R_a^* \sqrt{I_4}$. Differentiating using (2.2.4) yields

$$V^* = \frac{\mathrm{d}L_{def}^*}{\mathrm{d}t^*} = \frac{R_a^* \cos^2 \varphi r^*}{R^* \sqrt{(r^{*2} - R^{*2}) \cos^2 \varphi + R^{*2}}} \frac{\partial r^*}{\partial t^*}. \tag{2.3.5}$$

Secondly, we consider the rate of change of a contractile unit of length c^*. Within each smooth muscle cell we assume there are N contractile units in series (Fig. 2.3) and a smooth muscle cell has a reference length of L_{smc}^*. In a portion of fibre with reference length R_a^*, the number of smooth muscle cells in series is $N_c = R_a^*/L_{smc}^*$. Therefore, in the deformed state

$$L_{def}^* = NN_c(R^*)c^*(R^*, t^*). \tag{2.3.6}$$

Taking $v^* = -\partial c^*/\partial t^*$ and differentiating (2.3.6) yields

$$v^* = -\frac{V^*}{NN_c}. \tag{2.3.7}$$

Experimentally, $R_a^*/(NN_c) = L_{smc}^*/N$ ranges from 0.7 to 2.2μm [57, 171], with Politi *et al.* [140] letting $R_a^*/(NN_c) = 1\mu$m. We also assume this value. For a mouse it is reasonable for $R_a^* = 50\mu$m, giving $NN_c \approx 50$. This would be larger for many human airways. Therefore, since there are many cells, micro processes are able to add up and produce macro effects. Now, (2.3.1) can be rewritten as follows in terms of V^*:

$$\frac{\partial \mathbf{n}}{\partial t^*} + \frac{V^*}{NN_c}\frac{\partial \mathbf{n}}{\partial x^*} = \mathsf{Q}^*\mathbf{n}. \tag{2.3.8}$$

Initially we assume that all of the crossbridges are unattached and unphosphorylated, giving the additional initial condition,

$$\mathbf{n}(R,0) = (1,0,0,0). \tag{2.3.9}$$

2.3.3 Nondimensionalisation of the crossbridge mechanics

We finish this section by nondimensionalising the equations that govern the crossbridge mechanics. We introduce the nondimensional variables $x = x^*/h^*$, $t = t^*/T^*$ and $V = V^*T^*/R_a^*$, where $h \approx 15.6$nm is the powerstroke length [53, 68]. Now, (2.3.8) can be written as

$$\frac{\partial \mathbf{n}}{\partial t} + \gamma V\frac{\partial \mathbf{n}}{\partial x} = \mathsf{Q}\mathbf{n}, \tag{2.3.10}$$

where

$$\gamma = \frac{R_a^*}{NN_c h^*}. \tag{2.3.11}$$

The transition matrix satisfies

$$\mathsf{Q} = \begin{pmatrix} -k_1 & k_2 & 0 & 0 \\ k_1 & -k_2 - f_p(x) & g_p(x) & 0 \\ 0 & f_p(x) & -k_5 - g_p(x) & k_6 \\ 0 & 0 & k_5 & -k_6 - g(x) \end{pmatrix}, \tag{2.3.12}$$

with

$$f_p(x) = \begin{cases} 0, & x < 0 \\ f_{p1}x, & 0 \le x \le 1 \\ 0, & x > 1, \end{cases} \tag{2.3.13}$$

$$g_p(x) = \begin{cases} g_{p2}, & x < 0 \\ g_{p1}x, & 0 \le x \le 1 \\ (g_{p1} + g_{p3})x, & x > 1, \end{cases} \tag{2.3.14}$$

$$g(x) = \begin{cases} g_2, & x < 0 \\ g_1 x, & 0 \le x \le 1 \\ (g_1 + g_3)x, & x > 1. \end{cases} \tag{2.3.15}$$

Each of these rates have been multiplied by T^*. Nondimensionalising (2.3.5) gives

$$V = \frac{\cos^2 \varphi r}{R\sqrt{(r^2 - R^2)\cos^2 \varphi + R^2}} \frac{\mathrm{d}r}{\mathrm{d}t}. \tag{2.3.16}$$

while, nondimensionalising (2.3.4) gives

$$A(t; R) = \beta \int_{-\infty}^{\infty} x(n_C(x, R, t) + n_D(x, R, t))\mathrm{d}x, \tag{2.3.17}$$

where $\beta = \beta^* h^{*2}/\mu^{(a)*}$. The initial condition, (2.3.9), is unchanged.

2.4 Summary

In this chapter our model for an asthmatic airway, consisting of the airway wall embedded in parenchyma, has been presented. The dimensionless nonzero components of the Cauchy stress tensor have been found for each of the layers. For the airway wall, which is assumed to be incompressible and contains fibres to carry out the functions of the collagen and ASM, the components are given in (2.2.37). The nonzero components for the parenchyma, which is assumed to be an isotropic, homogeneous, compressible material, are given in (2.2.39) if the parenchyma is elastic or (2.2.40) if it is viscoelastic. The nonzero components must satisfy the conservation of momentum equation (2.2.41) (the linear version, that is used for the viscoelastic parenchyma, is given in (2.2.42)). The boundary are given by (2.2.43). The distribution of the crossbridges evolves according to (2.3.10) and the contractile force is given by (2.3.17). Initially, the crossbridges distribution satisfies (2.3.9).

As we solve the model, there are a number of factors that increase the level of complexity including the following:

- due to the nonlinearity of the airway wall, a root-finding algorithm is required to solve for the lumen radius;
- due to the compressibility of the parenchyma, a shooting algorithm must be used to ensure that the boundary conditions hold;
- with the viscoelastic model for the parenchyma, stress or strain history influences the current stresses and strain;
- the contractile force is space and time dependent, so crossbridge populations must be tracked and recorded for a range of radii;
- attached crossbridges can be stretched by different amounts, so the numerical method updating the crossbridge populations must find the number of crossbridges in each of the four states for each possible stretch.

Due to the level of complexity, we solve the mathematical model presented by beginning with a very simplified version of it and gradually adding other components in.

In chapter 3 we focus solely on the tissue-level mechanics as described in Sec. 2.2. Beginning with the airway in isolation, we find an analytical relationship between the transmural pressure and the lumen radius and where available we use data from the literature to select parameter values. We then investigate the displacement and stress distributions when the airway is embedded in parenchyma. Firstly we consider the case where the parenchyma is elastic, before considering the case where the parenchyma is viscoelastic. In each case we assume that external stresses or displacements are applied to the airway, but that there are no active contractile forces.

In chapter 4 we include the contributions of active contractile forcing, described in Sec. 2.3. Initially we find steady state solutions and compare the displacement and stress distributions with the predictions of Brook *et al.* [22]. We then prescribe a time-dependent contractile force that allows us to investigate how the displacement and stress distributions evolve, when the parenchyma is elastic or viscoelastic. Finally we investigate how the displacement and stress distributions evolve when the tissue mechanics is fully coupled to the crossbridge mechanics.

Chapter 3

Model development and effects of inflating the airway

An overview of the model for the asthmatic airway was presented in the previous chapter. We now begin to solve the model and in particular look at the effect of applying passive stresses or displacements to the boundaries of the airway. In this chapter we assume that there is no agonist so that the airway smooth muscle (ASM) does not produce an active contractile force; we thus assume that $A = 0$.

In Sec. 3.1 the airway wall is considered in isolation. We solve to find the relationship between the transmural pressure and the lumen radius and show that when small stresses are applied to the wall, the relationship matches the predictions of the linear elastic model of Brook *et al.* [22]. Using literature where possible, we select parameter values and make comparisons to the model of Lambert *et al.* [98], before investigating the effect of altering the parameter values on the results obtained. Having considered the airway wall in isolation, we consider the airway wall embedded within the parenchyma, first assuming the nonlinear elastic model for the parenchyma in Sec. 3.2, then the linear viscoelastic model for the parenchyma in Sec. 3.3.

In Sec. 3.2 we solve to find the equations that govern the stresses and displacements within the parenchyma and again make comparisons to the work of Brook *et al.* [22] in the case of small stresses. We introduce the numerical methods used to couple the parenchyma to the airway wall and consider the choice of the additional parameters. Having compared our results to those of Lai-Fook *et al.* [91], we investigate different methods of inflating the airway.

In Sec. 3.3 we solve to find the time-dependent equations that govern the stresses and displacements when the parenchyma is viscoelastic. We introduce the numerical meth-

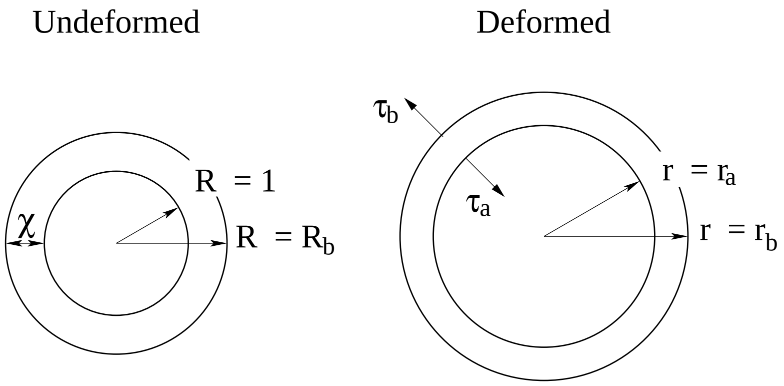

Figure 3.1: One-layer elastic model of the airway wall with stresses applied at the inner and outer edges.

ods used to solve these equations. We again use the literature to select values for the additional parameters and consider different methods of inflating the airway. In particular, we show that there are some important differences depending on whether pleural stresses or pleural displacements are prescribed.

Conclusions are drawn in Sec. 3.4.

3.1 Airway Wall

We begin by considering a simplified version of the full model; the airway wall in isolation. The wall is assumed to occupy $1 \leq R \leq R_b \equiv 1 + \chi$ (Fig. 3.1). We find a relationship between the stresses applied to the boundaries of the airway wall and the lumen radius. By comparing to data we are able to select some baseline parameters. We then show what effect varying each of the parameters has.

3.1.1 Pressure-radius relationship

In this subsection we solve to find a relationship between the the transmural pressure and the lumen radius, and equations that describe the stresses within the wall. The dimensionless nonzero components of the Cauchy stress tensor from (2.2.37) are

$$\tau_{rr} = -\,p^{(w)} + \frac{R^2}{r^2}, \tag{3.1.1a}$$

$$\tau_{\theta\theta} = -\,p^{(w)} + \frac{r^2}{R^2} + 4C_1 H(r_a - 1)\left(\frac{r_a^2 - 1}{R^2}\right)\frac{r^2}{R^2}\exp\left[C_2\left(\frac{r_a^2-1}{R^2}\right)^2\cos^4\varphi\right]\cos^4\varphi$$
$$+\,2A\frac{r^2}{R^2}\cos^2\varphi, \tag{3.1.1b}$$

$$\tau_{zz} = -\,p^{(w)} + 1 + C_1 H(r_a - 1)\left(\frac{r_a^2 - 1}{R^2}\right)\exp\left[C_2\left(\frac{r_a^2-1}{R^2}\right)^2\cos^4\varphi\right]\sin^2 2\varphi$$
$$+\,2A\sin^2\varphi, \tag{3.1.1c}$$

and the relevant boundary conditions from (2.2.43) are

$$\tau_{rr}(1) = \tau_a, \tag{3.1.2a}$$

$$\tau_{rr}(R_b) = \tau_b. \tag{3.1.2b}$$

From (2.2.18), the radii within the wall are related as follows:

$$r^2 = r_a^2 + R^2 - 1. \tag{3.1.3}$$

Using (3.1.3), the conservation of momentum, (2.2.41), requires that

$$\frac{\partial \tau_{rr}}{\partial R} = \frac{r'}{r}(\tau_{\theta\theta} - \tau_{rr}) = \frac{R}{r^2}(\tau_{\theta\theta} - \tau_{rr}), \tag{3.1.4}$$

thus using (3.1.1),

$$\frac{\partial \tau_{rr}}{\partial R} = \frac{1}{R} - \frac{R^3}{r^4} + 4C_1 H(r_a - 1)\left(\frac{r_a^2 - 1}{R^3}\right)\exp\left[C_2\left(\frac{r_a^2-1}{R^2}\right)^2\cos^4\varphi\right]\cos^4\varphi$$
$$+\,\frac{2A}{R}\cos^2\varphi. \tag{3.1.5}$$

Integrating and implementing the boundary condition (3.1.2a) yields

$$\tau_{rr} = \tau_a + \log\left(\frac{r_a R}{r}\right) + \frac{(r_a^2-1)(R^2-1)}{2r_a^2 r^2} + H(r_a - 1)C_1\sqrt{\frac{\pi}{C_2}}\cos^2\varphi$$
$$\left(\operatorname{erfi}\left\{\sqrt{C_2}\,(r_a^2-1)\cos^2\varphi\right\} - \operatorname{erfi}\left\{\sqrt{C_2}\left(\frac{r_a^2-1}{R^2}\right)\cos^2\varphi\right\}\right)$$
$$+\,2\cos^2\varphi\int_1^R \frac{A}{S}dS, \tag{3.1.6}$$

where, from (3.1.3), $r = \sqrt{r_a^2 + R^2 - 1}$ and

$$\operatorname{erfi}(x) \equiv \frac{2}{\sqrt{\pi}}\int_0^x \exp(t^2)\mathrm{d}t \tag{3.1.7}$$

is the imaginary error function. Implementing the second boundary condition, (3.1.2a), the dimensionless transmural pressure, $[\![\tau]\!] \equiv \tau_b - \tau_a$, satisfies

$$\begin{aligned}[\![\tau]\!] =& \log\left(\frac{r_a R_b}{r_b}\right) + \frac{(r_a^2-1)(R_b^2-1)}{2r_a^2 r_b^2} + H(r_a-1)C_1\sqrt{\frac{\pi}{C_2}}\cos^2\varphi \\ & \left(\operatorname{erfi}\left\{\sqrt{C_2}\,(r_a^2-1)\cos^2\varphi\right\} - \operatorname{erfi}\left\{\sqrt{C_2}\left(\frac{r_a^2-1}{R_b^2}\right)\cos^2\varphi\right\}\right) \\ & + 2\cos^2\varphi\int_1^{R_b}\frac{A}{R}dR, \end{aligned} \qquad (3.1.8)$$

where, from (3.1.3), $r_b = \sqrt{r_a^2 + R_b^2 - 1}$. Provided that A is known, (3.1.8) can be solved numerically to give the deformed inner radius, r_a.

τ_{rr} is found by inserting the value found for r_a into (3.1.6). Using the value of τ_{rr} and (3.1.1), yields the following expressions for $\tau_{\theta\theta}$ and τ_{zz}:

$$\begin{aligned}\tau_{\theta\theta} =& \tau_{rr} - \frac{R^2}{r^2} + \frac{r^2}{R^2} + 2A\frac{r^2}{R^2}\cos^2\varphi \\ & + 4C_1 H(r_a-1)\left(\frac{r_a^2-1}{R^2}\right)\frac{r^2}{R^2}\exp\left[C_2\left(\frac{r_a^2-1}{R^2}\right)^2\cos^4\varphi\right]\cos^4\varphi, \end{aligned} \qquad (3.1.9a)$$

$$\begin{aligned}\tau_{zz} =& \tau_{rr} - \frac{R^2}{r^2} + 1 + 2A\sin^2\varphi \\ & + C_1 H(r_a-1)\left(\frac{r_a^2-1}{R^2}\right)\exp\left[C_2\left(\frac{r_a^2-1}{R^2}\right)^2\cos^4\varphi\right]\sin^2 2\varphi. \end{aligned} \qquad (3.1.9b)$$

3.1.2 Small deformations

One of the aims of the modelling was to extend the work of Brook *et al.* [22], who produced a linear model of the asthmatic airway, to allow for finite deformations. We now show that if small stresses are applied, our model predictions match those of Brook *et al.*. This is done by linearising the results from the previous subsection. In the undeformed configuration the stresses are zero and $r = R$, thus we linearise by letting

$$\tau = \varepsilon\hat{\tau}, \quad A = \varepsilon\hat{A}, \quad r = R + \varepsilon\hat{r}, \qquad (3.1.10)$$

where $0 < \varepsilon \ll 1$ and $\hat{\tau}$, $\hat{A}$ and $\hat{r}$ are $O(1)$. This transforms (3.1.8) into

$$[\![\hat{\tau}]\!] = 2\hat{r}_a\big(1 + H(\hat{r}_a)2C_1\cos^4\varphi\big)\left(\frac{R_b^2-1}{R_b^2}\right) + 2\cos^2\varphi\int_1^{R_b}\frac{\hat{A}}{S}\mathrm{d}S + O(\varepsilon), \qquad (3.1.11)$$

where $[\![\hat{\tau}]\!] = \hat{\tau}_b - \hat{\tau}_a$ and is $O(1)$. The following expansion of erfi has been used:

$$\operatorname{erfi}(x) = \frac{1}{\sqrt{\pi}}\left[2x + \frac{2}{3}x^3 + \frac{1}{5}x^5 + \dots\right], \quad \text{for } x \ll 1. \qquad (3.1.12)$$

Ignoring the $O(\varepsilon)$ terms, in original variables (3.1.11) is

$$[\![\tau]\!] = 2(r_a - 1)\big(1 + H(r_a - 1)2C_1 \cos^4 \varphi\big) \left(\frac{R_b^2 - 1}{R_b^2}\right) + 2\cos^2 \varphi \int_1^{R_b} \frac{A}{R} \mathrm{d}R. \tag{3.1.13}$$

Linearising (3.1.3), the displacement satisfies

$$\begin{aligned} r - R =& \frac{r_a - 1}{R} \\ =& \frac{[\![\tau]\!] - 2\cos^2 \varphi \int_1^{R_b} (A/R)\mathrm{d}R)}{2R\big(1 + H(r_a - 1)2C_1 \cos^4 \varphi\big)} \left(\frac{R_b^2}{R_b^2 - 1}\right), \end{aligned} \tag{3.1.14}$$

while linearising (3.1.6) and (3.1.9), the stresses satisfy

$$\begin{aligned} \tau_{rr} =& \tau_a + \frac{[\![\tau]\!] - 2\cos^2 \varphi \int_1^{R_b} (A/R)\mathrm{d}R}{1 + H(r_a - 1)2C_1 \cos^4 \varphi} \left(\frac{R_b^2}{R_b^2 - 1}\right) \left(\frac{R^2 - 1}{R^2}\right) \\ & + 2\cos^2 \varphi \int_1^R \frac{A}{s} \mathrm{d}s, \end{aligned} \tag{3.1.15a}$$

$$\begin{aligned} \tau_{\theta\theta} =& \tau_a + \frac{[\![\tau]\!] - 2\cos^2 \varphi \int_1^{R_b} (A/R)\mathrm{d}R}{1 + H(r_a - 1)2C_1 \cos^4 \varphi} \left(\frac{R_b^2}{R_b^2 - 1}\right) \left(\frac{R^2 + 1}{R^2}\right) \\ & + 2\cos^2 \varphi \int_1^R \frac{A}{s} \mathrm{d}s + 2A\cos^2 \varphi, \end{aligned} \tag{3.1.15b}$$

$$\begin{aligned} \tau_{zz} =& \tau_a + \frac{[\![\tau]\!] - 2\cos^2 \varphi \int_1^{R_b} (A/R)\mathrm{d}R}{1 + H(r_a - 1)2C_1 \cos^4 \varphi} \left(\frac{R_b^2}{R_b^2 - 1}\right) \\ & + 2\cos^2 \varphi \int_1^R \frac{A}{s} \mathrm{d}s + 2A\sin^2 \varphi. \end{aligned} \tag{3.1.15c}$$

We are able to compare our model to the work of Brook *et al.* [22] provided we apply the following assumptions:

- there is no fibre-reinforcement, so $C_1 = 0$,
- the muscle fibres form rings, so $\varphi = 0$,
- the inner boundary is stress free, so $\tau_a = 0$,
- the contractile force is uniform.

With these assumptions (3.1.14) becomes

$$r - R = \frac{\tau_b - 2A\log(R_b)}{2R} \frac{R_b^2}{R_b^2 - 1}. \tag{3.1.16}$$

Re-dimensionalising,

$$r^* - R^* = \frac{\tau_b^* - 2A^* \log\left(R_b^*/R_a^*\right)}{2\mu^{(w)*} R^*} \frac{R_a^{*2} R_b^{*2}}{R_b^{*2} - R_a^{*2}}, \tag{3.1.17}$$

which matches up to equation (S.7a) in [22], when the fact that the Young's modulus satisfies $E^{(w)*} = 2\mu^{(w)*}(1+\nu^{(w)})$ is used, with $\nu^{(w)} \rightarrow 1/2$ and $F^* = 2A^*$. The 2 is present since originally there were two sets of fibres, which have been assumed to become parallel and form rings. Applying the assumptions and re-dimensionalising (3.1.15) similarly, yields an equation, which matches up with (S.6) for the muscle layer (using the corrected version of (S.6c)) in [22].

3.1.3 Comparisons to data

We now compare our pressure-radius relationship (3.1.8), with the phenomenological relationship derived by Lambert *et al.* [94, 98] between the normalised lumen area and the transmural pressure. Their model is based on the experimental data from [69], which is obtained when there is no agonist, meaning we can set $A = 0$. We use data from the literature to select values for the wall thickness χ, fibre angle φ and wall shear modulus $\mu^{(w)*}$. The parameters left to specify are C_1, which takes into account the density of the fibres in the matrix and their stiffness when a small stretch is applied, and C_2, which controls the nonlinear increase in stiffness of each fibre as it is stretched. We select suitable values for C_1 and C_2 by 'fitting' to the results of Lambert for an eighth generation airway. We choose the eighth generation airway since it is one of the smaller conducting airways, having much less cartilage than the larger airways.

Based on the histological data of Kuwano *et al.* [89], Affonce and Lutchen [2] published a table showing the airway wall areas for a peripheral and a central human airway. Given that we are considering an eighth generation airway, we use the data for the central airway. We thus let χ=0.1, although we note that the thickness could double in the case of mild asthma, or increase even further in the case of severe asthma.

A number of studies of the orientation of airway smooth muscle, in a number of different species, suggest a range of orientation angles between 0 and $\pi/6$ [39, 106, 154, 156], even within the same species. It would seem reasonable to use an angle of $\pi/12$. It is assumed that the collagen fibres act parallel to the ASM.

Based on excised strips of membranous trachea from sheep, average values of Young's modulus were found to be 3.3kPa in the circumferential direction and 9.3kPa in the axial direction (Codd [27]). We take 6kPa, so assuming incompressibility, the shear modulus $\mu^{(w)*}$ has a value of 2kPa$\approx$20cm water.

By choosing $C_1 = 0.05$ and $C_2 = 0.14$ we are able to produce a plot that captures the major features of the model of Lambert *et al.* [95] including strain-stiffening on inflation and deflation (Fig. 3.2(a)). This shows that the model produces reasonably

Figure	C_1	C_2	φ	χ	τ_a	τ_b
3.2	0.05	0.14	$\pi/12$	0.1	0	0.2
3.3	0.05, 0.1, 0.15	0.14	$\pi/12$	0.1	0	0.2
3.4	0.05	0.09, 0.14, 0.19	$\pi/12$	0.1	0	0.2
3.5	0.05	0.14	$0, \pi/12, \pi/6$	0.1	0	0.2
3.6	0.05	0.14	$\pi/12$	0.1, 0.2, 0.3	0	0.2

Table 3.1: The parameter values for the figures listed. τ_a and τ_b are only used in plots (b)-(e).

shaped pressure-area relationships that compare well with the Lambert model. When the transmural pressure is negative, our model predicts that the airway is stiffer than that of the Lambert model predictions. Some of the differences here could be due to the fact that our model does not take into account buckling. Plots are also shown of the displacement and stress distributions when $\tau_a = 0$ and $\tau_b = 0.2$. The radial displacement (b) and the hoop stress (d) decrease from the inner to the outer boundary of the airway wall, while the radial and hoop stress (c, e) increase. Each of the components of the stress are positive indicating that the wall is under tension.

3.1.4 Effect of altering the parameters

Having chosen baseline parameters, we investigate the effect of varying each of the parameter values. The parameter values are likely to change as a result of airway remodelling or vary across different airway generations. In each case, plots are shown of the pressure-radius curves, when the airway is inflated, and the distribution of the displacement and stresses, when $\tau_a = 0$ and $\tau_b = 0.2$. The parameter values used for each of the plots are shown in table 3.1.

Results are shown in Fig. 3.3 when C_1, which takes into account the density of the fibres and their stiffness with a small stretch, is varied. Increasing C_1 stiffens the airway. This means that as C_1 increases, larger transmural pressures are required for the same increase in the lumen radius (a). Increasing C_1 has little effect on the radial stress distribution (c), while the displacement (b), and the hoop and axial stresses (d, e) decrease. During airway remodelling, depending on the change in the various cell types within the wall, there is likely to be a change in the relative density of the collagen fibres, resulting in a change on C_1. Therefore, the greater the density of collgen in the remodelled airway, the stiffer the airway will be.

Results are shown in Fig. 3.4 when C_2, which controls the nonlinear increase in stiffness

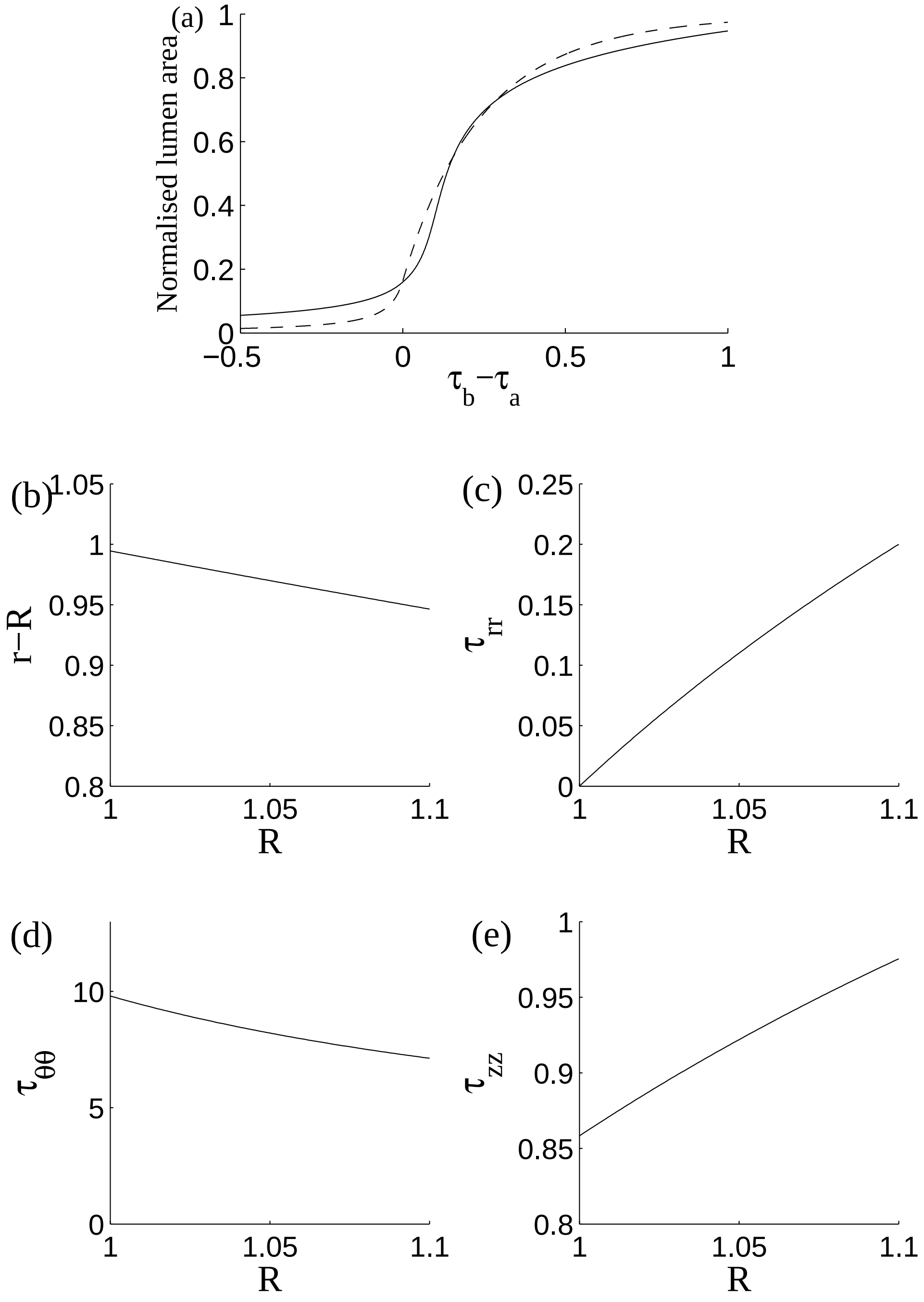

Figure 3.2: Pressure-area relationship from (3.1.8) with parameters $C_1 = 0.05$, $C_2 = 0.14$, $\chi = 0.1$, $\varphi = \pi/12$ and $\mu^{(w)*} = 20$cm H_20 (solid), and the model of Lambert *et al.* [94, 98] for an eighth generation airway (dashed). Also plotted are (b) the displacement and (c)-(e) the radial, hoop and axial stresses verses radial coordinate when $\tau_a = 0$ and $\tau_b = 0.2$.

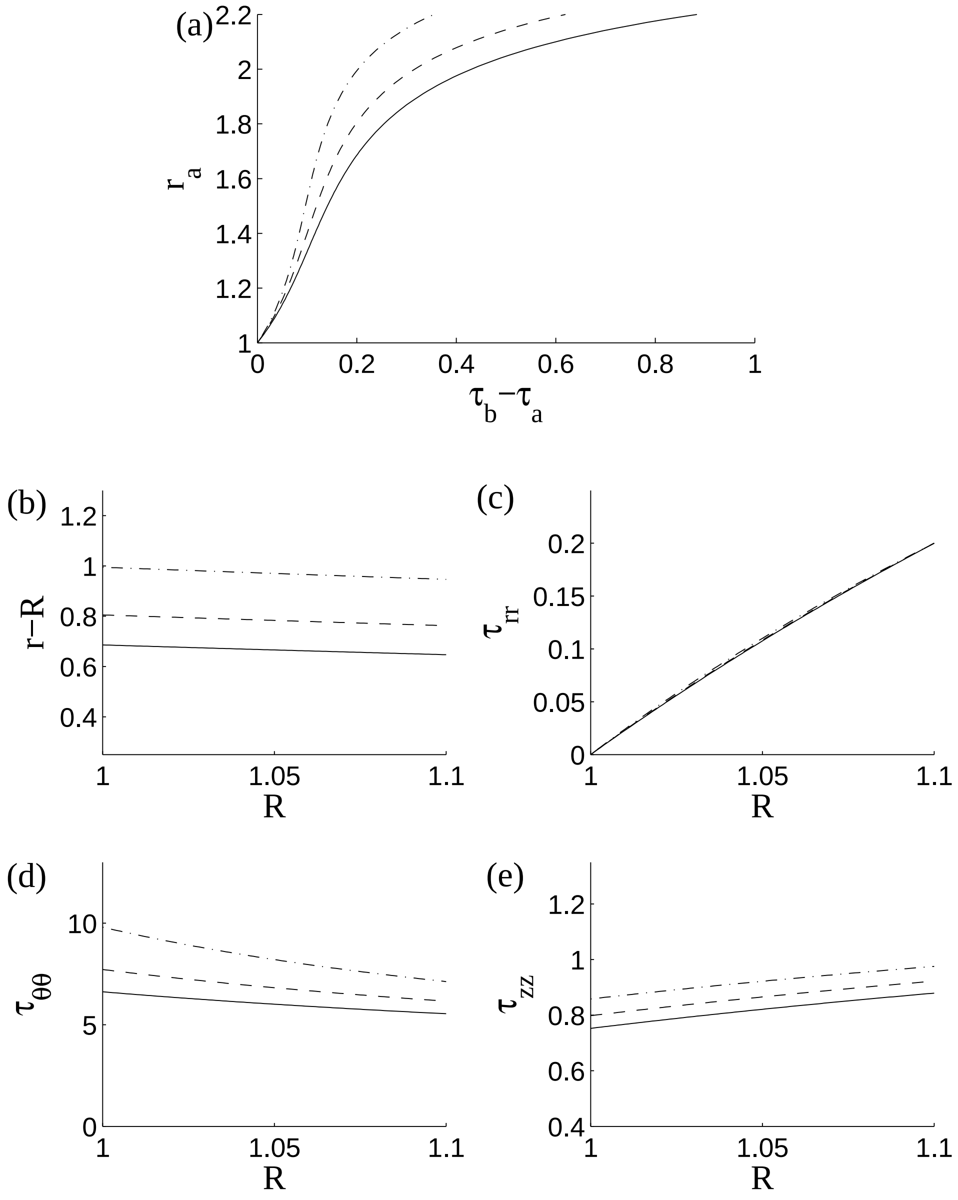

Figure 3.3: Plots showing the effect of varying C_1, which takes into account the density of the fibres and their stiffness with a small stretch. $C_1 = 0.05$ (dot-dashed), 0.1 (dashed) or 0.15 (solid). Plots of (a) the transmural pressure against lumen radius, and (b) the displacement and (c)-(e) the radial, hoop and axial stresses verses radial coordinate when $\tau_a = 0$ and $\tau_b = 0.2$. Parameter values are given in Table 3.1.

of each fibre as it is stretched, is varied. For small transmural pressures, varying C_2 has little effect (a). However, for larger values of the transmural pressure, increasing C_2 stiffens the airway wall. Similar to increasing C_1, increasing C_2 has little effect on the radial stress distribution (c), while the displacement (b), and the hoop and axial stresses (d, e) decrease. Physiologically C_2 depends on the degree of waviness of the fibres, with larger values indicating the fibres are less wavy. The amount of waviness could depend on the level of contraction within the airway when the collagen is deposited.

Results are shown in Fig. 3.5 when φ, which is the angle of the fibres from the circumferential direction, is varied. The smaller the angle the larger the component of the fibres that are in the circumferential direction and the stiffer the airway (a). Increasing φ has little effect on the radial stress distribution (c), while the displacement (b), and the hoop and axial stresses (d, e) increase. For $\varphi = \pi/6$ the axial stress decreases from the inner to the outer boundary of the wall (e). The angle of the ASM fibres is important when considering airways at different locations within the lung. It has been found that the fibre angle is greater in the distal airways than in the large proximal airways [31], so assuming the collagen fibres are aligned to the ASM fibres, the larger angle within the small airways indicates that the collagen will produce less resistance to inflation.

Finally, results are shown in Fig. 3.6 when χ, which is the dimensionless undeformed thickness of the airway wall, is varied. Thickening the wall results in a larger transmural pressures being required for the same increase in the lumen radius (a). Increasing χ, the displacement (b), and the hoop and axial stresses (d, e) decrease. The gradient of the radial stress is reduced in the thickened wall (c). Thickening of the wall is characteristic of airway wall remodelling in asthmatics [11, 58, 145], with these results showing that remodelled airways are stiffer, so less easily inflated.

3.2 Airway wall embedded in parenchyma

Having considered the airway wall in isolation, we consider the airway wall embedded in parenchyma. In this section we make the assumption that the parenchyma is nonlinearly elastic.

3.2.1 Elastic model of the parenchyma

In Sec. 3.1.1 a relationship was found between the pressures exerted on the airway wall and the lumen radius. Due its compressibility, it is not possible to find a similar analytical relationship for the parenchyma. An equation can however be found that

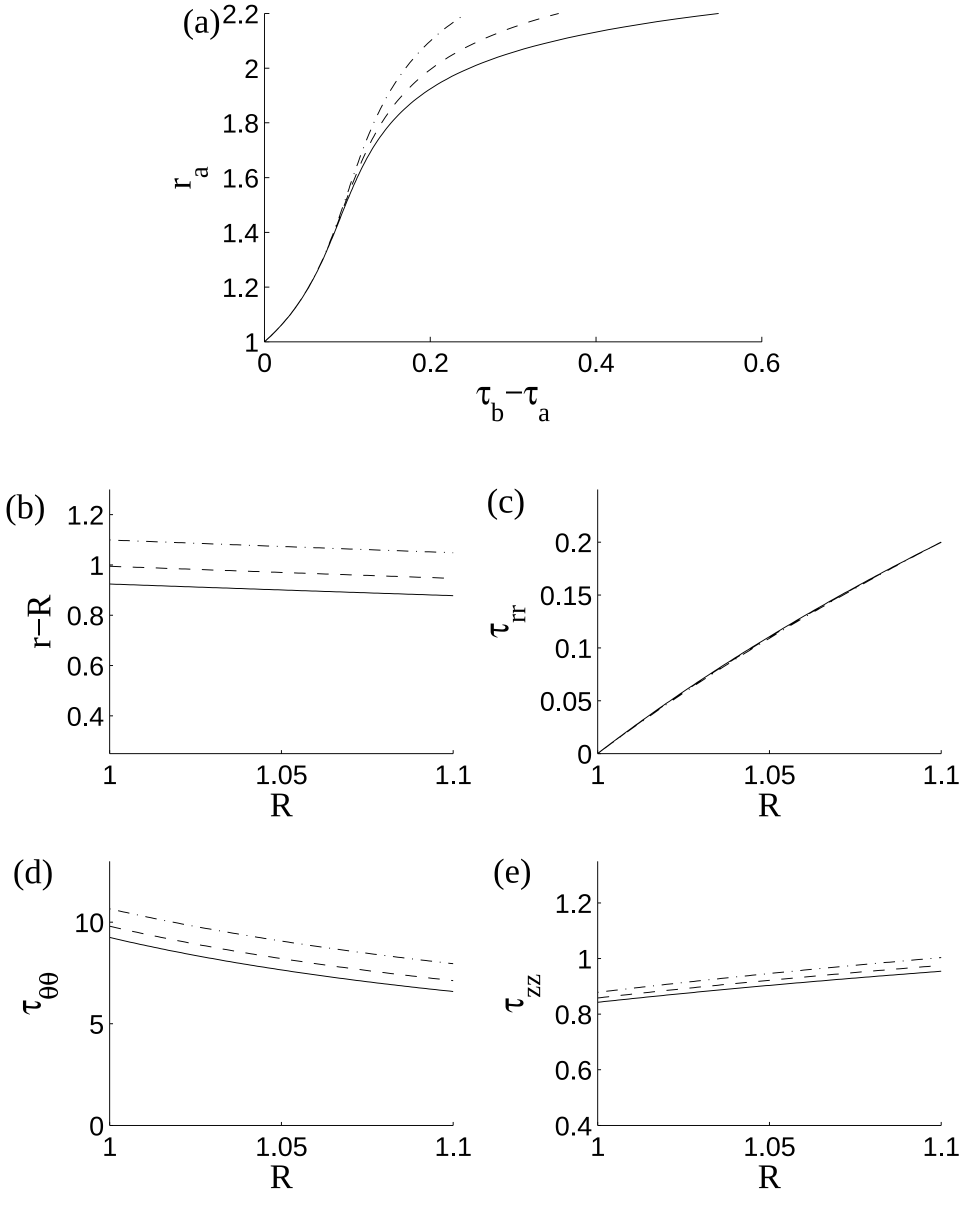

Figure 3.4: Plots showing the effect of varying C_2, which controls the nonlinear increase in stiffness of each fibre as it is stretched. $C_2 = 0.09$ (dot-dashed), 0.14 (dashed) or 0.19 (solid). Plots of (a) the transmural pressure against lumen radius, and (b) the displacement and (c)-(e) the radial, hoop and axial stresses verses radial coordinate when $\tau_a = 0$ and $\tau_b = 0.2$. Parameter values are given in Table 3.1.

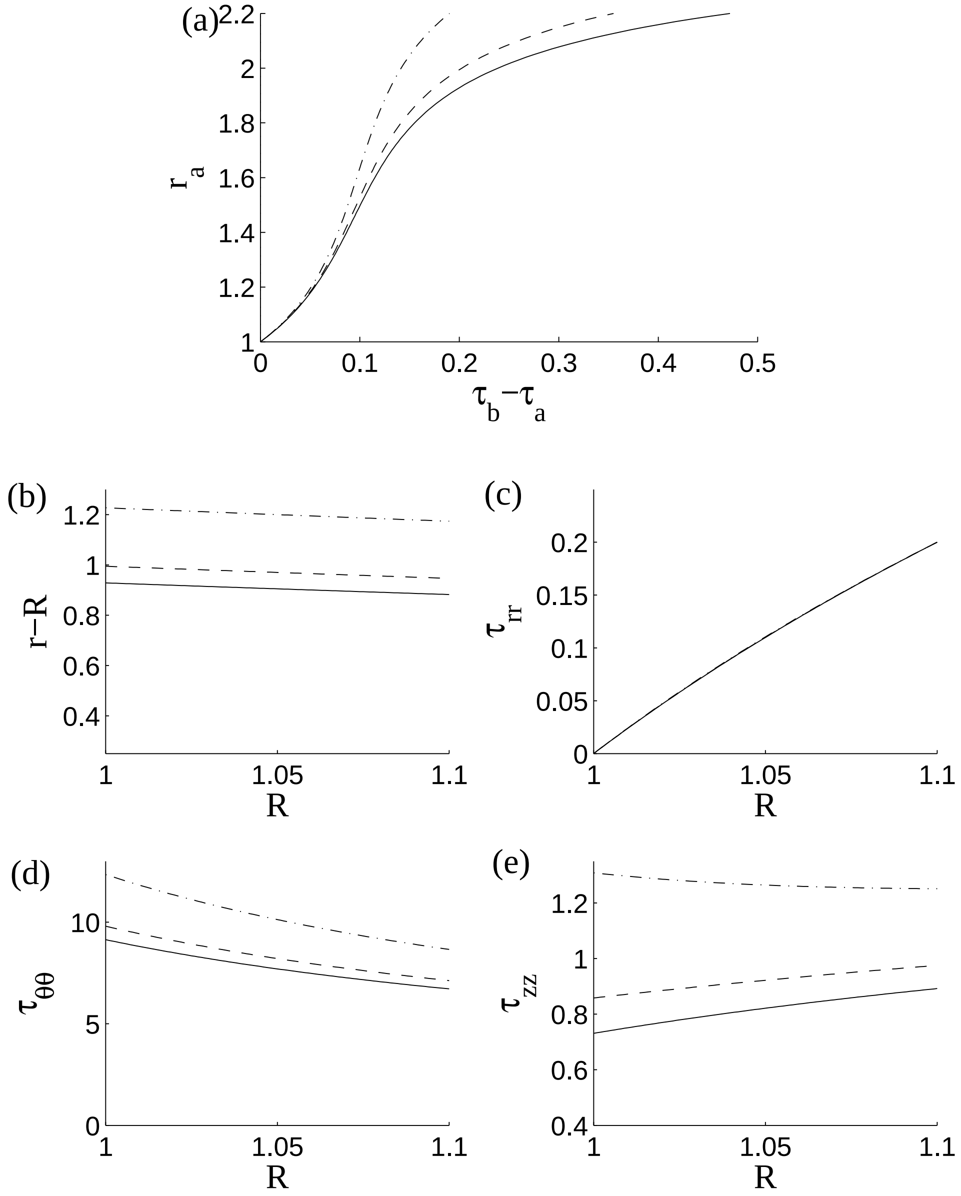

Figure 3.5: Plots showing the effect of varying φ, which is the angle of the fibres from the circumferential direction. $\varphi = 0$ (solid), $\pi/12$ (dashed) or $\pi/6$ (dot-dashed). Plots of (a) the transmural pressure against lumen radius, and (b) the displacement and (c)-(e) the radial, hoop and axial stresses verses radial coordinate when $\tau_a = 0$ and $\tau_b = 0.2$. Parameter values are given in Table 3.1.

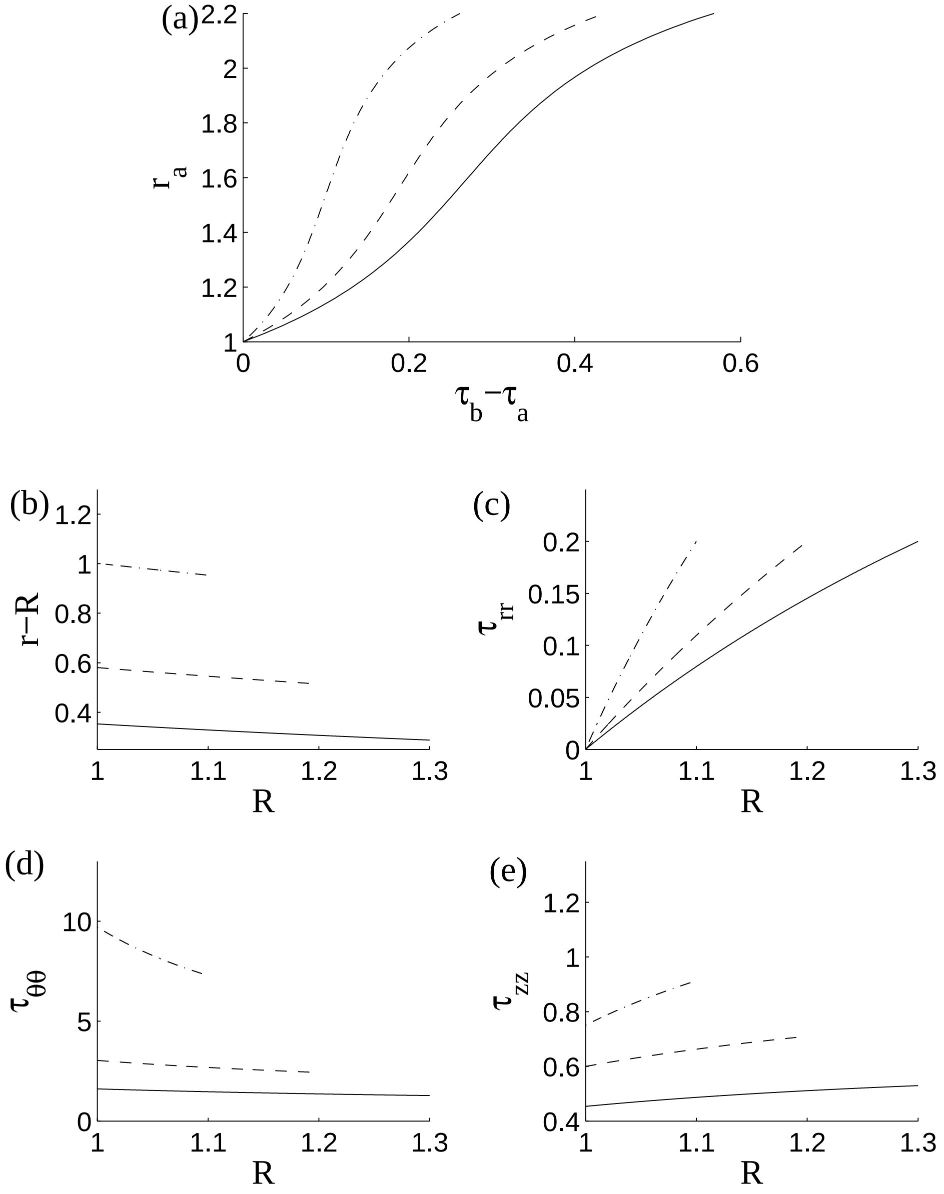

Figure 3.6: Plots showing the effect of varying χ, which is the dimensionless undeformed thickness of the airway wall. $\chi = 0.1$ (dot-dashed), 0.2 (dashed) or 0.3 (solid). Plots of (a) the transmural pressure against lumen radius, and (b) the displacement and (c)-(e) the radial, hoop and axial stresses verses radial coordinate when $\tau_a = 0$ and $\tau_b = 0.2$. Parameter values are given in Table 3.1.

can be solved numerically to find the radius across the parenchyma, which then allows the stress distributions to be found.

From (2.2.39), the nonzero components of the Cauchy stress tensor are given by

$$\tau_{rr} = \varrho\left\{\lambda^{(p)}\left(\frac{r'r}{R}-1\right)-\frac{R}{r'r}+\frac{r'R}{r}\right\}, \tag{3.2.1a}$$

$$\tau_{\theta\theta} = \tau_{rr}+\varrho\left(\frac{r}{Rr'}-\frac{r'R}{r}\right), \tag{3.2.1b}$$

$$\tau_{zz} = \tau_{rr}+\varrho\left(\frac{R}{r'r}-\frac{r'R}{r}\right). \tag{3.2.1c}$$

The equation for conservation of momentum is given by (2.2.41) and from (2.2.43) there are the following boundary conditions:

$$\tau_{rr}(R_b) = \tau_b, \tag{3.2.2a}$$

$$\tau_{rr}(R_p) = \tau_p \quad \text{or} \quad r(R_p) = r_p. \tag{3.2.2b}$$

Using (3.2.1) in (2.2.41) yields

$$\left(\frac{r''r}{R}+\frac{(r')^2}{R}-\frac{r'r}{R^2}\right)+\frac{1}{\lambda^{(p)}}\left(\frac{r''R}{r}+\frac{r'}{r}-\frac{1}{r'r}+\frac{Rr''}{(r')^2r}+\frac{R}{r^2}-\frac{1}{R}\right)=0, \tag{3.2.3}$$

where we have assumed that $\varrho \neq 0$. This can be solved numerically with (3.2.1a) and (3.2.2) to find r and r' across the layer. Before introducing the numerical methods to do this, we first show that when the boundary stresses are small our results match those of Brook *et al.* [22].

3.2.2 Small deformations

In this section the results for the parenchyma from the previous subsection are linearised, in order to ensure that the model predictions match those of the linear model of Brook *et al.* [22]. In the undeformed configuration the parenchyma is stress-free and $r = R$, thus we linearise by letting

$$\tau = \varepsilon\hat{\tau}, \quad r = R+\varepsilon\hat{r}, \tag{3.2.4}$$

where $0 < \varepsilon \ll 1$ and $\hat{\tau}$ and $\hat{r}$ are $O(1)$. Taking the leading order terms, (3.2.1) becomes

$$\tau_{rr} = \varrho\lambda^{(p)}\left(\frac{r}{R}+r'-2\right)+2\varrho(r'-1), \tag{3.2.5a}$$

$$\tau_{\theta\theta} = \tau_{rr}+2\varrho\left(\frac{r}{R}-r'\right), \tag{3.2.5b}$$

$$\tau_{zz} = \tau_{rr}-2\varrho(r'-1). \tag{3.2.5c}$$

Using the linearised version of the conservation of momentum equation, (2.2.42), yields

$$\frac{\partial \tau_{rr}}{\partial R} = \frac{2\varrho}{R}\left(\frac{r}{R} - r'\right), \tag{3.2.6}$$

hence differentiating (3.2.5a) to find an alternative expression for $\partial \tau_{rr}/\partial R$,

$$\varrho(\lambda^{(p)} + 2)\left(r'' + \frac{r'}{R} - \frac{r}{R^2}\right) = 0. \tag{3.2.7}$$

Therefore, the deformed radius is of the form

$$r = AR + \frac{B}{R}. \tag{3.2.8}$$

Substituting this into (3.2.5a) and applying the stress boundary conditions from (3.2.2), the nonzero components of the Cauchy stress tensor satisfy

$$\tau_{rr} = \tau_b + (\tau_p - \tau_b)\frac{R_p^2}{R_p^2 - R_b^2}\frac{R^2 - R_b^2}{R^2}, \tag{3.2.9a}$$

$$\tau_{\theta\theta} = \tau_b + (\tau_p - \tau_b)\frac{R_p^2}{R_p^2 - R_b^2}\frac{R^2 + R_b^2}{R^2}, \tag{3.2.9b}$$

$$\tau_{zz} = \left[\tau_b + (\tau_p - \tau_b)\frac{R_p^2}{R_p^2 - R_b^2}\right]\frac{\lambda^{(p)}}{\lambda^{(p)} + 1}. \tag{3.2.9c}$$

The displacement satisfies

$$r - R = B_2(R)\tau_p - B_1(R)\tau_b, \tag{3.2.10}$$

where

$$B_1(R) = \frac{R_b^2\left[R^2 + R_p^2(\lambda^{(p)} + 1)\right]}{2\varrho R(R_p^2 - R_b^2)(\lambda^{(p)} + 1)}, \quad B_2(R) = \frac{R_p^2\left[R^2 + R_b^2(\lambda^{(p)} + 1)\right]}{2\varrho R(R_p^2 - R_b^2)(\lambda^{(p)} + 1)}. \tag{3.2.11}$$

Redimensionalising (3.2.10) yields

$$\begin{aligned} r^* - R^* = & \frac{R_p^{*2}\left[R^{*2}\mu^{(p)*} + R_b^{*2}\left(\lambda^{(p*)} + \mu^{(p)*}\right)\right]}{2\mu^{(p)*}R^*\left(R_p^{*2} - R_b^{*2}\right)\left(\lambda^{(p)*} + \mu^{(p)*}\right)}\tau_p^* \\ & - \frac{R_b^{*2}\left[R^{*2}\mu^{(p)*} + R_p^{*2}\left(\lambda^{(p*)} + \mu^{(p)*}\right)\right]}{2\mu^{(p)*}R^*\left(R_p^{*2} - R_b^{*2}\right)\left(\lambda^{(p)*} + \mu^{(p)*}\right)}\tau_b^*, \end{aligned} \tag{3.2.12}$$

which agrees with the dimensional version of (S.8a) in [22]. Likewise, redimensionalising (3.2.9) agrees with the dimensional version of (S.6), for the parenchyma, in [22].

3.2.3 Numerical methods

We now introduce the numerical techniques used to solve (3.2.3) and couple the parenchyma to the airway wall. First we recall the following boundary conditions from (2.2.43):

$$\tau_{rr}^{(w)}(1) = \tau_a, \tag{3.2.13a}$$

$$r^{(w)}(R_b) = r^{(p)}(R_b) = r_b, \tag{3.2.13b}$$

$$\tau_{rr}^{(w)}(R_b) = \tau_{rr}^{(p)}(R_b) = \tau_b, \tag{3.2.13c}$$

$$\tau_{rr}^{(p)}(R_p) = \tau_p \quad \text{or} \quad r(R_p) = r_p. \tag{3.2.13d}$$

At present the values of r_b and τ_b are unknown. From (3.2.13b) the radius of the outer boundary of the airway wall is equal to the radius of the inner boundary of the parenchyma. τ_b is the value of the radial stress at the outer boundary of the airway wall and the inner boundary of the parenchyma (3.2.13c). For a given value of r_b, using (3.1.8) yields an estimate for τ_b in terms of r_b and τ_a, the radial stress at the inner boundary of wall, which is given by (3.2.13a). In order to ensure that the final boundary condition (3.2.13d) is satisfied, (3.2.3) must be solved.

Rearranging (3.2.3) yields

$$r'' = \frac{r'(r - r'R)\left(\lambda^{(p)}(r')^2 r^2 + r' r R + R^2\right)}{Rr(\lambda^{(p)}(r')^2 r^2 + R^2 (r')^2 + R^2)}, \tag{3.2.14}$$

which may be rewritten as the following two first order ODEs:

$$r' = y, \tag{3.2.15a}$$

$$y' = \frac{y(r - yR)\left(\lambda^{(p)} y^2 r^2 + y r R + R^2\right)}{Rr(\lambda^{(p)} y^2 r^2 + R^2 y^2 + R^2)}. \tag{3.2.15b}$$

In order to solve (3.2.15) across the parenchyma a shooting algorithm is applied. Selecting initial guesses for r_b and r_b', `ode45`, an ordinary differential equation solver in MATLAB, is used to shoot from $R = R_b$ to $R = R_p$. This yields values for r and r' for a series of points with $R_b \leq R \leq R_p$. Checks are made to see whether, when using (3.2.1a), $\tau_{rr}(R_b) = \tau_b$ to satisfy (3.2.13c) and $\tau_{rr}(R_p) = \tau_p$ or $r(R_p) = r_p$ to satisfy (3.2.13d). In general these conditions will not be satisfied and the estimates of r_b and r_b' must be altered. The MATLAB root-finding function `fzero` is used to alter r_b', so that the boundary condition (3.2.13c) is met when shooting from $R = R_b$ to $R = R_p$. In general (3.2.13d) will still not be satisfied and `fzero` is again used to update r_b. There are now two new estimates for r_b and r_b'. The process can be repeated until (3.2.13c) and (3.2.13d) are satisfied. Once met, the values of r and r' for a number of points of

R across the parenchyma are known. Inserting these into (3.2.1) gives the stress distributions within the parenchyma. The radius at each point within the airway wall can be found by using r_b and (3.1.3), while (3.1.6) and (3.1.9) can be used to find the stress distributions. The methods used to select an appropriate accuracy for the MATLAB ODE solver, used for the shooting, are described in Appendix A.

3.2.4 The choice of parameters

Embedding the airway wall in the parenchyma, values must be selected for the following additional parameters: the compressibility of the parenchyma given by $\lambda^{(p)} = 2\nu^{(p)}/(1 - 2\nu^{(p)})$, the ratio of the shear stress of the two layers given by ϱ and the undeformed outer boundary of the parenchyma given by R_p.

A number of experiments have been devised to try to establish properties of the lung parenchyma, with varying results. The Poisson ratio has been calculated as $\nu^{(p)} = 0.3$ [65] or $\nu =^{(p)} 0.43$ [92]. Unless otherwise stated we shall let $\nu^{(p)} = 0.3$, as used by Brook *et al.* [22].

$\varrho = \mu^{(p)*}/\mu^{(w)*}$, or in terms of the Young's modulus of the isotropic component of the inner and outer layers

$$\varrho = \frac{3E^{(p)*}}{2(1 + \nu^{(p)})E^{(w)*}}. \tag{3.2.16}$$

From Brook *et al.* [22] it is reasonable to set $E^{(w)*}/E^{(p)*} = 10$, so if $\nu^{(p)} = 0.3$, $\varrho = 3/26$.

The thickness of the parenchyma is much greater than that of the airway wall so that $R_p - R_b \gg \chi$. Unless otherwise stated, we let $R_p = 10$.

3.2.5 Comparison to previous work

Before going on to show results for the airway embedded within the parenchyma, our model predictions are compared to those of Lai-Fook *et al.* [91]. They carried out an experiment where they inflated the lung uniformly and then removed a cylindrical shaped piece of parenchyma. Due to a small reduction in the recoil pressure where the tissue was removed, there was an increase in the radius of the cylindrical hole. They used continuum modelling to predict the increase in the radius. Initially they used a linear model, which predicts that the shear modulus of the parenchyma, but not the Poisson ratio, affects the findings. The linear model predicts no change in the volume of the parenchyma. However, due to the size of the displacements, they repeated the calculations with a nonlinear model. With the revised model they found that there is

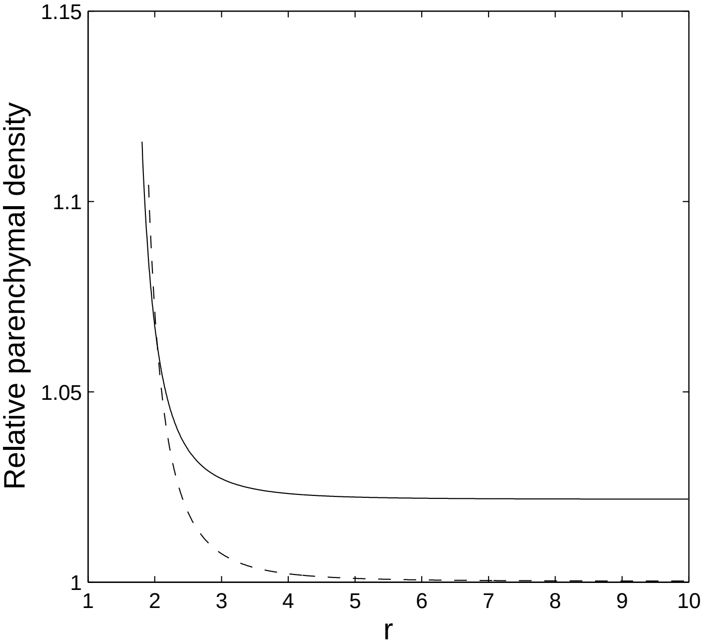

Figure 3.7: Plots of the parenchymal density relative to the density in the unstressed state. The internal normal pressure is $\tau_a = -1$, while $\tau_p = 0$ and $\nu = 0.3$. The two curves are for $R_p = 10$ (solid) and $R_p = 100$ (dashed).

in fact a small region localised about the cylinder, for which the parenchyma is compressed.

By ignoring the contribution of the airway wall, a stress is applied to the inner boundary of the parenchyma by prescribing τ_b, while letting $\tau_p = 0$. The density of the parenchyma after the deformation, relative to the density prior to the deformation, is found. This is done by dividing the cross-sectional area of a deformed region by the cross-sectional area of the region prior to deformation, so that the density

$$D = \frac{(R + \Delta R)^2 - R^2}{r(R + \Delta R)^2 - r(R)^2}. \tag{3.2.17}$$

Results are shown in Fig. 3.7. When $R_p = 10$ (solid), there is an increase in the parenchymal density across the parenchyma, although it is increased further near the inner boundary. One of the assumptions of the model of Lai-Fook *et al.* [91] though was that the parenchyma is infinite. If the size of the parenchyma is increased, so that $R_p = 100$ (dashed), the relative density is very close to 1 everywhere except near to the inner boundary, where it is increased. This shows that the majority of the compression occurs in a small region about the inner boundary, which is in agreement with the findings of Lai-Fook *et al.* [91].

Figure	τ_a	τ_p	$\nu^{(p)}$	$E^{(w)*}/E^{(p)*}$
3.8	*	*	0.3	10
3.9	0	0.1, 0.2, 0.3, 0.4	0.3	10
3.10	-0.1, -0.2, -0.3, -0.4	0	0.3	10
3.11	0	0.3	0.2, 0.3, 0.43	10
3.12	-0.3	0	0.2, 0.3, 0.43	10
3.13	0	0.3	0.3	5, 10, 100
3.14	-0.3	0	0.3	5, 10, 100

Table 3.2: The parameter values that vary for the figures listed. For all of the figures $C_1 = 0.05$, $C_2 = 0.14$, $\varphi = \pi/12$, $\chi = 0.2$, $R_p = 10$. $\varrho = 3E^{(p)*}/\left(2(1+\nu^{(p)})E^{(w)*}\right)$. *With Fig. 3.8 a range of values of τ_a and τ_p are used.

3.2.6 Results

In this subsection we show results for the airway embedded within the parenchyma. We show that the method used to inflate the airway is important. We also show the effect of altering the Poisson ratio of the parenchyma or the ratio of the shear moduli of the two layers on these distributions. The parameter values that are used for the graphs are given in Table 3.2.

We introduce two ways of inflating the airway, which we will refer to as internal and external inflation and define as follows:

- External inflation - $\tau_a = 0$ and τ_p is increased so that the outer boundary is pulled out,
- Internal inflation - $\tau_p = 0$ and τ_a is decreased so that the inner boundary is pushed out.

Physiologically, external and internal inflation correspond to normal breathing and artificial ventilation, respectively. Plots of the lumen radius against the transpulmonary pressure are shown in Fig. 3.8. Larger transpulmonary pressures are required for the same increase in the lumen radius when inflating the airway externally (dashed) than when inflating internally (solid). In both cases the fibres within the airway wall ensure that as the airway inflates, it stiffens. These results show that smaller pressure differences are required to inflate the airways with artificial ventilation than with normal breathing.

Plots are shown in Fig. 3.9 of the distribution of the radial displacement and the

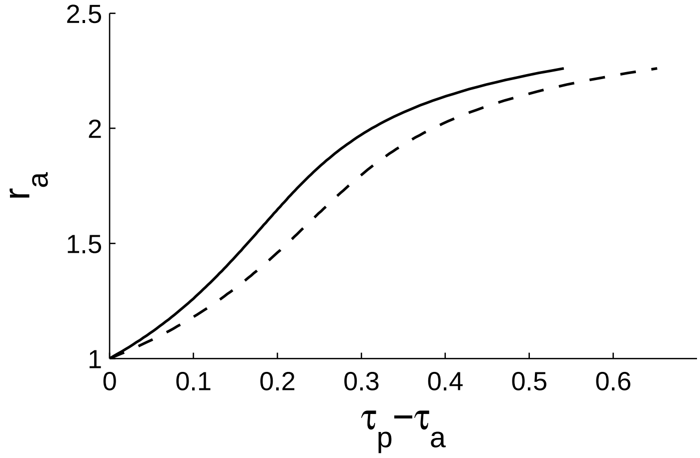

Figure 3.8: Curves of the lumen radius against the transpulmonary pressure, when the airway is inflated externally (dashed, $\tau_a = 0$) or internally (solid, $\tau_p = 0$). Parameter values are given in Table 3.2.

stresses across the airway for various values of the transpulmonary pressure, when the airway is inflated externally (corresponding to normal breathing). Considering the radial displacement, there are large displacements within the parenchyma (a). One method for ensuring that the displacement within the parenchyma is not unrealistically large, would be to use the alternate boundary condition for the outer boundary of the parenchyma, (3.2.2b), and prescribe r_p rather than τ_p. The stresses in the radial, hoop and axial directions are positive throughout indicating that the tissue is under tension (b-d). The radial stress varies a lot across the airway wall, whereas there is little variation within the parenchyma (b). The hoop and axial stresses are discontinuous at the boundary between the two layers (c, d). When modelling arteries as multi-layered structures, Holzapfel *et al.* [61] found similar discontinuities in the hoop and axial stresses at the boundaries between the layers. Also similar to their findings are that the magnitude of the hoop and axial stresses are much larger than those of the radial stresses, at least in the airway wall. Within the airway wall the hoop stress is greatest at the inner boundary (c), while the axial stress is greatest at the outer boundary (d).

Secondly for the case that the airway is inflated internally (mimicking artificial ventilation), the radial displacement and the stress distributions are shown in Fig. 3.10. The displacement is greatest at the inner boundary, with the airway wall shielding the parenchyma from large displacements (a). The radial stress is negative, indicating that the tissue is under tension in the radial direction (b). There is more variation in the radial stress within the airway wall than in the parenchyma. The hoop stress is similar to

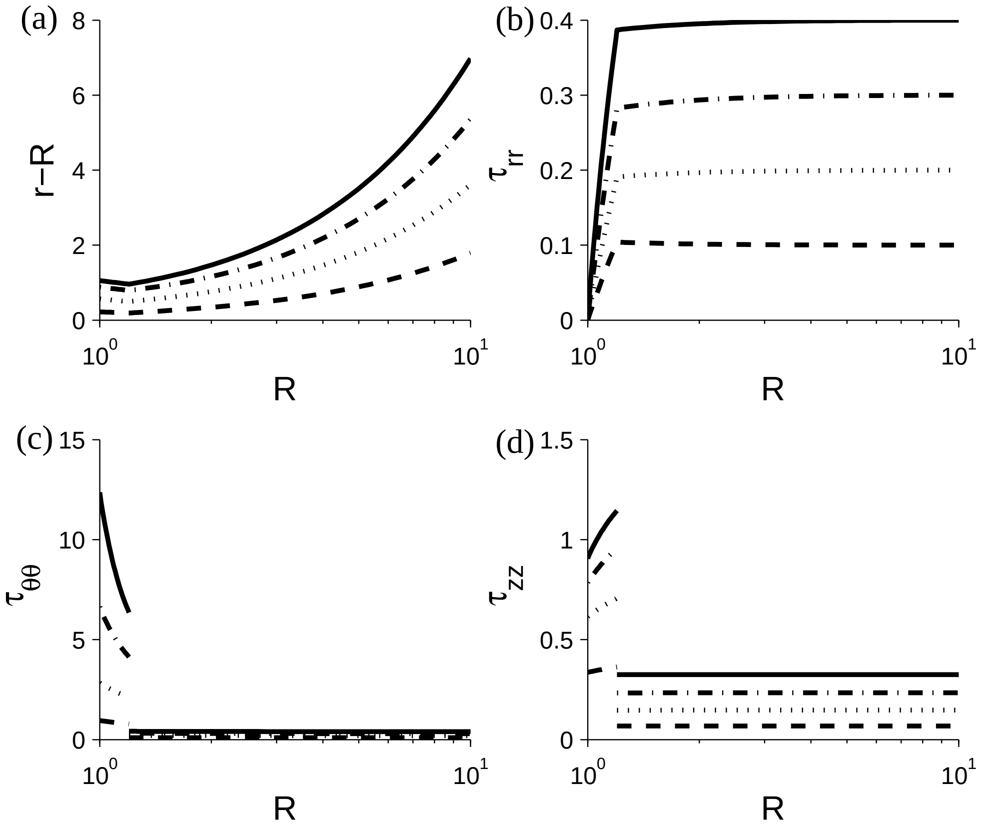

Figure 3.9: Curves showing the (a) displacement and (b)-(d) the radial, hoop and axial stresses verses radial coordinate for a two-layer annulus with $\tau_a = 0$ and $\tau_p = 0.1$ (dashed), $\tau_p = 0.2$ (dotted), $\tau_p = 0.3$ (dot-dashed) and $\tau_p = 0.4$ (solid). Parameter values are given in Table 3.2.

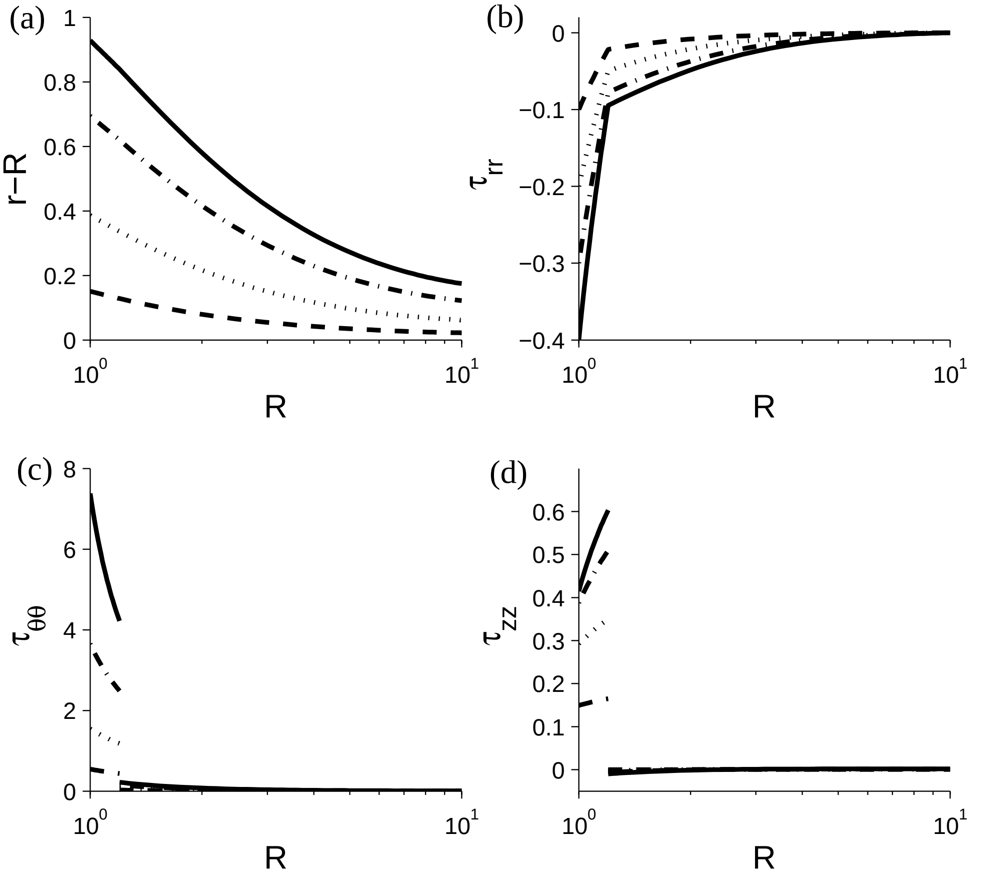

Figure 3.10: Curves showing the (a) displacement and (b)-(d) the radial, hoop and axial stresses verses radial coordinate for a two-layer annulus with $\tau_p = 0$ and $\tau_a = -0.1$ (dashed), $\tau_a = -0.2$ (dotted), $\tau_a = -0.3$ (dot-dashed) and $\tau_a = -0.4$ (solid). Parameter values are given in Table 3.2.

when the airway is inflated externally. Positive stresses indicate that the tissue is under compression in the circumferential direction (c), with a discontinuity at the boundary between the two layers and greatest stress at the inner boundary of the airway wall. Within the airway wall the axial stress is similar to when the airway is inflated externally, with positive stresses that are greatest at the outer boundary of the wall (d). Within the parenchyma the axial stress is very small, with compressive stresses close to the airway wall, while further away there are tensile stresses.

In Sec. 3.2.4 we noted that different values had been calculated experimentally for the Poisson ratio of the parenchyma. We therefore investigate what effect varying $\nu^{(p)}$ has on the results. In Fig. 3.11 results are shown when the airway is inflated externally, with $\nu^{(p)} = 0.2$, $\nu^{(p)} = 0.3$ (as found in [65]) or $\nu^{(p)} = 0.43$ (as found in [92]). Increasing

$\nu^{(p)}$, increases the transpulmonary pressure that is required for same increase in the lumen radius (a). For larger values of $\nu^{(p)}$, there is reduced radial displacement, and stress across the two layers (b, c), while the hoop and axial stresses are reduced within the airway wall, but increased within the parenchyma (d, e). With $\nu^{(p)} = 0.2$ the radial stress peaks at the boundary of the two layers. Therefore, smaller displacements result if the parenchyma is less compressible. These differences are most noticeable within the parenchyma.

The effect of changing the Poisson ratio when inflating the airway internally are shown in Fig. 3.12. There is less variation between the curves for the different levels of parenchymal compressibility than when the airway was inflated externally. The airway is again stiffer with larger values of $\nu^{(p)}$ (a). Larger values of $\nu^{(p)}$ also result in reduced displacement, except for the outer region of the parenchyma where there is an increase in the displacement (b). The radial stress (c) and the hoop and axial stresses within the airway wall (d, e) are smaller for larger values of $\nu^{(p)}$. Within the parenchyma, the hoop stress is increased slightly with increased $\nu^{(p)}$, while the axial stress is increased slightly in the inner part of the parenchyma, but decreased slightly in the outer part of the parenchyma. Similar to with external inflation, although to a smaller extent, the airway is inflated less if the parenchyma is less compressible.

We have considered a fixed value of the ratio of the shear modulus of the parenchyma to the base matrix of the airway wall. However, there is evidence that the shear modulus of the parenchyma is linearly related to the transpulmonary pressure [160], so that as the transpulmonary pressure increases, ϱ also increases. In the next two figures we consider the effect of altering ϱ. Firstly, the effect of altering ϱ when the airway is inflated externally is shown in Fig. 3.13. For smaller values of ϱ, when the stiffness of the airway wall is closer to that of the parenchyma, larger transpulmonary pressures, relative to the shear modulus of the wall matrix, are required for the same increase in the lumen radius (a). The distribution of the radial displacement and stress and the hoop and axial stresses are increased as ϱ is increased (b-e), except for the hoop stress within the parenchyma, where it has a decreased value (d). In particular, the shape of the radial stress distribution is altered, so that while $\tau_b < \tau_p$ for the curves drawn using the smaller two values of ϱ, τ_{rr} peaks at the boundary for the largest value. These results therefore show that increased values of the shear modulus of the parenchyma, and thus of ϱ, as may be appropriate for high transpulmonary pressures, lead to a stiffer airway and reduced inflation. The problem of large displacements predicted within the parenchyma is also reduced.

Similar alterations are seen when ϱ, the ratio of the shear stress of the two layers, is

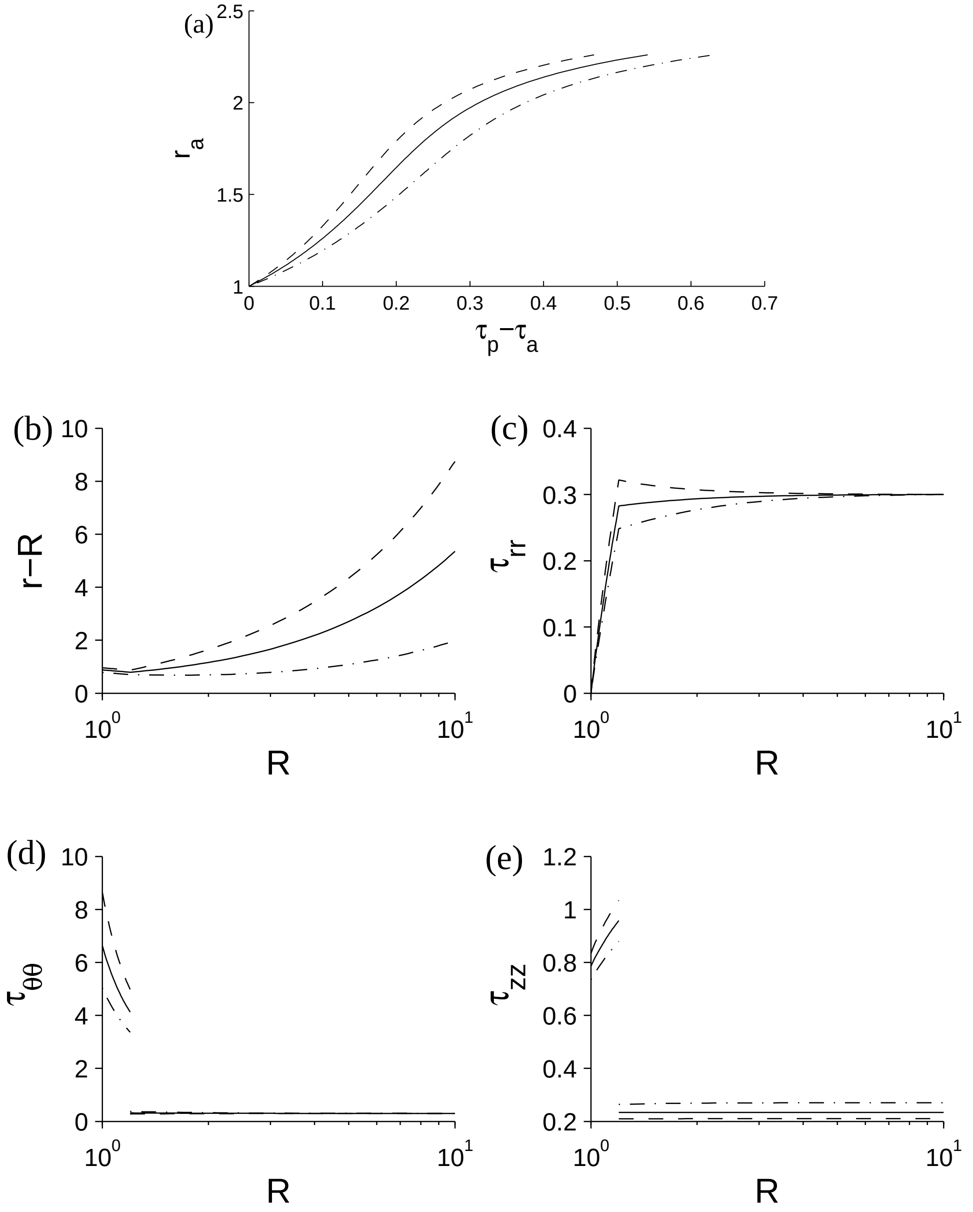

Figure 3.11: Plots showing the effect of $\nu^{(p)}$, the Poisson ratio of the parenchyma, when inflating the airway externally. $\nu = 0.2$ (dashed), 0.3 (solid) and 0.43 (dot-dashed). Plots of (a) the lumen radius against the transpulmonary pressure, and distributions of (b) the displacement and (c)-(e) the radial, hoop and axial stresses verses radial coordinate. Parameter values are given in Table 3.2.

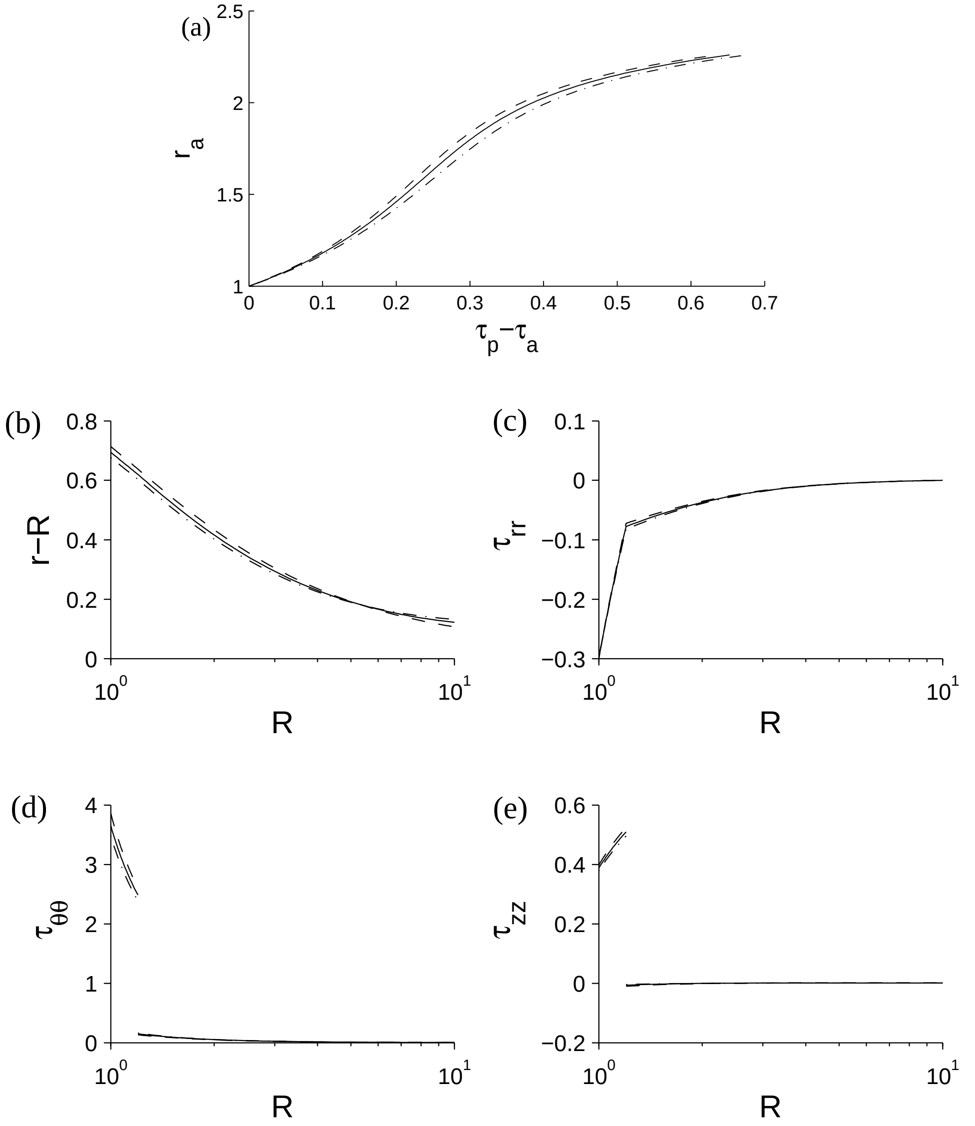

Figure 3.12: Plots showing the effect of $\nu^{(p)}$, the Poisson ratio of the parenchyma, when inflating the airway internally. $\nu = 0.2$ (dashed), 0.3 (solid) and 0.43 (dot-dashed). Plots of (a) the lumen radius against the transpulmonary pressure, and distributions of (b) the displacement and (c)-(e) the radial, hoop and axial stresses verses radial coordinate. Parameter values are given in Table 3.2.

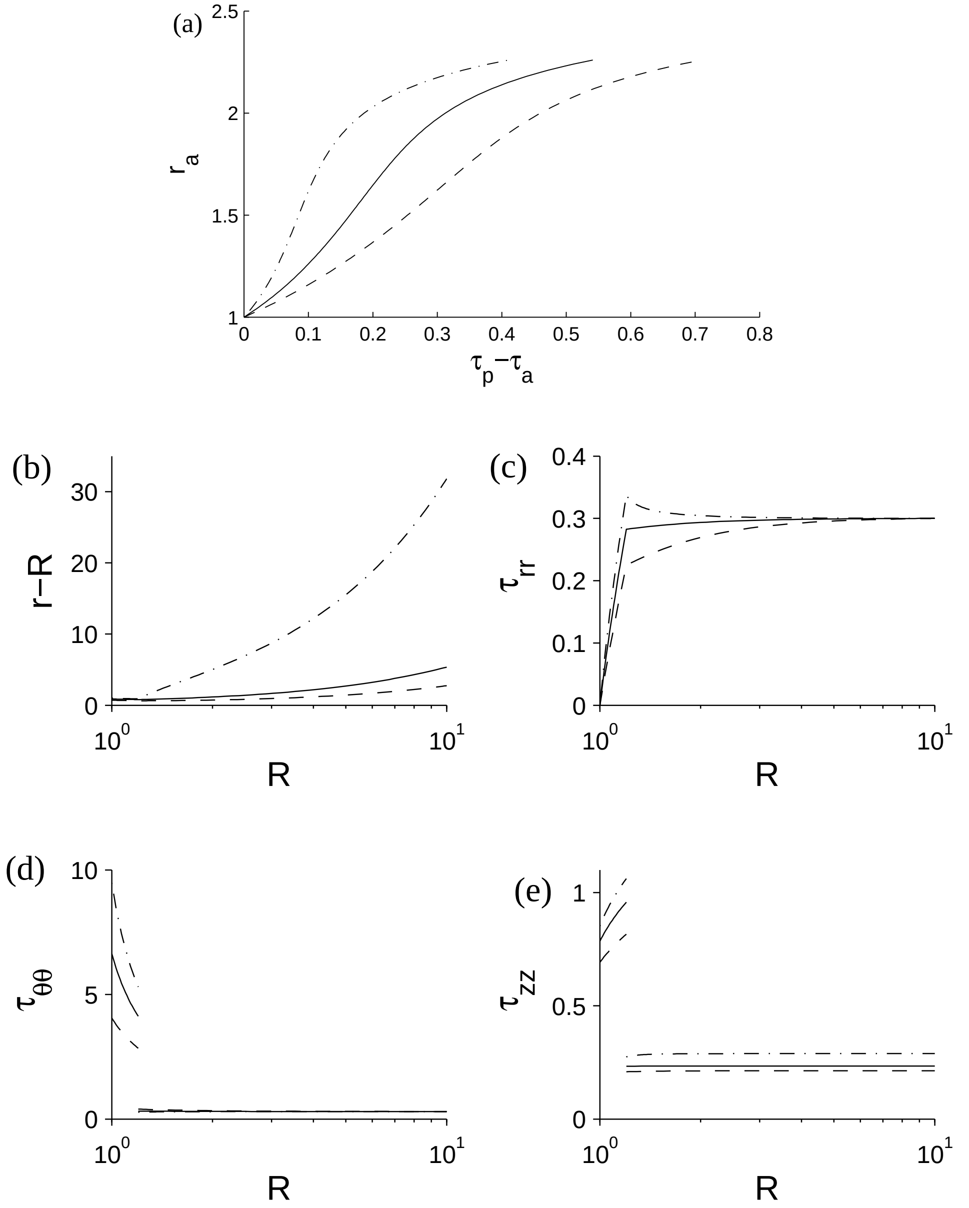

Figure 3.13: Plots showing the effect of ϱ, the ratio of the shear stress of the two layers, when inflating the airway externally. $\varrho = 3/13$ (dashed), $3/26$ (solid) and $3/260$ (dot-dashed). Plots of (a) the lumen radius against the transpulmonary pressure, and (b) the displacement and (c)-(e) the radial, hoop and axial stresses verses radial coordinate. Parameter values are given in Table 3.2.

altered and the airway is inflated internally, with a couple of exceptions (Fig. 3.14). The radial stress no longer peaks at the boundary between the two layers when $\varrho = 3/260$ (c, dot-dashed) and within the outer section of the parenchyma, the axial stress is now reduced for larger values of ϱ (e). These results therefore also show that increased values of the shear modulus of the parenchyma, and thus of ϱ, lead to a stiffer airway and reduced inflation when the airway is internally inflated.

3.3 Viscoelastic behaviour of airway wall embedded in parenchyma

In this section we again consider the airway wall embedded in parenchyma, but now assume that the parenchyma is linearly viscoelastic.

3.3.1 Viscoelastic model of the parenchyma

The nonzero components of the Cauchy stress tensor are given in (2.2.40). Assuming that times are nondimensionalised with respect $T^* = t_r^*$, from (2.2.42),

$$\left[\frac{\partial}{\partial t} + 1\right] \frac{\partial \tau_{rr}}{\partial R} + \frac{\tau_{rr} - \tau_{\theta\theta}}{R} = \varrho \left(\lambda^{(p)} + 2\right) \left[t_c \frac{\partial}{\partial t} + 1\right] \left(r'' + \frac{r'}{R} - \frac{r}{R^2}\right) = 0. \tag{3.3.1}$$

This may be rewritten in the form

$$\frac{\partial}{\partial t} \left\{ \exp\left(\frac{t}{t_c}\right) \left(r'' + \frac{r'}{R} - \frac{r}{R^2}\right) \right\} = 0, \tag{3.3.2}$$

which, integrating and assuming that initially the airway is in the stress-free undeformed steady state, yields

$$r'' + \frac{r'}{R} - \frac{r}{R^2} = 0, \tag{3.3.3}$$

so like in Sec. 3.2.2 the deformed radius is of the form

$$r = AR + \frac{B}{R}. \tag{3.3.4}$$

Substituting into (2.2.40) and applying the boundary conditions (3.2.2a) and the stress option from (3.2.2b), yields

$$\tau_{rr}(R,t) = \tau_b(t) + (\tau_p(t) - \tau_b(t)) \frac{R_p^2}{R_p^2 - R_b^2} \frac{R^2 - R_b^2}{R^2}, \tag{3.3.5a}$$

$$\tau_{\theta\theta}(R,t) = \tau_b(t) + (\tau_p(t) - \tau_b(t)) \frac{R_p^2}{R_p^2 - R_b^2} \frac{R^2 + R_b^2}{R^2}, \tag{3.3.5b}$$

$$\tau_{zz}(R,t) = \left[\tau_b(t) + (\tau_p(t) - \tau_b(t)) \frac{R_p^2}{R_p^2 - R_b^2}\right] \frac{\lambda^{(p)}}{\lambda^{(p)} + 1} \tag{3.3.5c}$$

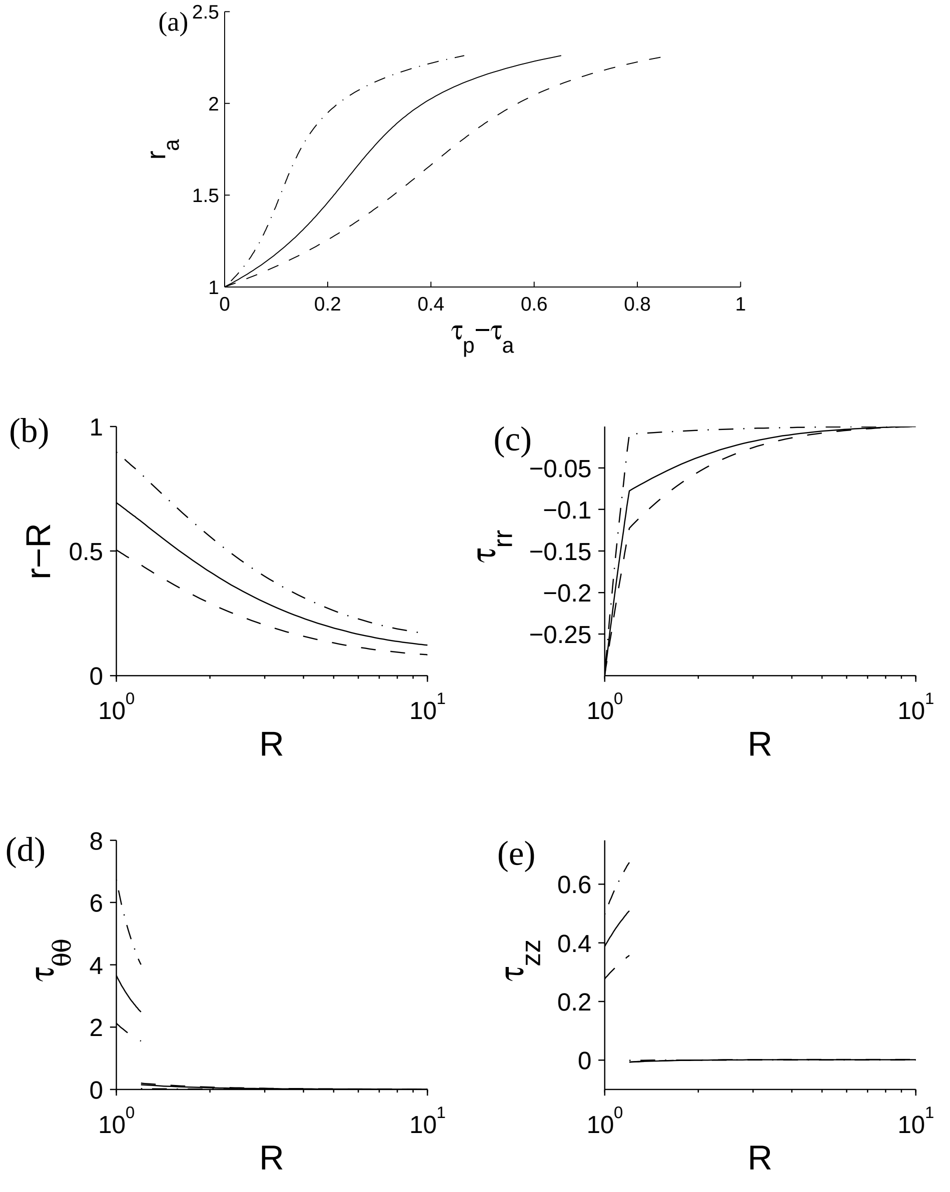

Figure 3.14: Plots showing the effect of ϱ when inflating the airway internally. $\varrho = 3/13$ (dashed), $3/26$ (solid) and $3/260$ (dot-dashed). Plots of (a) the lumen radius against the transpulmonary pressure, and (b) the displacement and (c)-(e) the radial, hoop and axial stresses verses radial coordinate. Parameter values are given in Table 3.2.

with the displacements satisfying

$$\left[t_c\frac{\partial}{\partial t}+1\right](r(R,t)-R)=\left[\frac{\partial}{\partial t}+1\right]\left[B_2(R)\tau_p(t)-B_1(R)\tau_b(t)\right], \tag{3.3.6}$$

where $B_1(R)$ and $B_2(R)$ are given in (3.2.11). Alternatively (3.3.5) and (3.3.6) may be obtained by applying the nondimensional version of (1.5.51),

$$\boldsymbol{\tau}\to\frac{\mathrm{d}\boldsymbol{\tau}}{\mathrm{d}t}+\boldsymbol{\tau},\quad r\to t_c\frac{\mathrm{d}r}{\mathrm{d}t}+r, \tag{3.3.7}$$

to the linear equations (3.2.9) and (3.2.10). While stresses within the parenchyma respond instantaneously to any changes in the τ_b and τ_p, displacements do not.

Integrating (3.3.6) and assuming that initially the airway is in the stress-free undeformed steady state yields

$$r(R,t)-R=B_2(R)I_2(t)-B_1(R)I_1(t), \tag{3.3.8}$$

where

$$I_1(t)=\exp\left(-\frac{t}{t_c}\right)\int_{s=0}^{t}\exp\left(\frac{s}{t_c}\right)\left[\frac{\mathrm{d}}{\mathrm{d}s}+1\right]\frac{\tau_b(s)}{t_c}\mathrm{d}s, \tag{3.3.9a}$$

$$I_2(t)=\exp\left(-\frac{t}{t_c}\right)\int_{s=0}^{t}\exp\left(\frac{s}{t_c}\right)\left[\frac{\mathrm{d}}{\mathrm{d}s}+1\right]\frac{\tau_p(s)}{t_c}\mathrm{d}s. \tag{3.3.9b}$$

In order to solve (3.3.8) or (3.3.13), to find the displacement, it is necessary to first find $\tau_b(t)$, the radial stress at the boundary. At present r_b, the radius of the boundary, is not known. Considering (3.3.6) at $R=R_b$ and using (3.1.8) to get an expression for τ_b in terms of r_b, if τ_p is prescribed,

$$\begin{aligned}F_1\frac{\mathrm{d}r_b}{\mathrm{d}t}=&\left[\frac{\mathrm{d}}{\mathrm{d}t}+1\right]\left\{B_2(R_b)\tau_p-B_1(R_b)\left(\tau_a+2\cos^2\varphi\int_1^{R_b}\frac{A}{R}\mathrm{d}R\right)\right\}-(r_b-R_b)\\&-B_1(R_b)\left\{\log\left(\frac{r_aR_b}{r_b}\right)+\frac{(r_b^2-R_b^2)(R_b^2-1)}{2r_a^2r_b^2}+H(r_b-R_b)C_1\sqrt{\frac{\pi}{C_2}}\cos^2\varphi\right.\\&\left.\left(\operatorname{erfi}\left\{\sqrt{C_2}\left(r_b^2-R_b^2\right)\cos^2\varphi\right\}-\operatorname{erfi}\left\{\sqrt{C_2}\left(\frac{r_b^2-R_b^2}{R_b^2}\right)\cos^2\varphi\right\}\right)\right\},\end{aligned} \tag{3.3.10}$$

where $r_a=\sqrt{r_b^2-R_b^2+1}$ and

$$\begin{aligned}F_1=&t_c+B_1(R_b)\left(\frac{(R_b^2-1)(R_b^2r_a^2+r_b^2)}{r_a^4r_b^3}+H(r_b-R_b)4C_1\cos^4\varphi r_b\right.\\&\left.\left\{\exp\left[C_2(r_b-R_b)^4\cos^4\varphi\right]-\frac{1}{R_b}\exp\left[\frac{C_2(r_b-R_b)^4\cos^4\varphi}{R_b^4}\right]\right\}\right).\end{aligned} \tag{3.3.11}$$

τ_a and τ_p are given by the boundary conditions and A is assumed to be known, with $A=0$ in this chapter.

Equations (3.3.5) to (3.3.11) are suitable when τ_p is prescribed. Alternatively if r_p is prescribed, by letting $R = R_p$ in (3.3.8) yields

$$\begin{aligned}\left[t_c\frac{\partial}{\partial t}+1\right](r(R,t)-R) = {} & \left[\frac{\partial}{\partial t}+1\right]\left[\frac{B_2(R)B_1(R_p)}{B_2(R_p)}-B_1(R)\right]\tau_b(t) \\ & + \frac{B_2(R)}{B_2(R_p)}\left[t_c\frac{\partial}{\partial t}+1\right](r_p-R_p). \end{aligned} \tag{3.3.12}$$

Integrating gives the displacement within the parenchyma as follows:

$$r(R,t)-R = \frac{B_2(R)}{B_2(R_p)}\left(r_p-R_p\right)+\left[\frac{B_2(R)}{B_2(R_p)}B_1(R_p)-B_1(R)\right]I_1(t). \tag{3.3.13}$$

Now $\mathrm{d}r_b/\mathrm{d}t$ satisfies

$$\begin{aligned} F_2\frac{\mathrm{d}r_b}{\mathrm{d}t} = {} & \frac{B_2(R_b)}{B_2(R_p)}\left[t_c\frac{\mathrm{d}}{\mathrm{d}t}+1\right]\left(r_p-R_p\right)+\left[\frac{\mathrm{d}}{\mathrm{d}t}+1\right]\Bigg\{\left[\frac{B_2(R_b)B_1(R_p)}{B_2(R_p)}-B_1(R_b)\right] \\ & \left(\tau_a+2\cos^2\varphi\int_1^{R_b}\frac{A}{R}\mathrm{d}R\right)\Bigg\}-(r_b-R_b)+\left[\frac{B_2(R_b)B_1(R_p)}{B_2(R_p)}-B_1(R_b)\right] \\ & \Bigg\{\log\left(\frac{r_aR_b}{r_b}\right)+\frac{(r_b^2-R_b^2)(R_b^2-1)}{2r_a^2r_b^2}+H(r_b-R_b)C_1\sqrt{\frac{\pi}{C_2}}\cos^2\varphi \\ & \left(\operatorname{erfi}\left\{\sqrt{C_2}\left(r_b^2-R_b^2\right)\cos^2\varphi\right\}-\operatorname{erfi}\left\{\sqrt{C_2}\left(\frac{r_b^2-R_b^2}{R_b^2}\right)\cos^2\varphi\right\}\right)\Bigg\}, \end{aligned} \tag{3.3.14}$$

where

$$\begin{aligned} F_2 = {} & t_c-\left[\frac{B_2(R_b)B_1(R_p)}{B_2(R_p)}-B_1(R_b)\right]\Bigg(\frac{(R_b^2-1)(R_b^2r_a^2+r_b^2)}{r_a^4r_b^3}+H(r_b-R_b)4C_1\cos^4\varphi r_b \\ & \left\{\exp\left[C_2(r_b-R_b)^4\cos^4\varphi\right]-\frac{1}{R_b}\exp\left[\frac{C_2(r_b-R_b)^4\cos^4\varphi}{R_b^4}\right]\right\}\Bigg). \end{aligned} \tag{3.3.15}$$

In order to solve (3.3.10) or (3.3.14), we introduce the following methods of inflating the airway:

1. τ_p is linearly increased until $\tau_p = \overline{\tau}_p$ and then held constant so that

$$\tau_a(t)=0, \forall t, \qquad \tau_p(t)=\begin{cases}0, & \text{if } t<0,\\ \overline{\tau}_p\frac{t}{t_i}, & \text{if } 0\le t\le t_i,\\ \overline{\tau}_p, & \text{if } t>t_i;\end{cases} \tag{3.3.16}$$

2. τ_a is linearly decreased until $\tau_a = \overline{\tau}_a$ and then held constant so that

$$\tau_a(t)=\begin{cases}0, & \text{if } t<0,\\ \overline{\tau}_a\frac{t}{t_i}, & \text{if } 0\le t\le t_i,\\ \overline{\tau}_a, & \text{if } t>t_i,\end{cases} \qquad \tau_p(t)=0,\forall t; \tag{3.3.17}$$

3. An oscillatory force is applied to the outer boundary so that

$$\tau_a(t) = 0 \qquad \tau_p(t) = \overline{\tau}_p(1 - \cos(\omega t)), \quad t \geq 0, \tag{3.3.18}$$

   where ω is the dimensionless angular frequency and $\overline{\tau}_p$ is the amplitude of the oscillations;

4. The position of the outer boundary is oscillated so that

$$\tau_a(t) = 0 \qquad r_p(t) = R_p + \overline{r}_p(1 - \cos(\omega t)), \quad t \geq 0, \tag{3.3.19}$$

   where ω is the dimensionless angular frequency and $\overline{r}_p$ is the amplitude of the oscillations.

Using `ode45` in MATLAB with the initial condition that $r_b(0) = R_b$ we are able to solve to find $r_b(t)$. The displacements within the airway wall can then be found using (3.1.3), while the stresses can be found using (3.1.6) and (3.1.9). In order to find the displacements within the parenchyma, we first use (3.3.8) at $R = R_b$ to find the following expression for I_1, which may then be inserted into (3.3.8):

$$I_1(t) = \frac{r_b(t) - R_b - B_2(R_b)I_2(t)}{B_1(R_b)}. \tag{3.3.20}$$

If r_p is prescribed, using (3.3.13) at $R = R_b$ there is the following expression for I_1, which may then be inserted into (3.3.13):

$$I_1(t) = \frac{B_2(R_p)\left(r_b(t) - R_b\right) - B_2(R_b)\left(r_p(t) - R_p\right)}{B_2(R_b)B_1(R_p) - B_1(R_b)B_2(R_p)}. \tag{3.3.21}$$

All that is left to find is the stresses within the parenchyma. If τ_p is prescribed, τ_b is given by (3.1.8) and the stresses are found using (2.2.40). If r_p is prescribed, (3.1.8) is first differentiated to find an expression for $\mathrm{d}\tau_b/\mathrm{d}t$. Using (3.3.12), (3.3.5) is altered to

C_1	C_2	φ	χ	R_p	$\nu^{(p)}$	ϱ	$\mu^{(w)*}$	t_c	ω
0.05	0.14	$\pi/12$	0.2	10	0.3	3/26	20 cm water	4	$2\pi/5$

Table 3.3: The parameter values that are used in Sec. 3.3 unless otherwise stated.

give the following equations, which may be updated to find the parenchymal stresses:

$$\left[\frac{\partial}{\partial t}+1\right]\tau_{rr}(R,t)=\left[\frac{\mathrm{d}}{\mathrm{d}t}+1\right]\tau_b(t)+\left\{\left[t_c\frac{\mathrm{d}}{\mathrm{d}t}+1\right]\frac{r_p-R_p}{B_2(R_p)}+\left[\frac{\mathrm{d}}{\mathrm{d}t}+1\right]\tau_b \left(\frac{B_1(R_p)}{B_2(R_p)}-1\right)\right\}\frac{R_p^2}{R_p^2-R_b^2}\frac{R^2-R_b^2}{R^2}, \tag{3.3.22a}$$

$$\left[\frac{\partial}{\partial t}+1\right]\tau_{\theta\theta}(R,t)=\left[\frac{\mathrm{d}}{\mathrm{d}t}+1\right]\tau_b(t)+\left\{\left[t_c\frac{\mathrm{d}}{\mathrm{d}t}+1\right]\frac{r_p-R_p}{B_2(R_p)}+\left[\frac{\mathrm{d}}{\mathrm{d}t}+1\right]\tau_b \left(\frac{B_1(R_p)}{B_2(R_p)}-1\right)\right\}\frac{R_p^2}{R_p^2-R_b^2}\frac{R^2+R_b^2}{R^2}, \tag{3.3.22b}$$

$$\left[\frac{\partial}{\partial t}+1\right]\tau_{zz}(R,t)=\left[\left[\frac{\mathrm{d}}{\mathrm{d}t}+1\right]\tau_b(t)+\left\{\left[t_c\frac{\mathrm{d}}{\mathrm{d}t}+1\right]\frac{r_p-R_p}{B_2(R_p)}+\left[\frac{\mathrm{d}}{\mathrm{d}t}+1\right]\tau_b \left(\frac{B_1(R_p)}{B_2(R_p)}-1\right)\right\}\frac{R_p^2}{R_p^2-R_b^2}\right]\frac{\lambda^{(p)}}{\lambda^{(p)}+1}. \tag{3.3.22c}$$

3.3.2 The choice of parameters

A value must be assigned to the parameter t_c, which describes the ratio of the creep timescale to the relaxation timescale. If methods 3 or 4 are used to inflate the airway, a value must also be chosen for ω. During normal breathing, it is reasonable to assume that the period of a breath is 5s. While from [135], we expect the stress relaxation time to be approximately one second. It is therefore appropriate to set $\omega = 2\pi/5$. The other parameter values are given in Table 3.3 and are as described previously.

Pressure-volume curves have been produced experimentally for the lung, by incrementally increasing the pressure applied around the lung and measuring the resulting lung volume. In Fig. 3.15, comparisons are made between the equilibrium loop formed when using (3.3.18) (left) and a representative pressure-volume curve (right). In order to take into account the increased period of the oscillation, due to stopping at intermediate pressures, we decrease the angular frequency, so that $\omega = 2\pi/20$. We set $\overline{\tau}_p = 0.75$ to match the range of transpulmonary pressures applied to the lung. This allows us to produce a prediction of the cross-sectional area of an airway for given transpulmonary pressures. For $t_c = 4$, assuming that the airway is of constant length, there is reasonable agreement between the model predictions and the representative

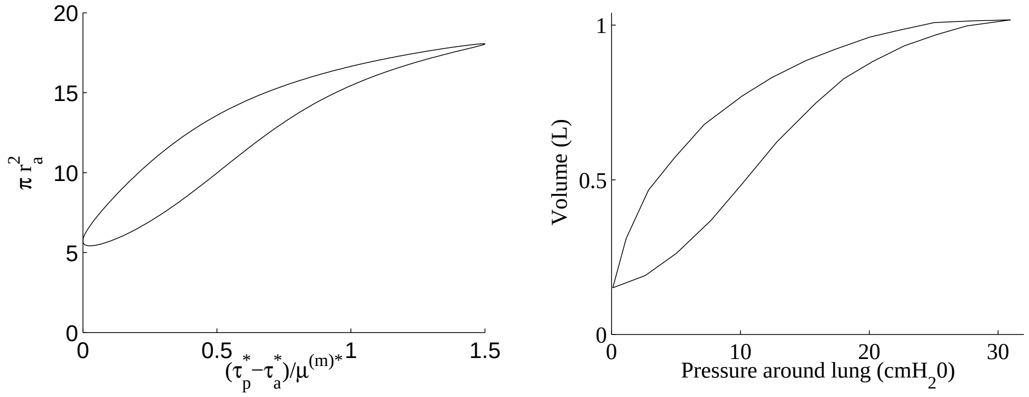

Figure 3.15: Left: Equilibrium loop of the cross-sectional area of an airway against the transpulmonary pressure from (3.3.18), when $t_c = 4$, $\overline{\tau}_p = 0.75$ and $\omega = 2\pi/20$. The other parameter values are given in Table 3.3. Right: Representative picture of a pressure-volume curve for the lung (Data taken from http://www.studydroid.com/imageCards/0c/fq/card-13101355-back.jpg).

pressure-volume curve.

Since the choice of t_c is based on experiments on the lung as a whole and not just an airway, the effect, on the relationship between pressure and area, of varying t_c is shown in Fig. 3.16. Increasing the size of t_c, increases the amount of hysteresis, with greater energy loses in each cycle. The airway area, at the point of zero pressure, also increases as t_c increases, resulting in a smaller range of lumen areas over the cycle. The shape of the curves also become more elliptical.

3.3.3 Results

In this subsection the different methods of inflating the airway described in (3.3.16-3.3.19) are investigated. Results are shown in Fig. 3.17 for method 1, where the airway is inflated externally. Initially as τ_p increases linearly, the radial displacement (a) and the stresses in the radial (b), hoop (c) and axial (e) directions increase (dot-dashed lines). The distributions are similar to those observed in Fig. 3.9, where the parenchyma was elastic. In contrast to the elastic parenchyma though, time is now important, with the displacement and stress distributions continuing to change once the boundary stresses are held steady (dashed lines). The radial displacement and stress (a, b) continue to increase, as do the hoop and axial stresses within the airway wall (d, f). However, within the parenchyma the hoop and axial stresses reduce slightly. At large time, the distributions tend towards those found if the parenchyma is modelled using linear

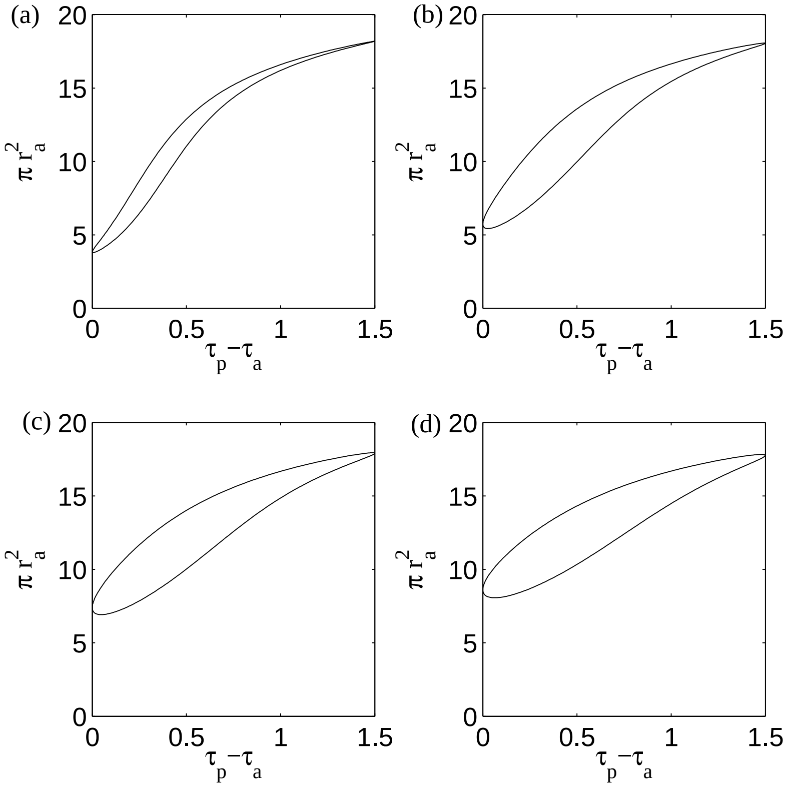

Figure 3.16: Plots of the cross-sectional area of an airway against the transpulmonary pressure from (3.3.18), when the ratio of the creep and relaxation timescales $t_c = 2$ (a), $t_c = 4$ (b), $t_c = 6$ (c) or $t_c = 8$ (d). $\overline{\tau}_p = 0.75$, $\omega = 2\pi/20$. The other parameter values are given in Table 3.3.

elasticity (solid line). These results provide evidence that the model is able to predict the viscoelastic phenomena of creep that has been observed in experiments.

Comparisons are made in Fig. 3.18 between the large-time steady state solution when the parenchyma is linear or nonlinear and the airway is inflated externally. This is achieved by making comparisons between models for the airway when the parenchyma is modelled using linear elasticity (Sec. 3.2.2) or nonlinear elasticity (Sec. 3.2.1). The linear predictions are shown with solid lines, while the nonlinear predictions are shown by dashed lines. There is little difference between the two sets of curves. In each case the distribution of the displacement and the stress is slightly greater in the nonlinear case, except for the hoop stress within the parenchyma (c), where it is slightly smaller. The simplification of the linear viscoelastic model over the nonlinear viscoelastic model appears to give sufficiently good results for this case.

Results are shown in Fig. 3.19 for method 2, where the airway is inflated internally. Initially as τ_a decreases linearly, the radial displacement (a) and the stresses in the hoop and axial directions (d, f) increase (dot-dashed lines). The stress in the radial direction decreases, indicating that the airway experiences increased compressive forces in this direction (b). The distributions are similar to those observed in Fig. 3.10, where the parenchyma was elastic. In contrast to the elastic parenchyma, time is again important, with the displacement and stress distributions continuing to change once the boundary stresses are held steady (dashed lines). The radial displacement and stress (a, c) both increase, thus the size of the compressive stresses in the radial direction decrease. The changes to the hoop and axial (e, g) stresses are different within the airway wall and within the parenchyma. Within the airway wall the stresses continue to increase, indicating increased tensile stress, while within the parenchyma the stresses decrease, indicating decreased tensile stress. At large time, the distributions tend towards those found if the parenchyma is modelled using linear elasticity (solid line). These results provide further evidence of the models ability to predict creep.

Comparisons are made in Fig. 3.20 between the large-time steady state solution when the parenchyma is linear or nonlinear and the airway is inflated internally. There are greater differences between the two models than when the airway was inflated externally (Fig. 3.18), although they are still quite small. The displacement and the stresses are generally a bit larger for the nonlinear case (dashed) compared to the linear case (solid). Within the outer part of the parenchyma, the radial stress is slightly smaller with the nonlinear case (b). Within the parenchyma, the axial stress is independent of R with the linear model (c.f. (3.2.9c)), while this is not the case with the nonlinear model (c.f. (3.2.9c)), which predicts a smaller value near the inner boundary of the

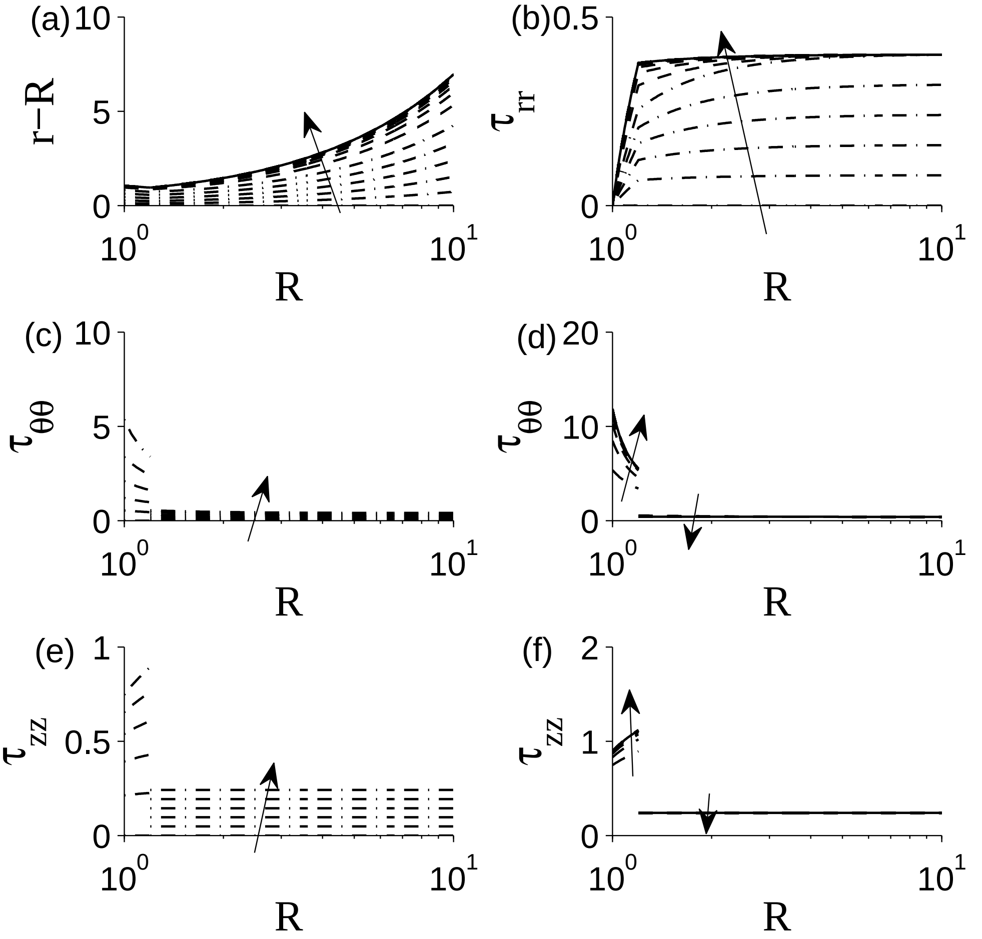

Figure 3.17: Plots of (a) the radial displacement and the (b) radial, (c, d) hoop and (e, f) axial stresses verses radial coordinate, when the airway is inflated externally using (3.3.16). $\overline{\tau}_p = 0.4$ and $t_i = 1$. The dashed lines at plotted at intervals of Δt=0.2, while τ_p is linearly increasing, the dotted lines are plotted thereafter at intervals of Δt=1, while τ_p is held constant, and the solid line is the corresponding elastic solution. Arrows indicate increasing time. The other parameter values are given in Table 3.3.

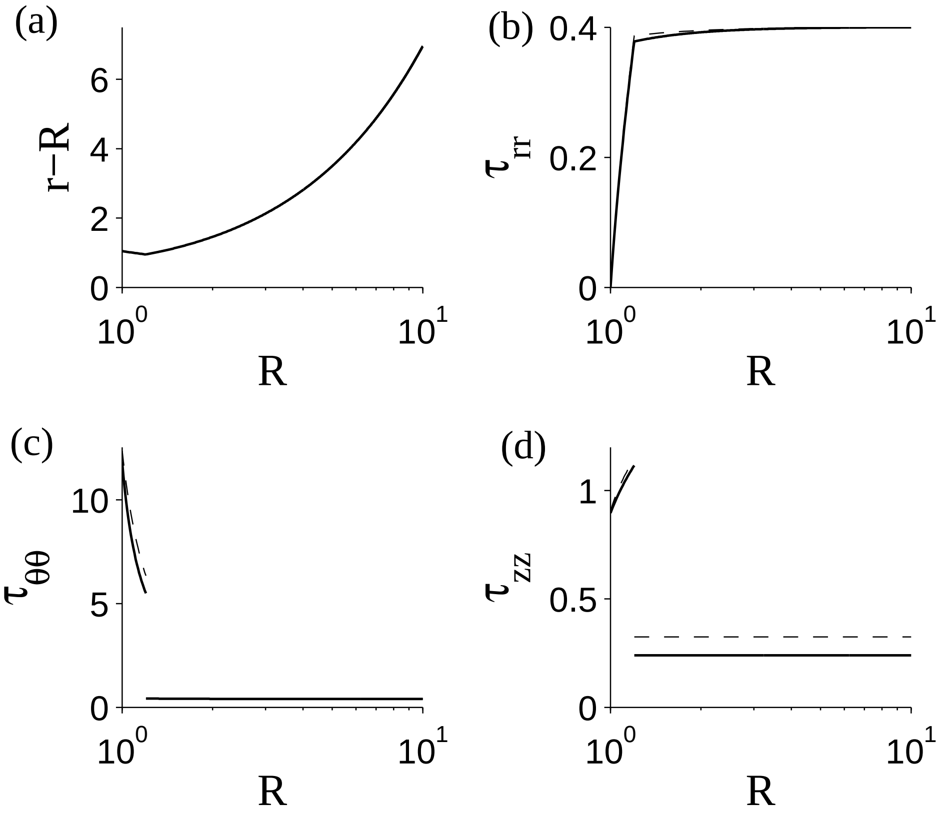

Figure 3.18: Comparison of the large-time equilibrium solution when the parenchyma is linearly viscoelastic (solid) or nonlinearly viscoelastic (dashed) when the airway is inflated externally so that $\tau_p = 0.4$ and $\tau_a = 0$. The other parameter values are given in Table 3.3.

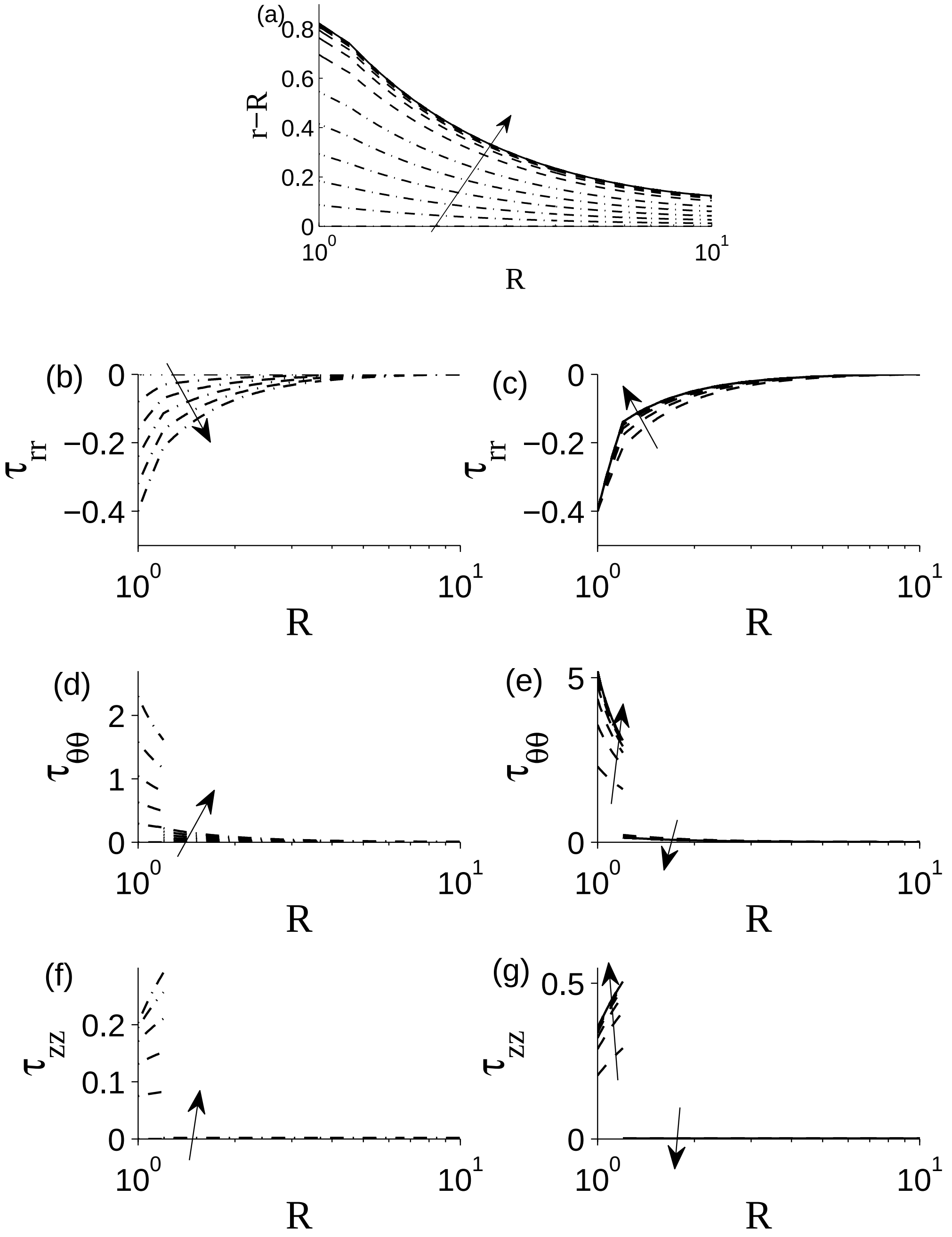

Figure 3.19: Plots of (a) the radial displacement and the (b) radial, (c, d) hoop and (e, f) axial stresses verses radial coordinate when the airway is inflated internally using (3.3.17). $\overline{\tau}_a = -0.4$ and $t_i = 1$. The dashed lines at plotted at intervals of Δt=0.2, while τ_a is linearly decreasing, the dotted lines are plotted thereafter at intervals of Δt=1, while τ_a is held constant, and the solid line is the corresponding elastic solution. Arrows indicate increasing time. The other parameter values are given in Table 3.3.

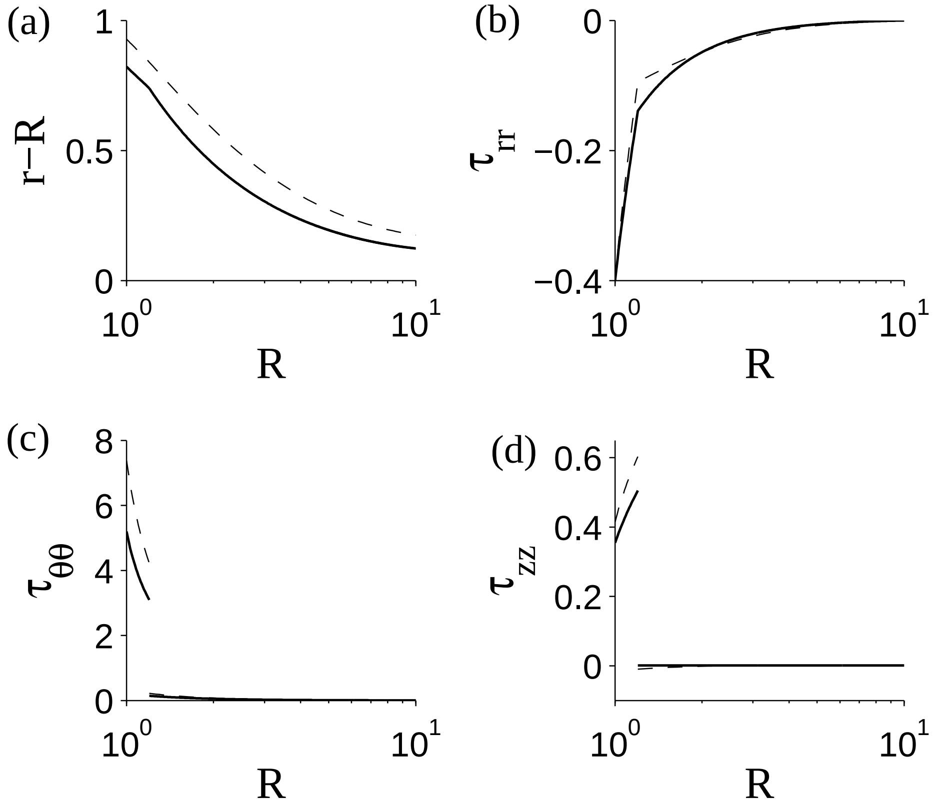

Figure 3.20: Comparison of the large-time equilibrium solution when the parenchyma is linearly viscoelastic (solid) or nonlinearly viscoelastic (dashed) when the airway is inflated internally so that $-\tau_a = 0.4$ and $\tau_p = 0$. The other parameter values are given in Table 3.3.

parenchyma and a larger value near the outer boundary of the parenchyma (d). For a small section near the inner boundary of the parenchyma, the nonlinear model predicts a negative value for the axial stress, indicating compressive stresses, which the linear model is unable to show.

Methods 3 and 4, which have oscillatory boundary conditions, are now considered. There are differences if the outer radial stress is oscillated (3.3.18) to if the outer radial displacement is oscillated (3.3.19). Plots of the development of the radial stress, the displacement at the outer boundary of the parenchyma and at the lumen boundary are shown in Fig. 3.21. When τ_p is prescribed, as shown in (a), over the first few oscillations $r_p - R_p$ increases on average (c), before tending to a limit cycle, such that the outer boundary of the parenchyma does not return to its undeformed position. Similarly, the displacement at the lumen boundary increases on average (e), so that when a limit cycle is reached, at all points within the cycle the radius of the lumen is greater than in the undeformed state. If instead r_p is prescribed, so the displacement at the outer boundary of the parenchyma is as in (d), within the first oscillation τ_p initially increases before decreasing and becoming negative (b). When a limit cycle is reached there is part of each oscillation where τ_p is positive, indicating tensile stresses and part that is negative, indicating compressive stresses. At the end of each cycle the displacement of the lumen radius is negative (f), indicating airway narrowing. With this method, the parenchyma initially expands and then as its boundary is brought in, the parenchyma does not contract fully back to its previous configuration, so that the lumen narrows. It can also be shown that if the airway were to start from some pre-stressed starting position, so that $r_p > R_p$, the airway would become narrower than it started at. In reality breathing is probably a combination of the two methods, at least in normal tidal breathing, with the ribcage lifting to prescribe a displacement, but then the airway deflating due to lung recoil rather than a prescribed displacement. This may stop the reduction in the airway lumen being seen as in (b). The reduction of the airway lumen would also be less of an issue if the airway was initially pre-stressed, and thus slightly inflated.

The plots in Fig. 3.21 showed that following some initial transient behaviour, limit cycles were approached. These cycles for the case that τ_p is prescribed are shown in Fig. 3.22. There is now evidence of hysteresis, due to the viscoelasticity of the parenchyma. There are differences between when the airway is inflated to when it deflates. The displacement is larger as the airway deflates than when inflating (a). The loop at the edge of the parenchyma is also fatter, indicating that there are larger energy losses here. At the boundary between the two layers, the radial stress is greater during deflation than during inflation (b). Within the airway wall the hoop stress (c) and axial stress (d) are also greater during deflation than inflation. However, within the parenchyma, the hoop and axial stresses are smaller during deflation than during inflation.

3.4 Conclusions

In this chapter we have simplified the equations presented in Chapter 2 for an asthmatic airway. In particular, we concentrated on the dimensionless governing equations for the tissue-level mechanics (Sec. 2.2.6) and in solving them we assumed that passive stresses or displacements were applied to the boundaries of the airway, but that there was no active contractile forcing. These solutions are therefore concerned with the airways when the ASM has not been activated.

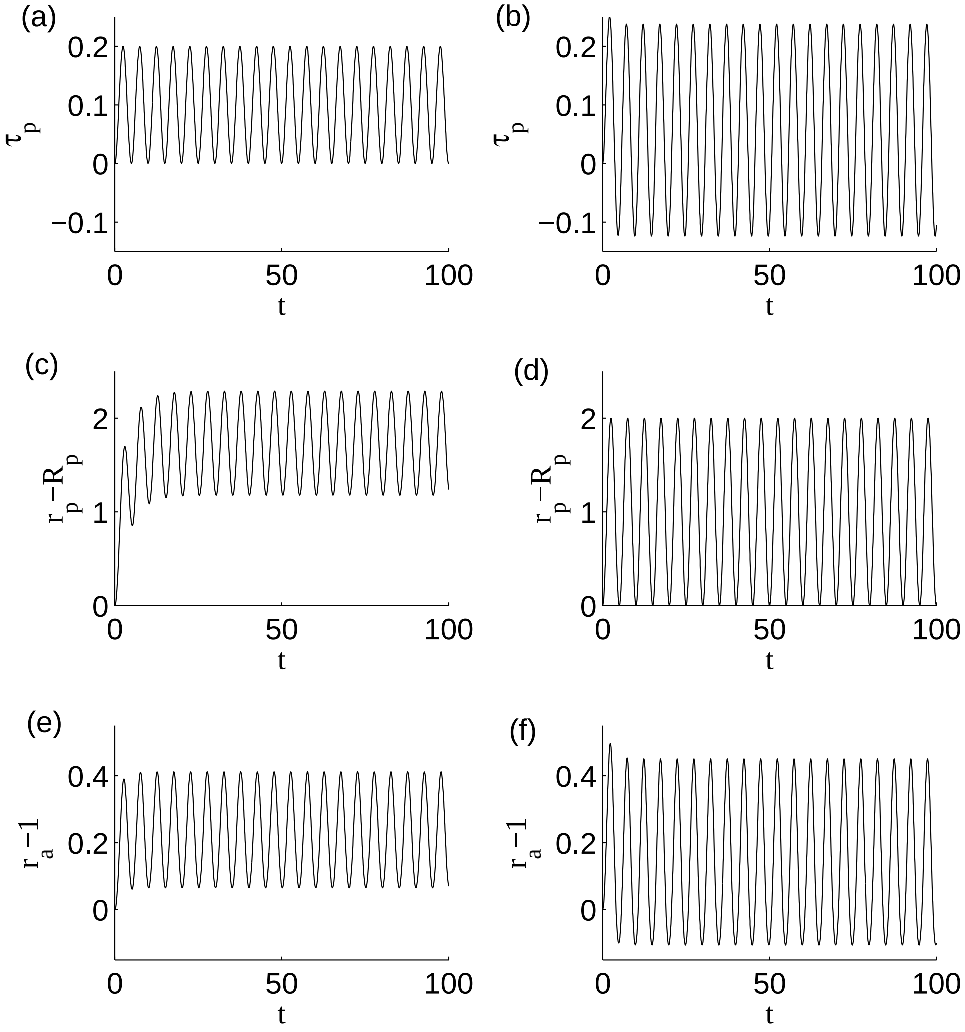

Figure 3.21: Plots of the radial position and stress at the parenchyma, r_p and τ_p, and the displacement of the lumen boundary $r_a - 1$ against time. Results are given for (a, c, e) method 3, when τ_p is prescribed, and (b, d, f) method 4, when r_p is prescribed. The other parameter values are given in Table 3.3.

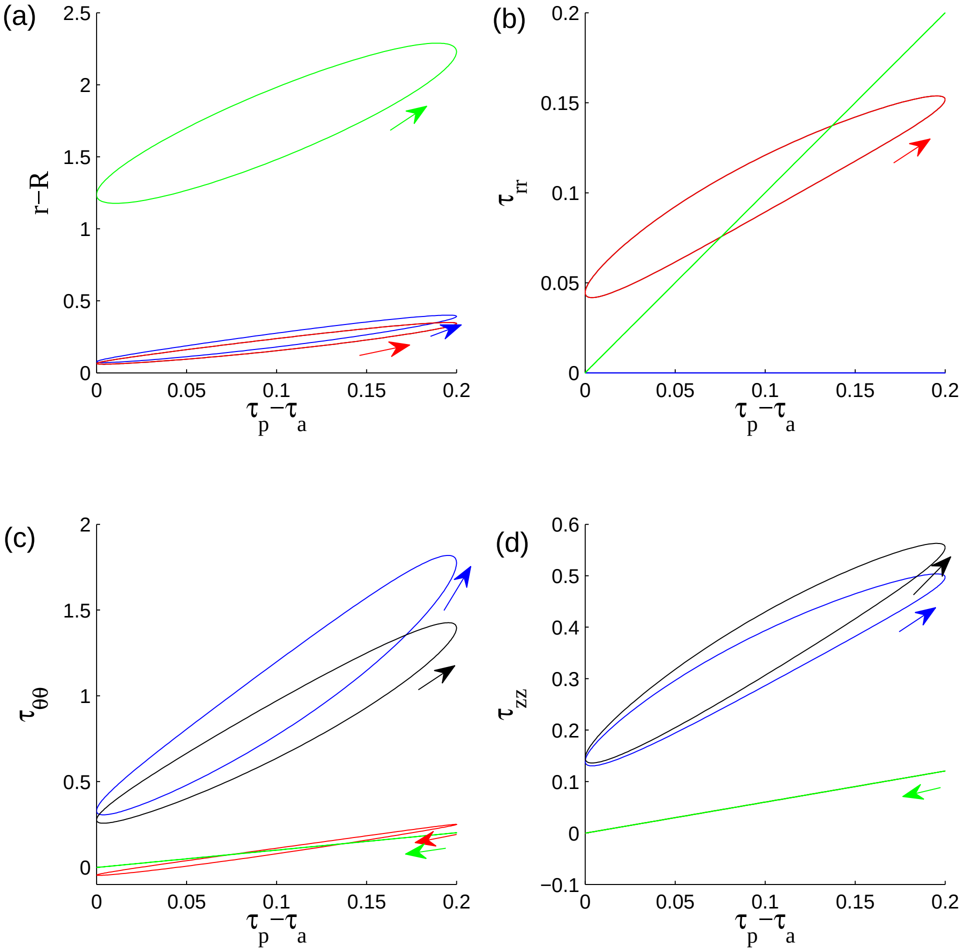

Figure 3.22: Plots of the limit cycles of (a) the radial displacement and (b-d) the radial, hoop and axial stresses verses radial coordinate when oscillatory forcing is applied to the external boundary. The curves are plotted at $R = 1$ (blue), R_b^- (black, where not equal to curve at R_b^+), R_b^+ (red, where not equal to curve at R_p) and R_p (green). The arrows show the direction of the loops. The other parameter values are given in Table 3.3.

We began in Sec. 3.1 by considering the airway wall in isolation. We found a relationship between the pressures applied to the boundaries of the wall and the lumen radius. (The relationship also includes a contribution from the integral of the contractile force across the wall, although this was set to zero in this chapter.) The relationship also takes into account the thickness of the airway wall, which is important due to the airway remodelling that is associated with asthma as discussed in Sec. 1.3.2. By linearising the results in Sec. 3.1.1, we were able to show that when small stresses are applied to the airway wall, our model matches the linear model of Brook *et al.* [22], providing we make a few assumptions. The assumptions are that a uniform force is exerted, across the wall, by fibres that are aligned in the circumferential direction, and that there is no fibre-reinforcement.

Experimental data from the literature was used to select parameter values where possible. To select C_1 and C_2, the parameters that govern the strain-stiffening of the fibres, we made comparisons to the pressure-area model of Lambert *et al.* [94, 98], which were based on experimental data. The relationship from our model then exhibited strain-stiffening on both inflation and deflation. It was also shown that if the airway wall thickens or the parameters associated with the collagen, C_1 and C_2, increase or the fibre angle decreases, the airway becomes stiffer. Wall thickening is particularly significant as it is a feature of airway remodelling, while C_1 takes into account the density of the collagen fibres, which could vary depending on how the wall remodelled, and φ has been found to increase with airway generation.

In Sec. 3.2 we considered the airway wall embedded within parenchyma. The nonlinear elastic model of the parenchyma first developed in Sec. 2.2.1.1 was used. In order to solve the equations for the airway wall embedded within parenchyma and satisfy the boundary conditions, we introduced a algorithm involving shooting. Inflating the parenchyma internally, we were able to show that the results were comparable to those of Lai-Fook *et al.* [91]. In particular if the parenchyma is very thick, the compression within the parenchyma is concentrated within a small region near the inner boundary.

Coupling the airway wall to the parenchyma, we showed that there are important differences if the airway is inflated externally, which mimics normal breathing, or internally, which mimics artificial ventilation. If the airway is inflated externally, the parenchyma undergoes large displacements, while if the airway is inflated internally the airway wall shields the parenchyma from large displacements. In each case, due to the fibres within the airway wall, there is strain stiffening. It is possible to control the size of the displacements within the parenchyma when the airway is inflated externally, by prescribing the displacement rather than the radial stress at the outer boundary.

Alternatively, a more complicated model could be considered that takes into account other airways and blood vessels within the surrounding parenchyma, which will limit the displacement.

Since viscoelastic behaviour is an important feature of lung parenchyma (Sec. 1.2.2), in Sec. 3.3 we again considered the airway wall embedded within the parenchyma, but now assumed the linear viscoelastic model of the parenchyma first introduced in Sec. 2.2.3. Literature was again used to choose parameter values and numerical methods, required to solve for the coupled problem, were introduced. Increasing the transpulmonary pressure linearly, by inflating the airway externally or internally, and then holding it steady resulted in creep. Qualitatively the large-time steady state solutions were similar to those those if the parenchyma was nonlinearly elastic. An exception was with the predictions of τ_{zz}, which with the linear model had a uniform value across the parenchyma, while with the nonlinear model, τ_{zz} is spatially dependent. In particular, when inflating the airway internally, the nonlinear model predicts that most of the parenchyma is under tension, but a small region at the inner boundary of the parenchyma is under compression. These results show that the model is able to reproduce viscoelastic phenomena observed in experiments.

We also applied oscillatory boundary conditions to inflate the airway. Important differences were found when the stress or the displacement at the outer boundary of the parenchyma was oscillated. These cases correspond to the pleural pressure being oscillated or an oscillatory displacement of the ribcage. When the stress was prescribed, following some transient oscillations, equilibrium loops were approached, with the airway dilating. In contrast, when the displacement was prescribed, narrowing of the airway wall was observed, with the radial stress at the outer boundary of the parenchyma switching between negative and positive values during the equilibrium loop. In reality breathing is probably governed by a combination of the two conditions. By plotting the displacement or principal stresses against the transpulmonary pressure, we also showed evidence of hysteresis, with the airway on average being narrower during inflation than during deflation.

Chapter 4

Effects of applying contractile forces to the airway

In the previous chapter we considered our two-layer model of an airway from Chapter 2, and investigated the effects of passively forcing the airway. In this chapter we also allow for active forcing, to take into account the force generated by the ASM. Initially we consider the steady state solutions when there is active contractile forcing. We then consider time-dependent contractile forces, firstly by simply prescribing A, before going on to develop the coupling of the fibres, and the contractile force they produce, to the sub-cellular crossbridge mechanics, as introduced in Chapter 2.

Previously there have been some attempts to model contractions of asthmatic airways and also numerous experiments to try to understand the effects of airway smooth muscle as described in Chapter 1. From the modelling perspective we concentrate on the work of Brook *et al.* [22], who modelled the airway with linear elasticity, including a uniform active force along hoops of fibres within the airway wall. Their model predicted that for thickened walls, as found in asthmatics due to remodelling, some regions within the the airway wall can experience compressive stresses in the radial and hoop directions, while other regions experience tensile stresses.

Experimental results on strips of tracheal ASM tissue (e.g.Fredberg *et al.* [43]) revealed that application of length fluctuations caused the mean contractile force to decrease. Other experiments have also shown the possibility of length adaptation in ASM. Again experimenting with strips, Fredberg *et al.* [44] allowed the strip to contract from some reference length, before applying an oscillatory force along the length of the strip. Increasing the amplitude of the oscillations resulted in the mean length of the strip increasing. Moreover, reducing the amplitude back to previous values did not result in the length returning to its previous mean value. We compare our model predictions to these findings.

In Sec. 4.1 we consider the steady state solutions by applying a uniform steady force along the fibres in the airway wall, using our nonlinear model from Sec. 3.2. This enables us to investigate the stress distributions and to establish when stress heterogeneities exist and how they compare to those predicted by Brook *et al.* [22]. We compare the results from our nonlinear model to the linearised version of it, in order to see the effect of using the more complex model. Finally, we compare the results from the fully-nonlinear model to a model where the parenchyma is assumed to be linearly elastic.

In Sec. 4.2 we develop the theory needed to couple the contractile force, A to the crossbridge mechanics. The nonlinear model of the airway wall and the viscoelastic parenchyma are assumed. The relevant equations and also those for the limiting case that the parenchyma is linearly elastic are presented and an overview is given of the numerical methods that are used.

In Sec. 4.3 we select a special case, for which we prescribe a uniform time-dependent but space-independent contractile force, $A(t)$. We consider the evolution of the lumen displacement and the stresses within the airway wall when the parenchyma is elastic or viscoelastic. We investigate how the choice of boundary conditions and the parameter values affect the results.

In Sec. 4.4 we relax the approximations made in Sec. 4.3 so that the tissue and crossbridge mechanics are fully coupled. We compare the results of a contracting airway when the parenchyma is linearly elastic or viscoelastic. We also investigate the effect of applying an oscillatory displacement to the pleura on airway contraction and the stresses within the airway wall, and make comparisons to the findings in [43, 44].

In Sec. 4.5 we make further comparisons between the model predictions and experimental findings. We use the data of LaPrad *et al.* [103], who experimented on airways dissected from the parenchyma, and tested the effect of tidal forcing on bronchoconstriction. We compare their results with the prediction of our model for the airway wall when coupled to HHM.

Due to the questions about the differences in geometry of tissue strips and airways and the experimental results that they yield, in Sec. 4.6 we make some comparisons between the two. We present a simple model for the tissue strip and compare the predicted stresses in the strip with those in the airway. To do this we apply comparable stretches to the strip.

fig.	A	χ	R_p	τ_a	τ_p	$\nu^{(p)}$	ϱ
4.1	1	0.1, 0.2, 0.3	10	0	0	0.3	3/26
4.2	1	0.2, 0.3	10	0	0	0.3	3/26
4.3	1	0.1, 0.2, 0.3	10	0	-	0.3	3/26
4.4	1	0.2	10	0	0	0.3	3/26

Table 4.1: The parameter values for the figures listed.

Finally conclusions are drawn in Sec. 4.7.

4.1 Steady state solutions

In this section, we consider the steady state solutions by assuming a steady uniform contractile force and steady boundary conditions. We recall the nondimensional version of the boundary conditions, (2.2.32). In particular, we prescribe conditions at $R = 1$ and $R = R_p$. We prescribe the radial stress at the inner boundary of the airway, which for this chapter we shall assume is stress free so that

$$\tau_{rr}(1) = 0. \tag{4.1.1}$$

At the outer boundary of the parenchyma we describe two case; either the radial stress or the deformed radius is prescribed, so

$$(i) \quad \tau_{rr}(R_p) = \tau_p \quad \text{or} \quad (ii) \quad r(R_p) = r_p. \tag{4.1.2}$$

Each of these cases will be considered in turn and with one exception in each case, for this section, we set $\tau_p = 0$ or $r_p = R_p$. As a result the stresses and displacement predicted are due to the active contractile force.

Firstly case (i), where the pleural radial stress is prescribed, is considered. Fig. 4.1 shows the effect of increasing the thickness of the airway wall or the size of A. Thicker walls lead to larger contractions (a) and larger transpulmonary pressure are required for the same increase in lumen radius (b). For each of the airways, irrespective of the wall thickness, the tissue is stretched in the radial direction (c) and compressed in the circumferential direction (e). However, with the radial (d) and hoop stresses (f), for the thicker walls there can be distinct regions within the airway wall for which the stresses are compressive or tensile. In the axial direction, there is no stretch due to the plane strain assumption, while the stresses are compressive (g). Both the hoop and axial stresses are much larger in magnitude in the airway wall than in the parenchyma. Increasing A results in larger contractions (h). As well as the thickness of the airway wall, the size of A is important in determining when stress heterogeneities occur. Within the airway wall, for small contractile forces τ_{rr} and $\tau_{\theta\theta}$ are minimum at $R = 1$, with $\tau_{rr}(1) = 0$ and $\tau_{\theta\theta} > 0$, indicating tension. As A increases there can be regions of the airway wall that experience compressive stresses in the radial or hoop directions (i, j).

The model prediction, that increased thickness of the airway wall can lead to stress heterogeneities, is consistent with the predictions of Brook *et al.* [22], where the airway was modelled using linear elasticity. The differences arising from a nonlinear constitutive assumption can be considered, by comparing the predictions of the nonlinear model to those of its linearised version (from Sec. 3.1.2 for the airway wall and Sec. 3.2.2 for the parenchyma). Given that the region of most interest is the airway wall, results are only shown for the lumen radius r_a and the maximum and minimum values of radial, hoop and axial stresses within the wall. This enables us to determine regions of both tension and compression. Plots for $\chi = 0.2$ and 0.3 are shown for a range of values of A in figure 4.2. Under the nonlinear model, the airway stiffens, resulting in smaller contractions (a). The maximum values of the radial and hoop stresses are greater with the linear model, while the minimum values are greater in magnitude with the nonlinear model (b, c). This shows that where heterogeneities exist, the nonlinear model predicts regions under greater compression. Stress heterogeneities also arise more readily, since for $\chi = 0.2$, unlike the nonlinear model, the linear model predicts no regions of compression, while for $\chi = 0.3$, the linear model predicts that a larger value of A is required for regions of compression, in comparison to the nonlinear model predictions. The nonlinear model also predicts axial stresses that are smaller in magnitude than those predicted by the linear model (d).

Having considered case (i) and made comparisons to the work of Brook *et al.* [22], case (ii) is now considered. The results are shown in Fig. 4.3 and are very similar to those for case (i) in Fig. 4.1. By plotting the lumen radius against the outer parenchymal radius, the model predicts that large displacements are required in the parenchyma to inflate the lumen, especially when the airway wall is thicker (b). Even to simply return the lumen radius to its undeformed radius requires fairly large parenchymal displacements. The other main differences, when prescribing the outer parenchymal radius, are that the radial displacement now tends to zero as $R \to R_p$ (a) and $\tau_{rr}(R_p)$ is now slightly larger than zero (d).

In the previous chapter results were presented when passive forcing was applied to the airway, consisting of the nonlinear airway wall and the linear viscoelastic parenchyma. The steady state solutions are now considered when active contractile forces are applied if the parenchyma is linear (elastic or viscoelastic). Any time-dependence associ-

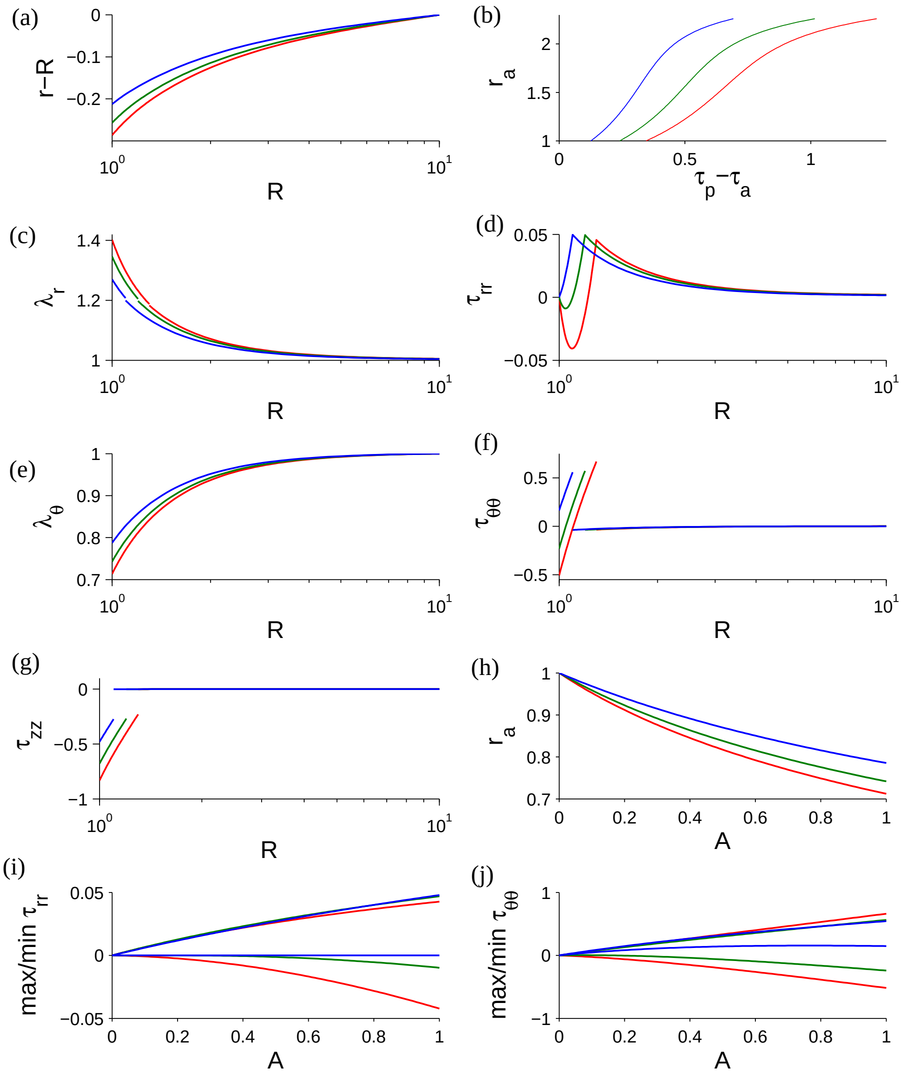

Figure 4.1: Plots of (a) the displacement verses radial coordinate, (b) relationship between the transpulmonary pressure and the lumen radius, when the airway is externally inflated, and the (c) radial stretch, (d) radial stress, (e) hoop stretch, (f) hoop stress, and (g) axial stress verses radial coordinate. R axes have a logarithmic scale. Also shown are plots of the relationship between the contractile force A and (h) the lumen radius, and the maximum and minimum (i) radial and (j) hoop stresses. $\tau_p = 0$ in (a, c-j). Curves are for undeformed wall thickness $\chi = 0.1$ (blue), $\chi = 0.2$ (green) and $\chi = 0.3$ (red). Within the parenchyma the three curves overlap in (f, g). The max blue and green curves overlap in (i, j). The other parameter values are given in Table 4.1.

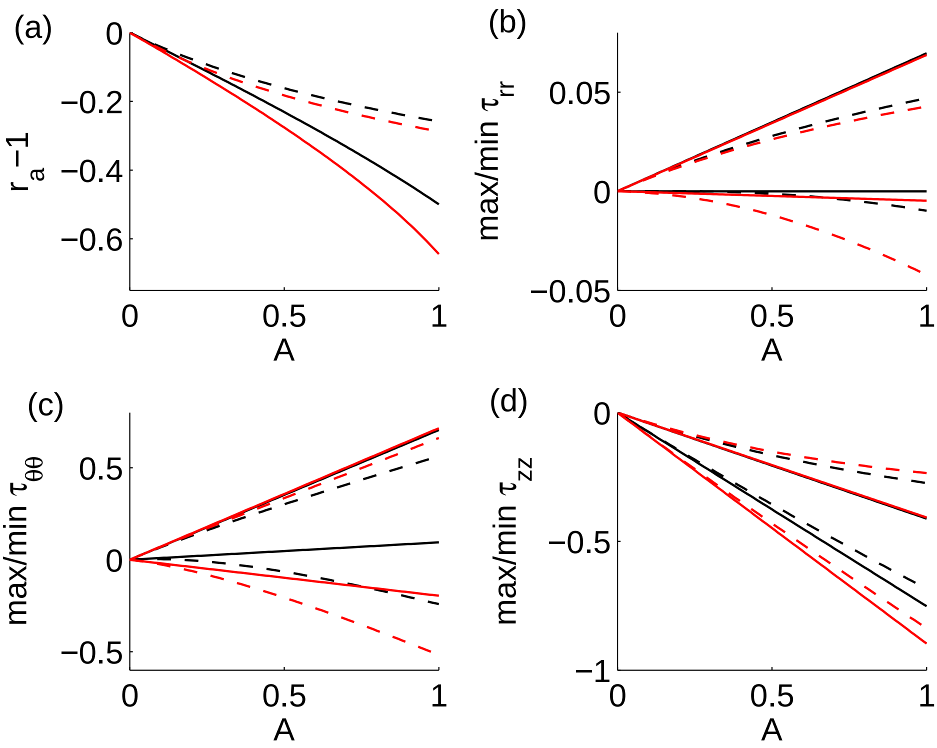

Figure 4.2: Plots of (a) the displacement of the lumen, and (b-d) the maximum and minimum values of the radial, hoop and axial stresses in the airway wall verses the radial coordinate, when using the nonlinear model (dashed) or its linearised version (solid). The airway wall has thickness $\chi = 0.2$ (black) or 0.3 (red). The other parameter values are given in Table 4.1.

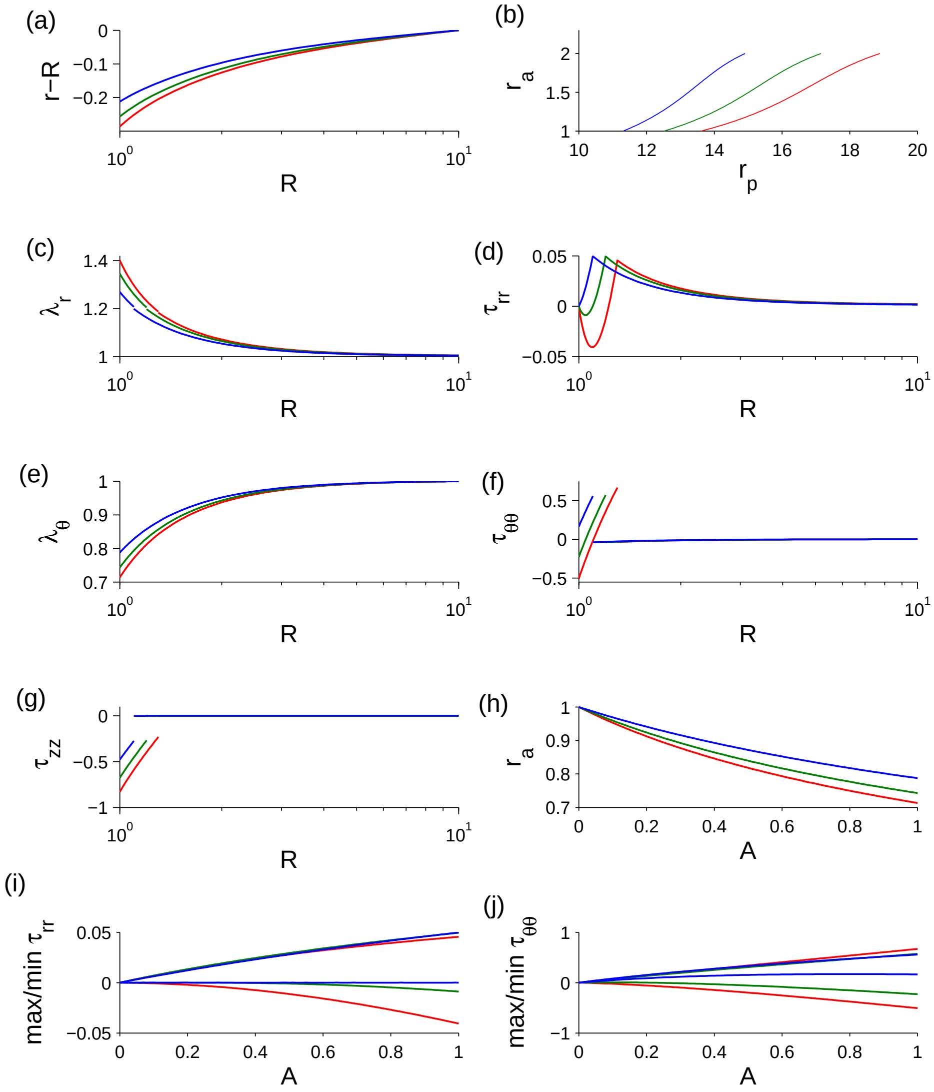

Figure 4.3: Plots similar to those in Fig. 4.1, but now r_p is prescribed (case (ii)) rather than τ_p (case (i)). $r_p = R_p$ in (a, c-j). In (b) is a plot of the relationship between the outer parenchymal radius and the lumen radius, when r_p is increased. Within the parenchyma the three curves overlap in (f, g). The max blue and green curves overlap in (i, j).

ated with the viscoelasticity can be ignored for the steady state solution. The differences between this semi-nonlinear model and the fully-nonlinear model (Fig. 4.4) are much less than those between the fully-linear model and the fully-nonlinear model (Fig. 4.2). The findings of the two different cases for the boundary condition at $R = R_p$ are very similar. There is slightly more contraction in the case of the linear parenchyma model (Fig. 4.4(a, e)). Where they are positive, the maximum and minimum stresses are a bit lower with the semi-linear model than with the fully-nonlinear model, but when they are negative, the maximum and minimum stresses are smaller in magnitude with the fully-nonlinear model (b-d, f-h). The stresses are not as closely matched as the lumen displacement, with the difference between the fully and semi-nonlinear models being most noticeable for the maximum value of the radial stress (b,f).

In this section it has been shown that thicker walls contract to a greater extent. This is physiologically significant, since wall thickening is an outcome of remodelling that is characteristic of asthma. These results show that asthmatics can expect greater problems with breathing, with increased difficulty for those with severe asthma for whom the airways are thickest [89]. Increasing the force produced by the ASM, as might occur in the case of a larger agonist concentration, also leads to increased levels of airway narrowing.

4.2 Coupling to the crossbridge mechanics

We now consider the airway wall embedded in viscoelastic parenchyma, where the airway wall mechanics are coupled to the crossbridge mechanics. The equations from Sec. 2.3.3 are used to do this.

4.2.1 Model development

First the relevant equations are developed. Using the fact that $r\mathrm{d}r/\mathrm{d}t = r_b\mathrm{d}r_b/\mathrm{d}t$, the tissue velocity, (2.3.16), may be written as

$$V = \frac{\cos^2 \varphi r_b}{R\sqrt{(r_b^2 - R_b^2)\cos^2\varphi + R^2}} \frac{\mathrm{d}r_b}{\mathrm{d}t}. \tag{4.2.1}$$

Now in order to calculate $r_b\mathrm{d}r_b/\mathrm{d}t$, $\mathrm{d}A/\mathrm{d}t$ will be required. Letting $\mathbf{a}(x) = (0, 0, x, x)$, multiplying (2.3.10) through by $\beta\mathbf{a}$ and integrating with respect to x yields

$$\beta \int_{-\infty}^{\infty} \mathbf{a}(x) \cdot \frac{\partial \mathbf{n}}{\partial t} \mathrm{d}x + \beta\gamma V \int_{-\infty}^{\infty} \mathbf{a}(x) \cdot \frac{\partial \mathbf{n}}{\partial x} \mathrm{d}x = \beta \int_{-\infty}^{\infty} \mathbf{a}(x) \cdot \mathrm{Q}\mathbf{n} \mathrm{d}x. \tag{4.2.2}$$

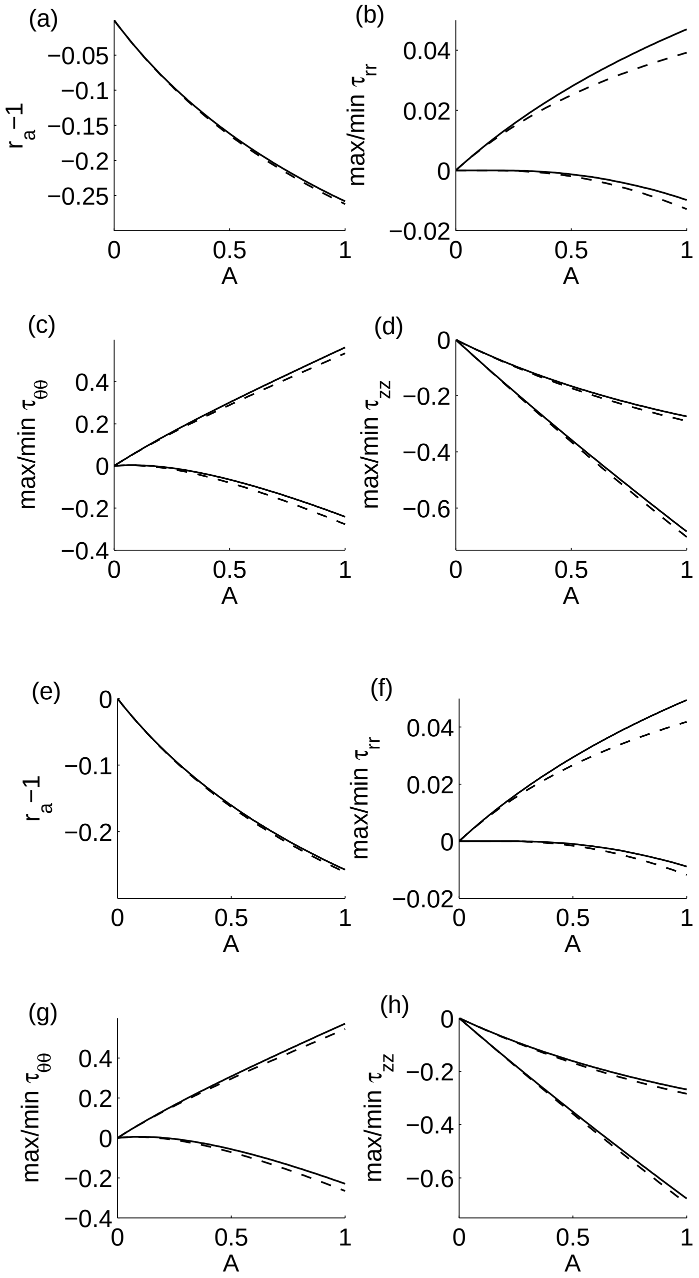

Figure 4.4: Plots of (a, e) the displacement of the lumen, and the maximum and minimum values of (b, f) the radial stress, (c, g) the hoop stress and (d, h) the axial stress in the airway wall verses contractile force A, when the nonlinear model is used for the parenchyma (solid) or its linearised version (dashed). The airway wall is modelled nonlinearly in both cases. $\tau_p = 0$ in (a-d), while $r_p = R_p$ in (e-h). The other parameter values are given in Table 4.1.

Parameter		Comments
k_1	3.5	$t < 0.5$
k_1	0.6	$t > 0.5$
k_2	1	
k_5	1	
k_6	3.5	$t < 0.5$
k_6	0.6	$t > 0.5$
f_{p1}	8.8	
g_{p1}	2.2	
g_{p2}	44	
g_{p3}	6.6	
g_1	0.1	
g_2	2	
g_3	0.3	

Table 4.2: Rate parameters used to solve HHM. The rates, which were taken from [116], have been nondimesionalised by dividing through by $k_2^* = 0.1$, with the times multiplied by k_2^*.

Since $n_C = n_D = 0$ at $x = \pm\infty$, integrating the second term on the left hand side by parts gives

$$\frac{\partial A}{\partial t} = \beta \left(\mathcal{H}_1 + \gamma V \mathcal{H}_2 \right), \tag{4.2.3}$$

where

$$\mathcal{H}_1 \equiv \int_{-\infty}^{\infty} \mathbf{a}(x) \cdot \mathrm{Q}\mathbf{n} \, \mathrm{d}x, \quad \mathcal{H}_2 \equiv \int_{-\infty}^{\infty} \frac{\partial \mathbf{a}(x)}{\partial x} \cdot \mathbf{n} \, \mathrm{d}x. \tag{4.2.4}$$

The equations governing the evolution of r in the parenchyma are now described. For case (i), when the outer parenchymal stress is prescribed and nondimensionalising time with respect to $T^* = 1/k_2^*$, (3.3.6) becomes

$$\left[t_2 t_c \frac{\partial}{\partial t} + 1 \right] (r(R,t) - R) = \left[t_2 \frac{\partial}{\partial t} + 1 \right] \Big[B_2(R) \tau_p(t) - B_1(R) \tau_b(t) \Big], \tag{4.2.5}$$

where, from (3.1.8),

$$\begin{aligned} \tau_b = & \tau_a - \log \left(\frac{r_b}{r_a R_b} \right) + \frac{(r_a^2 - 1)(R_b^2 - 1)}{2 r_a^2 r_b^2} + 2 \cos^2 \varphi \int_1^{R_b} \frac{A}{R} dR \\ & + H(r_b - R_b) C_1 \sqrt{\frac{\pi}{C_2}} \cos^2 \varphi \Bigg[\operatorname{erfi} \left(\sqrt{C_2} (r_a^2 - 1) \cos^2 \varphi \right) \\ & - \operatorname{erfi} \left(\sqrt{C_2} \frac{(r_a^2 - 1)}{R_b^2} \cos^2 \varphi \right) \Bigg], \end{aligned} \tag{4.2.6}$$

$t_c = t_c^*/t_r^*$ as before and $t_2 = t_r^* k_2^*$. Setting $R = R_b$ and rearranging (4.2.5), $\mathrm{d}r_b/\mathrm{d}t$ satisfies

$$\begin{aligned} D_1 \frac{\mathrm{d}r_b}{\mathrm{d}t} =& -\left[t_2 \frac{\mathrm{d}}{\mathrm{d}t} + 1\right] B_1(R_b)\tau_a + B_2(R_b)\left[t_2 \frac{\mathrm{d}}{\mathrm{d}t} + 1\right]\tau_p \\ & - (r_b - R_b) - B_1(R_b)\Bigg\{ 2\cos^2\varphi \int_1^{R_b} \frac{\beta\mathcal{H}_1 + A}{R}\mathrm{d}R \\ & + \log\left(\frac{r_a R_b}{r_b}\right) + \frac{(r_b^2 - R_b^2)(R_b^2 - 1)}{2r_a^2 r_b^2} + H(r_b - R_b)C_1\sqrt{\frac{\pi}{C_2}}\cos^2\varphi \\ & \left(\operatorname{erfi}\left\{\sqrt{C_2}\left(r_b^2 - R_b^2\right)\cos^2\varphi\right\} - \operatorname{erfi}\left\{\sqrt{C_2}\left(\frac{r_b^2 - R_b^2}{R_b^2}\right)\cos^2\varphi\right\}\right)\Bigg\}, \end{aligned} \tag{4.2.7}$$

where

$$\begin{aligned} D_1 =& t_2 t_c + t_2 B_1(R_b)\Bigg(\int_1^{R_b} \frac{2\beta\gamma r_b \cos^4\varphi \mathcal{H}_2}{R^2\sqrt{(r_b^2 - R_b^2)\cos^2\varphi + R^2}}\mathrm{d}R \\ & + \frac{(R_b^2 - 1)(R_b^2 r_a^2 + r_b^2)}{r_a^4 r_b^3} + H(r_b - R_b)4C_1 r_b \cos^4\varphi \\ & \left\{\exp\left[C_2(r_b^2 - R_b^2)^2\cos^4\varphi\right] - \frac{1}{R_b^2}\exp\left[\frac{C_2(r_b^2 - R_b^2)^2\cos^4\varphi}{R_b^4}\right]\right\}\Bigg). \end{aligned} \tag{4.2.8}$$

Alternatively for case (ii), when the pleural radius is prescribed, (3.3.12) becomes

$$\begin{aligned} \left[t_2 t_c \frac{\partial}{\partial t} + 1\right](r(R,t) - R) =& \left[t_2 \frac{\partial}{\partial t} + 1\right]\left[\frac{B_2(R)B_1(R_p)}{B_2(R_p)} - B_1(R)\right]\tau_b(t) \\ & + \frac{B_2(R)}{B_2(R_p)}\left[t_2 t_c \frac{\partial}{\partial t} + 1\right](r_p - R_p). \end{aligned} \tag{4.2.9}$$

Now $\mathrm{d}r_b/\mathrm{d}t$ satisfies

$$\begin{aligned} D_2 \frac{\mathrm{d}r_b}{\mathrm{d}t} =& \left[t_2 \frac{\mathrm{d}}{\mathrm{d}t} + 1\right]\left\{B_1(R_p)\frac{B_2(R_b)}{B_2(R_p)} - B_1(R_b)\right\}\tau_a + \frac{B_2(R_b)}{B_2(R_p)}\left[t_2 t_c \frac{\mathrm{d}}{\mathrm{d}t} + 1\right](r_p - R_p) \\ & - (r_b - R_b) + \left\{B_1(R_p)\frac{B_2(R_b)}{B_2(R_p)} - B_1(R_b)\right\}\Bigg\{2\cos^2\varphi \int_1^{R_b} \frac{\beta\mathcal{H}_1 + A}{R}\mathrm{d}R \\ & + \log\left(\frac{r_a R_b}{r_b}\right) + \frac{(r_b^2 - R_b^2)(R_b^2 - 1)}{2r_a^2 r_b^2} + H(r_b - R_b)C_1\sqrt{\frac{\pi}{C_2}}\cos^2\varphi \\ & \left(\operatorname{erfi}\left\{\sqrt{C_2}\left(r_b^2 - R_b^2\right)\cos^2\varphi\right\} - \operatorname{erfi}\left\{\sqrt{C_2}\left(\frac{r_b^2 - R_b^2}{R_b^2}\right)\cos^2\varphi\right\}\right)\Bigg\}, \end{aligned} \tag{4.2.10}$$

where

$$\begin{aligned} D_2 =& t_2 t_c - t_2 \left\{ B_1(R_p)\frac{B_2(R_b)}{B_2(R_p)} - B_1(R_b) \right\} \left(\int_1^{R_b} \frac{2\beta\gamma r_b \cos^4\varphi \mathcal{H}_2}{R^2\sqrt{(r_b^2 - R_b^2)\cos^2\varphi + R^2}} \mathrm{d}R \right. \\ &+ \frac{(R_b^2-1)(R_b^2 r_a^2 + r_b^2)}{r_a^4 r_b^3} + H(r_b - R_b) 4 C_1 r_b \cos^4\varphi \\ &\left. \left\{ \exp\left[C_2 (r_b^2 - R_b^2)^2 \cos^4\varphi \right] - \frac{1}{R_b^2} \exp\left[\frac{C_2 (r_b^2 - R_b^2)^2 \cos^4\varphi}{R_b^4} \right] \right\} \right). \end{aligned} \tag{4.2.11}$$

A simplification to using the linear viscoelastic model for the parenchyma is to use a linear elastic model. The elastic case is found by taking the limit $t_2 \to 0$. For case (i), where the pleural stress is prescribed, taking the limit of (4.2.5) yields

$$r(R,t) - R = \Big[B_2(R)\tau_p(t) - B_1(R)\tau_b(t) \Big]. \tag{4.2.12}$$

Differentiating and rearranging yields

$$D_3 \frac{\mathrm{d}r_b}{\mathrm{d}t} = -B_1(R_b) \left(\frac{\mathrm{d}\tau_a}{\mathrm{d}t} + 2\cos^2\varphi \int_1^{R_b} \frac{\beta\mathcal{H}_1}{R} \mathrm{d}R \right) + B_2(R_b)\frac{\mathrm{d}\tau_p}{\mathrm{d}t}, \tag{4.2.13}$$

where

$$\begin{aligned} D_3 =& 1 + B_1(R_b) \left(\int_1^{R_b} \frac{2\beta\gamma r_b \cos^4\varphi \mathcal{H}_2}{R^2\sqrt{(r_b^2 - R_b^2)\cos^2\varphi + R^2}} \mathrm{d}R \right. \\ &+ \frac{(R_b^2-1)(r_a^2 R_b^2 + r_b^2)}{r_b^3 r_a^4} + H(r_b - R_b) 4 C_1 r_b \cos^4\varphi \\ &\left. \left\{ \exp\left[C_2 (r_b^2 - R_b^2)^2 \cos^4\varphi \right] - \frac{1}{R_b^2} \exp\left[C_2 \frac{(r_b^2 - R_b^2)^2}{R_b^4} \cos^4\varphi \right] \right\} \right). \end{aligned} \tag{4.2.14}$$

Alternatively for case (ii), when the pleural radius is prescribed, taking the limit $t_2 \to 0$ of (4.2.9) yields

$$r - R = \left[\frac{B_2(R)B_1(R_p)}{B_2(R_p)} - B_1(R) \right] \tau_b(t) + \frac{B_2(R)}{B_2(R_p)}(r_p - R_p). \tag{4.2.15}$$

Differentiating and rearranging yields

$$D_4 \frac{\mathrm{d}r_b}{\mathrm{d}t} = \left\{ B_1(R_p)\frac{B_2(R_b)}{B_2(R_p)} - B_1(R_b) \right\} \left(\frac{\mathrm{d}\tau_a}{\mathrm{d}t} + 2\cos^2\varphi \int_1^{R_b} \frac{\beta\mathcal{H}_1}{R} \mathrm{d}R \right) + \frac{B_2(R_b)}{B_2(R_p)}\frac{\mathrm{d}r_p}{\mathrm{d}t}, \tag{4.2.16}$$

where

$$\begin{aligned} D_4 =& 1 - \left\{ B_1(R_p)\frac{B_2(R_b)}{B_2(R_p)} - B_1(R_b) \right\} \left(\int_1^{R_b} \frac{2\beta\gamma r_b \cos^4\varphi \mathcal{H}_2}{R^2\sqrt{(r_b^2 - R_b^2)\cos^2\varphi + R^2}} \mathrm{d}R \right. \\ &+ \frac{(R_b^2-1)(r_a^2 R_b^2 + r_b^2)}{r_b^3 r_a^4} + H(r_b - R_b) 4 C_1 r_b \cos^4\varphi \\ &\left. \left\{ \exp\left[C_2 (r_b^2 - R_b^2)^2 \cos^4\varphi \right] - \frac{1}{R_b^2} \exp\left[C_2 \frac{(r_b^2 - R_b^2)^2}{R_b^4} \cos^4\varphi \right] \right\} \right). \end{aligned} \tag{4.2.17}$$

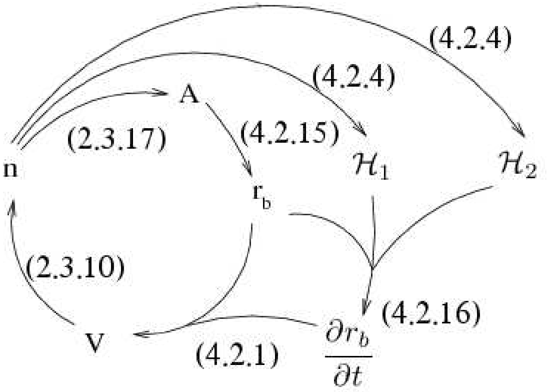

Figure 4.5: Outline of the setup of the airway problem for case (ii) with an elastic parenchyma. Case (i) and the cases when the parenchyma is viscoelastic are similar.

If r_b is known for a given time, the deformed radius and stresses for each of the points within the airway wall can be found using (2.2.18) and (3.1.9). The stresses within the parenchyma can be found using (2.2.40).

4.2.2 Numerical methods

We now outline the structure of the problem and how we go about solving it (further details are shown in Appendix B). R appears parametrically in $\mathbf{n} = \mathbf{n}(x, t; R)$, $A = A(t; R)$, $\mathcal{H}_1 = \mathcal{H}_1(t; R)$, $\mathcal{H}_2 = \mathcal{H}_2(t; R)$ and $V = V(t; R)$, while t appears parametrically in $r = r(R; t)$, $r_b = r_b(t)$ and $\mathrm{d}r_b/\mathrm{d}t = \mathrm{d}r_b(t)/\mathrm{d}t$. Details of how they feed into one another are shown in Fig. 4.5.

We discretise the airway wall in the radial direction into points spaced by a distance ΔR. Given a crossbridge distribution at each point, A, $\mathcal{H}_1$ and $\mathcal{H}_2$ can be found. Modelling the parenchyma with linear elasticity, the values of A, $\mathcal{H}_1$ and $\mathcal{H}_2$, at each of the points in R, at the current time, can be used to find the values of r_b and $\partial r_b/\partial t$ analytically. (If instead the parenchyma was assumed to be nonlinearly elastic, in order to satisfy the boundary condition, it would be necessary to shoot across the parenchyma to find r_b and $\mathrm{d}r/\mathrm{d}t$, which could no longer be found analytically. This would lead to the possibility of additional instability when finding $\partial r_b/\partial t$.) Having found r_b and $\partial r_b/\partial t$ it is possible to find the new velocity at each of the discretised points in R. This is used to decide on a timestep for a second order Godunov algorithm, used to update the crossbridge populations $\mathbf{n}$ for each of the discretised points in R.

If the parenchyma is viscoelastic, r_b and $\mathrm{d}r_b/\mathrm{d}t$ must be updated numerically. This is

χ	R_p	ϱ	β	τ_a	$\nu^{(p)}$	t_c	t_2
0.2	10	3/26	2	0	0.3	4	0.1

Table 4.3: The standard parameter values for Sec. 4.3 and Sec. 4.4.

done using a midpoint method (See Appendix B.2).

4.3 Airway with prescribed time-dependent forcing

Although it is assumed that the velocity of the deformations affects the size of the contractile force, before considering the fully coupled system, we first study an intermediate case. To find the steady state it was assumed that A was uniform and steady. In this section A is prescribed to be time-dependent. In the next two subsections we solve to find the evolution of the stresses and displacement as the airway contracts when the parenchyma is elastic or viscoelastic. The effect of varying the parameters β, t_c and t_2 is also considered.

Rather than simply choosing A arbitrarily, we determine $A(t)$ by solving the Huxley-Hai-Murphy model for the isometric case. For an isometric contraction, $V = 0$ so (2.3.10) reduces to

$$\frac{\partial \mathbf{n}}{\partial t} = \mathrm{Q}\mathbf{n}, \tag{4.3.1}$$

thus there is a system of ordinary differential equations. Since the velocity is independent of R, the solution of (4.3.1) will also be independent of R. Having discretised x as described in Appendix B.1, `ode45` in MATLAB can be used to solve (4.3.1). The stresses and displacements can then be found as described in Sec. 4.2 (If the parenchyma is assumed to be viscoelastic, (4.2.7) or (4.2.10) should be solved simultaneously to (4.3.1), depending on the boundary conditions used.) An example of the time-dependence of A is shown in figure 4.6. There is an initial rapid increase, before it levels off and approaches some steady state. This shows that when agonist is present, ASM can rapidly produce, and then sustain, a contractile force.

4.3.1 Contraction with elastic parenchyma

If both the airway wall and the parenchyma are elastic, any deformations are quasi-static, so as A evolves the airway responds instantaneously. The resulting distributions are of the form seen in Fig. 4.1 if simulations are run for case (i) with zero pleural stress, or Fig. 4.3 if simulations are run for case (ii) with zero pleural displacement.

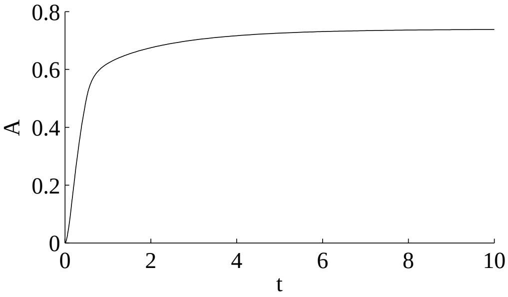

Figure 4.6: Value of A when $\beta = 2$ and the rate parameters are as in Table 4.2.

Fig. 4.7 visualises and compares the evolution of the contraction of the airway under the two different boundary conditions. Here the lumen radius and the maximum and minimum principal stresses within the airway wall are shown against time. There are no major differences between the curves for the two cases. With the exception of the minimum values of the radial and hoop stresses, there is an initial rapid increase in the magnitude of the displacement or the stress (the axial stress is negative), before the magnitude of the displacement or stress levels off and approaches an equilibrium. For small t, $\tau_{rr} = 0$ (a) and $\tau_{\theta\theta} > 0$ (c), but as t increases they both become negative, producing increased stress heterogeneity. They then rapidly increase in magnitude before levelling off. The contraction is slightly less with case (ii) and the maximum and minimum stresses are slightly greater in magnitude if they are tensile, but slightly smaller in magnitude if they are contractile. These comparisons are found, since case (ii) is equivalent to having a small radial stress on the pleura, whereas with case (i) it is assumed that there is no radial stress at the pleura. These results show that during an asthma exacerbation, assuming there are no oscillations due to breathing, there is an initial rapid of narrowing of the airways, which then remain contracted.

In Fig. 4.7 we had set $\beta = 2$, where β depends on a number of factors (Sec. 2.3.2), including the stiffness of the crossbridges and the area fraction of ASM fibres within the airway wall. We now show the effect of altering β. Assuming case (ii) with zero pleural displacement, the evolution of the lumen radius and the maximum and minimum stresses within the airway wall are shown in figure 4.8 for three values of β. Increasing the value of β results in greater contractions (a). The stresses are also more heterogeneous and regions of compressive radial and hoop stresses (b, c) are predicted to arise earlier, due to larger contractile forces. Simulations for case (i) with zero pleural stress yield similar plots. These results therefore show that the larger the area fraction of the ASM following airway wall remodelling, the narrower the airway can become.

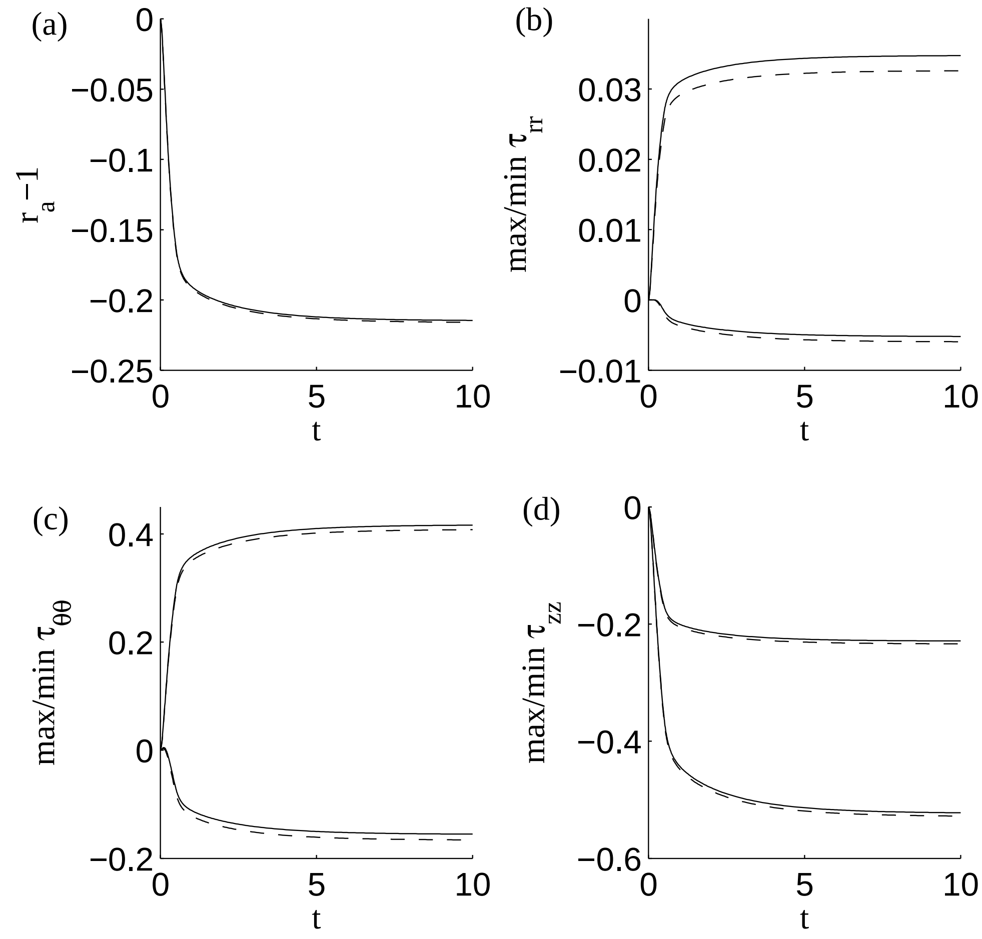

Figure 4.7: Figure comparing contractions with zero stress (case (i), dashed) or zero displacement at $R = R_p$ (case (ii), solid). Curves show the evolution of (a) the lumen displacement, and (b-d) the maximum and minimum radial, hoop and axial stresses as the airway contracts. Other parameter values are given in Table 4.3, while the HHM rates are given in Table 4.2.

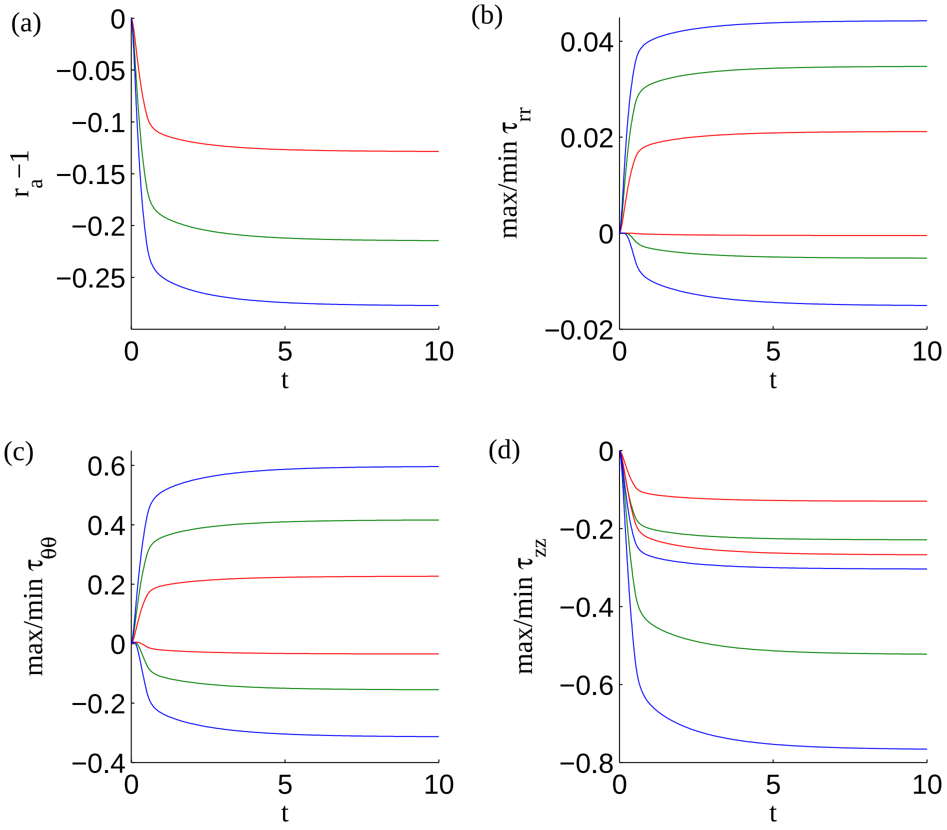

Figure 4.8: Curves showing the effect of changing β, where β depends on a number of factors, including the stiffness of the crossbridges and the area fraction of ASM fibres within the airway wall. $\beta = 1$ (red), 2 (green) or 3 (blue). Curves show the evolution of (a) the lumen displacement, and (b-d) the maximum and minimum radial, hoop and axial stresses, as the airway contracts. Other parameter values are given in Table 4.3, while the HHM rates are given in Table 4.2.

4.3.2 Contraction with viscoelastic parenchyma

Having considered the limiting case for which the parenchyma is elastic, we now consider the more general case in which the parenchyma is viscoelastic, which is more representative of reality. We will concentrate on case (ii), where there is zero pleural displacement, so $r_p = R_p$. With the viscoelastic parenchyma, the following two parameters must be considered: $t_c = t_c^*/t_r^*$, the ratio of the creep and relaxation timescales, and $t_2 = k_2^* t_r^*$, the the ratio of the relaxation timescale to the timescale for dephosphorylation of crossbridges. In Sec. 3.3.2 we set $t_c = 4$, while from [135] we expect the stress relaxation time to be approximately one second, so set $t_2 = 0.1$.

Plots of the lumen displacement and maximum and minimum principal stresses within the airway wall, when a contraction is applied are shown in Fig. 4.9 (solid). Also shown are the corresponding curves when the parenchyma is elastic (dashed). The rate of contraction of the airway is slightly reduced when the parenchyma is viscoelastic rather than elastic (a), but at large times the results are equivalent. Similarly the stresses are the same at large times, but there are a number of differences at small times. Considering the radial stress (b), with the viscoelastic model the maximum value initially rises rapidly, before peaking and decreasing a little, before once again rising and levelling off, while the minimum value remains equal to zero for longer. The minimum value of the hoop stress (c) also increases significantly initially, before decreasing and becoming negative. The rate of decrease in the axial stress is reduced with the viscoelastic parenchyma (d). From a physical viewpoint, assuming viscoelasticity, as a stress is applied to the inner boundary of the parenchyma, creep is expected to occur. Initially, therefore the parenchyma does not displace as far as with the elastic parenchyma, which in turn limits the displacement of the airway wall. Meanwhile as the airway wall is displaced there is an initial build up of the stresses, which then reduce due to stress relaxation. These results again predict that during an asthma exacerbation, assuming there are no oscillations due to breathing, there is an initial rapid of narrowing of the airways, which then remain contracted.

Since the parameter value for the relaxation timescale was not measured in humans and the ratio of the creep and relaxation timescale was only a rough estimate, the effect of varying t_c and t_2 is now investigated. The effect of varying t_c, the ratio of the creep timescale to the relaxation timescale, is shown in Fig. 4.10. The larger the value of t_c the more pronounced the phenomena observed in Fig. 4.9 are and the contraction also occurs slightly slower. The initial peak of the maximum radial stress is larger and compressive stresses are only seen at later times (b). The minimum hoop stress is also larger (c) and there can also be an initial peak in the maximum value of the hoop stress (c).

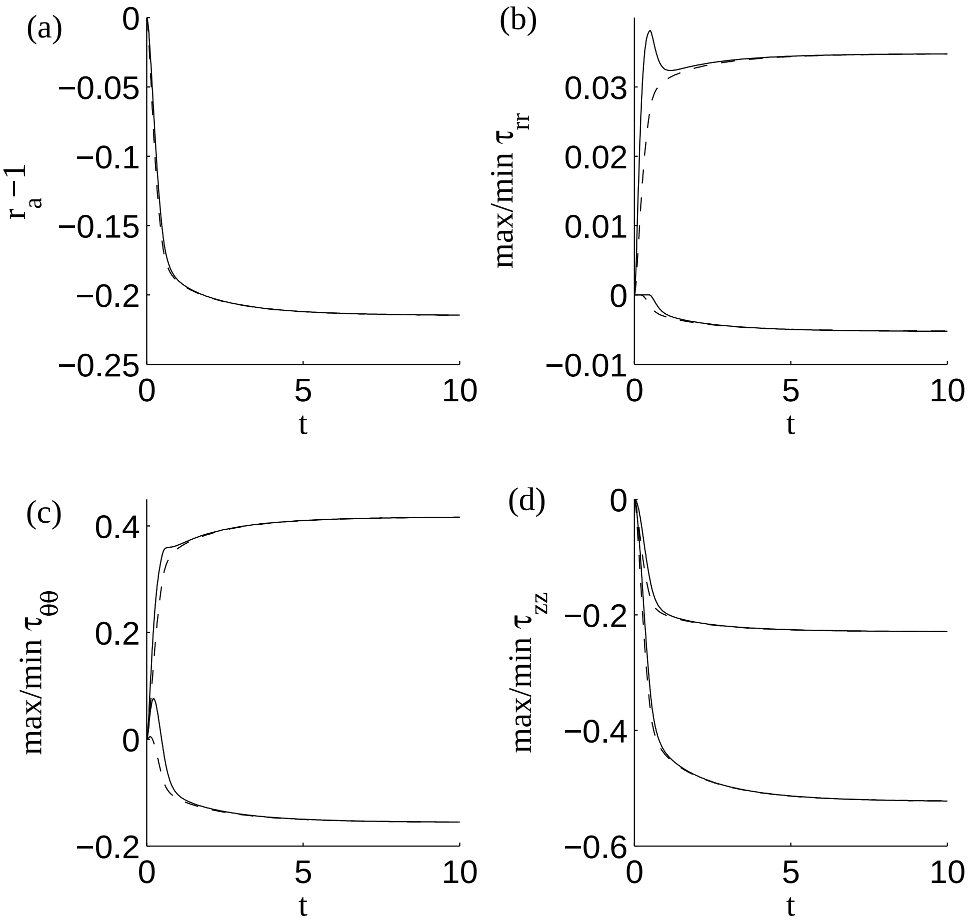

Figure 4.9: Curves show the evolution of the lumen displacement (a), and (b-d) the maximum and minimum radial, hoop and axial stresses as the airway contracts, with $r_p = R_p$ (case (ii)). The parenchyma is either viscoelastic (solid) or elastic (dashed). Other parameter values are given in Table 4.3, while the HHM rates are given in Table 4.2.

A very small peak also exists for small time for the axial stress when $t_c = 10$ (d, blue). Larger values of t_c correspond to larger values of the creep timescale, thus indicating a slower response of the parenchyma to the added stress, due to the contractile force. This allows for a greater build up in the initial radial and hoop stresses.

The effect of varying t_2, the ratio of the relaxation timescale to the timescale for dephosphorylation of crossbridges, is shown in Fig. 4.11. For small values of t_2 the results are similar to those of an elastic parenchyma, which is the limit case that $t_2 \to 0$ (dots). However, as t_2 increases, the viscoelastic phenomenae become more prominent. As well as just increasing the size of the initial peaks, increasing t_2 also slows the rate of convergence to the equilibrium state. So for example, when $t_2 = 1$, the maximum value of the radial stress no longer peaks before decreasing, then rising again to the equilibrium solution; rather it simply slowly decreases to the equilibrium after peaking (b, blue). Physically, decreasing t_2 relates to decreasing the relaxation timescale, therefore any increase in the radial or hoop stresses, due to the slowness of the parenchymal response, will decay more quickly and so not build up as much.

4.4 Airway coupled to HHM model

Having prescribed A as some time-dependent function, by solving the HHM equations for an isometric contraction, we now use the fully coupled HHM model to find A. This enables the velocity of contraction to feed back into crossbridge populations evolution and means that in general A is no longer uniform. We again adopt the nonlinear fibre-reinforced model for the airway wall and consider both the linear elastic and linear viscoelastic models of the parenchyma. For this section we focus on case (ii), where the pleural radius is prescribed. Again unless otherwise stated, the parameters for this section are given in Table 4.3.

Plots are shown in Fig. 4.12 for a contracting airway when either the parenchyma is elastic (blue) or viscoelastic (green). (In reality the parenchyma is viscoelastic.) The pleural boundary is held so that $r_p = R_p$. At large time, the lumen displacement and the maximum and minimum stresses are the same as those found in the previous section, where A was prescribed by solving HHM in the isometric case (red). However, these equilibrium solutions are now reached a lot slower having coupled the continuum model fully to HHM. Again, when the parenchyma is viscoelastic, the contraction is slower (a) and there are initial peaks in the maximum radial stress (b) and the hoop stress (c). The axial stress also reduces more slowly (d). While the equilibrium solution has attached crossbridges only within the region $0 < x < 1$, as the airway

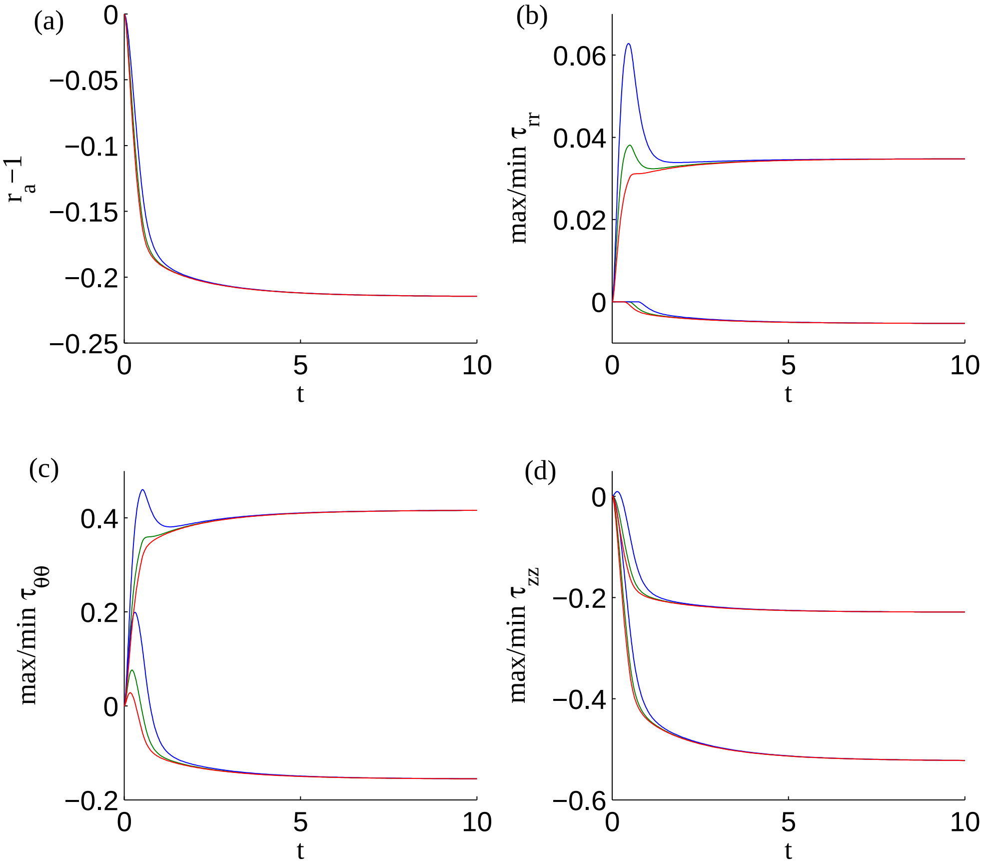

Figure 4.10: Plots showing the effect of varying t_c, the ratio of the creep and relaxation timescales. Curves show the evolution of (a) the lumen displacement, and (b-d) the maximum and minimum radial, hoop and axial stresses, as the airway contracts, with $t_c = 2$ (red), 4 (green) or 10 (blue). Other parameter values are given in Table 4.3, while the HHM rates are given in Table 4.2.

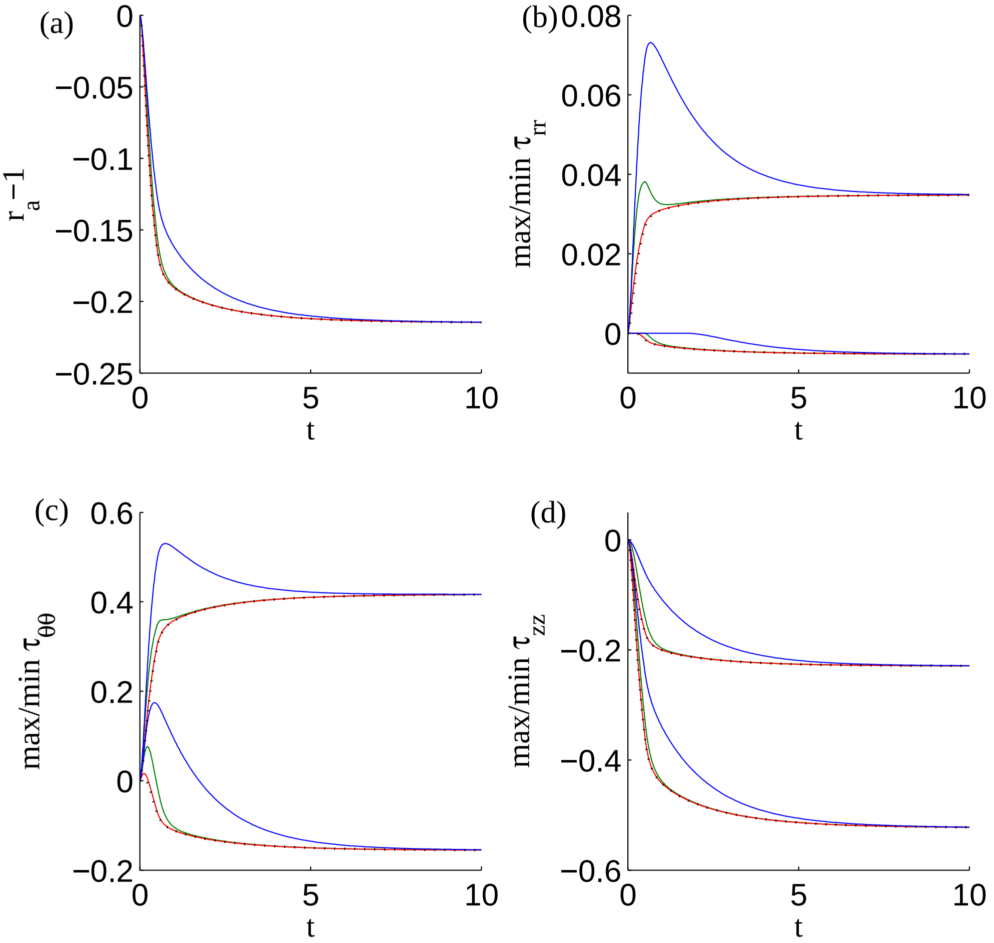

Figure 4.11: Plots showing the effect of varying t_2, the ratio of the relaxation timescale to the timescale for dephosphorylation of crossbridges. Curves show the evolution of (a) the lumen displacement, and (b-d) the maximum and minimum radial, hoop and axial stresses as the airway contracts, with $t_2 = 0.01$ (red), 0.1 (green) or 1 (blue). Dots are the elastic limit case. Other parameter values are given in Table 4.3, while the HHM rates are given in Table 4.2.

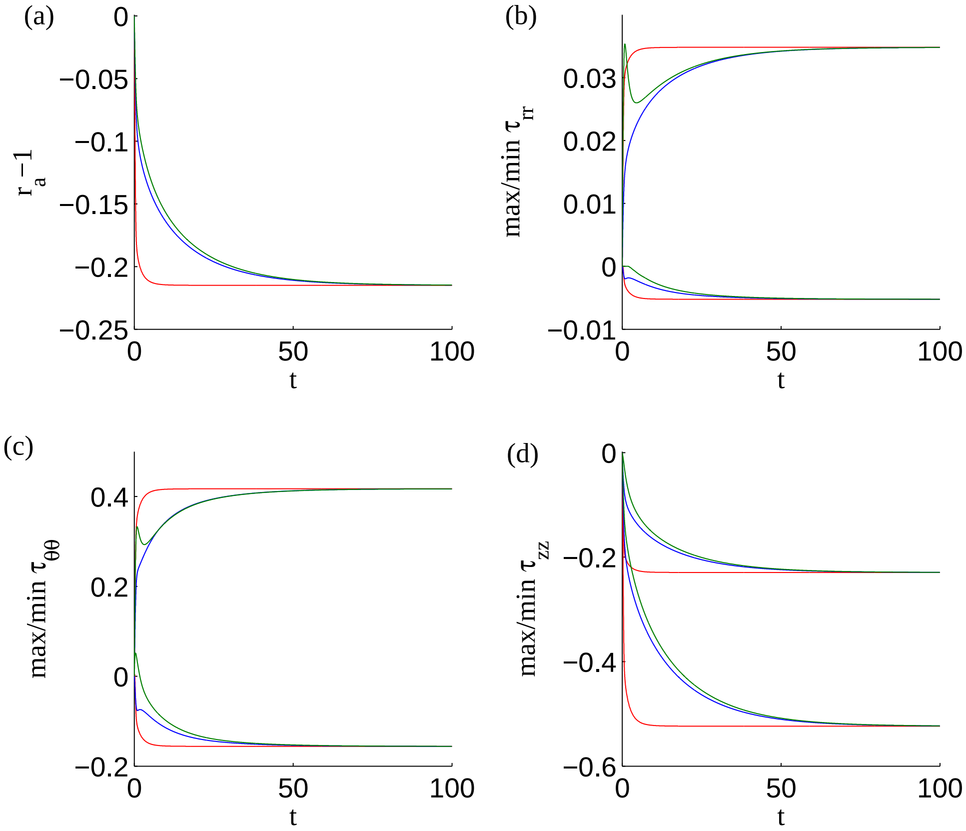

Figure 4.12: Curves of (a) the lumen displacement, and (b-d) the maximum and minimum radial, hoop and axial stresses for a contraction, when coupled to HHM theory where the parenchyma is elastic (blue) or viscoelastic (green), or when the contractile force is prescribed as in the previous section and the parenchyma is elastic (red). Other parameter values are given in Table 4.3, while the HHM rates are given in Table 4.2.

contracts they move out of this region. The approach to equilibrium is reached more slowly, since these crossbridges must detach, while the number of crossbridge within $0 < x < 1$ must build up. These results predict that during an asthma exacerbation, assuming there are no oscillations due to breathing, that rather than the airways initially rapidly narrowing and then remaining contracted, as was predicted in the previous subsection, they contract more steadily.

4.4.1 Effect of including oscillatory forcing

We now consider the effect of displacing the outer boundary of the parenchyma. Starting from the steady contracted state, oscillations of the following form are applied:

$$r_p = R_p + a\left(1 - \cos\left(\frac{2\pi t}{P^* k_2^*}\right)\right), \tag{4.4.1}$$

where a is the amplitude of the oscillations and P^* is the dimensional period of a cycle. Physiologically it is reasonable to let $P^* = 5$s. Unless otherwise stated, we let $a = 0.5$, which at its peak corresponds to a 10% displacement of the pleura. Plots are shown in Fig. 4.13 when the parenchyma is elastic. Initially there is a transient period before equilibrium loops are approached. Introducing the oscillations results in a reduction in the amount of contraction (a), with the red line joining the points of minimum displacement in each cycle of oscillation. Similarly, the magnitude of the smallest value, in each cycle of oscillation, of the maximum and minimum radial, hoop and axial stresses within the airway wall and the contractile force at the inner boundary of the airway wall (red lines) get smaller (b-e). During each cycle, the oscillations increase the range of values of the radial stress, while for a portion of each cycle, the radial stress is purely tensile (b). Similarly the oscillations can cause the regions where the hoop stress is compressive to become tensile (c). During the oscillations the crossbridges are stretched further, which increases the contractile force that they produce; however, this also results in more of them detaching. Over time the average force is thus reduced (e). The range of velocities initially increases, before decreasing to an equilibrium, with the velocity varying smoothly (f). Coupling the continuum model to the HHM model in effect inparts viscoelastic properties to the airway wall, resulting in hysteresis (g). These results are physiologically significant since they show that tidal breathing is able to reduce the amount of airway contraction by a small amount.

The effect of varying the amplitude of the oscillations is shown in Fig. 4.14. The minimum value, in each cycle of oscillation, of each of the quantities, as was shown in Fig. 4.13 by the red lines, are plotted. Increasing the amplitude of the oscillations reduces the magnitude of the stresses and the contraction of the airway. The only points where this is not the case are for the the minimum radial stress (b) and the maximum and minimum hoop stresses (c) at small time. In these cases, for the larger amplitudes the stresses initially increase in magnitude before starting to decrease. This can be explained by the increased stretch of the attached crossbridges before they detach. These results are consistent with the experimental findings of Fredberg *et al.* [43] and many others, that revealed that application of length fluctuations to tissue strips causes the mean contractile force to decrease. These results therefore predict that increasing the

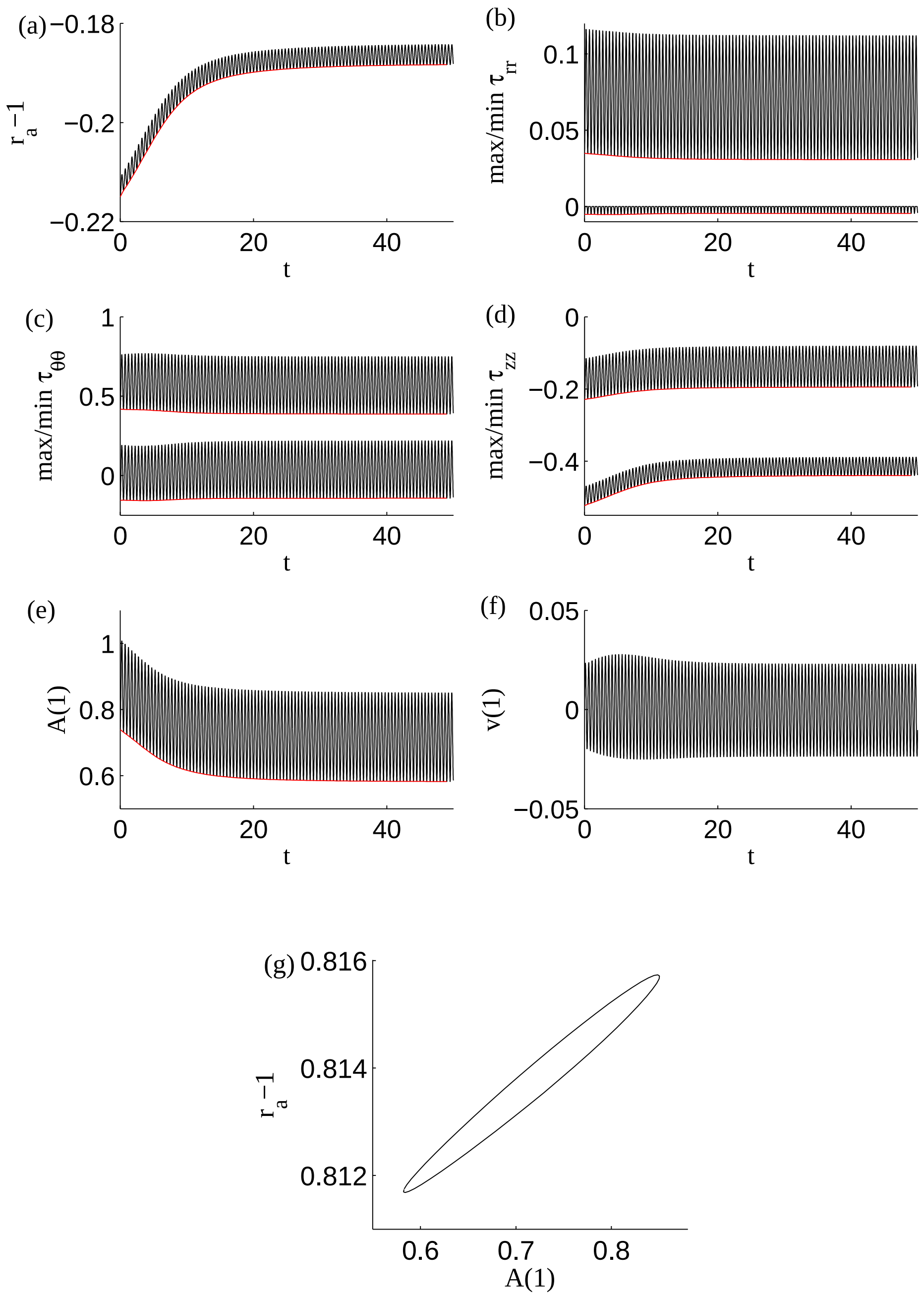

Figure 4.13: Curves of the evolution of (a) the lumen displacement, (b-d) the maximum and minimum radial, hoop and axial stresses, (e) the contractile force and (f) the relative filament velocity at the inner boundary of the airway wall. Starting from the contracted steady state, oscillations are applied to the pleural radius using (4.4.1) with $a = 0.5$. The red lines join the minimum values in each cycle of oscillation. Also plotted (g) an equilibrium curve, showing hysteresis, of the lumen displacement against the inner contractile force. Other parameter values are given in Table 4.3, while the HHM rates are given in Table 4.2.

depth of breathing helps to reduce the level of contraction of the airways to a greater extent. This suggests that deep breathing can be used as a protection method to reduce the effects of asthma.

The effect of increasing the amplitude of the oscillations and then reducing them to the previous value are shown in Fig. 4.15, with $a = 0.5$ for $t \leq 150$ and $300 < t \leq 450$, and $a = 1$ for $150 < t \leq 300$. When the amplitude of the oscillations returns to 0.5 again, the same level of contraction and the same stresses and contractile forces are approached as previously. This is not surprising as the equilibrium loops that are formed do not take into account the history of previous oscillations. In order to match up to the experimental findings of Fredberg *et al.* [44], that the airway remodels depending on the conditions that are applied to it, it is necessary to adapt the model further. One way to do this would be to use the techniques of Brook and Jensen [21], to allow for remodelling of the structure of the contractile units within the ASM.

Finally, results are shown in Fig. 4.16 when oscillations of the form (4.4.1) are applied to the airway, when the parenchyma is viscoelastic. In comparison to the results where the parenchyma is elastic (Fig. 4.14), oscillations lead to a greater reduction in the level of contraction (a). The range of displacements in each cycle of oscillation is also greater. Similarly the range within a cycle of oscillation is greater for the stresses (b-d). At points within the cycle the radial or hoop stresses can be purely tensile, while at other points they can be purely compressive. There is also a greater reduction in the size of the contractile force, which for a short period of the oscillations becomes negative indicating that the crossbridges are resisting contraction (e). The range of velocities initially increases before levelling off and the range is greater than with the elastic parenchyma (f). These results are significant since they not only take into account the fact that the parenchyma is viscoelastic, but show that tidal breathing can quite noticeably reduce the level of contraction of the airways.

4.5 Comparisons to experimental data

We now make further comparisons to experimental data to test the validity of our model, before making comparisons between the airway and the tissue strip in the next section. In particular we consider the data of LaPrad *et al.* [103], for which experiments were carried out on an airway dissected from the surrounding parenchyma. They designed two protocols to test the significance of the tidal breathing and deep inspirations on bronchoconstriction. They found that tidal oscillations have little effect on the mean lumen radius in comparison to when there are no oscillations. We describe the methods

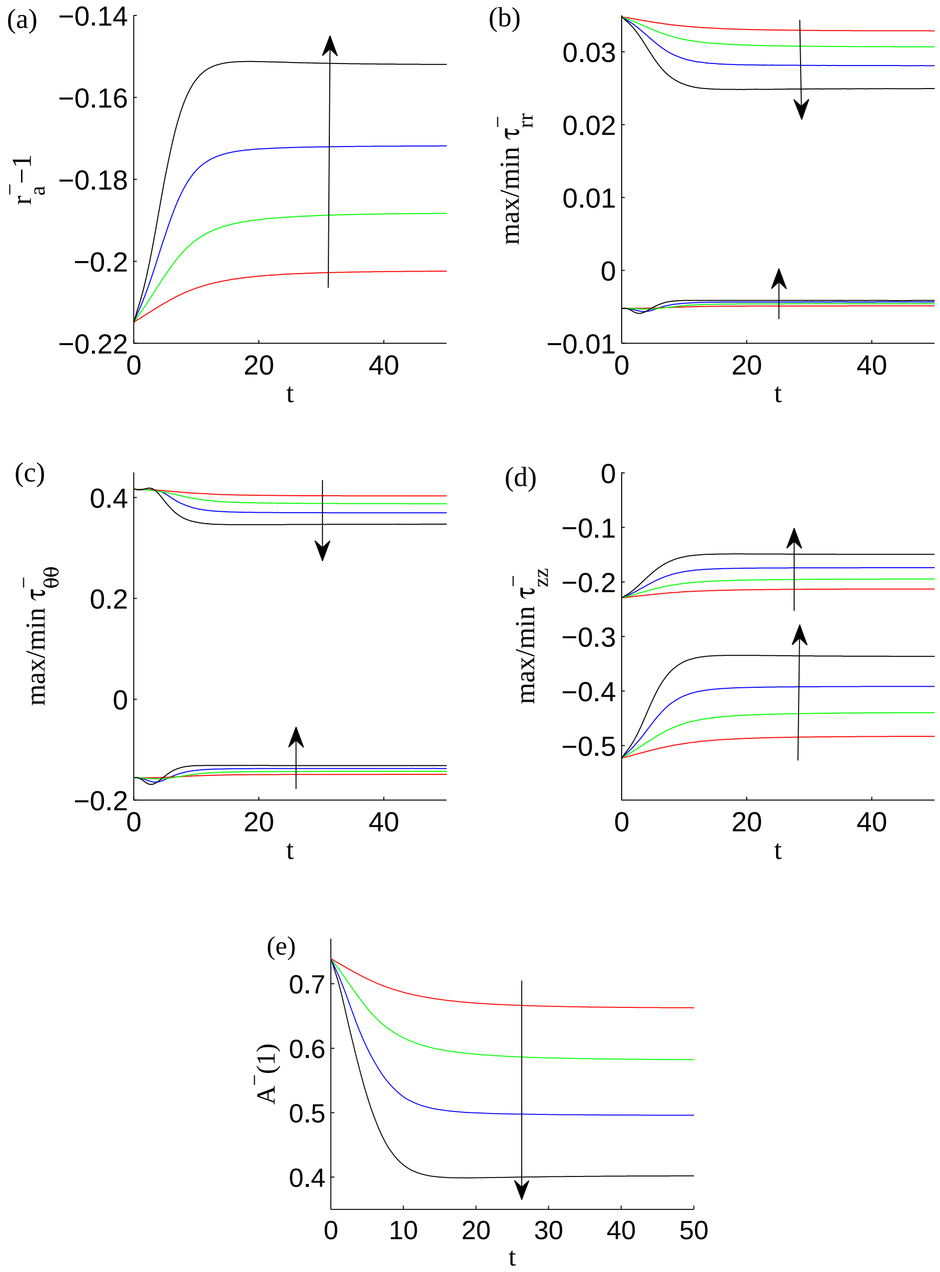

Figure 4.14: Curves joining the minimum values in each cycle of oscillation of (a) the lumen displacement, (b-d) the maximum and minimum radial, hoop and axial stresses and (e) the contractile force at the inner boundary. Oscillations are applied to the pleural radius using (4.4.1) with $a = 0.25$ (red), 0.5 (green), 0.75 (blue) and 1 (black). Arrows indicate increasing amplitude oscillations. Other parameter values are given in Table 4.3, while the HHM rates are given in Table 4.2.

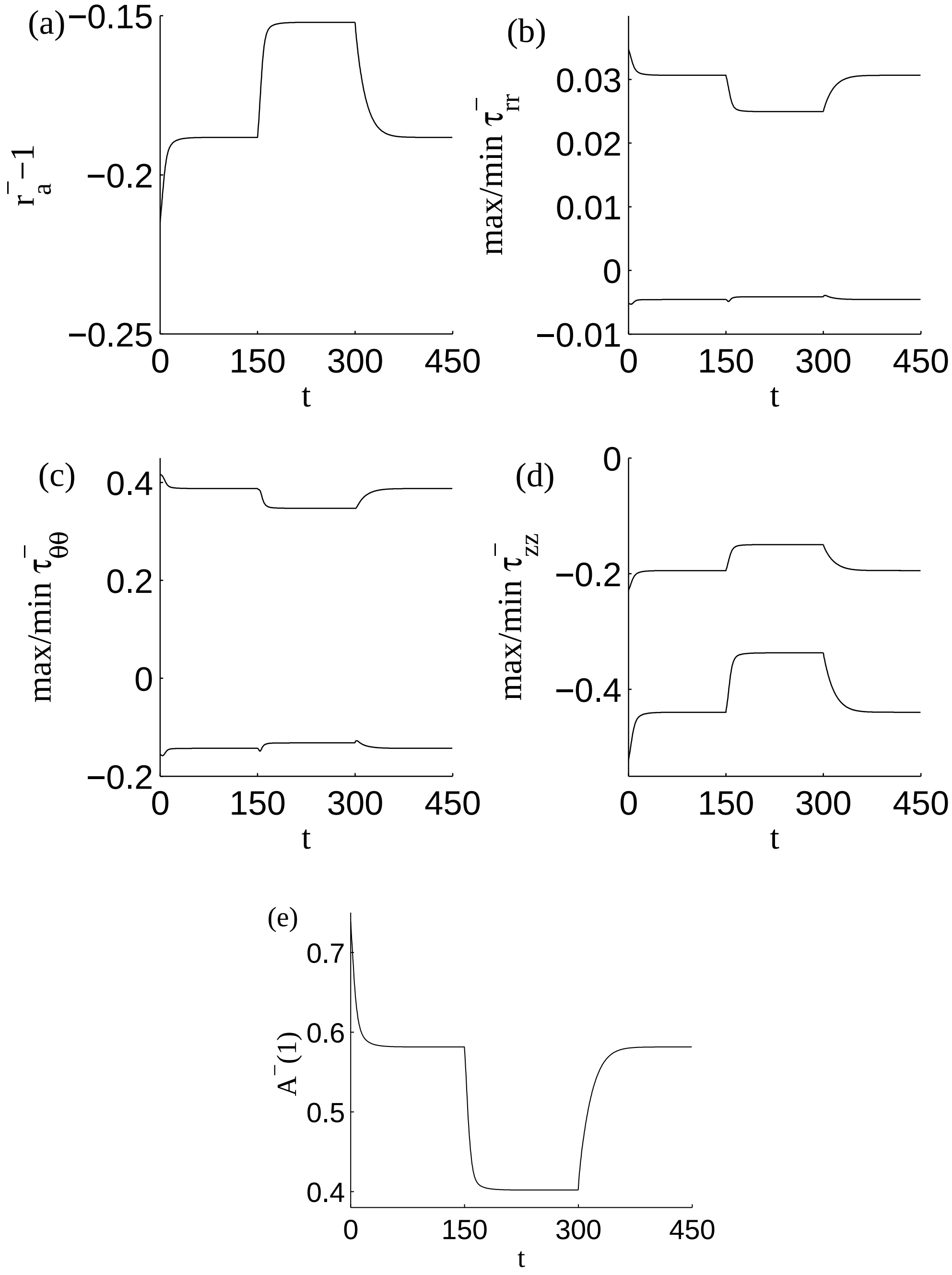

Figure 4.15: Curves joining the minimum values in each cycle of oscillation of (a) the lumen displacement, (b-d) the maximum and minimum radial, hoop and axial stresses and (e) the contractile force at the inner boundary. Oscillations are applied to the pleural radius using (4.4.1) with $a = 0.5$ for $t \leq 150$ and $t > 300$ and $a = 1$ for $150 < t \leq 300$. Other parameter values are given in Table 4.3, while the HHM rates are given in Table 4.2.

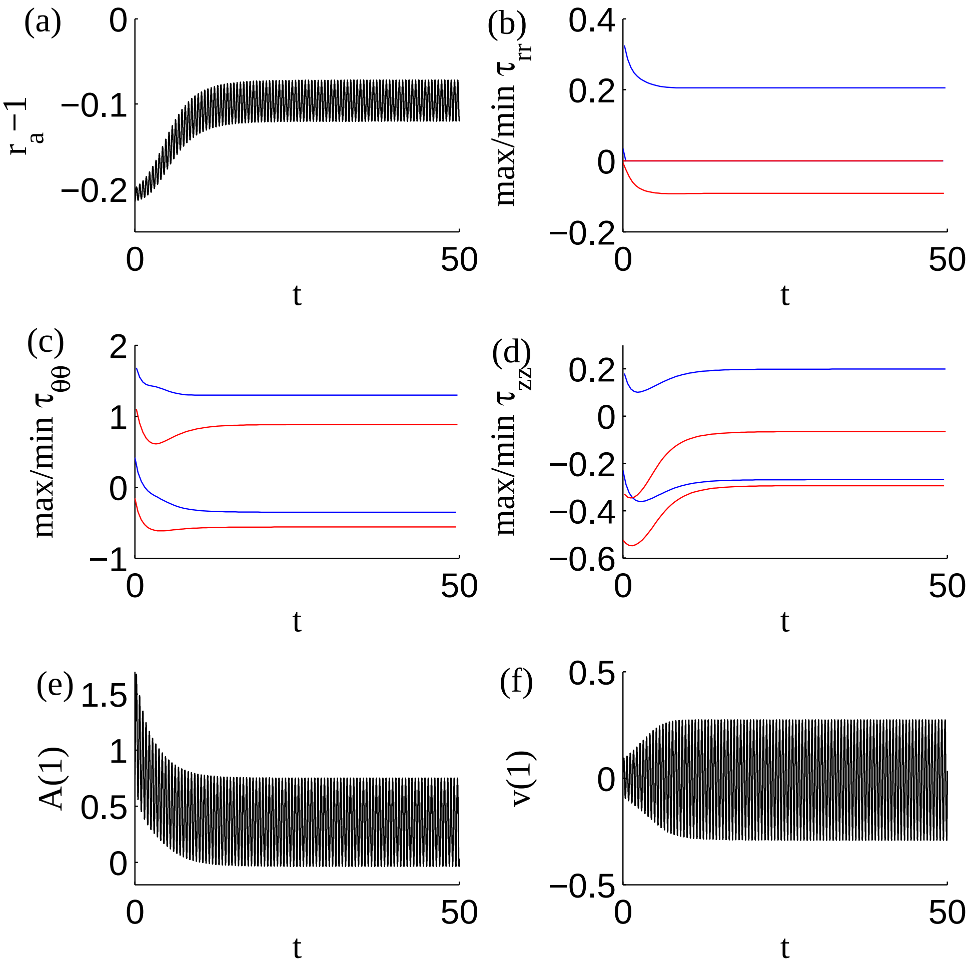

Figure 4.16: Curves of the evolution of (a) the lumen displacement, (b-d) the range of the maximum (blue) and minimum (red) radial, hoop and axial stresses in each cycle of oscillation, (e) the contractile force and (f) the relative filament velocity at the inner boundary of the airway wall. Starting from the contracted steady state, oscillations are applied to the pleural radius using (4.4.1) with $a = 0.5$. The smallest value of max τ_{rr} and the largest value of min τ_{rr} overlap. Other parameter values are given in Table 4.3, while the HHM rates are given in Table 4.2.

used to compare our model predictions and show the results.

4.5.1 Methods

Previously values were selected for C_1 and C_2 by fitting to the model of Lambert *et al.* [98] (Sec. 3.1.3). We update these values by using the mean pressure-radius plot shown in Fig. 8 of [103]. For ease of comparison with tissue strips, we assume the fibres form hoops, so that $\varphi = 0$. Again assuming that $\mu^{(w)*} = 20\text{cmH}_2 0$, we set $C_1 = 0.05$ and $C_2 = 1.8$ based on the fit with LaPrad *et al.* [103] data. We let $\chi = 0.3$ for both protocols.

We now briefly describe the two protocols of LaPrad *et al.* [103] and describe how we mimic them.

- Protocol 1: LaPrad *et al.* [98] applied an initial transmural pressure of 7.5 $\text{cmH}_2 0$ and every 12 minutes increased the concentration of Acetylcholine (ACh) applied to the airway. During this process they either kept the transmural pressure static, applied tidal oscillations or applied tidal oscillations with periodic deep inspirations. They recorded the airway radius and thickness when the transmural pressure was equal to 7.5 $\text{cmH}_2 0$ when applying oscillations.

  In order to mimic the increased agonist concentrations, we select the following three values for k_1 and k_6 and let $\beta = 5$, so that at steady state the airway contracts to approximately 95, 75 or 60% of the starting radius:

  $$k_1 = k_6 = \begin{cases} 0.05 & \text{if } t \leq 72, \\ 0.25 & \text{if } 72 < t \leq 144, \\ 0.5 & \text{if } 144 < t \leq 216. \end{cases} \tag{4.5.1}$$

  Here, as in [52, 116], we have assumed that the rates of phosphorylation of unattached and attached crossbridges are the same. Times have once again been nondimesionalised with respect to $1/k_2^*$. We consider the static and tidal cases, for which we let

  $$[\![\tau]\!] = \begin{cases} \frac{3}{8} & \text{(static)}, \\ \frac{3}{8} + \frac{1}{8}\sin\left(\frac{2\pi t}{0.5}\right) & \text{(tidal)}. \end{cases} \tag{4.5.2}$$

  To ensure that there are no sudden changes in the velocity with the tidal simulation, that could cause the numerical methods to become unstable, we ramp up the amplitude of the oscillation over the first oscillation as follows:

  $$[\![\tau]\!] = \frac{3}{8} + \frac{1}{8}\left(\frac{t}{0.5}\right)\sin\left(\frac{2\pi t}{0.5}\right), \quad \text{for } t \leq 0.5. \tag{4.5.3}$$

Protocol	χ	β	$\mu^{(w)*}$	φ	C_1	C_2
1	0.3	5	20cmH_20	0	0.05	1.8
2	0.3	5	20cmH_20	0	0.05	1.8

Table 4.4: The parameter values for Sec. 4.5.

- Protocol 2: LaPrad *et al.* [98] applied an initial transmural pressure of 5 cmH_20 and then added 10^{-5} M ACh to the airway. They increased the peak-to-peak amplitude of sinusoidal oscillations to the transmural pressure every 15 minutes. For the first 15 minutes there were no oscillations, then the amplitudes that followed were 2.5, 5 and 10 cmH_20.

  We again let $k_1 = k_6 = 0.25$ and $\beta = 5$, which ensures that at steady state the airway radius is about 60% of its starting value, and apply the following transmural pressures to the airway wall:

$$[\![\tau]\!] = \begin{cases} \frac{1}{4} & \text{if } t \leq 90, \\ \frac{1}{4} + \frac{1}{16}\sin\left(\frac{2\pi t}{0.5}\right) & \text{if } 90 < t \leq 180, \\ \frac{1}{4} + \frac{1}{8}\sin\left(\frac{2\pi t}{0.5}\right) & \text{if } 180 < t \leq 270, \\ \frac{1}{4} + \frac{1}{4}\sin\left(\frac{2\pi t}{0.5}\right) & \text{if } 270 < t \leq 360. \end{cases} \tag{4.5.4}$$

  Similar to protocol 1, we ramp up the size of the amplitude over the first cycle each time, to ensure that there are no sudden changes in the velocity. Initially at $t = 0$ the airway is said to be in the baseline state (B), while at $t = 90$, following contraction, the airway is said to be in the contracted state (C).

We slightly adapt the rate of Mijailovich *et al.* [116] for g and take it to be ten times larger as used by Wang *et al.* [173]. We normalise the radius by dividing r_a by $r_a(0)$ and we find the normalised wall thickness by dividing $r_b - r_a$ by $r_b(0) - r_a(0)$. The strain amplitude is found by dividing $\max(r_a) - \min(r_a)$ by $2r_a(0)$. The strain amplitude for the baseline and contracted states in protocol 2 are found by briefly oscillating the transmural pressure with amplitude 1/16.

4.5.2 Results

Fig. 4.17 shows the plots of the radius normalised to the radius at $t = 0$ for the static (a) and tidal (b) cases of protocol 1. In each case, as k_1 increases, the airway contracts further (c) and the wall gets thicker (d). Considering the airway radius, tidal oscillations reduce the level of contraction slightly when $k_1 = 0.05$ or 0.5, while the difference is more pronounced when $k_1 = 0.25$ (c). The results of LaPrad *et al.* [103] show little difference in the radius in the two cases for each concentration of ACh. By considering the evolution of the radius in (a, b), with the rate parameters that are used, the equilibrium state has not yet been reached when $k_1 = 0.25$, which could be causing the difference here. There are similar differences with the airway thickness when $k_1 = 0.25$ (d). For the tidal case, when $k_1 = 0.05$, there is little difference in comparison to the strain amplitude if $k_1 = 0$ (e). However, for the larger values of k_1, the strain amplitude is much reduced. These findings for the strain amplitude are consistent with those in [103] (h).

Fig. 4.18 shows the plots for protocol 2. Considering the evolution of the radius, each time that the amplitude of the oscillations is increased, there is a large increase in the radius, with the airway then gradually contracting once again (a). These features can be explained by the increased value of g, which means that the latch crossbridges are more likely to detach when they are stretched. However, considering the equilibrium states of the radius (b), there is little reversal in the level of contraction for the two smallest amplitudes of oscillations, with the results contained within the error bars of the results shown in [103] (e). For the largest amplitude oscillations, the model predicts greater reductions in the level of contraction than the experimental results of [103]. As the oscillation amplitude increases the airway thickens (c). The strain amplitude is decreased following contraction and raises a small amount when the oscillations with the smallest two amplitudes are applied, with a much greater increase in strain amplitude for the largest amplitude oscillations (d). This is consistent with the results in [103] (g).

Due to the issues observed in Fig. 4.18 with the increased value of g, the simulations can be repeated with the original value for g. The results are shown in Fig. 4.19. There are now no large deformations of the radius each time the amplitude of the oscillations is increased (a) and there are now only small changes in the mean airway radius (b) and thickness (c) when each amplitude of oscillations is applied, consistent with [103] (Fig. 4.18 (e, f)). However, the model now no longer predicts such a large increase in strain amplitude when the greatest amplitude oscillations are applied (d). In the contracted state the airway is more contracted, which could be causing this.

4.5.3 Discussion

Overall the model predictions are consistent with the findings of LaPrad *et al.* [103], which therefore gives credibility to our model. However, there are still questions about what appropriate rate parameters for the HHM model are.

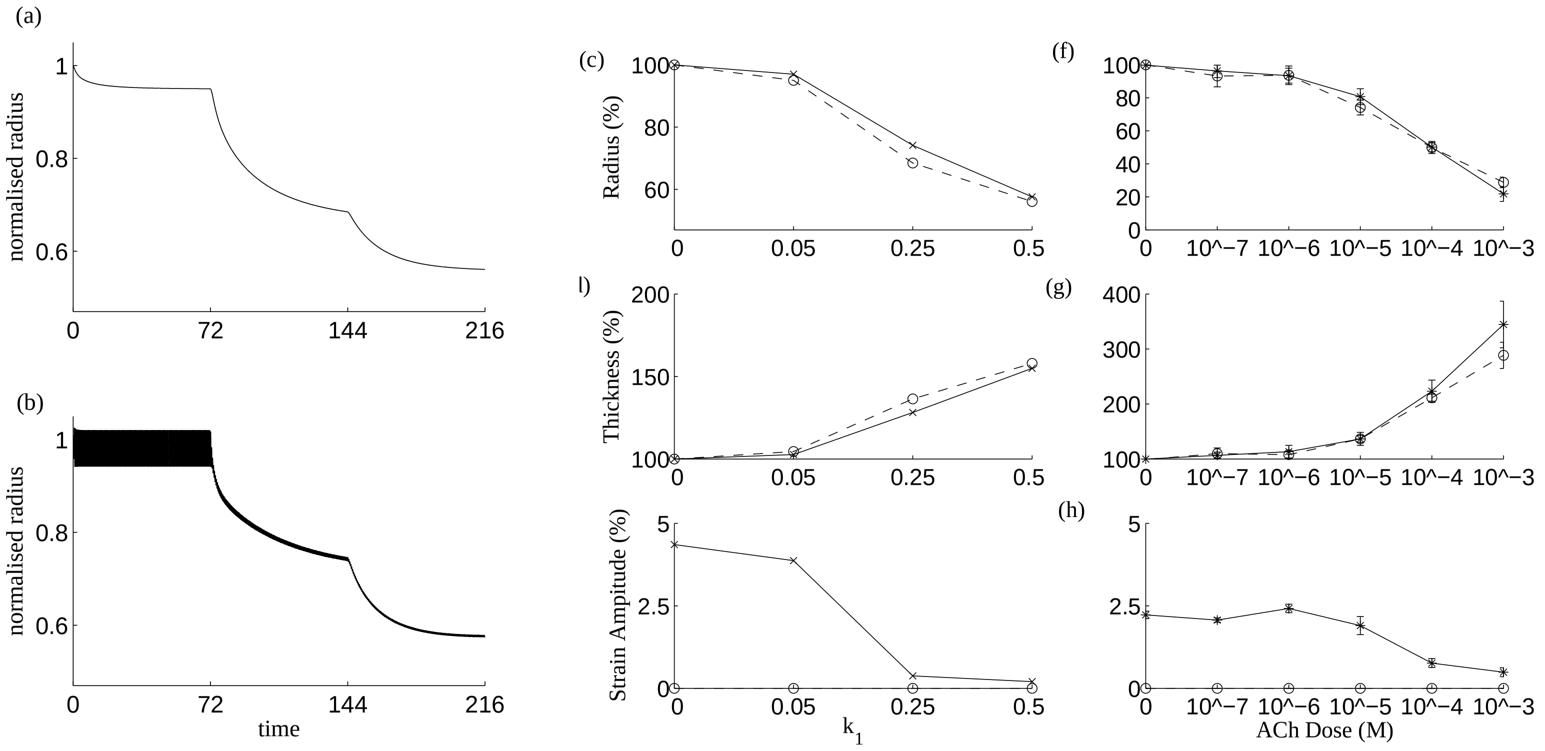

Figure 4.17: Protocol 1: Plots of the normalised radius against time for the (a) static and (b) tidal transmural pressure. Also shown are plots of the final (c) lumen radius, (d) airway thickness and (e) strain amplitude for the mean transmural pressure, for each value of k_1 for the static (circles) and tidal (crosses) cases. (f-h) The corresponding plots for the radius, thickness and strain amplitude when the experimental data [103] is used.

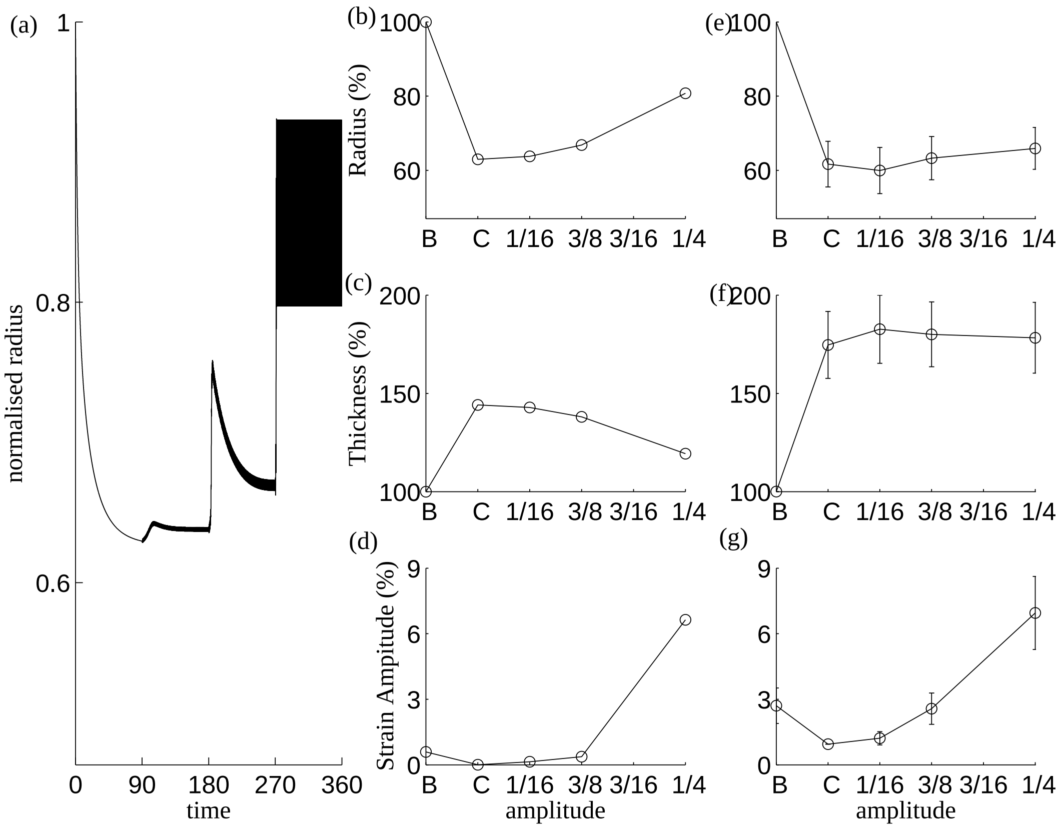

Figure 4.18: Protocol 2: (a) Plot of the normalised radius against time. Also shown are plots of (b) the lumen radius, (c) airway thickness and (d) strain amplitude for the mean transmural pressure, for each value of the amplitude of the transmural pressure oscillations. $g_1 = 1$, $g_2 = 20$ and $g_3 = 3$. (e-g) The corresponding plots for the radius, thickness and strain amplitude when the experimental data [103] is used. B and C refer to the baseline and contracted states.

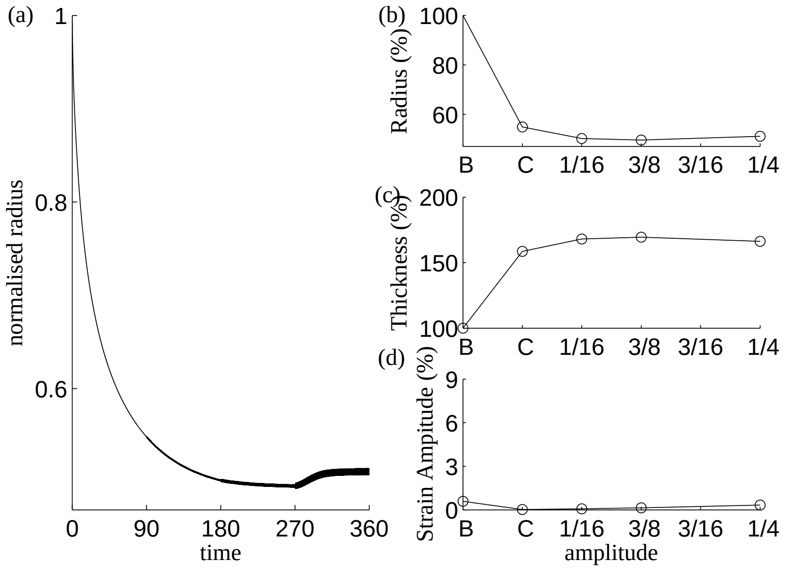

Figure 4.19: Protocol 2: (a) Plot of the normalised radius against time. Also shown are plots of the (b) lumen radius, (c) airway thickness and (d) strain amplitude for the mean transmural pressure, for each value of the amplitude of the transmural pressure oscillations. $g_1 = 0.1$, $g_2 = 2$ and $g_3 = 0.3$. B and C refer to the baseline and contracted states.

One of the main conclusions of LaPrad *et al.* [103] is that introducing tidal breathing does not significantly alter the level of contraction of the airway. However, there are a number of questions about the results that they found. For example, they have carried out experiments where the airway is dissected from the parenchyma, which could have an important impact *in vivo*. For instance, in the previous section, the model predicted that if the airway was embedded within elastic parenchyma, applying oscillatory boundary conditions resulted in small changes to the airway radius (Fig. 4.14). However, when embedded within viscoelastic parenchyma, applying the same oscillatory boundary conditions resulted in much larger reductions in the amount of airway contraction.

4.6 Comparisons of airway with tissue strip

Finally, we make a few comparisons between the airway and the tissue strip. We introduce a simple model of the tissue strip and the relevant numerical methods, before showing results.

4.6.1 Modelling a tissue strip

We model the strip as closely as possible to mimic the airway wall (Sec. 2.2). It is assumed that the tissue strip is long and thin, since the strips used by Fredberg *et al.* [43] measured 2 x 3 x 20mm. As the length is much greater than the height and width, which are roughly equal, any boundary layers at the ends, that arise due to clamping, are ignored.

Considering a strip of unstressed equilibrium length L_u^* subject to uniaxial strain,

$$x^* = \lambda_1 X^*, \quad y^* = \lambda_1 Y^*, \quad s^* = \lambda S^*, \tag{4.6.1}$$

Here X^*, Y^*, S^* are Lagrangian Cartesian coordinates and x^*, y^*, s^* are coordinates in the deformed configuration. (S^* is used, so as not to be confused with Z^* in the airway.) $\mathsf{F} = \mathrm{diag}(\lambda_1, \lambda_1, \lambda)$, so assuming incompressibility, as assumed for the airway wall, $\lambda\lambda_1^2 = 1$, implying that $\lambda_1 = 1/\sqrt{\lambda}$. Now $\mathsf{B} = \mathsf{C} = \mathrm{diag}(1/\lambda, 1/\lambda, \lambda^2)$.

Since the smooth muscle fibres form rings in the trachea, we assume that both sets of fibres are aligned to the s-axis of the strip, meaning $\mathbf{M}_1 = \mathbf{M}_2 = \mathbf{e}_s$. In the deformed configuration $\mathbf{m}_1 = \mathbf{m}_2 = \lambda\mathbf{e}_s$, thus the anisotropic invariants satisfy $I_4 = I_6 = \lambda^2$.

The same strain-energy function as was used for the airway wall (see (2.2.7)) is used. However, lengths are now nondimensionalised by L_u^*, so that

$$W = \frac{I_1 - 3}{2} + H(\lambda - 1)\frac{C_1}{C_2}\left(\exp\left[C_2\left(\lambda^2 - 1\right)^2\right] - 1\right) + A\lambda^2. \tag{4.6.2}$$

The non-zero components of the Cauchy stress tensor are

$$\tau_{xx} = \tau_{yy} = -p + \frac{1}{\lambda}, \tag{4.6.3}$$

$$\tau_{ss} = -p + \lambda^2(1 + 2A) + H(\lambda - 1)4C_1(\lambda^2 - 1)\lambda^2 \exp\left[C_2(\lambda^2 - 1)^2\right]. \tag{4.6.4}$$

Assuming that the sides of the strip are stress-free, $p = 1/\lambda$ and

$$\tau_{xx} = \tau_{yy} = 0, \tag{4.6.5}$$

$$\tau_{ss} = \lambda^2(1 + 2A) - \frac{1}{\lambda} + H(\lambda - 1)4C_1(\lambda^2 - 1)\lambda^2 \exp\left[C_2(\lambda^2 - 1)^2\right]. \tag{4.6.6}$$

Conservation of momentum is satisfied and

$$x = \frac{X}{\sqrt{\lambda}}, \quad y = \frac{Y}{\sqrt{\lambda}}, \quad s = \lambda S. \tag{4.6.7}$$

We assume that λ is being prescribed, however, an alternative is that τ_{ss} is prescribed.

4.6.2 Numerical methods for the tissue strip

If λ is prescribed, then V can immediately be found at each time step. The Godunov scheme (Appendix B.1) is used to update n and thus A, from which τ_{ss} is given by (4.6.6). Alternatively if τ_{ss} is prescribed, a similar method can be used as shown in Fig. 4.5 for the airway. Instead of r_b, we now solve for λ. Differentiating (4.6.6) and using (4.2.3), rearranging gives

$$V(t) = \frac{\partial \lambda}{\partial t} = \frac{\partial \tau_{ss}/\partial t - 2\lambda^2 \beta \mathcal{H}_1}{2\lambda(1+2A) + 2\lambda^2 \beta \gamma \mathcal{H}_2 + \lambda^{-2} + H(\lambda - 1)E}, \tag{4.6.8}$$

where

$$E = 4C_1 \exp\left(C_2\left(\lambda^2 - 1\right)^2\right)\left[2\lambda^3 + 2\lambda\left(\lambda^2 - 1\right)\left\{1 + 2C_2\left(\lambda^2 - 1\right)\lambda^2\right\}\right]. \tag{4.6.9}$$

4.6.3 Results

In Sec. 4.5.2, results were shown when the protocols of LaPrad *et al.* [103] were mimicked. Results were shown for the airway radius and thickness and the strain amplitude, but not the stress. For these results it was assumed that the fibres formed hoops with $\varphi = 0$, meaning that the stress that the fibres experienced was $\tau_{\theta\theta}$. Comparisons are now made between the airway and the strip by applying the same stretch to the tissue strip as was experienced by the fibres at the mid point within the airway wall. The values for k_1 are also assumed to be the same.

Fig. 4.20 shows the stress that the fibres experience at the inner and outer boundaries of the airway wall and in the strip, when protocol 1 is applied. Also plotted is the relationship between the stretch of the fibres in the strip (equal to the stretch of the fibres at the mid point of the airway wall) and the stresses, for each value of k_1 (b-d). In each of the cases, the stress experienced by the fibres within the strip is similar to that of the fibres at the outer boundary of the airway wall, and is quite different from the stress of the fibres at the inner boundary of the airway wall.

Fig. 4.21 shows the results for protocol 2 when g takes either the value as described in [116] or ten times this value as used in [173]. Unlike protocol 1, where the stress within the strip was always within the range of stresses experienced in the airway wall, with protocol 2 this is not always the case (d). At some points within the equilibrium loops the fibres at the inner boundary of the airway can be under compression, while those at the outer boundary are under tension. Such heterogeneities are not seen within the strip for which there is a single stress along its length.

These results therefore show that due to the simplified geometry of the tissue strip,

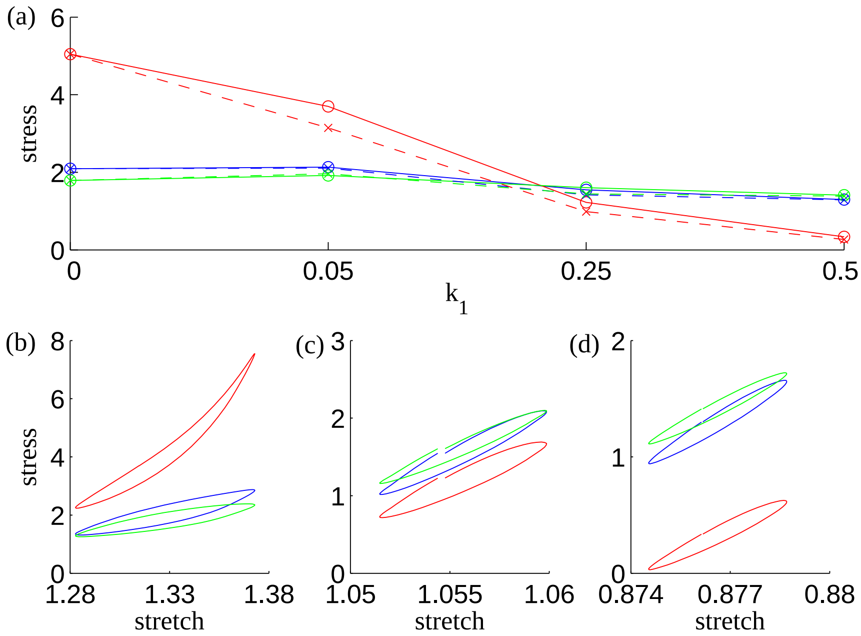

Figure 4.20: Protocol 1: (a) Plots of the stress within the fibres in the strip (blue) and the inner (red) and outer (green) boundaries of the airway, when the transmural pressure is static (solid) or tidal (dashed). Also plots of fibre stretch against the reference fibre stretch when (b) $k_1 = 0.05$, (c) $k_1 = 0.25$ and (d) $k_1 = 0.5$.

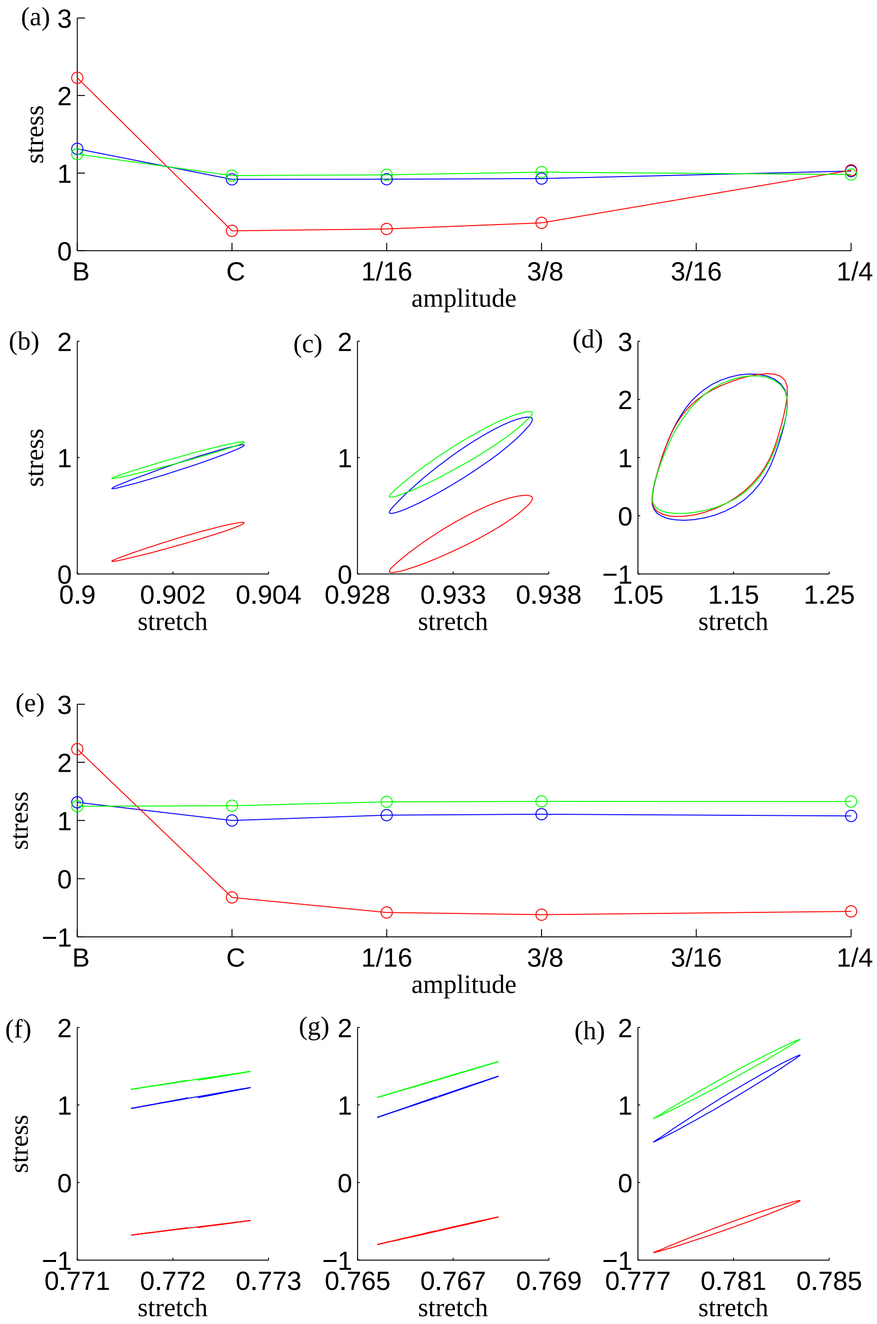

Figure 4.21: Protocol 2: (a, e) Plots of the stress within the fibres in the strip (blue) and the inner (red) and outer (green) boundaries of the airway. Also plots of fibre stretch against the reference fibre stretch when the amplitude is (b, f) 1/16, (c, g) 1/8 and (d, h) 1/4. $g_1 = 1$, $g_2 = 20$ and $g_3 = 3$ in (a-d), while $g_1 = 0.1$, $g_2 = 2$ and $g_3 = 0.3$ in (e-h). B and C refer to the baseline and contracted states.

some of the complex features predicted in the airway are lost and the results can be quantitatively different.

4.7 Conclusions

In this chapter we have focused on what happens to the airway when contractile forces are applied along the fibres within the airway wall. We began by looking at steady state solutions, before prescribing the contractile force by solving HHM theory for an isometric contraction. Results were also shown when the tissue mechanics is coupled to the crossbridge mechanics described by HHM theory.

Applying a uniform steady force, the model predicts that the stresses within the airway wall are heterogeneous. Increasing the thickness of the airway wall, as occurs during remodelling associated with asthma, can lead to compressive stresses (in the radial or hoop direction) existing in some regions of the wall, while tensile stresses exist in the other regions. Thickening of the airway wall due to remodelling also leads to greater contraction of the airway. Recalling the finding from Chapter 3, that thicker walls are also stiffer means that airways of asthmatics not only contract more but are also harder to return to the original configuration. The results found are qualitatively consistent with the previous work of Brook *et al.* [22], although the nonlinear model predicts that compressive stresses are more likely to arise and are larger in magnitude, while the amount of contraction is reduced for the same contractile force. The model also predicts that increasing the magnitude of the contractile force, which could be caused by an increase in agonist concentration, results in greater levels of contraction and can lead to the existence of the compressive stresses. Comparing a zero stress and zero displacement condition at the pleura, the model predicts that there is little difference with just a small decrease in the contraction and increase in the stresses with the zero displacement case.

As the airway contracts, there is an initial rapid contraction, which then slows down. Taking into account that the parenchyma is viscoelastic, the airway contracts more slowly and short-time peaks in the radial and hoop stresses are predicted. These features are exaggerated if the ratio of the creep and relaxation timescales or the relaxation timescale increase. Applying an oscillatory increase to the radius of the pleura results in the contractile force reducing on average and the airway re-inflates a little. Increasing the amplitude of the oscillations enhances these features. The reduction in the contractile force can be explained by the fact that stretching results in more of the crossbridges detaching. This shows that tidal breathing can help to lessen the effect of airway contraction, with greater reductions with increased depth of breathing.

Subtracting the parenchyma, the model predictions are consistent with the experimental results of LaPrad *et al.* [103], which gives our model further credibility. However, there are still some questions about the most suitable rate parameters for the cross-bridge mechanics.

Finally, the range of stresses exerted on the fibres within the airway wall and the stress in the fibres within a tissue strip were compared, when the stretch experienced by the mid point of the airway wall is applied to the strip. The stress heterogeneities predicted in the airway wall are not predicted in the strip, with the stress in the strip being generally closer to the stress at the outer boundary of the airway wall than the stress at the inner boundary. It is also possible for the stress in the strip to be outside of the range of stresses predicted for the airway wall. This indicates that misleading hypothese about ASM *in vivo* might be deduced from interpreting experiments using tissue strips.

Chapter 5

Image analysis of lung slice experiments

A mathematical model of the asthmatic airway has been developed in the preceding chapters. In this chapter the focus shifts to using imaging techniques to analyse lung slice experiments. We begin by giving an overview of experimental techniques used to obtain precision-cut lung-slices and to study their contractile response. Techniques are then developed that enable comparisons to be made between the mathematical model and experimental data.

In Sec. 5.2 we introduce methods for tracking the area of the lumen during an experiment. One of the features that has been observed previously by Bergner and Sanderson [12] is that there is "an initial steep phase of fast narrowing ... followed by an asymptotic phase". Using the areas calculated for the lumen, we fit exponential functions to the contraction and investigate the evidence for multiple timescales. Finally we make comparisons to the predictions of our model.

As well as studying how the lumen area changes, it is of interest to consider how points within the parenchyma surrounding the lumen are displaced during a contraction. There have been some previous attempts to do this. For example, Adler *et al.* [1] calculated displacements at a number of points in the parenchyma surrounding the airway, before finding an average curve to relate the radial displacement to the distance from the lumen. In Sec. 5.3 we develop techniques to find estimates for the displacement at more regularly spaced intervals. The importance of spatial variations are investigated and comparisons are made between the radius-displacement plots found and those predicted by the mathematical model.

5.1 Lung slice experiments

Lung slice experiments provide a physiologically relevant system to study airway contraction, since slices of tissue contain airways that are structurally intact. The precision-cut lung-slice technique was first developed by Bergner and Sanderson [12] for use on mouse tissue. In this section an overview of the method for obtaining the slices and the experiments that can be carried out on these slices is given. Mouse, pig and human lung slices are considered. The data from mouse and pig slices is from experiments carried out at Queen's Medical Centre in Nottingham [42], while the data from human slices is from experiments carried out in Chicago, USA [105].

5.1.1 Obtaining the lung slices

We now give an overview of the methods for obtaining lung slices as described in [42]. First the lung is gently inflated and deflated to ensure that it is airtight. It is then slowly injected with agarose gel solution until the lung is 90% full. The remaining 10% is filled with air, which clears the main airways, forcing the agarose into the alveoli. The agarose solidifies within twenty minutes and the lung is stored in buffer on ice. The buffer provides the cells with the required concentrations of chemicals, for them to function. Due to the increased size of the pig lung, rather than inflating the whole lung, only a portion may be inflated and sliced.

Prior to slicing, a scalpel is used to cut off a small section of the agarose-filled lung. Segments, where the main airways are free of agarose, are sliced with a `EMS 5000` oscillating tissue slicer into slices of 130μm thickness. For the pig tissue the thickness is set between 140-170μm depending on the likelihood of tearing the segment. The slices are stored in a buffer solution with added antibiotics and antifungals and incubated overnight.

In Nottingham I was only able to see the equipment that is used to prepare the lungs and slice them. However, during an extended visit to Harvard University I had the chance to observe a mouse lung being sliced.

5.1.2 Measuring the contractile response

Fox [42] measured the contractile response of lung slices to various chemicals. We received data from Fox that involved adding acetylcholine (ACh) to the slices, which resulted in the ASM contracting and the airways narrowing. The changes in the airways were observed with a microscope and recorded for image processing. We received a selection of data sets from these experiments, in the form of videos.

Slices with intact airways with beating cilia (indicating that the cells are living) and a lumen free of agarose and of diameter approximately 100μm were chosen for the experiments, with preference given to airways that would have been perpendicular to the slice. The chosen slice was floated on a small amount of buffer in a petri dish. In order to hold the slice in place, while allowing liquid to circulate, a nylon mesh, with a hole over the airway, and a coverslip were placed on top of the slice. Two tubes were placed at opposite sides of the dish, with one being used to pump in buffer solution or the ACh solution at a rate of 5ml/min, while the other was a suction tube, ensuring that there is a constant turnover of solution.

There were a number of stages of a contraction experiment. Initially buffer was perfused for about a minute to allow the the slice to settle. 10μM ACh was then added for five minutes, to initiate ASM contraction. Finally buffer was perfused for a further ten minutes to wash out the ACh. Due to the length of the tube, there was some delay from when the tap was turned on to when the ACh reached the lung slice. In order to record the experiments a laser scanning microscope (`Zeiss Axio Observer D1, Hamatsu electron multiplier CCD camera C19100-13`) was used. This enabled bright field images to be taken at a rate of 0.5 frames per second.

5.1.3 "Breathing" lung-slice experiments

An overview of the experiments of Lavoie *et al.* [105] is now given. Human lung slices were used, which were obtained in a similar way to the mouse and pig slices. When setting up the experiment, rather than placing a coverslip on top of the mesh, a metal ring was used. This allowed for a cylindrical indenter, with inner radius 2mm and outer radius 3mm, to be positioned so that it was just touching/above the slice, with an airway centred under it. By lowering the indenter, the parenchyma could be stretched.

The experimental techniques of Lavoie *et al.* [105] were developed to investigate the effect of breathing on contracted airways. For the data shown in this thesis, 10^{-5}M of Methacholine (MCh) was added to the slice to initiate ASM contraction. The airway was allowed to contract for ten minutes. Following this, a computer program was used to periodically oscillate the indenter up and down, in order to mimic breathing, for a further ten minutes. The amplitude of the oscillations was chosen so that for the relaxed airway the lumen area increased by between 16 and 20%. Each oscillation consisted of the indenter being lowered for two seconds, held for half a second, raised for two seconds and held for half a second. The experiment was completed by having

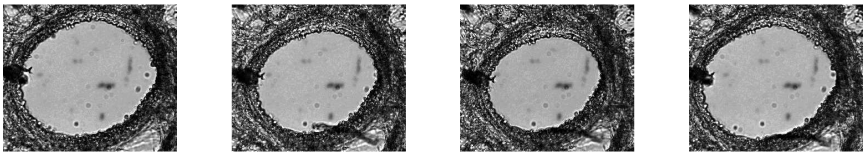

Figure 5.1: Cropped versions of frames 25, 100, 260 and 460 of an experiment on a mouse. The cross-sectional area of the lumen reduces in response to the addition of ACH($\approx$ frame 80), and then relaxes as the ACh is washed out ($\approx$ frame 260).

another ten minutes of no tidal oscillations. A sequence of images were again taken to record the developments. While visiting Harvard University I was able to observe experiments that used this technique.

5.2 Lumen area analysis

Having outlined the methods used to obtain lung slices and the experimental techniques used to obtain a series of images, two different ways of analysing these images are considered. In this section we focus mainly on the contraction experiments carried out on lung slices from mice and pigs at The University of Nottingham. From the experiments it is observed that the airway narrows as the ACh is added and then the slice relaxes again as the ACh is washed out (c.f. Fig. 5.1). We consider the lumen area and how it changes during a contraction. In particular we investigate the timescales involved and compare them to the results from the model presented in the previous chapters.

5.2.1 Methods

In this subsection the methods used to find the lumen area are explained. Having received the data in the form of videos, the free software Virtualdub (see www.virtualdub.org) is used to save the individual frames. The image processing toolbox in MATLAB is used to find the area of the lumen in each frame.

Depending on the lung slice being considered, there are a few different procedures that are used to find the area of the lumen in each of the frames. The following tools are used in at least one of the procedures (`I` is used to represent the latest version of the image):

- `imread(N)`: used to load up the image from a file N;

- `imcrop(I, rect)`: used to take a rectangular section (`rect` specifies the coordinates of the section) of the image around the airway;
- `level = graythresh(I)`: computes a threshold of the image, which can be used to produce a binary image;
- `im2bw(I,level)`: changes the image to a binary image;
- `rgb2gray(I)`: converts an image to greyscale;
- `bwareaopen(I, numpixel, 4)`: removes from the binary image any groups of less than numpixel of connected pixels (4 means that two pixels are only connected if they share an edge);
- `imfill(I,'holes')`: fills in any small holes in an object;
- `edge(I,'canny', thresh)`: detects edges using the Canny method (Edges are found by searching for local maxima of the gradient of `I`. The derivative of a Gaussian filter is used to calculate the gradient. The method uses two thresholds, to detect strong and weak edges, only including the weak edges if they are connected to strong edges.);
- `imdilate(I, [strel('line', 3, 90) strel('line', 3, 0)])`: lines are dilated by three pixel each way in the horizontal and vertical directions;
- `imcomplement(I)`: the binary image is inverted;
- `cc = bwconncomp(I,4)`: the binary image is split up into sections depending on the connectivity of the pixels (the resulting number of objects can be obtained using `cc.NumObjects`);
- `imagedata = regionprops(cc, 'Area', 'Centroid', 'Orientation', 'MajorAxisLength', 'MinorAxisLength')`: finds the area and centroid of each object and the length of the major and minor axis and the orientation of the major axis to the horizontal of an ellipse that has the same second-moments as the object;
- `BWoutline = bwperim(I)`; `Segout = I2`; `Segout(BWoutline) = 255`: draws the outline found onto the original image.

The two procedures developed for the mouse experiments are outlined in figs. 5.2 and 5.3. In each of the two methods, an estimate for the edge of the lumen is found, which can be used to fit an ellipse to the lumen. In the example in Fig. 5.2 there is a

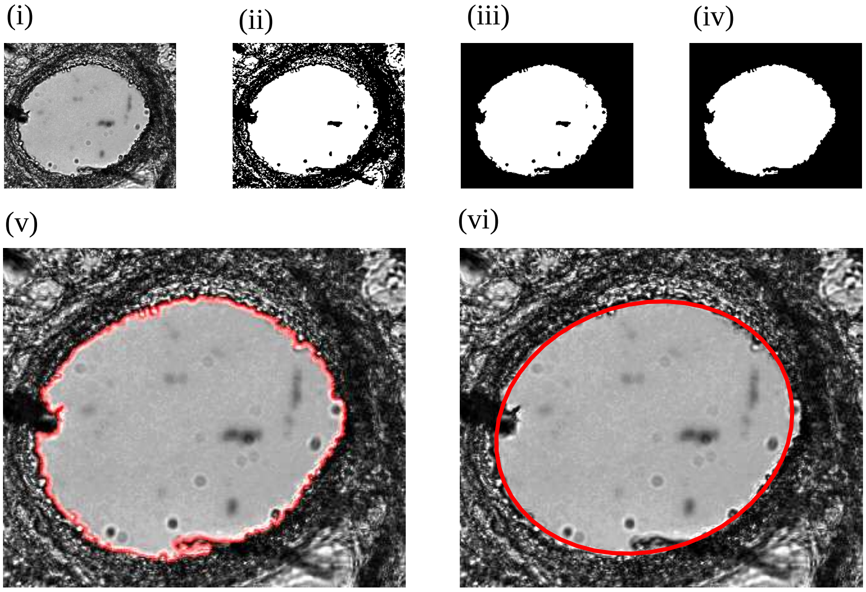

Figure 5.2: For the mouse lung slices that had a clear contrast between the lumen and the airway wall we use the following sequence of tools: `imread`, `imcrop` (i), `graythresh`, `im2bw` (ii), `bwareaopen` (iii), `imfill` (iv), `bwconncomp`, `regionprops`. From `regionprops` we obtain two estimates for the area of the lumen at each frame. An area can either be calculated within the region found (shown using `pwperim` in (v)) or an ellipse can be fitted to the region (shown using `regionprops` in (vi)).

loose piece of tissue that moves in and out at the bottom of the lumen and an object on the left of the lumen is also picked up. Occasionally the method may also include small regions outside of the lumen, due to lack of contrast. Fitting an ellipse can reduce the effect of these features on the calculated lumen area. The first method (Fig. 5.2) works well when there is a fairly clear change in intensities at the lumen boundary. However, for some slices this is not the case, for example if the airway was not sliced parallel to the lumen cross-section. In these cases, the second method can give a more accurate area estimation (Fig. 5.3 (v,vi)). It may pick up small objects within the lumen (Fig. 5.3 (v)), but it is less likely to include large areas outside of the lumen.

When considering the pig slices, due to their increased thickness, the contrast between the lumen and the surrounding tissue is increased. This means that it is easier to find the edge of the lumen and hence find an accurate estimation of the lumen area. The following sequence of tools are used: `imread`, `imcrop`, `greythresh`, `im2bw`, `bwareaopen`, `imfill` (often the lumen is clear so this step is not required), `bwconncomp` and `regionprops` to find the area of the lumen. Due to the increased accuracy, compared to with the mouse slices, it is no longer necessary to fit ellipses. Ellipses would also be less suitable now, since there are various different shapes that the pig lumen can take; some are fairly round, while others have a buckled mucosa (c.f. Fig. 5.4). The same sequence of tools are also used when analysing the lumen of human lung slices.

When analysing the lung slices we first ensure that they are contracting and then relaxing and ignore any examples where it is clear that the airway wall has been torn away from the surrounding tissue. With the pig slices there are differences in the amount of mucosa between different airways. In some cases during contraction the airways buckle so that the airway splits in two or may close up fully. These examples are ignored and we concentrate on the examples where measurements of the lumen can be taken throughout the duration of the experiment.

5.2.2 Results

We now present results from the lumen area analysis of contracting airways and investigate the timescales involved. Fig. 5.5 shows how the lumen area, calculated by fitting an ellipse, changes over the experiments, with similar features in each of the graphs, although initially as the slices settle there are some differences. As ACh is added (by (i)) there is a rapid narrowing of the airway, followed by a decreased rate of narrowing. As the ACh is washed out, the airway rapidly dilates (near (ii)) before slowly levelling off. At the end of the experiment the area remains smaller than before the ACh was initially added. In each case there is some fluctuation in the area estimate.

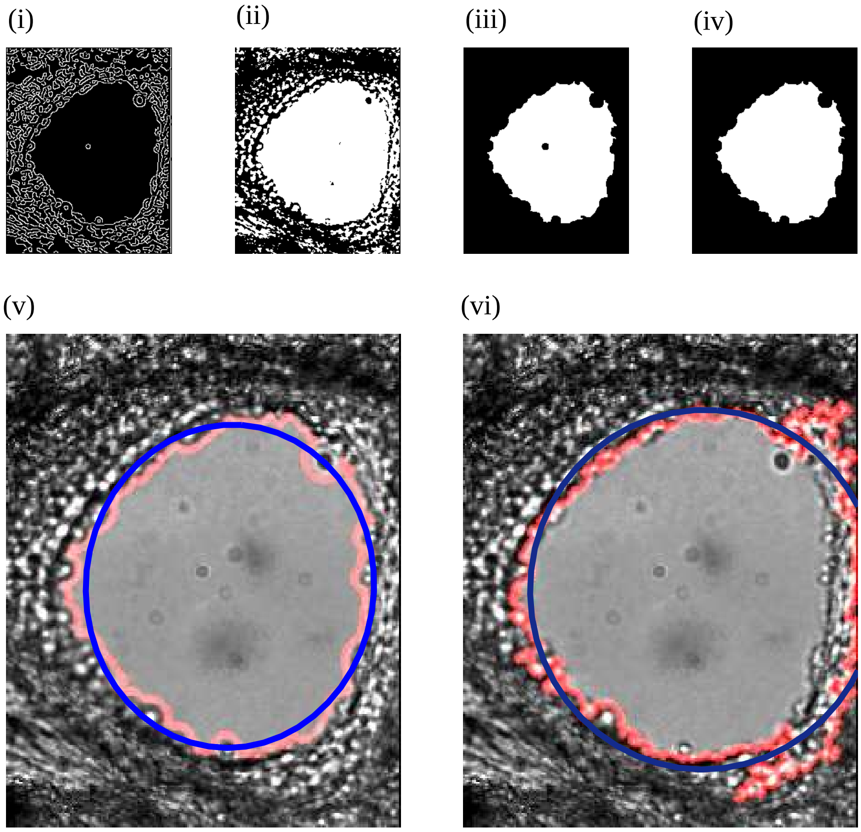

Figure 5.3: An alternative method for finding the lumen area uses the following sequence of tools: `imread`, `imcrop`, `rgb2gray`, `edge(I,’canny’, thresh)` (i), `imdilate(I, [se90 se0])` (ii) (this closes the gaps between the edges that have been found), `imcomplement`, `bwareaopen` (iii), `imfill` (iv). (v) The area of the region found or that within a fitted ellipse can be found using `bwconncomp` and `regionprops`. (vi) The output from the first method (described in Fig. 5.2) is less accurate in this example.

Figure 5.4: Outputs when finding the lumen of a two pig airways. In some cases the airways are fairly round, while others show a buckling pattern.

We are able to consider further the timescales over which the airway contracts by fitting to an exponential function. The data between (i) and (ii) in Fig. 5.5 (a) is fitted to an exponential function of the form

$$a_1 + a_2 \exp(-(t - t_{sc})/\tau_1) + a_3 \exp(-(t - t_{sc})/\tau_2), \tag{5.2.1}$$

where t_{sc} is the time of the first data point considered. a_1, a_2 and a_3 are areas and τ_1 and τ_2 are timescales. Alternatively, the data is fitted to an exponential function with a single timescale τ_1, by setting $a_3 = 0$. The function `exp2fit` available from the MATLAB file exchange[1] is used to carry out the fitting. The results in Fig. 5.6 clearly show that there is a good fit when there are two timescales, and the fit is superior to when there is a single timescale and $a_3 = 0$. The physical reason for multiple timescales will be discussed in Sec. 5.2.3.

Since the single exponential model is just a special case of the double exponential model, it is not surprising that it does not give as good a fit as it is able to take into account fewer features. An extra sum-of-squares F test [118] is carried out to test the hypothesis that the simpler model is sufficiently good. For each of the models the error can be found by finding the sum of the squares (SS) of the difference between the predicted values and the data points. The degrees of freedom (DF) of each model are found by subtracting the number of parameters from the total number of data points. The F ratio is calculated as follows:

$$F = \frac{(SS_1 - SS_2)/(DF_1 - DF_2)}{SS_2/DF_2}, \tag{5.2.2}$$

where subscripts 1 and 2 represent the exponential models with one or two timescales, respectively. If $F \approx 1.0$ the simpler model is correct, while if $F \gg 1.0$ there are two pos-

---

[1] http://www.mathworks.co.uk/matlabcentral/fileexchange/21959-exponential-fit-without-start-guess/content/exp2fit.m

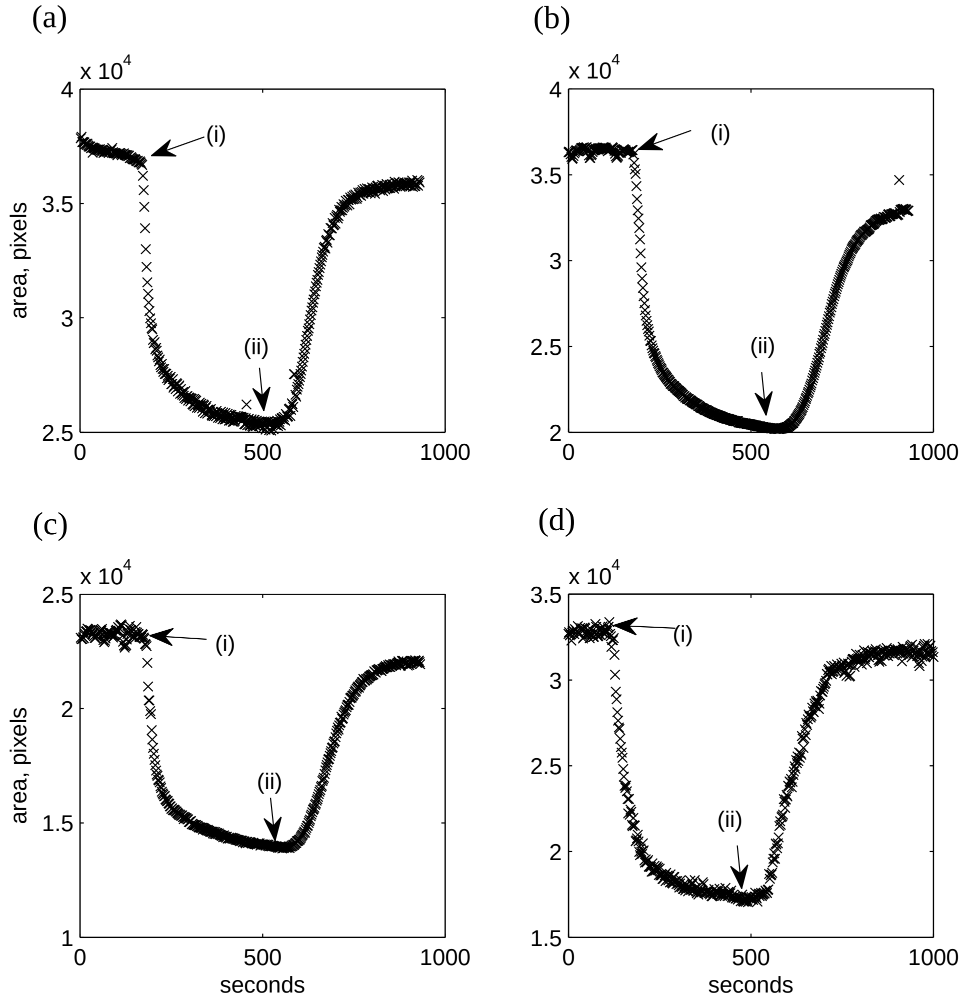

Figure 5.5: Plots of the changes of lumen area, for replicates of the contractile response experiment (Sec. 5.1.2), using lung slices from mice. The timepoints (i): pre-contraction and (ii): max-contraction will be used in the Sec. 5.3. The timescales of the contraction are given in Table 5.1.

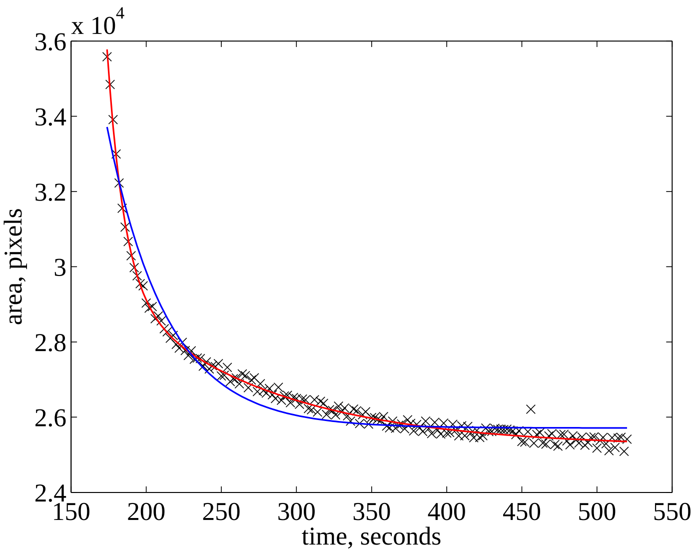

Figure 5.6: Fitting exponential curves of the form (5.2.1) to the contraction. When two timescales are used (red) a much better fit is obtained than when just one timescale is used (blue).

sibilities: either the more complicated model is correct or the simpler model is correct, but random scattering has led to the more complicated model fitting the data better. Using the F-distribution (also known as the Fisher-Snedecor distribution) the probability that scattering is the cause can be found. MATLAB is used to find the p-value by subtracting the F cumulative distribution function, which depends on the F-ratio and the degrees of freedom of the numerator and the denominator of (5.2.2), from one, such that

$$p = 1 - \texttt{fcdf}\left(F, DF_1 - DF_2, DF_2\right). \tag{5.2.3}$$

Functions of the form (5.2.1) can similarly be fitted to the other plots of the contracting airways shown in Fig. 5.5 and test whether two timescales are more appropriate than one. Results are shown in Table 5.1. In the table, lengths have been nondimesionalised by the average radius of the ellipse fitted to the lumen in the first frame. The initial area is thus π. There can be quite large differences in the parameters. For example the timescales are significantly larger for (d). The ratio of the two timescales, however, is very similar in each of the experiments. In each of the examples, $F \gg 1$ and the p-value is less than 10^{-16}, which shows that there is overwhelming statistical support to reject the hypothesis that the simple model with one timescale is sufficiently good and instead accept the more complex model with two timescales.

We now focus on the experiments on pig lung slices. The results from the lumen area analysis are shown in Fig. 5.7. Although contraction occurs in all of the airways, it can

	start time	end time	duration	a_1	a_2	τ_1	a_3	τ_2	F value	τ_2/τ_1
(a)	174	520	346	2.21	0.562	22.9	0.368	210	742	9.16
(b)	194	560	366	1.96	0.601	29.2	0.582	247	14600	8.48
(c)	182	540	358	1.90	0.831	32.8	0.416	308	2020	9.40
(d)	126	490	364	1.65	1.16	67.5	0.328	617	99.8	9.14

Table 5.1: Summary of mouse results shown in Fig. 5.5. τ_1 and τ_2 are timescales in seconds. a_1, a_2, and a_3 are areas nondimesionalised by the square of the radius at the start time. The difference in timescales τ_2/τ_1 is fairly consistent in these examples. (b) and (c) are separate airways from the same lungslice. In each of the case the p value is less than 10^{-16}.

vary a lot from slice to slice. In some slices an initial rapid response is followed by a sustained slower response, however, in other examples this second timescale is not so prominent and the graph flattens off. In other examples the airway begins to dilate again immediately following the initial contraction.

We again now look for evidence of the existence of multiple timescales and if they exist whether the ratio of the timescales is similar to that with the mice. For the slices that have an initial rapid contraction followed by a slower contraction, an exponential function is fitted. A summary of the parameters found are shown in Table 5.2. The start and end times have been chosen so that the contraction has started and is stopped before the washout process has an effect. On initial observation there appears to be quite a bit of variation in the results obtained with fitting the data. There is less variation if the cases being considered is narrowed to those where the duration is greater than 250s (highlighted yellow within the table). In this case, for four out of the five experiments, the ratio of timescales is within a range of two, while the ratio of the fifth is of the same order of magnitude. The ratio of timescales is reduced in comparison to the results for the mouse data. Also as with the mouse data, the F ratio is large and for each of the highlighted cases the p-value is less than 10^{-16} again indicating overwhelming support for rejecting the hypothesis that there is only a single timescale. However, there remain questions about why some of the other airways react like they do.

Finally we consider a few of the experiments of Lavoie *et al.* [105], that used human lung slices. Once again in each case there is a rapid contraction on the onset of agonist. However, the subsequent motion is varied (Fig. 5.8). In one of the plots there is a sustained contraction, while in another the contraction levels off, with a slight relaxation, while in the third more relaxation is observed. In order to further consider human lung slices, access to additional experimental data would be needed.

5.2.3 Comparisons to mathematical model

The predictions from the mathematical model described in Sec. 4.2 can be compared with experimental data. In particular it can be shown that the model predicts multiple timescales of contraction as shown by the data. First comparisons are made to the contraction shown in Fig. 5.5 (a). By taking the frame at (i), using the lumen boundary and an estimation of the outer edge of the airway wall, an estimate for the average thickness of the airway wall can be calculated, thus we let $\chi = 0.21$. We also set $\tau_a = 0$, $R_p = 10$ and to mimic the parenchyma being fixed far from the airway, as in the lung slice experiment, we prescribe $r_p = R_p$. $\beta = 3.5$ so that at steady state, the percentage contraction is roughly that of the maximum contraction of the lung slice experiment.

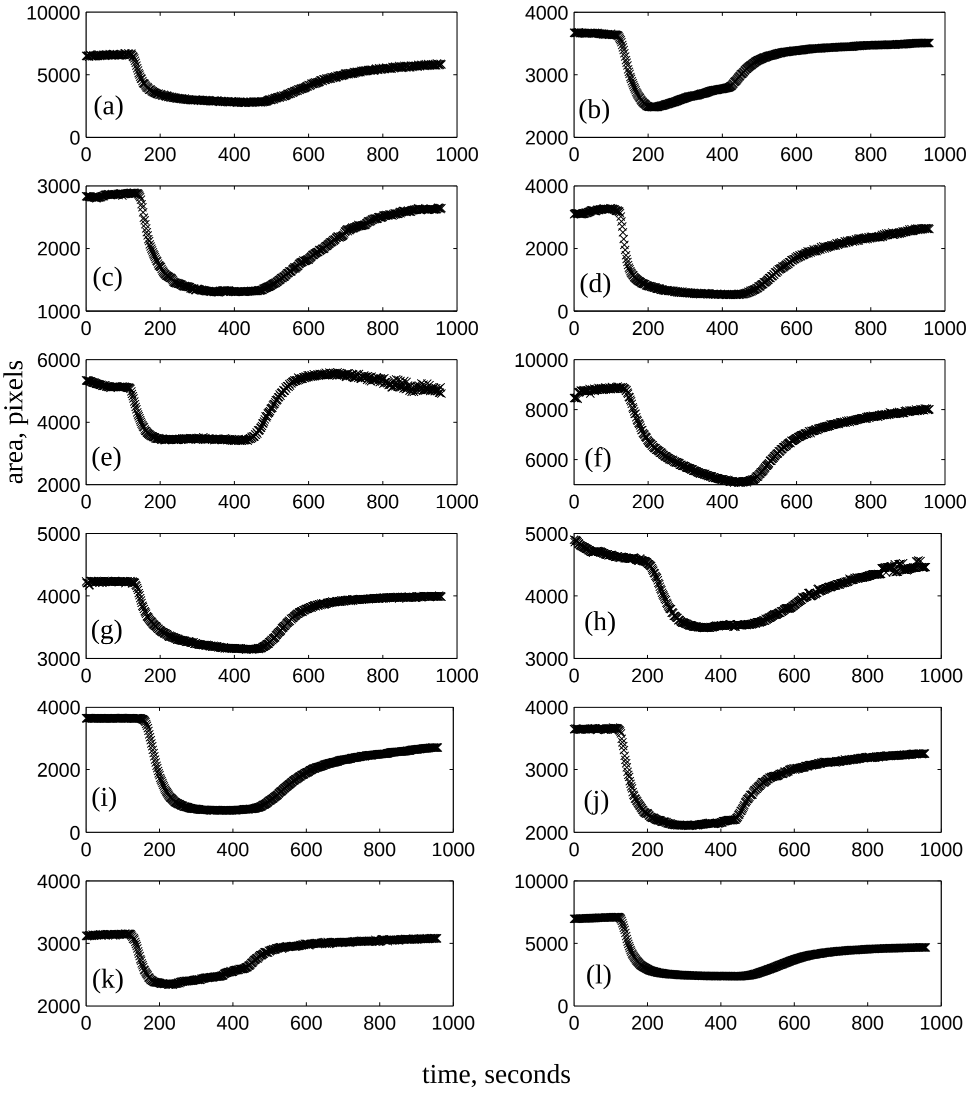

Figure 5.7: Plots of the changes of lumen area, for replicates of the contractile response experiment (Sec. 5.1.2), using lung slices from pigs. Contraction timescales are given in Table 5.2.

	start time	end time	duration	a_1	a_2	τ_1	a_3	τ_2	F value	P value	τ_2/τ_1
(a)	134	420	286	1.45	1.07	37.1	0.619	195	399	$< 10^{-16}$	5.24
(c)	148	360	212	1.43	0.856	49.5	0.852	124	95.2	$< 10^{-16}$	2.50
(d)	132	420	288	0.638	1.56	21.4	0.939	143	2130	$< 10^{-16}$	6.68
(f)	150	440	290	1.62	0.563	63.2	0.954	423	641	$< 10^{-16}$	6.69
(g)	140	400	260	238	0.357	46.3	0.400	223	595	$< 10^{-16}$	4.82
(j)	128	320	192	1.65	1.23	59.8	0.261	967	17.2	4.36e-07	16.2
(l)	138	454	316	1.22	1.34	43.5	0.574	127	2820	$< 10^{-16}$	2.91

Table 5.2: Summary of pig results shown in Fig. 5.7. τ_1 and τ_2 are timescales in seconds. a_1, a_2, and a_3 are areas nondimesionalised by the square of the radius at the start time. The examples where the duration is greater than 250s are highlighted yellow.

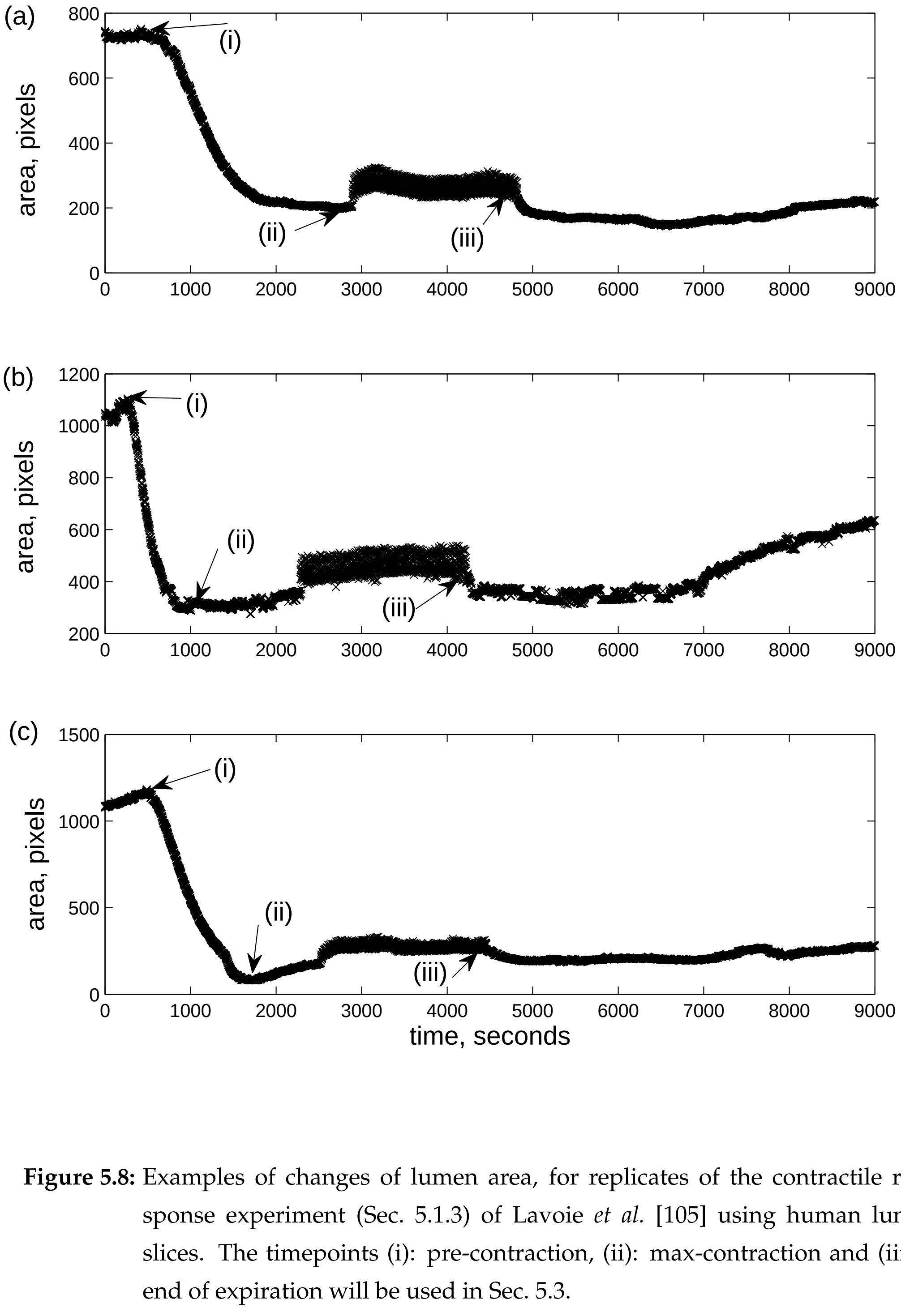

Figure 5.8: Examples of changes of lumen area, for replicates of the contractile response experiment (Sec. 5.1.3) of Lavoie *et al.* [105] using human lung slices. The timepoints (i): pre-contraction, (ii): max-contraction and (iii): end of expiration will be used in Sec. 5.3.

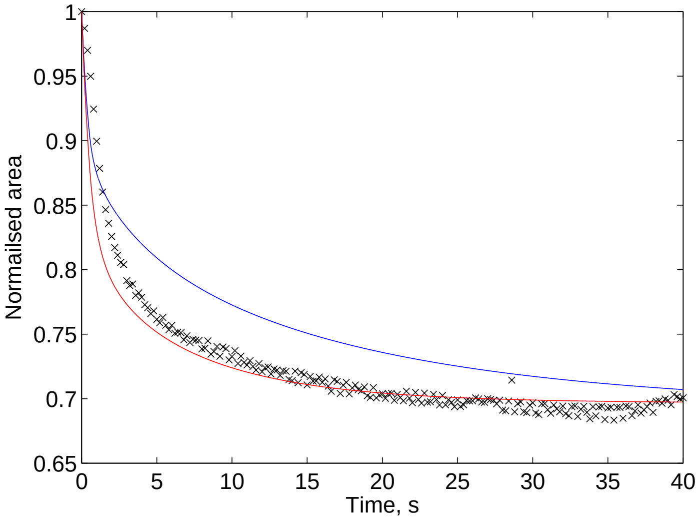

Figure 5.9: Comparisons are made between the lumen area (crosses) from Fig. 5.5 (a) and the model prediction (using Sec. 4.2). $\chi = 0.21$, $\tau_a = 0$, $R_p = 10$, with $r_p = R_p$ and rates given by Table. 4.2. Predictions when $\beta = 3.5$ (blue) or when g_1, g_2 and g_3 are multiplied by 10 and $\beta = 5$ (red).

Initially the airway is assumed to be unstressed and using the rate parameters of HHM, as given in Table. 4.2, a simulation of the contracting airway is run.

A plot showing the area from the image analysis (crosses) and the model prediction (blue) are shown in Fig. 5.9. The curve shows evidence of multiple timescales. However, the initial contraction is too rapid, and then for most of the time the predicted area is greater than that of the data. It has been suggested that it is more appropriate to increase the rate of detachment of latch bridges tenfold [173]. Assuming this, we now choose $\beta = 5$, so that at steady state, the percentage contraction is again roughly that of the maximum contraction of the lung slice experiment. This provides a closer fit (red) although the initial contraction is still too rapid. These comparisons show that the model predicts that multiple timescales are associated with the contraction. However, further analysis of the correct rate parameters is required.

The reason for the multiple timescales is now considered. The active force is related to the crossbridge distribution as recalling (2.3.17),

$$A(t;R) = \beta \int_{-\infty}^{\infty} x(n_C(x,R,t) + n_D(x,R,t))\mathrm{d}x. \tag{5.2.4}$$

Recalling (2.3.10),

$$\frac{\partial \mathbf{n}}{\partial t} - v\frac{\partial \mathbf{n}}{\partial x} = \mathrm{Q}\mathbf{n}, \tag{5.2.5}$$

the evolution of the crossbridge distribution is affected by the velocity of sliding between the filaments, v. For now we consider the simpler case when $v = 0$ and show

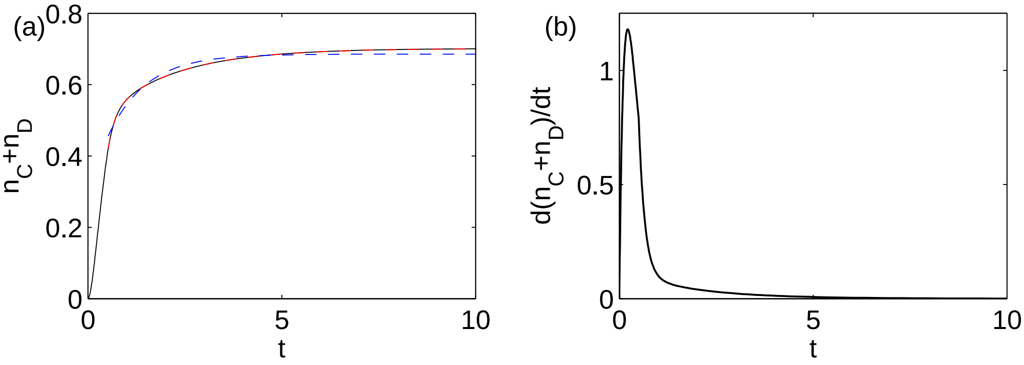

Figure 5.10: Plots of (a) $n_C + n_D$ and (b) its derivative against time. Also shown in (a) are results of fitting the latter part of the curve with one (blue) or two (red) timescales.

that in this case there is evidence of multiple timescales being associated with the evolution of the total of the attached crossbridges $n_C + n_D$. The rate constants for HHM from [116], as described in Table 4.2, are applied. There is a rapid increase in the number of of attached crossbridges, before the number levels off (Fig. 5.10 (a)). Considering the timescales involved, initially the rate of change of $n_C + n_D$ (Fig. 5.10 (b)) increases before peaking and then decreasing. This is due to the crossbridges first needing to be phosphorylated before they can attach. Exponential curves of the form given in (5.2.1) are fitted to $n_C + n_D$ after $t = 0.5$, which is thus after the step change in the value of k_1 and k_6, which could affect the timescales observed. Fig. 5.10 (a) shows that including two timescales (red), the fit is very close to the total of the attached crossbridges and better than the fit with a single timescale (blue). The ratio of the two timescales is 11.1.

Comparing Tables 5.1 and 5.2, in general the ratio of the two timescales related to the contraction of the airways was larger for the mouse slices than the pig slices. One possibility for the difference is that the rate parameters, associated with the crossbridge mechanics, could be species specific. By multiplying the nondimensional rate of attachment of crossbridges by 0.75 and again fitting to a function of the form (5.2.1), the ratio of the two timescales in the HHM model reduces from 11.1 to 9.7.

This shows that multiple timescales can be explained by the evolution of the distribution of the crossbridges. However, there are a number of other factors that could also have an effect. First, rather than the rates of phosphorylation having one value for the initial 5 seconds and then a lower value thereafter, the value is more time dependent. During a contraction it is also the case that $v \neq 0$ and is coupled to the tissue mechanics.

Recalling (3.1.8),

$$\begin{aligned}\llbracket \tau \rrbracket = &\log\left(\frac{r_a R_b}{r_b}\right) + \frac{(r_a^2-1)(R_b^2-1)}{2r_a^2 r_b^2} + H(r_a-1)C_1\sqrt{\frac{\pi}{C_2}}\cos^2\varphi \\ &\left(\operatorname{erfi}\left\{\sqrt{C_2}\left(r_a^2-1\right)\cos^2\varphi\right\} - \operatorname{erfi}\left\{\sqrt{C_2}\left(\frac{r_a^2-1}{R_b^2}\right)\cos^2\varphi\right\}\right) \\ &+ 2\cos^2\varphi\int_1^{R_b}\frac{A}{R}dR, \qquad (5.2.6)\end{aligned}$$

thus for a given transmural pressure, there is a nonlinear relationship between the integral, which give the contribution of the contractile force over the wall, and the lumen radius, with the airway stiffening as the airway contracts. This stiffening can affect the timescales of contraction, by reducing the speed of contraction as the airway narrows. Furthermore, in Chapter 4 the model predicted that the contraction is slower if the parenchyma is viscoelastic than if it is elastic.

5.3 Displacement analysis and strain fields

Having considered how the lumen area changes during a contraction, the focus shifts to finding the displacement field for the tissue surrounding the lumen, between two frames from a video of a lung slice experiment. We introduce two methods that provide estimates of the displacement field, which we test, and choose the one that is superior. Using the chosen method, the displacement fields formed when mouse and human lung slices contract are investigated. In particular, we consider the level of heterogeneity and how the displacement varies with distance from the lumen, and compare the findings to our model predictions.

5.3.1 Methods

In this subsection we present two methods to find an estimate of the displacement field, which we will test in the following subsection. We base our methods on the work of Farnebäck [41] and Butler *et al.* [24]. We also describe a method that enables us to consider the displacement of sets of points that radiate out from the lumen. Finally we describe how strain fields can be found from displacement fields.

5.3.1.1 Farnebäck method

We now introduce the methods used with the Farnebäck algorithm [41]. The algorithm as implemented in the opencv code cv::calcOpticalFlowFarneback[2], which calculates an estimate of the displacement vector between an initial and final image, for each of the pixels, was used. In order to make the features in each of the images more prominent, prior to using the algorithm the contrast of each image is increased. Each of the images is converted to greyscale and the range of the pixel intensities is stretched so that 1% of the pixels are saturated at the brightest value and 0.01% are saturated at the darkest value. The following MATLAB commands are used to do this: `imread`, `rgb2gray`, `stretchlim`, `imadjust` and `imwrite`. It is possible that some regions may remain, where there are not enough features and so insufficient contrast, yielding spurious displacements. Provided that in these regions the pixels are all very light or dark, thresholds can be set, beyond which the displacements are recalculated by interpolating. For any such points, the displacement is first set to `NAN` and then `griddata` in MATLAB is used, with the `v4` method, to update the displacement each of these points.

In the next few paragraphs we give an overview of the Farnebäck algorithm, following [41]. Suppose that the two images are approximated by quadratic polynomial functions that describe the intensity of the pixels at position $\mathbf{x}$. The polynomials for the first and second image have the form

$$f_1(\mathbf{x}) = \mathbf{x}^T \mathsf{A}_1 \mathbf{x} + \mathbf{b}_1^T \mathbf{x} + c_1, \tag{5.3.1}$$

$$f_2(\mathbf{x}) = \mathbf{x}^T \mathsf{A}_2 \mathbf{x} + \mathbf{b}_2^T \mathbf{x} + c_2, \tag{5.3.2}$$

where A_1, A_2 are matrices, $\mathbf{b}_1$, $\mathbf{b}_2$ are vectors and c_1, c_2 are scalars. If the two images are only different by a rigid shift, $f_1(\mathbf{x}) = f_2((\mathbf{x} - \mathbf{d}))$, where $\mathbf{d}$ is the displacement of the shift to be found. In this case

$$\mathsf{A}_2 = \mathsf{A}_1, \quad \mathbf{b}_2 = \mathbf{b}_1 - 2\mathsf{A}_1\mathbf{d}, \quad c_2 = \mathbf{d}^T \mathsf{A}_1 \mathbf{d} - \mathbf{b}_1^T \mathbf{d} + c_1, \tag{5.3.3}$$

where, assuming that A_1 is non-singular, $\mathbf{d}$ is given by

$$\mathbf{d} = -\mathsf{A}_1 \frac{\mathbf{b}_2 - \mathbf{b}_1}{2}. \tag{5.3.4}$$

In general it is more complicated than this, since the displacement is spatially dependent and will also involve rotation and stretching. Rather than finding intensity polynomial functions over the whole region, local polynomial functions are found over a small neighbourhood surrounding each of the pixels. A spatially-dependent displacement $\mathbf{d}(\mathbf{x})$ is found using the local polynomials of the two images. If however, the

---

[2] http://opencv.willowgarage.com/documentation/cpp/motion_analysis_and_object_tracking.html

displacements are large, the comparison of local polynomials in the two images may be insufficient, since the displaced point may not be located within the local neighbourhood of the initial position used to form the polynomial. In this case a false displacement will be found. The algorithm is able to overcome this problem by using *a priori* knowledge. Given an *a priori* displacement $\tilde{d}(\mathbf{x})$, a relative displacement can be found using $f_1(\mathbf{x})$ and $f_2(\tilde{\mathbf{x}})$, where $\tilde{\mathbf{x}} = \mathbf{x} + \tilde{d}(\mathbf{x})$. $\tilde{d}(\mathbf{x})$ (which is measured relative to pixel width) is rounded to the nearest integer, so that the polynomial in the second image is centred on a pixel. Now in general, $\mathsf{A}_1 \neq \mathsf{A}_2$, but introducing

$$\mathsf{A}(\mathbf{x}) = \frac{\mathsf{A}_1(\mathbf{x}) + \mathsf{A}_2(\tilde{\mathbf{x}})}{2}, \quad \Delta\mathbf{b}(\mathbf{x}) = -\frac{1}{2}(\mathbf{b}_2(\tilde{\mathbf{x}}) - \mathbf{b}_1(\mathbf{x})) + \mathsf{A}(\mathbf{x})\tilde{d}(\mathbf{x}), \tag{5.3.5}$$

the constraint for the updated displacement is

$$\mathsf{A}(x)\mathbf{d}(\mathbf{x}) = \Delta\mathbf{b}(\mathbf{x}). \tag{5.3.6}$$

In practice the displacement field that is found will be too noisy. The algorithm overcomes this by assuming that the displacement field is only slowly varying. In this case, for each pixel, it is possible to solve with an appropriate weight function $w(\Delta\mathbf{x})$ over a region Ω, which forms a square of pixels around the current pixel. This results in having to find the minimum of

$$\sum_{\Delta\mathbf{x}\in\Omega} w(\Delta\mathbf{x})\|\mathsf{A}(\mathbf{x}+\Delta\mathbf{x})\mathbf{d}(\mathbf{x}) - \mathbf{b}(\mathbf{x}+\Delta\mathbf{x})\|^2. \tag{5.3.7}$$

Increasing the size of Ω results in smoother displacement fields.

In reality an initial guess of the displacements is generally not available, in which case an iterative system can be used. The initial iterations are used to find an approximation of the displacements, with further iterations improving the approximation. If the displacement between the two frames is large, the initial size of the neighbourhood, used to fit the polynomials $f_1(\mathbf{x})$ and $f_2(\mathbf{x})$, can be increased, in order to find a rough but reasonable displacement estimation. This displacement can then be used as the *a priori* displacement, which can be improved in two ways. Further iterations can be carried out with the same neighbourhood size, or in order to find more of the local features of the displacement field, the size of the neighbourhood of the pixels used to find the polynomials can be reduced.

When implementing the opencv code, unless otherwise stated we use three sizes of square neighbourhoods to form the pixel intensity polynomials. For each subsequent square size we halve the length of sides and iterate three times for each size. Using the suggested values in the opencv documentation, we use a final side length of 5 pixels and set the standard deviation of the Gaussian, used to smooth derivatives in order to form the polynomials $f_1(\mathbf{x})$ and $f_2(\mathbf{x})$, as 1.1 pixels. We find that introducing additional larger squares does not improve the results.

5.3.1.2 Butler method

The algorithm of Butler *et al.* [24] was developed to track fluorescent beads on a contracting gel, estimating a sparse displacement field between two images. We adapt this algorithm to track features of the lung slice. In comparison to the fluorescent beads, since the lung slices are lit from behind, the brightest areas are regions where there is no tissue. Prior to using the algorithm, we take the complement of the original images, so that the tissue is light and the background is dark. For the rest of this subsection we give an overview of the code of Butler *et al.* [24].

There are a number of similarities between the Butler *et al.* [24] and Farnebäck [41] algorithms. Functions describing the intensities of squares of pixels in the two images are compared to find the shift in the second image that yields the best match. To overcome issues with large displacements, larger regions of pixels are first compared before reducing the number of pixels that are compared to acquire more of the local subtleties.

The algorithm of Butler *et al.* [24] consists of splitting the two images into a number of squares. Cross-correlation is used to compare a square in the first image to the corresponding square in the second image and find the coordinates of the shift of the second square so that the two squares have the highest correspondence. Functions $f(x, y)$, for a square of pixels in the first image, and $g(x, y)$, for the corresponding square of pixels in the second image, describe the pixel intensities for each of the coordinates (x, y). By definition [16, 180] the cross-correlation of the two functions is

$$(f \star g)(x, y) \equiv \sum_{u,v=-\infty}^{\infty} f^*(u, v) g(u + x, v + y), \tag{5.3.8}$$

where f^* is the complex conjugate of the function f. Since the intensity is a real value, the complex conjugate is equal to the original value. The largest value of (5.3.8) indicates the best correspondence. Taking Fourier transforms of each side of (5.3.8) yields

$$\mathscr{F}(f \star g) = \overline{\mathcal{F}}\mathcal{G}, \tag{5.3.9}$$

where $\overline{\mathcal{F}}$ is the complex conjugate of the Fourier transform of the function f and $\mathcal{G}$ is the Fourier transform of the function g. Due to the possibility of light intensity changes between the two images, the Fourier transforms of the two images can be normalised. They are normalised by dividing the two functions by the maximum value of the correlation of the whole image with itself. The fast Fourier transform of a square of pixels

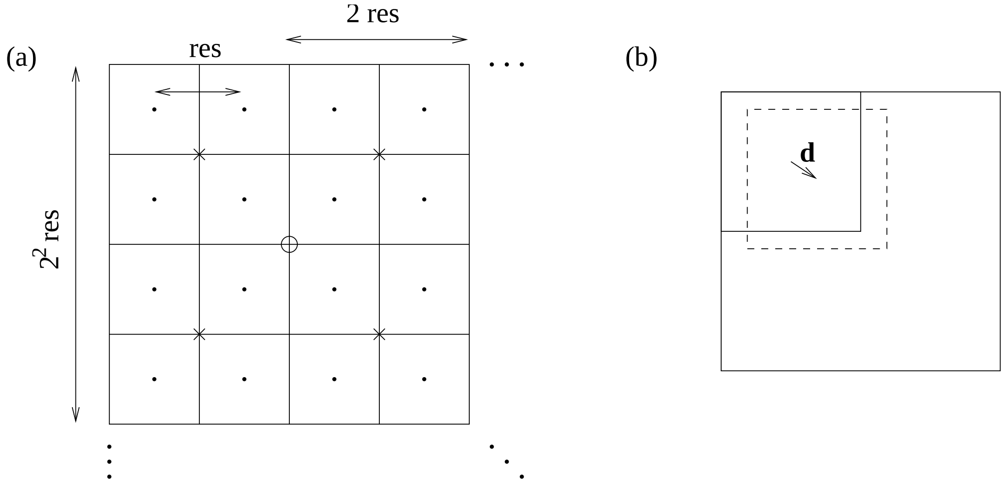

Figure 5.11: (a) Each of the two images are split up into squares. Once a good approximation of the displacement has been found, each of the squares is split into four smaller squares. The smaller squares of pixels are then used to carry out the cross-correlation to fine-tune the displacement. This is repeated until the distance between the mid points of adjacent squares equals the required resolution (res). (b) Having found an approximation for the displacement, this displacement is used to alter the coordinates of the square in the second image. Cross-correlation can then be repeated to fine-tune the displacement.

can be calculated using the MATLAB function `fft2(x)`, the complex conjugate, using `conj(x)` and the inverse fast Fourier transform, using `ifft2(x)`.

Due to the possibility of large displacements, the algorithm includes a number of iterations over squares of reducing size. An initial size, whose choice is limited by the dimensions of the image, is chosen to find a rough estimate of the displacement field, which can be used to select the location of the squares in the second image. Having found a reasonable estimate of the displacement, the width of the square is halved (Fig. 5.11 (a)) and the displacements are fine tuned. This is repeated until the size of the squares matches the resolution required. For each size of square, a number of steps are carried out. Having split up the image into squares, for each of the squares the normalised cross-correlation with the corresponding square in the second image is found. The maximum correlation gives the displacement required of the second square. The square in the second image is shifted by this current estimation of the displacement (Fig. 5.11 (b)), and the cross-correlation step is repeated in order to fine tune the displacement. These two steps are repeated until there is no additional displacement or a maximum number of steps have been taken.

After the final iteration with a given square size, a number of checks are carried out. If for any of the points any of the following do not hold, the point is declared as being unreliable and the displacement at that point is set to `NAN`:

- the latest change in the displacement was not zero, indicating the squares are not best aligned;
- the latest change in the displacement in the x or y direction is greater than half of the current size of the squares, indicating too much displacement at this level;
- the maximum pixel intensity is below some minimum value, indicating that the square consisted of data for the background but not the tissue;
- the maximum correlation is below a threshold.

In order to improve the displacement by comparing smaller squares, every square is split into four smaller squares and the new coordinates of the centre of the squares in the first image are calculated. Estimates of the displacements at each of these points are found by fitting a smooth surface to the old accepted displacements. The estimates of the displacements are used to choose the starting positions of the squares in the second image. Following the final level, a surface is fitted to approximate for points where the displacement was rejected.

5.3.1.3 Finding displacements for points along normal vectors

An alternative to finding the displacement field is to find the displacement at selected points. By selecting points along a normal vector to the lumen, it is easy to show how the displacement changes with radius. By doing likewise at various points around the lumen the displacement-radius relationship at each can be compared. We split the airway into eight sections, within each of which we select points along normal vectors that begin at seven points on the lumen boundary. We solve to find displacements in the tangential and normal directions, averaging the predictions within each of the sections for each radial position, to try to remove any small errors. As it is expected that there will be little variation in each of the sections, checks can be made that the standard deviation is small.

We begin by fitting an ellipse to the lumen at the start of the contraction, using the techniques described in section 5.2.1. In parametric form an ellipse centred at (x_0, y_0), with major and minor axis of length $2a$ and $2b$ and angle α between the x axis and the major axis, has coordinates

$$x = x_0 + a\cos t\cos\alpha - b\sin t\sin\alpha, \tag{5.3.10a}$$

$$y = y_0 + a\cos t\sin\alpha + b\sin t\cos\alpha, \tag{5.3.10b}$$

where $t \in [0, 2\pi)$ is the parametric parameter. The unit vectors in the tangential and normal directions are

$$\mathbf{t} = \frac{(-a\sin t\cos\alpha - b\cos t\sin\alpha, -a\sin t\sin\alpha + b\cos t\cos\alpha)}{\sqrt{a^2\sin^2 t + b^2\cos^2 t}}, \tag{5.3.11a}$$

$$\mathbf{n} = \frac{(-a\sin t\sin\alpha + b\cos t\cos\alpha, a\sin t\cos\alpha + b\cos t\sin\alpha)}{\sqrt{a^2\sin^2 t + b^2\cos^2 t}}. \tag{5.3.11b}$$

We now explain how the points are chosen. Eight groups of seven points are chosen on the ellipse with the coordinates

$$(x_e, y_e) = (x(t), y(t)), \quad t = \alpha + m\pi/4 + n\pi/180, \tag{5.3.12}$$

with $m = 0, 1, .., 7$ and $n = -3, -2, .., 3$. If the ellipse was a perfect fit to the lumen each of the points would be located at the lumen boundary. In practice the lumen is not so regular, so the choice of points given in (5.3.12) may need to be slightly altered. Where required, we slightly inflate or deflate the ellipse, while fixing the ratio of a and b, in order to select a point on the boundary. For each of the new points we find the normal to the lumen and select further points spaced by k pixels in the direction of the normal. This yields the points

$$(x, y) = (x_e, y_e) + \mathbf{n}(t)ks, \quad s = 0, 1, ... \tag{5.3.13}$$

An illustration of how one line of points are chosen and an example of the points chosen is shown in Fig. 5.12. Since in general the coordinates are not integer values, bilinear interpolation of the four nearest pixels is used to find the displacement. The radial and azimuthal components of the displacements are found by taking the dot product of the displacement with the unit normal and tangent vectors.

5.3.1.4 From displacement fields to strain fields

An alternative to plotting displacement fields is to plot strain fields. An advantage of strains over displacements is that, if there is a rigid displacement of a lung slice that is not related to the contraction of the airway, while the displacement field will be affected, the strain field will not. Below we describe the theory that enables the strain field to be found from the displacement field. In the results section (Sec. 5.3.3), plots

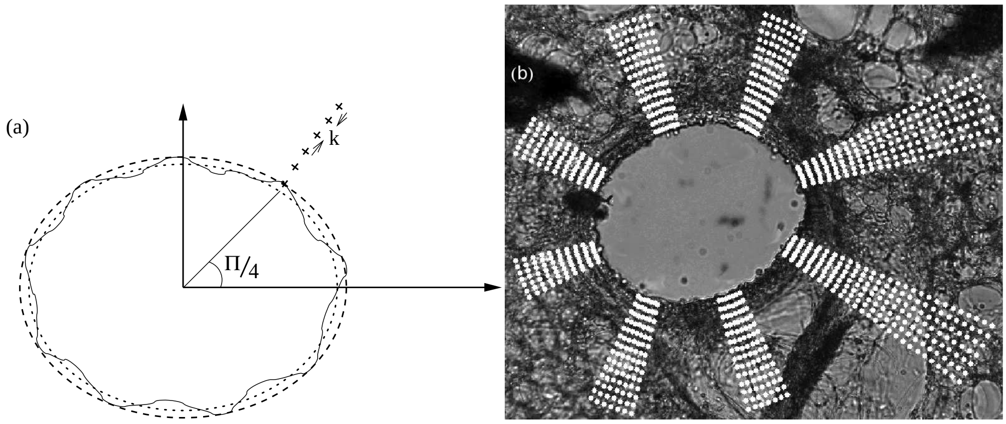

Figure 5.12: (a) An ellipse (dotted line) is fitted to the edge of the lumen (solid line). However, a particular point on the lumen boundary may not lay on this ellipse, in which case we inflate (or deflate) the ellipse accordingly so that the point lies on the adjusted ellipse (dashed line). The normal to the adjusted ellipse is found and points are chosen at intervals of *k* pixels. (b) An example of the initial set of points (white dots) superimposed on an image of a lung slice.

are shown of the strain fields for the contracting lung slice to see if they give more information than the plots of the displacement fields.

We assume that displacements between two frames are known, where the coordinates have the form (X, Y) in the first image and (x, y) in the second image. The deformation gradient tensor is given by

$$\mathsf{F} = \begin{pmatrix} \frac{\partial x}{\partial X} & \frac{\partial x}{\partial Y} \\ \frac{\partial y}{\partial X} & \frac{\partial y}{\partial Y} \end{pmatrix}. \tag{5.3.14}$$

The Lagrangian strain tensor is defined as $\mathsf{E} \equiv (\mathsf{C} - \mathsf{I})/2$, where $\mathsf{C} \equiv \mathsf{F}^T\mathsf{F}$ is the right Cauchy-Green deformation tensor. Thus,

$$\mathsf{E} = \begin{pmatrix} E_{11} & E_{12} \\ E_{12} & E_{22} \end{pmatrix} = \begin{pmatrix} (\frac{\partial x}{\partial X})^2 + (\frac{\partial y}{\partial X})^2 - 1 & \frac{\partial x}{\partial X}\frac{\partial x}{\partial Y} + \frac{\partial y}{\partial X}\frac{\partial y}{\partial Y} \\ \frac{\partial x}{\partial X}\frac{\partial x}{\partial Y} + \frac{\partial y}{\partial X}\frac{\partial y}{\partial Y} & (\frac{\partial x}{\partial Y})^2 + (\frac{\partial y}{\partial Y})^2 - 1 \end{pmatrix} /2. \tag{5.3.15}$$

One way to visualise the strain is to find the eigenvalues and eigenvectors of the tensor in (5.3.15) so that the magnitude and direction of the principal strains can be plotted. The characteristic polynomial for the tensor is

$$\lambda^2 - (E_{11} + E_{22})\lambda + (E_{11}E_{22} - E_{12}^2) = 0, \tag{5.3.16}$$

from which the strain invariants $I_1 = E_{11} + E_{22}$ and $I_2 = E_{11}E_{22} - E_{12}^2$ are found. Solving the characteristic polynomial yields the eigenvalues in terms of the invariants,

$$\lambda^{\pm} = \frac{I_1 \pm \sqrt{I_1^2 - 4I_2}}{2}. \tag{5.3.17}$$

The eigenvalues depend on a combination of the invariants and so are independent of the coordinate system used. Now

$$I_1^2 - 4I_2 = (E_{11} - E_{22})^2 + 4E_{12}^2 \geq 0, \tag{5.3.18}$$

so in general there are two real eigenvalues. The only exception is when the tensor is symmetric and the diagonal elements are equal, for which there is a repeated eigenvalue.

To find the eigenvectors the following equation must be solved:

$$\begin{pmatrix} E_{11} - \lambda^{\pm} & E_{12} \\ E_{12} & E_{22} - \lambda^{\pm} \end{pmatrix} \begin{pmatrix} x \\ y \end{pmatrix} = \begin{pmatrix} 0 \\ 0 \end{pmatrix}. \tag{5.3.19}$$

From the first row, the unit eigenvectors satisfy

$$\frac{(E_{12}, \lambda^{\pm} - E_{11})}{\sqrt{E_{12}^2 + (\lambda^{\pm} - E_{11})^2}}.$$

The second row provides an equivalent relationship. The eigenvalue could equally point in the opposite direction. We assume that for a single contracted airway, a component of the major principal strain will point towards, rather than away from, the lumen.

5.3.2 Testing the codes

We have presented two different approaches for estimation of the displacements from one image to another. In this subsection we present two tests to find out how well they perform. The first test is used to see how well the tissue, in general, is tracked, while the second test is used to see how well the lumen radius is tracked.

- Test 1: A single lung slice image is taken and is cropped in two different ways, so one is a uniform rigid shift of the other. The coordinates of the rigid shift in pixels are (5,7) for the mouse example and (3,4) for the human example. A smaller shift is chosen for the human slice since the lumen takes up less of the image and the displacements are in general smaller in terms of pixel number. Each algorithm is used to predict the displacement from one of the images to the other, which are subtracted from the imposed displacement to yield an error. Vectors showing the size of the errors are superimposed on to the first of the images, to show where errors occur. Near the edge of the image features may be in one of the images but not the other, due to the nature of the cropping. The errors are thus set to zero near the edge of the image and within the lumen, where there is no tissue.

- Test 2: Each of the algorithms is used to estimate the displacement field between the frame just before contraction starts and the frame of maximum contraction. Using the techniques described in the section 5.2.1 the edge of the lumen in the two frames is found and for the points within the lumen the displacement is set to zero. By plotting the lumen outline for each of the frames and the displacement vectors, it is possible to establish whether or not each of the algorithms provide a good approximation of the displacement at the lumen boundary.

We now proceed to use these tests, firstly on frames from experiments that use lung slices from mice and then from those using lung slices from humans. We do not consider lung slices from pigs, since due to the added thickness of the slices the tissue is very dark with insufficient contrast.

5.3.2.1 Testing for the mouse slices

Firstly, test 1 is applied to the Farnebäck method (Sec. 5.3.1.1). The importance of including the steps to increase the contrast in the images prior to estimating the displacement field and to interpolate over regions where the contrast remains small is shown in Fig. 5.13. The errors given by the displacement predicted by the algorithm minus the imposed displacement are plotted at every eight pixels, leaving a gap of twelve pixels around the edge of the image to account for the image cropping. If the contrast is not altered, but the original images are used, there is generally good agreement with small errors, however, there are some regions with large errors (a). The errors are observed in regions where the pixels are all dark, with little variation. Including the step to alter the contrast, so that the full range of available pixel intensities is used, there are only a couple of small (black) regions with large errors (b). If the interpolation step is included these errors are greatly reduced (c). In this example this algorithm is able to accurately predict the displacement across the slice.

Secondly, test 1 is applied to the Butler method (Sec. 5.3.1.1). The error, representing the difference between the estimated value of the displacement and the prescribed rigid shift, is shown in Fig. 5.14 for two cases. Using the Butler method, initially the image is split into squares of width 32 pixels, with iterations being carried out until the squares have a width of 8 pixels. In this case there are some errors, especially around the edge of the black object in the top left hand corner of the image (a). Doubling the initial width of the squares, greatly reduces many, but not all, of these errors (b). Increasing the width of the initial squares further may lead to further reductions in the errors. However, since the dimensions of the image analysed must be multiples of the width

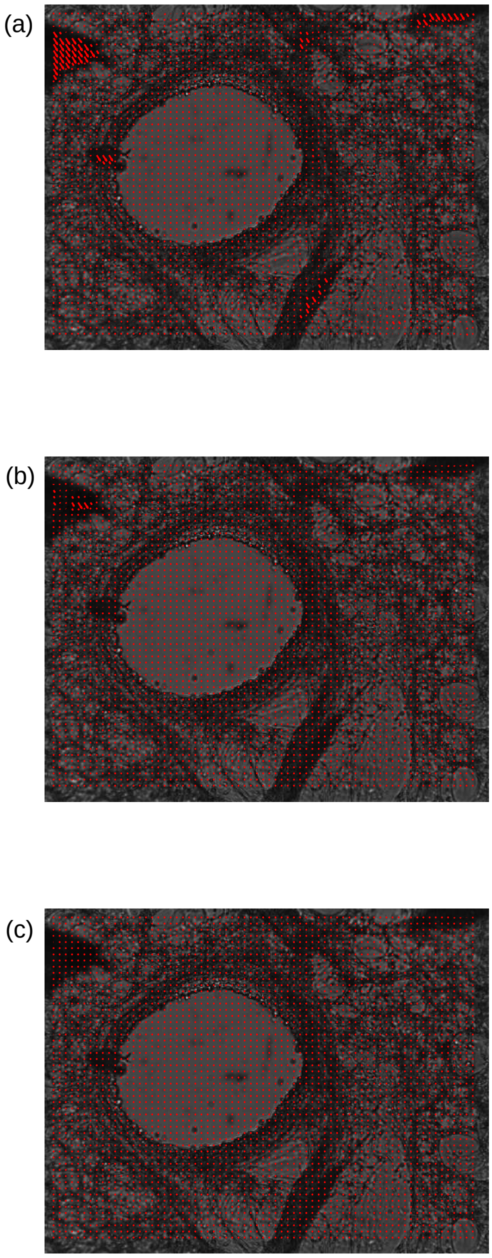

Figure 5.13: Plots of the errors (red arrows), representing the displacement predicted by the Farnebäck method (Sec. 5.3.1.1) minus the imposed displacement, when using test 1 on a mouse slice. The same scale is used for the arrows in each of the images. In (a) neither of the steps to alter the contrast of the images or to interpolate over regions where the contrast remains small are included. In (b) the step to alter the contrast of the images is included. In (c) both the steps to alter the contrast of the images and to interpolate over regions where the contrast remains small are included.

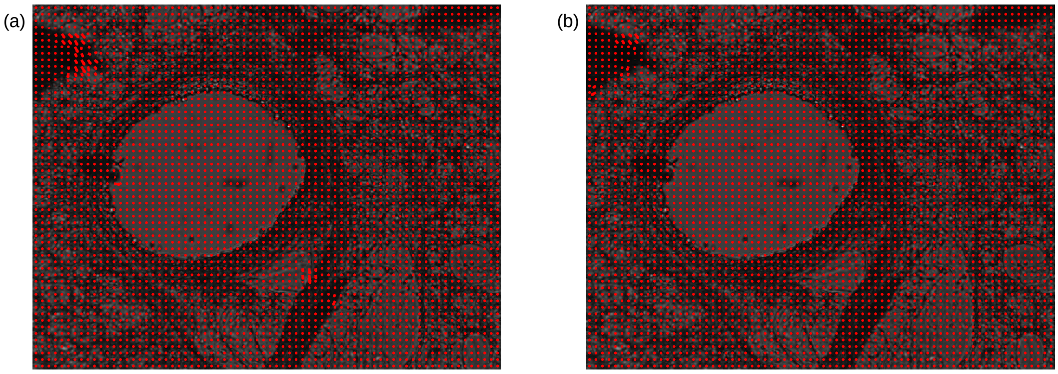

Figure 5.14: Plots of the errors (red arrows), representing the displacement predicted by the Butler method (Sec. 5.3.1.2) minus the imposed displacement, when using test 1 on a mouse slice. The same scale is used for the arrows in the two images. Initially the image is split into squares of width (a) 32 pixels or (b) 64 pixels. In both cases the final resolution is 8 pixels.

of the initial square size, this limits the values that can be chosen.

Thirdly, test 2 is applied to an example mouse slice when using the two algorithms. The lumen edges pre- and post-contraction and the estimated displacement vectors are shown in Fig. 5.15. Comparing the contour plots of the magnitude of the estimated displacements in (b, d), in general the two methods predict similar sized displacements. However, there are some notable differences, especially at the lower left-hand section of the lumen boundary. In (a, c) the arrows, indicating the predicted displacements, should point from the outer to the inner red line, which indicate the lumen boundary pre- and post-contraction. Using the Farnebäck method (a), the arrows provide a good estimate, whereas with the Butler method the arrows do not point from the outer to the inner line, indicating errors (c). If the initial size of the squares used in the Butler method is increased, these problems are not resolved (not shown). In this instance it can therefore be concluded that the Farnebäck method is superior.

5.3.2.2 Testing for the human slices

We now concentrate on the human lung slices and again test the two methods. There are a couple of ways in which these slices are different from those from mice; the fraction of the image taken up by the lumen is smaller and there are more gaps in the tissue surrounding the lumen.

Firstly, test 1 is applied to the Farnebäck method (Sec. 5.3.1.1). In Fig. 5.16 the error, given by the displacement predicted by the algorithm minus the imposed displacement, is shown. An interpolation step was included into the Farnebäck method, to

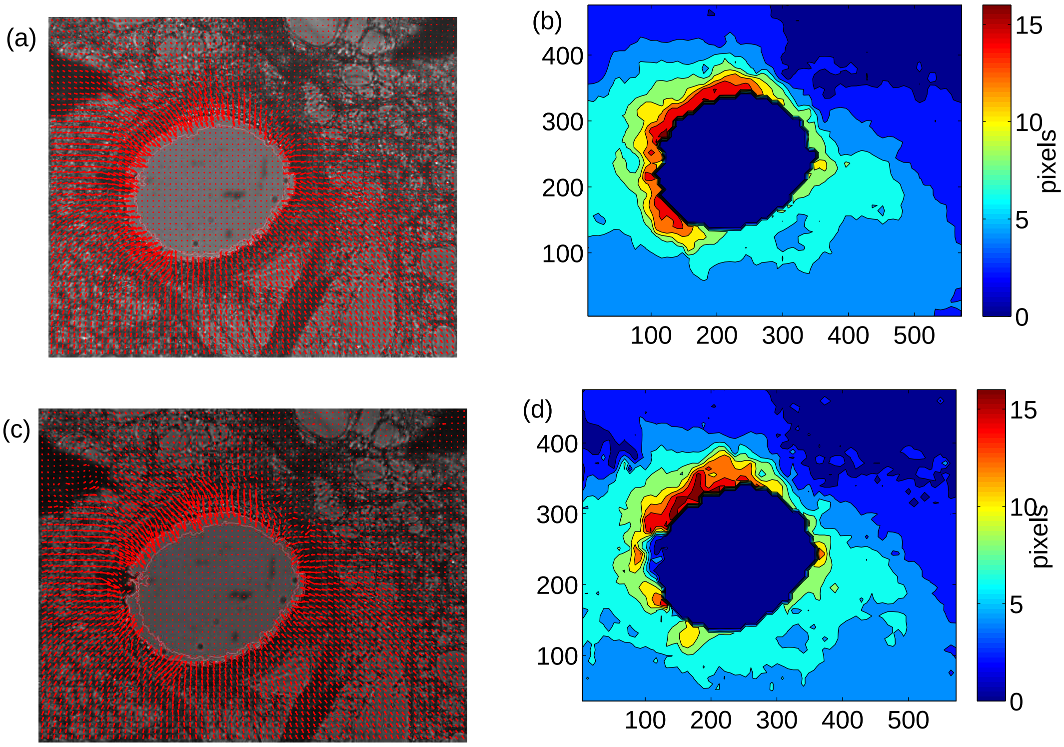

Figure 5.15: Test 2 with mouse slices. Plots of (a, c) the estimated displacement vectors (red arrows) and the outline of the lumen pre- and post-contraction (red lines), and (b, d) the magnitude of the estimated displacements. The Farnebäck method (Sec. 5.3.1.1) is used in (a, b) and the Butler method (Sec. 5.3.1.2) is used in (c, d).

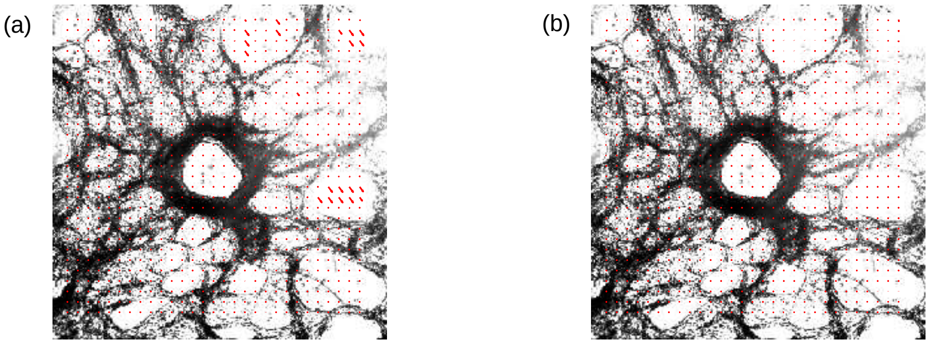

Figure 5.16: Plots of the errors (red arrows), representing the displacement predicted by the Farnebäck method (Sec. 5.3.1.1) minus the imposed displacement, when using test 1 on a human slice. The same scale is used for the arrows in the two images. Errors when the final interpolation step of the method is (a) included or (b) not included.

take account of areas where there are no features to track. In the case of the human lung slices the gaps in the parenchyma are example regions of this. If the interpolation step is not included then errors are shown in the gaps (a), while including the interpolation step, the errors are greatly reduced (b) and the method provides a good estimate of the displacements.

Secondly, test 1 is applied to the Butler method (Sec. 5.3.1.1). The error, representing the difference between the estimated value of the displacement and the prescribed rigid shift, is shown in Fig. 5.17 for three cases. If initially the image is split into squares of width 32 pixels and iterations are carried out until there are squares of width 16 pixels, there are a few points within the airway wall where the deformation is not detected and errors are shown (a). Doubling the width of the initial square greatly reduces these errors (b). The final size of the squares can be halved to give estimates of the displacement at a finer resolution (c).

Thirdly, test 2 is applied to an example human slice using the two algorithms. The lumen edges pre- and post-contraction and the estimated displacement vectors are shown in Fig. 5.18. The estimated displacements from the Farnebäck method track the boundary well, showing small arrows near the top of the lumen where there is little change and larger arrows at the bottom where the lumen boundary moves further (a). In contrast the estimated displacements from the Butler method do not track the boundary well (b). This is particularly noticeable on the left hand side of the lumen. In the example shown the starting and final widths of the squares used are 64 and 8 pix-

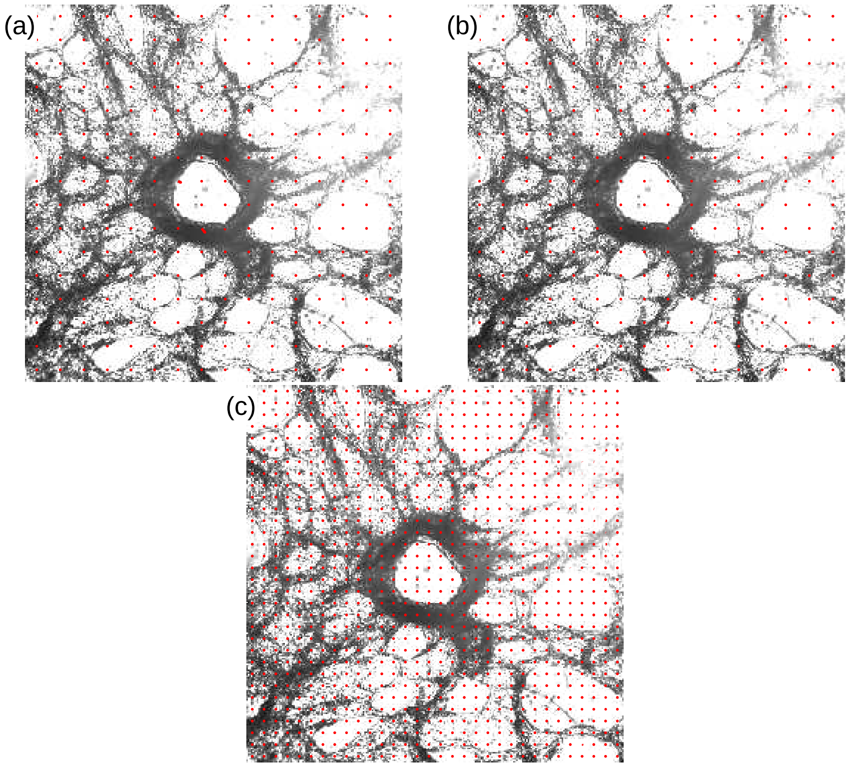

Figure 5.17: Plots of the errors (red arrows), representing the displacement predicted by the Butler method (Sec. 5.3.1.2) minus the imposed displacement, when using test 1 on a human slice. The same scale is used for the arrows in each of the images. Initially the image is split into squares of width (a) 32 pixels or (b, c) 64 pixels, with the final resolution equal to (a, b) 16 pixels or (c) 8 pixels.

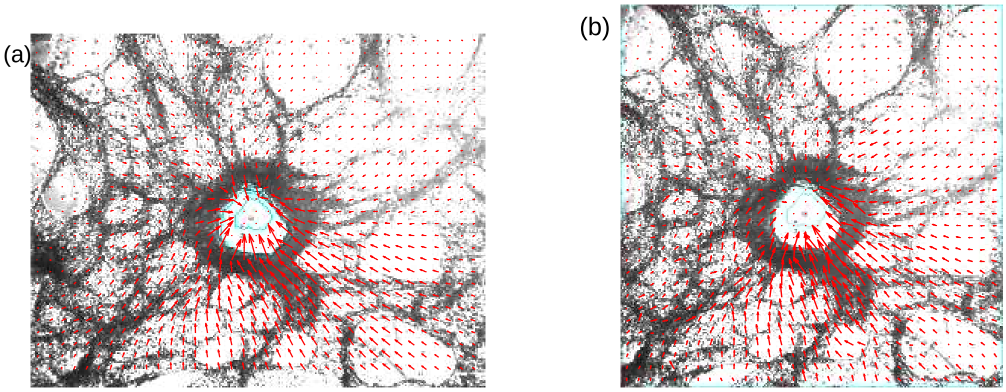

Figure 5.18: Test 2 with human slices. Plots of the estimated displacements (red arrows) when using (a) the Farnebäck method (Sec. 5.3.1.1) or (b) the Butler method (Sec. 5.3.1.2). The blue lines in the indicate the outline of the lumen pre- and post-contraction.

els. Doubling or halving the initial blocksize or increasing the final blocksize is found not to improve the tracking of the boundary (not shown).

Having carried out the two different tests on both the mouse and human slices, the Farnebäck method has proved to be superior. In particular it is better at tracking the lumen boundary. In the following results section the Farnebäck method is used to estimate the displacement field.

5.3.3 Results

In this subsection the Farnebäck method is used to consider the displacements in the tissue surrounding an airway. Firstly the displacement fields in three lung slice experiments with contracting mouse airways are considered (Fig. 5.19). For the first slice (a, b) there are much smaller displacements in the bottom-right section of the image. In this region of the image of the lung slice there is a thick black diagonal strip. This is likely to be an arteriole, that may already have collapsed affecting this region and inhibiting further contraction. Similarly, for the second slice (c, d) the displacements are smaller in the bottom half of the slice. Again there is a large dark region that could be affecting the ability of the tissue to contract here. An interesting feature of this slice is that there are two airways present. In the top half of the slice the displacements are largely symmetric. With the third slice (e, f) there are some issues in the region above the lumen. Here there is very little contrast between the tissue and the lumen itself. These issues have been improved a little by increasing the number of iterations carried out for each successive size of neighbourhood, used to fit a polynomial function to the pixel intensities, from three to five. While there are some regions where there are reduced displacements or where the displacements are not picked up, in general the largest displacements in each example are seen at the lumen boundary. With distance from the lumen, the magnitude of the displacement initially rapidly reduces before starting to level off.

In Sec. 5.3.1.4 the theory required to find Lagrange strain tensor from the displacement field was presented. The size and direction of the principal strains can be found by finding eigenvalues and vectors. Using this theory, plots of the major and minor strains are shown in Fig. 5.20 for the first two examples shown in Fig. 5.19. The white lines show that the major principal strain is predominantly in the radial direction. Except for a few small regions, the major principal strains are positive indicating radial stretching. The minor principal strains are perpendicular to those of the major principal strains so are predominantly in the circumferential direction. Except for a few small regions, the minor principal strains are negative indicating compression. For the slice with two airways (c, d), there is a region between the two airways where the major and minor eigenvalues are quite large. This is due to this region experiencing biaxial tension as both of the airways contract. A disadvantage of these plots is that they are quite noisy, since any noise from the displacement field will be emphasised when finite difference schemes are used to find the strain.

In Sec. 5.3.1.3 we showed how, rather than simply finding the displacement field, we are able to find the displacement at selected points. By selecting points along spokes radiating out of the lumen, we are able to give further consideration to the heterogeneity of the airway and can find the size of the components of the displacement in the radial and circumferential directions. Slice (a) from Fig. 5.19 is used and the initial points are shown in Fig. 5.21 (a). For the initial time point, the time just prior to the start of contraction is used. Four further points are chosen (b), for which the slice experiences increasing amounts of contraction, and the displacement, relative to the frame at the initial time point, is found at each of these times. Taking each section in turn, the average radial component of the displacement is plotted for each of the radial positions and time points (c-j). Within each of the sections there is little variation, as shown by the small error bars. Considering the shape of the radius-displacement curves, the largest displacement is generally seen at the lumen boundary ($R = 1$). For a number of the sections, close to the lumen the gradient of the curves is quite steep, before levelling off as R increases. There are also similar shapes at the four time points. Comparing the different regions, however, there is significant heterogeneity.

The extent of heterogeneity in the tissue surrounding an airway can be further investi-

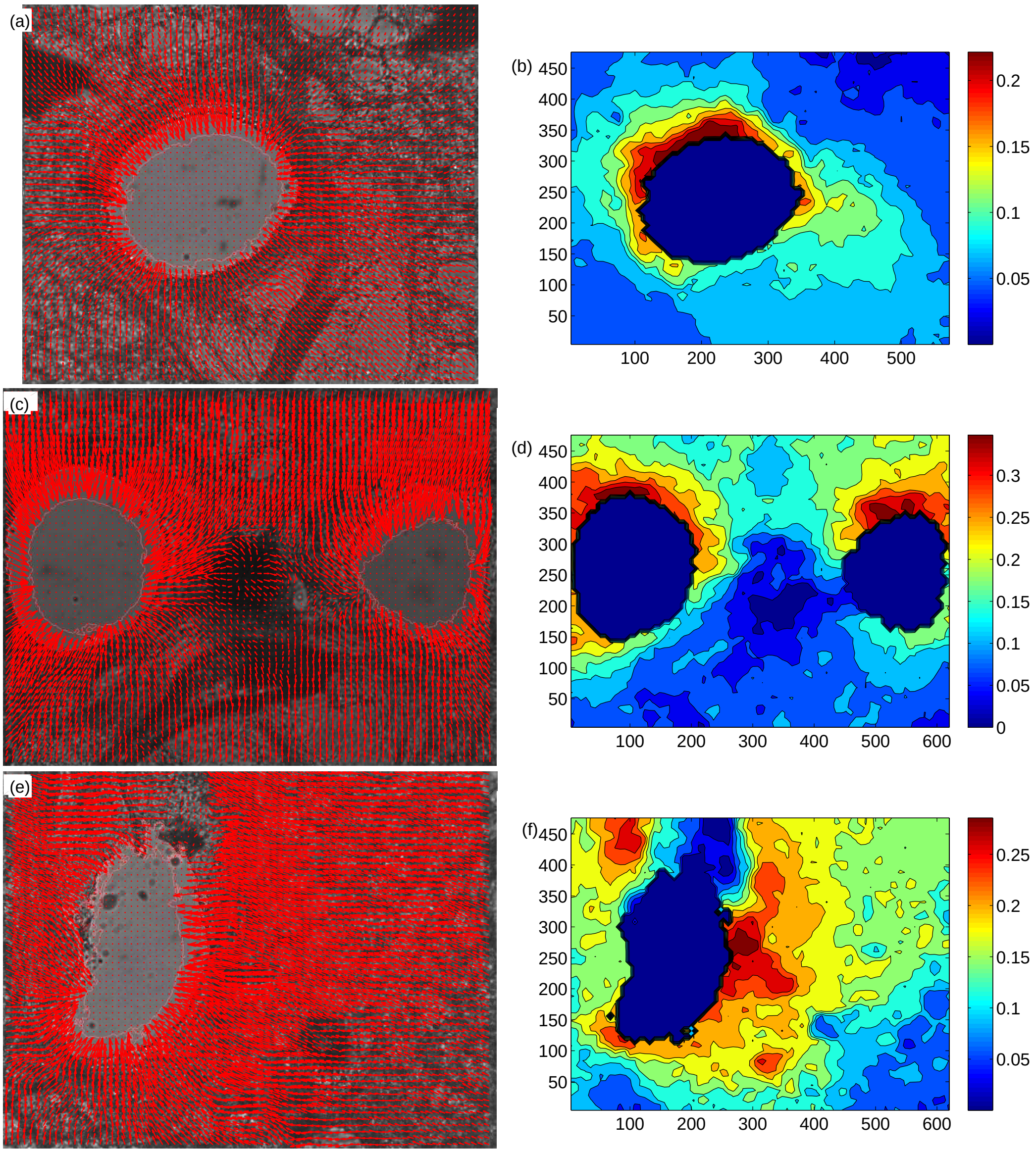

Figure 5.19: Three examples of the displacement fields in contracting mouse lung-slices. Plots of (a, c, e) the estimated displacement vectors and the lumen boundary pre- and post-contraction and (b, d, f) the corresponding displacement magnitudes. (The magnitudes have been normalised by dividing through by the average radius of the lumen.) The initial and final time points are labelled (i) and (ii) in Fig. 5.5, with (a, b), (c, d) and (e, f) showing respectively the airways labelled (a), (b, c) and (d) in Fig. 5.5.

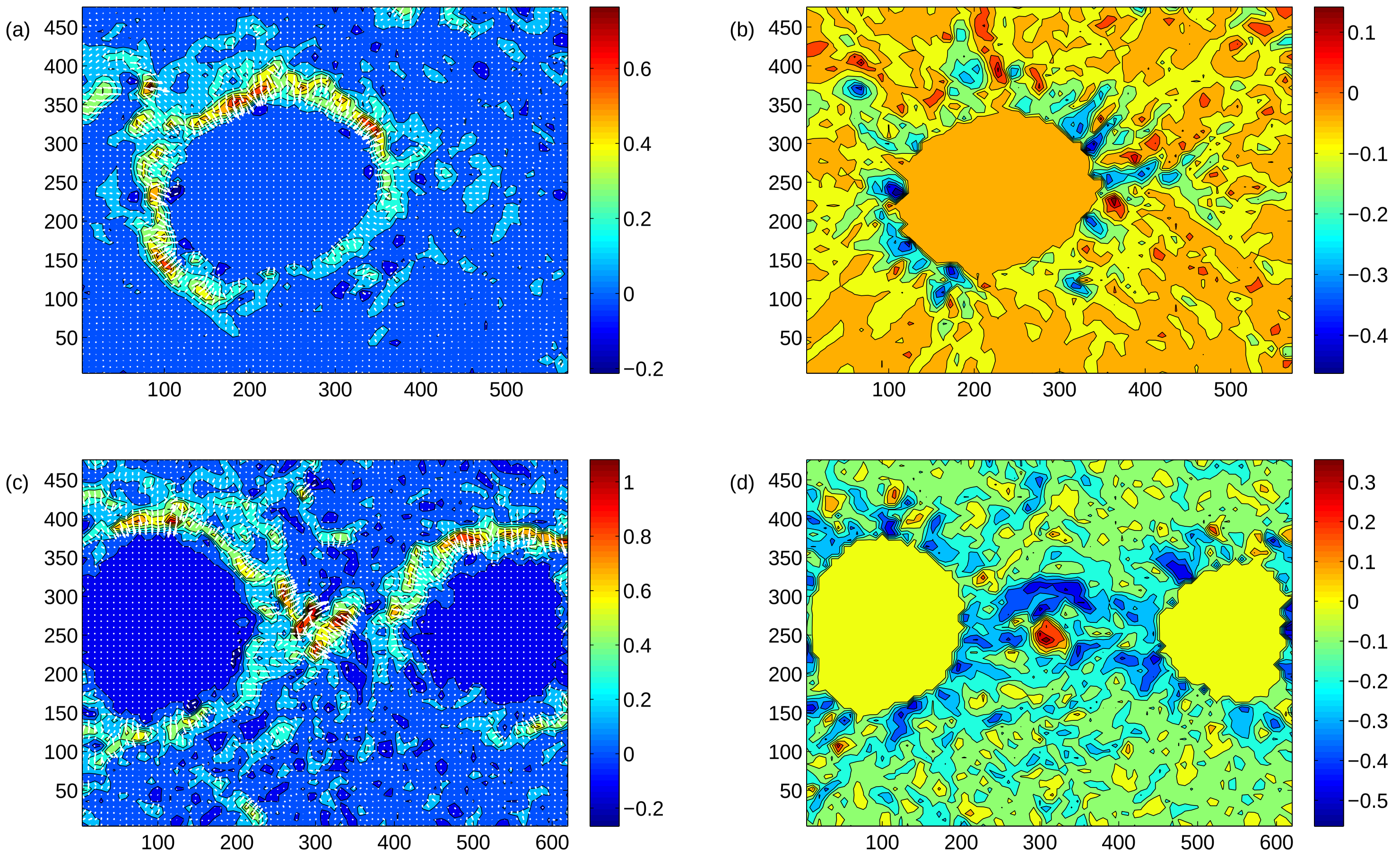

Figure 5.20: Plots of (a, c) the major eigenvalues of the Lagrange strain tensor (with arrows showing direction of eigenvectors) and (b, d) the minor eigenvalues (vectors are perpendicular to those of the major eigenvectors). These strains in (a, c) and (b, d) correspond respectively to the airways shown in (a, c) and (b, d) in Fig. 5.19.

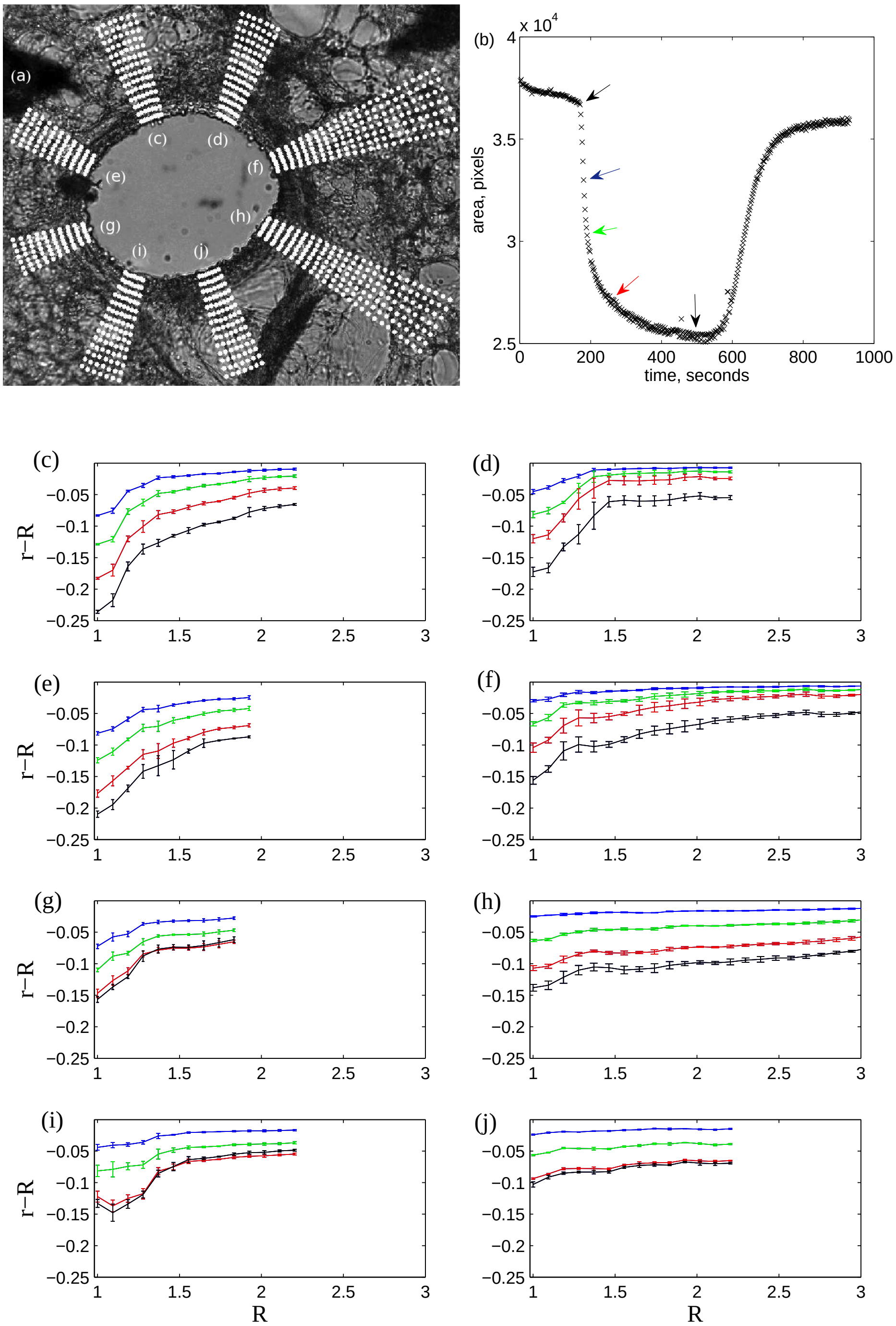

Figure 5.21: (a) The initial location of the points in eight regions of the lung slice. (b) Arrows showing the frame, just prior to contraction (used as the initial frame) and frames at four further time points. Also plots of (c-j) the average radial displacements and the standard deviation, for points with initial distance R from the lumen, for each of the regions and time points. (Lengths have been nondimensionalised by the average initial lumen radius).

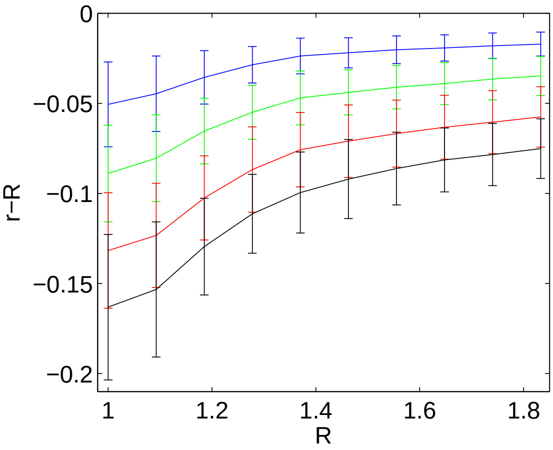

Figure 5.22: Plot showing the average radial displacements and standard deviation when averaging over all the spokes in Fig. 5.21.

gated, if instead of averaging within each of the sections separately, an average is taken over all of the sections together. The resulting averages of the radial components of the displacement are shown in Fig. 5.22. Again on average the largest displacements are found at the lumen. Now there are large error bars indicating a lot of variation in the radial displacements, whereas when averaging within each of the sections individually the error bars were small (Fig. 5.21).

Having considered the component of the displacement in the radial direction, the component in the circumferential direction is considered. Averaging within each of the sections, the standard deviations are generally very small (Fig. 5.23). In comparison to the results for the radial component, the displacements are much smaller and do not necessarily increase with time. Comparing the distributions of the displacement in the different sections, there is no one fixed shape. At some points the displacement is in the positive direction, while at other points it is in the negative direction. This can be explained by the fact that the shape of the airway and the distribution of the smooth muscle is non-axisymmetric.

Having considered the displacement fields for various mouse lung slices, we consider some examples for human lung slices. In particular we use the lung slice experiments of Lavoie *et al.* [105], for which the lumen-area timecourses were shown in Fig. 5.8. As described in Sec. 5.1.3, the experiment consisted of ten minutes for the airway to contract following the addition of MCh, ten minutes where tidal oscillations were applied to the parenchyma and ten further minutes with no oscillations. Three timepoints were indicated in Fig. 5.8, that were situated (i) just prior to contraction, (ii) by the maximum contaction and (iii) following the application of oscillations in the parenchymal strain.

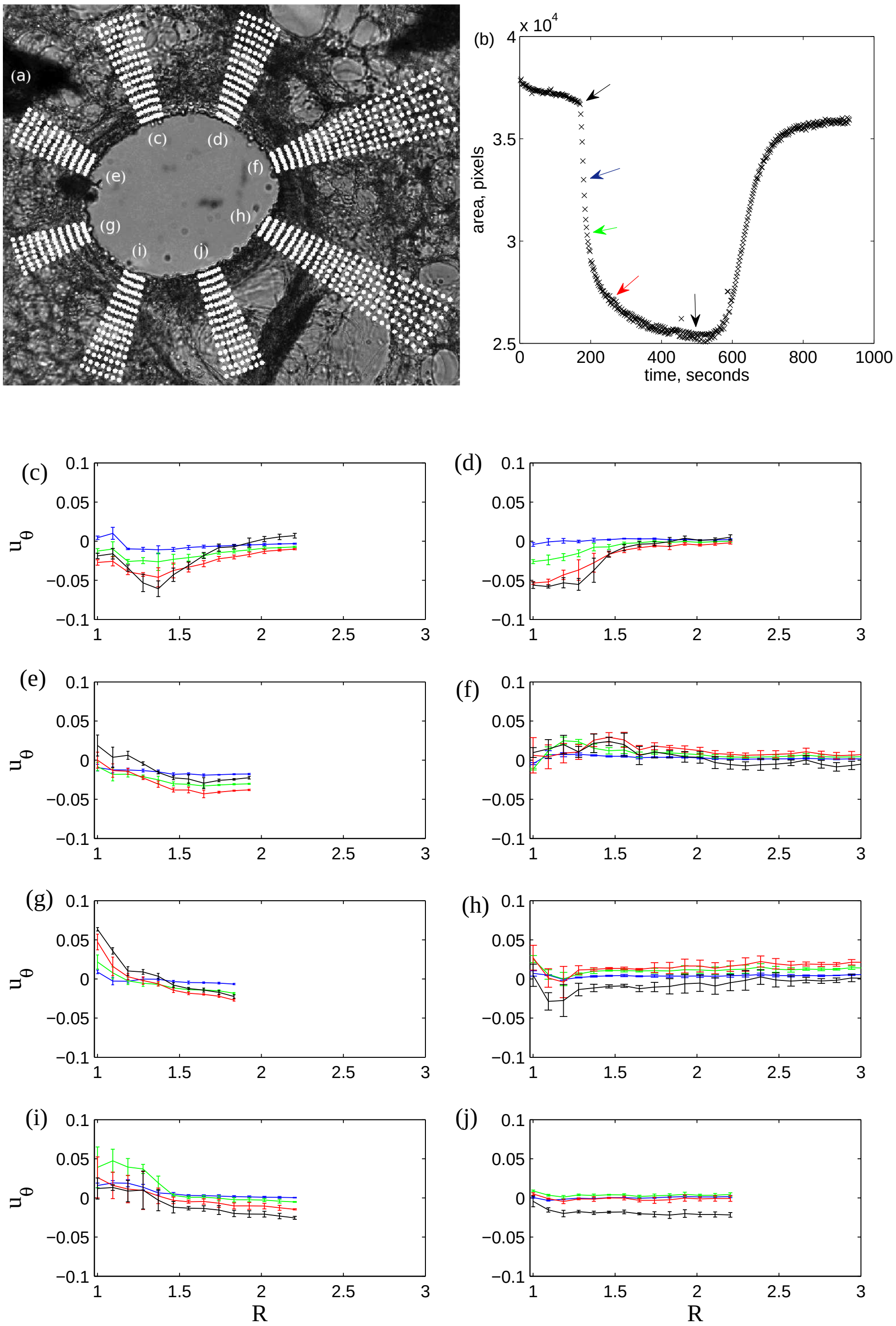

Figure 5.23: (a, b) as in Fig. 5.21. Also plots of (c-j) the average circumferential displacements and the standard deviation, for points with initial distance R from the lumen, for each of the regions and time points. (Lengths have been nondimensionalised by the average initial lumen radius).

Results will now be shown for displacements from (i) to (ii) and then from (i) to (iii).

Plots showing the displacements from (i) prior to contraction to (ii) maximal contraction are shown in Fig. 5.24. Again there is strong evidence of heterogeneity. Where there is more tissue, rather than gaps, there are larger displacements. So for example in slice (a) there is a thick piece of tissue that protrudes from the bottom-right section of the wall into the parenchyma. In this region there is clear evidence of increased displacement. Similarly to the results for mice airways, the magnitude of the displacement decreases with distance from the lumen.

Plots showing the displacements from (i) prior to contraction to (iii) after the application of oscillations, as described in Sec. 5.1.3, are shown in Fig. 5.25. The strain oscillations result in reduced displacements in comparison to those shown in Fig. 5.24, although in general the regions of the slice with larger or smaller than average displacements are the same. Again the magnitude of the displacement generally decreases as the distance from the lumen increases.

5.3.4 Comparisons to the mathematical model

In this subsection, we make some comparison between the model predictions and experimental data. The model presented in the previous chapters assumes plane strain, while for an intact airway plane stress may be more appropriate. Using the model of Brook *et al.* [22] we make comparisons between the two approaches. Ensuring that the outer radius of the airway wall is the same in both cases, there are smaller displacements within the airway wall for the plane stress case, while there is no noticeable difference in the displacements within the parenchyma (Fig. 5.26).

Having taken this consideration into account, we make some direct comparisons between our model predictions and the displacements found for the mouse lung slice in Fig. 5.21. We focus on a couple of locations away from the lower section of the slice, where there was a collapsed arteriole that affected the displacements found. Comparisons are shown in Fig. 5.27 for the sections labelled (e) and (f) in Fig. 5.21. Results are shown for the elastic model that assumes a nonlinear airway wall and linear parenchyma, since it has been shown how this model can be coupled to HHM. Since a plane strain assumption was used in the development of the model, we can expect the model to have some weakness within the airway wall. We set $\chi = 0.21$, having found the average thickness of the undeformed airway wall. A value must also be prescribed for the radius of the edge of the parenchyma R_p, which is assumed to be fixed in place. However, it is unclear what value R_p should take, since the slice is not visible beyond

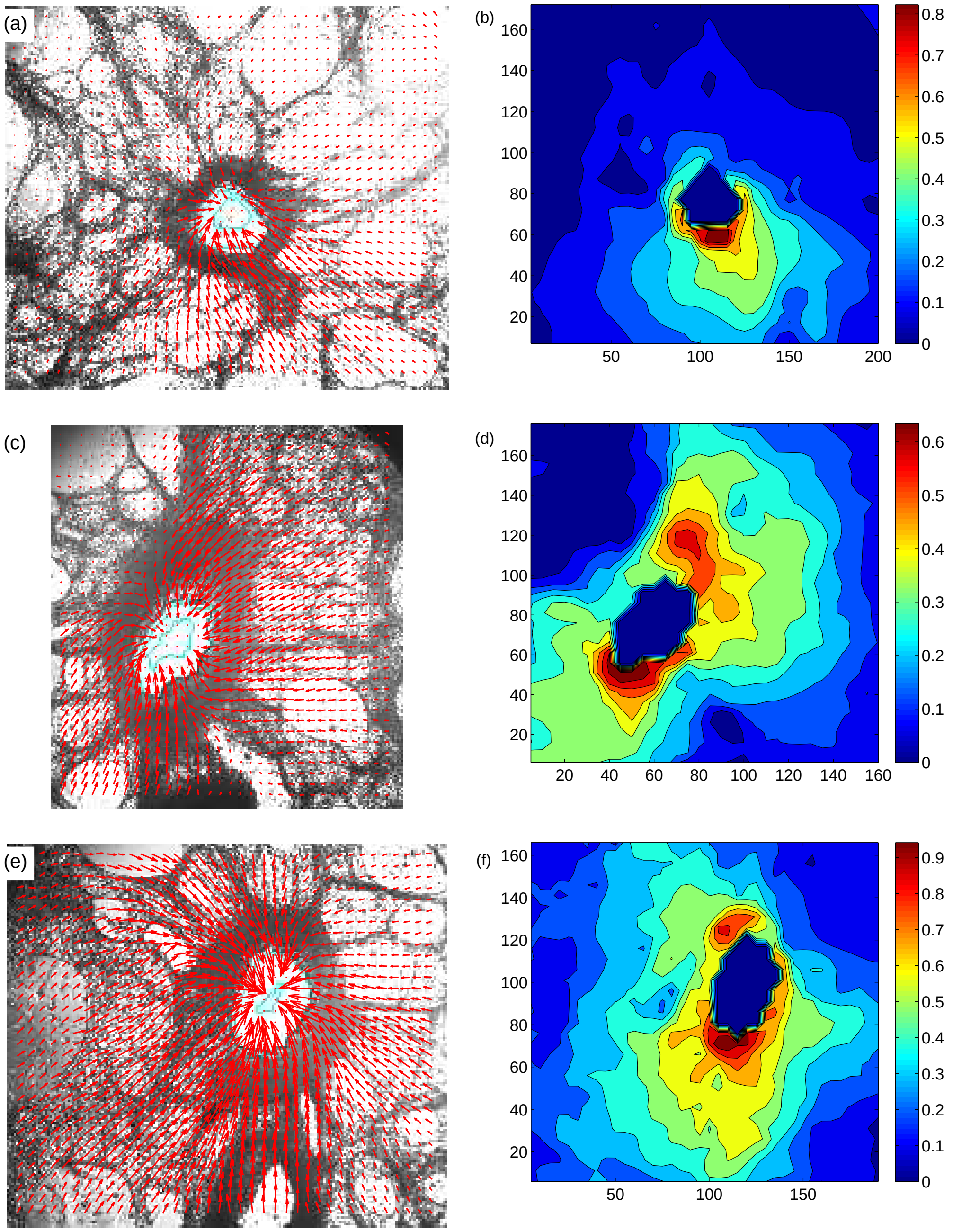

Figure 5.24: Plots of (a, c, e) displacement vectors with (b, d, f) the corresponding displacement magnitudes for contracting human lung slices. (The magnitudes have been normalised by dividing through by the average radius of the lumen.) The displacements are from pre-contraction to the maximum contraction ((i) to (ii) in Fig. 5.8).

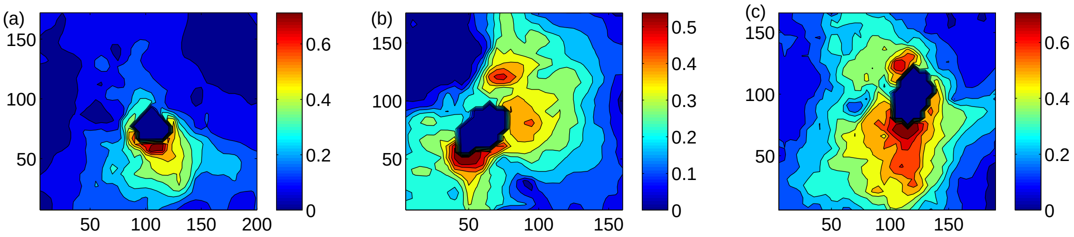

Figure 5.25: Plots of the displacement magnitudes for the contracting human lung slices [105], following oscillations as described in Sec. 5.1.3. (The magnitudes have been normalised by dividing through by the average radius of the lumen.) The displacements are from pre-contraction to the end of an oscillation ((i) to (iii) in Fig. 5.8) (a-c) correspond to (b), (d) and (f) in Fig. 5.24.

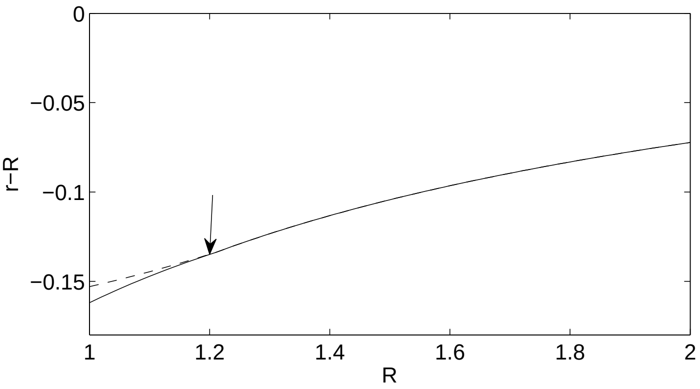

Figure 5.26: Comparisons between the linear elastic models of Brook *et al.* [22] assuming plane stress (dashed) or plane strain (solid). r_b is matched for the two models. The average values of A are 0.249 for the plane stress case and 0.271 for the plane strain case. Other parameters are $\chi = 0.2$, $\varrho = 10/13$, $\nu^{(p)} = 0.3$, $\tau_a = 0$ and $R_p = 5$ (taken from [22]). The arrow shows the boundary between the airway wall and the parenchyma at $R = 1.2$.

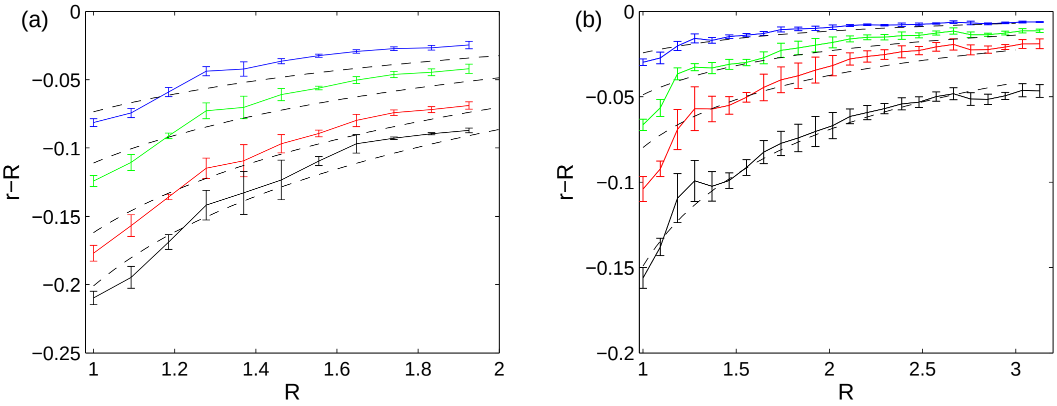

Figure 5.27: Panels (a) and (b) show respectively the radial displacements and standard deviation from (e) and (f) in Fig. 5.21 (solid) and the predicted values from the elastic model with nonlinear airway wall and linear parenchyma (dashed). The different coloured lines represent the different time points. A takes values of 0.123, 0.186, 0.271 and 0.336 in (a) and 0.038, 0.076, 0.124 and 0.233 in (b), where A is uniform across the wall. Other parameters are $\chi = 0.21$, $\varrho = 10/13$, $\varphi = \pi/12$ $\nu^{(p)} = 0.3$, $\tau_a = 0$ and $R_p = 5$ in (a) or $R_p = 7.5$ in (b).

the edge of the images. If $R_p = 5$ making comparisons with Fig. 5.27 (e) by choosing appropriate values of the active force A, the model predicts less variation in the radial displacements, as R increases, than the experiment does (a). If $R_p = 5$ and comparisons are made with Fig. 5.27 (f), the model predicts more variation in the displacements as R increases. Increasing R_p to 7.5, however, flattens the curve a little, resulting in a good fit (b). The point where there is the most difference is in the airway wall, although this is only notcable for the middle two time points. From the above comparison between the plane stress and strain cases, it would be expected that the plane strain model overpredicts the size of the displacement, when in fact it is under predicted.

Here we have been able to show that, at least in some circumstances, the model can predict the experimental data well. In order to check the model more thoroughly it would be desirable to have more examples to compare against. In particular it would be preferable if the parenchyma could be held fixed at some known distance from the lumen. This would allow for better comparisons between the model predictions and the experimental data. One possible way of doing this would be to use a method similar to Lavoie *et al.*, and use an indenter to pinch the parenchyma at a known position. Of the other airways considered in Fig. 5.19, the imaging technique failed to yield a good estimate of the displacement field for one of the slices, while in the other there were two airways. The example with two airways would be of interest for further study. At present however, the mathematical model presented only accounts for a single airway.

5.4 Summary

Two approaches have been used to to analyse lung slice experiments. First, the lumen area and how it changes as an agonist is added to the slice was investigated. Second, methods were developed to find an estimate of the displacement field of the tissue surrounding the lumen.

When considering the lumen area, a few slightly different techniques were developed to take into account the differences due to the type of tissue and how sharp the contrast is at the lumen boundary. The resulting area-time plots showed evidence that there are multiple timescales in the contraction. This finding was clarified by fitting exponential equations to the data with either one or two timescales, for which the equation with two timescales was shown to be overwhelmingly statistically superior. It was shown that fitting to an equation with two timescales, the ratio of the timescales was consistent, between repetitions of the experiment, with the mouse slices. More variation was found with the pig slices, with some of the slices starting to relax while ACh was still being added. With those that remained contracted, however, the ratio of the timescales was again fairly consistent, although smaller than the ratio for the mouse slices. This suggests that the rate of contraction to ACh is species specific. Considering the reason for the multiple timescales, we found that solving the differential equations of HHM theory also results in multiple timescales. Coupling to the tissue model and including viscoelasticity adds further complexity to the timescales observed.

Two methods, based on the algorithms of Farnebäck [41] and Butler *et al.* [24], were presented for estimating the displacement field between two video frames from lung slice experiments. The methods were tested and the one based on the Farnebäck [41] algorithm was selected as it gave the most accurate displacement field. The algorithm was used to consider contractions of both mouse and human lung slices. A large amount of heterogeneity within the displacements of the slices was found, as demonstrated by plots of the magnitude of the displacement field, or by sets of points that radiated out from the lumen. Finding the average radial displacement over all of the points around the lumen led to large standard deviations, while they were much smaller when only comparing points in a sector. In general however, the radial displacements were largest nearest to the lumen, quickly dropping off further from the lumen. In comparison the circumferential component of the displacement was small. It was also shown that, with appropriate model parameters, the deformations predicted by the mathematical model are consistent with the experimental data.

In summary it has been shown that there is a decent qualitative match between theory and experiment, both in terms of the rates of contraction of an airway when agonist is added and the displacement of the tissue surrounding the airway. However, the data emphasises the variability within real airways, with features such as arterioles and alveoli causing regions of reduced displacement. It has been shown that two timescales can be used to describe the contraction of an airway, where the ratio of the timescales is consistent between lung slices from the same species. In general the displacement of the tissue about the lumen is greatest at the lumen boundary and decreases with distance from the lumen.

Chapter 6

Conclusions

Mathematical modelling may be used to provide insight into the biological phenomena and to investigate biologically relevant questions. Models allow for the description of physical laws and constraints, bringing understanding of other disciplines in science and engineering to bear on biomedical applications. Modelling may also be able to help with the agenda of the NC3Rs, the National Centre for Replacement, Refinement & Reduction of Animals in Research, who aim to see the continued advancement of scientific knowledge but with reduced dependence on animal models [170].

In this thesis we focused on asthma, which affects millions of people around the world. Characteristic to asthma is the remodelling of the airway wall and the hyperresponsiveness of ASM. This can lead to difficulties with breathing, reduction in quality of life, and premature death. There are various questions that remain unanswered about asthma. Most notably, there remain questions about the effectiveness of tidal breathing and deep inspirations to reduce the contractile force produced by ASM and the amount of bronchoconstriction. There have been a large number of experiments on tissue strips, dissected airways and lung slices to try to answer this question (e.g. [8, 43, 50, 103, 105, 125, 129]); however, the experiments have not provided a definitive answer. The aim of this thesis was to develop a mathematical model of an asthmatic airway that may be used to give insight on this question and to investigate biophysical and biomechanical features of asthmatic airways in general. In this chapter we summarise the main results and give suggestions for further experiments and mathematical modelling.

In Chapter 2, the two-layered model of an asthmatic airway developed by Brook *et al.* [22], consisting of the airway wall embedded in parenchymal tissue, was extended. The airway wall was modelled using nonlinear elasticity to allow for finite deformations. To mimic the thickening of the airway wall that occurs during remodelling, the wall was allowed to have finite thickness. In order to take into account the collagen and ASM, two families of helically-oriented fibres were embedded within the wall. The fibres both reinforced the airway, so that the airway stiffens when inflated and provided a contractile force to the wall in the presence of agonist. The size of the contractile force was calculated by coupling to the Huxley-Hai-Murphy model, which enables prediction of the time-dependent evolution of the subcellular crossbridge populations. The parenchyma was assumed to be isotropic, homogeneous and compressible, and developed a nonlinear elastic model and also a linear viscoelastic model, to allow the viscoelastic nature of the parenchyma to be considered. In order to mimic breathing, stresses or displacements were applied to the boundaries.

In Chapter 3, results were shown for the airway when it is passively inflated. With an appropriate choice of parameter values, the airway wall exhibits strain-stiffening, similar to that of the model of Lambert *et al.* [98] (Fig. 3.2), which was based on experimental data. When the airway is embedded within parenchyma, the method of inflation of the airway has an important quantitative effect on the displacements that are predicted. When the airway is inflated externally, which corresponds to normal breathing, there are large displacements within the parenchyma (Fig. 3.9), whereas when the airway is inflated internally, which corresponds to artificial ventilation, the airway wall shields the parenchyma from large displacements (Fig. 3.10). For the same degree of inflation, larger transpulmonary pressures are required when the airway is inflated externally than when it is inflated internally, due to energy being used to expand the parenchyma (Fig. 3.8). Assuming the viscoelastic model for the parenchyma, creep was shown to be predicted when the transpulmonary pressure is increased and then kept constant (Fig. 3.17, 3.19). Hysteresis is also predicted when oscillatory boundary conditions are applied, with the lumen having a greater cross-sectional area during deflation than during inflation (Fig. 3.22), in agreement with experimental results [64].

The methods required to include active contractile forces were developed in Chapter 4, and results were shown. In the contracted steady state, the model predicts that within the airway wall there can exist distinct regions where the radial or hoop stresses are compressive or tensile (Fig. 4.1, 4.3). This is consistent with the predictions of the linear model of Brook *et al.* [22]. However, with the nonlinear model, regions of contractile radial or hoop stresses are more likely and where they exist are larger in magnitude, while the maximal decrease in airway calibre is reduced (Fig. 4.2).

Currently these stress heterogeneities have not been confirmed experimentally. If possible it would be desirable to validate that these distributions exist. Further investigations could also be carried out, to test whether the stress distribution lead to differential growth within the airway wall, and how the stresses affect remodelling.

From the steady state solutions, the model predicts that if the thickness of the airway wall is reduced then the level of contraction is also reduced. This suggests that the therapy of thermoplasty, where some of the ASM is thermally ablated, can have a positive effect on asthma. However, our model is unable to take into account other effects of the treatment that may be detrimental.

In agreement with experimental findings for lung slices [12, 42], our mathematical model predicted that, as agonist is applied to the airway, there is an initial rapid contraction, which slows down as the airway approaches the steady state (Fig. 4.12). In the case of a viscoelastic parenchyma the airway contracts more slowly and short-time peaks in the radial and hoop stresses are predicted. Upon the application of oscillations of the pleural displacement, to mimic breathing, the model predicts that there is a reduction in the active contractile force and as a result, reduced bronchoconstriction (Fig. 4.13). Increasing the amplitude of the oscillations, increases the decrease in contractile force (Fig. 4.14). These results are comparable to results where length oscillations were applied to contracted tissue strips [43]. Furthermore, if the parenchyma is viscoelastic, greater reductions in the amount of contractile force and bronchoconstriction are predicted (Fig. 4.16). However, by removing the parenchyma and applying the protocols described in [103], the model predicts that applying tidal oscillations to the transmural pressure has little effect on the level of contraction, in comparison to when the transmural pressure is static (Fig. 4.17-4.19). These predictions are consistent with those of LaPrad *et al.* [103]. Brief comparisons were also made between the stresses predicted within the airway wall and those predicted in a tissue strip, when comparable length oscillations are applied to the strip. While a range of stresses are predicted along the fibres within the airway wall, with the possibility of distinct regions experiencing compressive and tensile stresses, within the strip there is a single stress (Fig. 4.20, 4.21). The stress within the strip is predicted to be closer to the stress at the outer boundary of the airway wall, although it is possible for the stress in the strip to be outside of the range of stresses experienced by the fibres in the airway.

For segments of airways that are dissected from the parenchyma, the ASM exists in a geometry closer to that *in vivo* in comparison to ASM in tissue strips. However, they still lack some key features. In particular, as shown in Chapter 4, the viscoelasticity of the parenchyma can have a large impact on the effectiveness of tidal oscillations in reversing bronchoconstriction. This raises questions about the physiological suitability of the experiments of LaPrad *et al.* [103], for which the parenchyma was removed. It would be desirable to repeat some of the experiments of LaPrad *et al.* [103] on airways that have some parenchymal tissue surrounding them. As shown in Chapter 3 the method of inflation would then be important. Alternatively, the lung-slice techniques of Lavoie *et al.* [105], where oscillatory strains can be applied to the parenchyma surrounding an activated airway wall, could be utilised further.

In Chapter 5, the focus shifted from mathematical modelling of asthmatic airways to image analysis of lung slice experiments. Initially the timescales involved during bronchoconstriction were investigated, by considering the experiments of Fox [42], where ACh was added to lung slices to induce ASM contraction. By fitting exponential functions to the lumen area, strong evidence was shown for the existence of multiple timescales. In some instances the airway started to relax before the ACh was initially washed out, the reason for which is unclear. However, where the airway remained contracted, it was shown that fitting to a function with two timescales, there was a robust ratio between the two timescales, although the ratio was different for mice and pigs (Table. 5.1, 5.2). For the experiments with mice, the ratio was approximately 9, while for pigs the ratio was approximately 5, suggesting that the ratio is species specific. It would be of interest for further repetitions of the experiments to be carried out to ensure that these findings hold for larger samples of data.

The mathematical model also predicts multiple timescales (Fig. 5.9), and in particular the HHM model yields multiple timescales (Fig. 5.10). Further work could be carried out to find suitable rate parameters for the HHM model for different species. Furthermore, if a particular experiment provided a ratio that was significantly different from the expected value, investigations could be carried out to try to find other factors that affect the ratio.

A technique was also developed to analyse images from lung slice experiments, in order to give the displacement field of the tissue surrounding a contracted airway. Splitting the displacement into the radial and circumferential components, the circumferential component was small in comparison to the radial component, giving support for our model which assumes that there is no torsion (Fig. 5.21, 5.23). As found by Adler *et al.* [1], in general the radial component is greatest at the lumen boundary and reduces and levels off further from the lumen. However, significant heterogeneity was found in the displacements. The presence of arterioles or alveoli reduced the magnitude of the displacements.

With appropriate parameter values, the mathematical model predicts the displacements well (Fig. 5.27). Given experimental data for suitable lung slices, the imaging technique could be used to further investigate the effect of having two airways close to one another or other structures, such as a blood vessel, close to the airway.

Finally, we suggest a few directions for further modelling, that would incorporate more of the relevant aspects of airways and asthma.

- Buckling: In the case of large contractions, the assumption of axisymmetric deformations will become unsuitable and mucosal folding will be important. This is widely seen in pig lung slices, as in Fig. 5.4. The methods of Wiggs *et al.* [179] or the simplified model of Donovan and Tawhai [38] could be used to take buckling into account.
- Mucus and surfactant: The effect of mucus that lines the airway and surfactant that sits at the air-liquid interface have been neglected. It would be of interest to investigate the surface-tension-driven instabilities that these give rise to [56], when included within the airway model presented in this thesis. Such instabilities could also have an effect on the viscoelastic phenomena observed and plugging that may occur within the airways.
- Airflow: Given that the reduction of lung function is a key aspect of asthma symptoms, it would be of interest to couple the airway model described in this thesis to the airflow within the airway. This would build on previous models including the model for expiratory flow of Lambert *et al.* [98] and various models for flow in collapsible tubes [49, 79, 134]. It would be of particular interest to understand how the flow rate and the level of contraction of the airway interact, and how this affects lung function and peak flow readings that are used to diagnose asthma.
- Molecular/sub-cellular models: There is significant scope for improving models at the molecular/sub-cellular level. These models and any rate parameters could be made specific to ASM and could take into account features such as remodelling. Investigations could then be carried out to see what effect the changes in these models have on the larger scale mechanics.

In conclusion, a mathematical model has been developed, that reproduces many experimental findings, while giving a basis for further understanding of ASM. Image analysis techniques have also been presented that enable greater understanding of the timescales involved in airway contraction and the heterogeneous nature of the displacement fields about an airway.

Appendix A

Nearly incompressible case

In section 2.2.2 the incompressible limit in the airway wall when $\nu \to 0.5$ or $\lambda \to \infty$ was considered. In this appendix the nearly incompressible case for the parenchyma is considered.

For a nearly incompressible material, J can be expanded so that

$$J = 1 + \frac{J_1}{\lambda} + \frac{J_2}{\lambda^2} + \dots, \tag{A.1}$$

where λ is large and J_1 and J_2 are $O(1)$. Likewise

$$\boldsymbol{\tau} = \boldsymbol{\tau}_0 + \frac{\boldsymbol{\tau}_1}{\lambda} + \frac{\boldsymbol{\tau}_2}{\lambda^2} + \dots, \tag{A.2a}$$

$$r = r_0 + \frac{r_1}{\lambda} + + \frac{r_2}{\lambda^2} + \dots, \tag{A.2b}$$

$$p = p_0 + \frac{p_1}{\lambda} + \frac{p_2}{\lambda^2} + \dots. \tag{A.2c}$$

The boundary conditions in (3.2.2) become

$$\tau_{rr0}(R_b) = \tau_b, \tag{A.3a}$$

$$\tau_{rr0}(R_p) = \tau_p \quad \text{or} \quad r(R_p) = r_p, \tag{A.3b}$$

with all higher order terms equal to zero.

Now $J = \det(\mathsf{F}) = r'r/R$, so expanding and using (A.1) and (A.2b),

$$\frac{r_0' r_0}{R} = 1, \quad \frac{r_0 r_1' + r_0' r_1}{R} = J_1. \tag{A.4}$$

Integrating the first of these expressions and using the definition that $r_0(R_b) = r_{b0}$ gives

$$r_0^2 = r_{b0}^2 + R^2 - R_b^2. \tag{A.5}$$

At leading order, the nonzero components of the Cauchy stress tensor, (2.2.39), are

$$\tau_{rr0} = -\varrho p_0 + \varrho \frac{R^2}{r_0^2}, \tag{A.6a}$$

$$\tau_{\theta\theta 0} = \tau_{rr0} + \varrho \left(\frac{r_0^2}{R^2} - \frac{R^2}{r_0^2} \right), \tag{A.6b}$$

$$\tau_{zz0} = \tau_{rr0} + \varrho \left(1 - \frac{R^2}{r_0^2} \right), \tag{A.6c}$$

where

$$p_0 = 1 - J_1. \tag{A.7}$$

At present both p_0 and J_1 are unknown.

Applying the conservation of momentum equation, (2.2.41), at leading order and implementing (A.3a) yields

$$\tau_{rr} = \tau_b + \varrho \log \left(\frac{r_{b0} R}{r_0 R_b} \right) + \varrho \frac{(r_{b0}^2 - R_b^2)(R^2 - R_b^2)}{2 r_{b0}^2 r_0^2} \tag{A.8}$$

and applying the stress condition from (A.3b),

$$\tau_p - \tau_b = \log \left(\frac{r_b R_p}{r_p R_b} \right) + \frac{(r_b^2 - R_b^2)(R_p^2 - R_b^2)}{2 r_b^2 r_p^2}. \tag{A.9}$$

Now from (A.6a), (A.7) and (A.8), J_1 satisfies

$$J_1 = \frac{\tau_b}{\varrho} + \log \left(\frac{r_{b0} R}{r_0 R_b} \right) + \frac{(r_{b0}^2 - R_b^2)(R_p^2 - R^2)}{2 r_{b0}^2 r_0^2} + 1 - \frac{R^2}{r_0^2}, \tag{A.10}$$

or alternatively from (A.4)

$$R J_1 = \frac{\mathrm{d}}{\mathrm{d}R}(r_0 r_1). \tag{A.11}$$

Integrating (A.11) yields

$$r_0 r_1 = \frac{R^2}{2} \left[\frac{\tau_b}{\varrho} + \log \left(\frac{r_{b0} R}{r_0 R_b} \right) + \frac{r_{b0}^2 - R_b^2}{2 r_{b0}^2} \right] + C, \tag{A.12}$$

where C is a constant of integration. Using the notation $r_1(R_b) = r_{b1}$ yields

$$r_1 = \frac{1}{r_0} \left\{ \frac{R^2 - 1}{2} \left[\frac{\tau_b}{\varrho} + \frac{r_{b0}^2 - R_b^2}{2 r_{b0}^2} \right] + \frac{R^2}{2} \log \left(\frac{r_{b0} R}{r_0 R_b} \right) + r_{b0} r_{b1} \right\}, \tag{A.13}$$

with

$$\begin{aligned} r_1' = & \frac{R}{r_0^3} \left\{ \frac{r_0^2 + r_{b0}^2}{2} \left[\frac{\tau_b}{\varrho} + \frac{r_{b0}^2 - R_b^2}{2 r_{b0}^2} \right] + \frac{2 r_0^2 - R^2}{2} \log \left(\frac{r_{b0} R}{r_0 R_b} \right) \right. \\ & \left. + \frac{r_{b0}^2 - R_b^2}{2} - r_{b0} r_{b1} \right\}. \end{aligned} \tag{A.14}$$

r_0 is known from the leading order solution, thus if r_{b1} was known, r_1 could be found for each value of R in the parenchyma.

At $O(1/\lambda)$, the nonzero components of the Cauchy stress tensor, (2.2.39), are

$$\tau_{rr1} = -\varrho p_1 + \varrho \frac{r_1' R}{r_0} - \varrho \frac{r_1 R^2}{r_0^3}, \tag{A.15a}$$

$$\tau_{\theta\theta 1} = -\varrho p_1 + \varrho \frac{r_1 r_0}{R^2} - \varrho \frac{r_0^3 r_1'}{R^3}, \tag{A.15b}$$

$$\tau_{zz1} = -\varrho p_1 - \varrho \frac{r_1}{r_0} - \varrho \frac{r_0 r_1'}{R}, \tag{A.15c}$$

where

$$p_1 = -J_1 - J_2. \tag{A.16}$$

At present both p_1 and J_2 are unknown.

At $O(1/\lambda)$ the equation for conservation of momentum, (2.2.41), becomes

$$\frac{\partial \tau_{rr1}}{\partial R} = \frac{2R^2}{r_0^3}\left[\frac{R r_1}{r_0^2} - r_1'\right] \tag{A.17}$$

$$= 2\frac{R^3}{r_0^6}\left[2 r_{b0} r_{b1} - r_{b0}^2 \frac{\tau_b}{\varrho} - (r_{b0}^2 - R_b^2)\left\{1 + \log\left(\frac{r_{b0} R}{r_0 R_b}\right)\right\}\right]. \tag{A.18}$$

Integrating and implementing the boundary condition $\tau_{rr1}(1) = 0$ yields

$$\tau_{rr1} = \frac{-(R^2 - R_b^2)(r_0^2 R_b^2 + r_{b0}^2 R^2)(4 r_{b0}^2 \tau_b - 8\varrho r_{b0} r_{b1} + 3\varrho(r_{b0}^2 - R_b))}{8\varrho r_0^4 r_{b0}^4} - \frac{R^4}{2 r_0^4}\log\left(\frac{r_{b0} R}{r_0 R_b}\right). \tag{A.19}$$

Also implementing that $\tau_{rr1}(R_b) = 0$ yields

$$0 = \frac{(R_p^2 - R_b^2)(r_{p0}^2 R_b^2 + r_{b0}^2 R_p^2)(4 r_{b0}^2 \tau_{b0} - 8\varrho r_{b0} r_{b1} + 3\varrho(r_{b0}^2 - R_b^2))}{8\varrho r_{b0}^4 r_{p0}^4} + \frac{R_p^4}{2 r_{p0}^4}\log\left(\frac{r_{b0} R_p}{r_{p0} R_b}\right). \tag{A.20}$$

Therefore

$$r_{b1} = \frac{1}{8 r_{b0}}\left[4 r_{b0}^2 \frac{\tau_b}{\varrho} + 3(r_{b0}^2 - R_b^2) + \frac{4 r_{b0}^4 R_p^4}{(R_p^2 - R_b^2)(r_{p0}^2 R_b^2 + r_{b0}^2 R_p^2)}\log\left(\frac{r_{b0} R_p}{r_{p0} R_b}\right)\right]. \tag{A.21}$$

Using (A.15) and (A.19), p_1 may be found and

$$\tau_{\theta\theta 1} = \tau_{rr1} - \frac{r_1' R}{r_0} + \frac{r_1 R^2}{r_0^3} + \frac{r_1 r_0}{R^2} - \frac{r_0^3 r_1'}{R^3}, \tag{A.22a}$$

$$\tau_{zz1} = \tau_{rr1} - \frac{r_1' R}{r_0} + \frac{r_1 R^2}{r_0^3} - \frac{r_1}{r_0} - \frac{r_0 r_1'}{R}. \tag{A.22b}$$

The equations found for the radius and the stresses at leading order and at $O(1/\lambda)$ may be inserted into (A.2) to find the radius and stresses across the parenchyma in the nearly incompressible case, where terms of $O(1/\lambda^2)$ are ignored. The results shown in this appendix were used to select an appropriate accuracy for the calculations in the MATLAB ODE solver used to shoot across the parenchyma, as described in Sec. 3.2.3.

Appendix B

Numerical Methods

In this appendix the details from Sec. 4.2.2 are expanded and details are given about how the crossbridge populations are updated. The populations will in general depend on R, therefore the airway is discretised into points spaced by ΔR. A Godunov scheme may be used to update the crossbridge population at each of these points. Without loss of generality, the method used to update the population at one of these points is shown. A couple of tests are then carried out to validate the choice of discretisation used for R and x.

B.1 Godunov scheme used to update the crossbridge distribution

Once the airway is discretised, calculations can be made to find how $\mathbf{n}$ changes with time, at each radial location. Without loss of generality, one of these radial locations is considered. Equation (2.3.10) can be written in the following conservative form:

$$\frac{\partial \mathbf{n}}{\partial t} + \frac{\partial \mathbf{X}}{\partial x} - \mathbf{S} = 0, \tag{B.1}$$

where $\mathbf{X} = \gamma V \mathbf{n}$ is a vector of fluxes, and $\mathbf{S} = \mathrm{Q}\mathbf{n}$ represents the source terms. This can be solved using a Godunov scheme. For reasons of stability, a second order Godunov scheme is used [55, 146]. Using the methods described in [20, 55], the discretisation and methods for solving the scheme are presented. Time is split up into steps, where V and $\mathbf{n}$ at t^j are known and assumed to be constant over the timestep. $\mathbf{n}$ at t^{j+1} must be found. Initially a first-order step is carried out to find $\mathbf{n}$ at $t^{j+1/2}$, which is used to update $\mathbf{X}$ and $\mathbf{S}$. A second order step is then carried out to find $\mathbf{n}$ at t^{j+1}.

The x-domain is discretised into cells of width Δx, where the domain of the i^{th} cell is

$[x_{i-1/2}, x_{i+1/2}]$. Integrating (B.1) over the i$^{\text{th}}$ cell gives

$$\frac{\mathrm{d}}{\mathrm{d}t}\int_{x_{i-1/2}}^{x_{i+1/2}} \mathbf{n}(x,t)\mathrm{d}x + \mathbf{X}(\mathbf{n}(x_{i+1/2})) - \mathbf{X}(\mathbf{n}(x_{i-1/2})) - \int_{x_{i-1/2}}^{x_{i+1/2}} \mathbf{S}\mathrm{d}x = 0. \tag{B.2}$$

Also integrating over the time step between t^j and t^{j+1}, where $t^{j+1} = t^j + \Delta t$, yields

$$\begin{aligned}\int_{x_{i-1/2}}^{x_{i+1/2}} \mathbf{n}(x,t^{j+1})\mathrm{d}x = &\int_{x_{i-1/2}}^{x_{i+1/2}} \mathbf{n}(x,t^j)\mathrm{d}x - \\ &\int_{t^j}^{t^{j+1}} \left[\mathbf{X}(\mathbf{n}(x_{i+1/2},t)) - \mathbf{X}(\mathbf{n}(x_{i-1/2},t)) - \int_{x_{i-1/2}}^{x_{i+1/2}} \mathbf{S}\mathrm{d}x\right]\mathrm{d}t.\end{aligned} \tag{B.3}$$

Letting $\mathbf{n}_i^j$ represent the mean value of $\mathbf{n}$ over the i$^{\text{th}}$ cell at time t^j, $\mathbf{X}_{i\pm1/2}$, the mean value of $\mathbf{X}(\mathbf{n}(x_{i\pm1/2},t))$ over the timestep and $\mathbf{S}_i$, the mean value of $\mathbf{S}$ over the i$^{\text{th}}$ cell and the time step, so that

$$\mathbf{n}_i^j = \frac{1}{\Delta x}\int_{x_{i-1/2}}^{x_{i+1/2}} \mathbf{n}(x,t^j)\mathrm{d}x, \tag{B.4a}$$

$$\mathbf{X}_{i\pm1/2} = \frac{1}{\Delta t}\int_{t^j}^{t^{j+1}} \mathbf{X}(\mathbf{n}(x_{i\pm1/2},t))\mathrm{d}t, \tag{B.4b}$$

$$\mathbf{S}_i = \frac{1}{\Delta x\Delta t}\int_{t^j}^{t^{j+1}}\int_{x_{i-1/2}}^{x_{i+1/2}} \mathbf{S}(x,t)\mathrm{d}x\mathrm{d}t. \tag{B.4c}$$

(B.3) can be rewritten as follows:

$$\mathbf{n}_i^{j+1} = \mathbf{n}_i^j - \frac{\Delta t}{\Delta x}\left(\mathbf{X}_{i+1/2} - \mathbf{X}_{i-1/2}\right) + \Delta t\mathbf{S}_i^{j+1/2}. \tag{B.5}$$

Now initially a first-order step is applied. The equation for $\mathbf{n}_i^{j+1/2}$ is similar to (B.5), but it has $\Delta t/2$ instead of Δt. $\mathbf{S}$ can be calculated using $\mathbf{n}_i^j$, but when calculating the fluxes the discontinuities at each of the cell boundaries must be dealt with. This is an example of a Riemann problem. However, due to the linearity of the problem, the first-order upwind method introduced by Courant *et al.* [29] can be used, resulting in (B.5) becoming

$$\mathbf{n}_i^{j+1/2} = \begin{cases} \mathbf{n}_i^j - \gamma V\frac{\Delta t}{2\Delta x}\left(\mathbf{n}_i^j - \mathbf{n}_{i-1}^j\right) + \frac{\Delta t}{2}\mathrm{Q}\mathbf{n}_i^j & \text{if } V > 0, \\ \mathbf{n}_i^j - \gamma V\frac{\Delta t}{2\Delta x}\left(\mathbf{n}_{i+1}^j - \mathbf{n}_i^j\right) + \frac{\Delta t}{2}\mathrm{Q}\mathbf{n}_i^j & \text{if } V < 0. \end{cases} \tag{B.6}$$

Here, using (4.2.1), it is noted that $\gamma > 0$ as $\varphi \in [0, \pi/2]$.

A second-order step is now carried out. Using the solution to $\mathbf{n}$ at $t^{j+1/2}$, a gradient $\mathbf{G}_i^{j+1/2}$ is constructed in each cell. This is given by

$$\mathbf{G}_i^{j+1/2} = Av\left(\mathbf{n}_i^{j+1/2} - \mathbf{n}_{i-1}^{j+1/2}, \mathbf{n}_{i+1}^{j+1/2} - \mathbf{n}_i^{j+1/2}\right), \tag{B.7}$$

where $Av(a,b)$ is an averaging function. The averaging function of Brook *et al.* [20], namely

$$Av(a,b) = \begin{cases} \frac{a^2b+b^2a}{a^2+b^2} & \text{if } ab > 0, \\ 0 & \text{if } ab < 0, \end{cases} \tag{B.8}$$

is assumed. The gradient function is used to update the fluxes so that

$$\mathbf{X}_{i+1/2} = \begin{cases} \gamma V \left(\mathbf{n}_i^{j+1/2} + \frac{1}{2}\mathbf{G}_i^{j+1/2} \right) & \text{if } V > 0, \\ \gamma V \left(\mathbf{n}_{i+1}^{j+1/2} - \frac{1}{2}\mathbf{G}_{i+1}^{j+1/2} \right) & \text{if } V < 0, \end{cases} \tag{B.9}$$

$$\mathbf{X}_{i-1/2} = \begin{cases} \gamma V \left(\mathbf{n}_{i-1}^{j+1/2} + \frac{1}{2}\mathbf{G}_{i-1}^{j+1/2} \right) & \text{if } V > 0, \\ \gamma V \left(\mathbf{n}_{i}^{j+1/2} - \frac{1}{2}\mathbf{G}_{i}^{j+1/2} \right) & \text{if } V < 0. \end{cases} \tag{B.10}$$

Using $\mathbf{n}_i^{j+1/2}$, $\mathbf{S}$ may also be updated, in which case (B.5) becomes

$$\mathbf{n}_i^{j+1} = \begin{cases} \mathbf{n}_i^j - \frac{\Delta t}{\Delta x}\gamma V \left(\mathbf{n}_i^{j+1/2} - \mathbf{n}_{i-1}^{j+1/2} + \frac{1}{2}\left(\mathbf{G}_i^{j+1/2} - \mathbf{G}_{i-1}^{j+1/2} \right) \right) + \Delta t \mathrm{Q} \mathbf{n}_i^{j+1/2} & \text{if } V > 0, \\ \mathbf{n}_i^j - \frac{\Delta t}{\Delta x}\gamma V \left(\mathbf{n}_{i+1}^{j+1/2} - \mathbf{n}_{i}^{j+1/2} - \frac{1}{2}\left(\mathbf{G}_{i+1}^{j+1/2} - \mathbf{G}_{i}^{j+1/2} \right) \right) + \Delta t \mathrm{Q} \mathbf{n}_i^{j+1/2} & \text{if } V < 0. \end{cases} \tag{B.11}$$

At the start of each time step it is required to choose a step size that ensures the scheme is stable. By considering (2.3.16) it is noted that R only appears in the denominator, therefore V will take a maximum when $R = 1$, so Δt must satisfy [20]

$$\Delta t \leq \frac{\Delta x}{|-\gamma V(1)|}. \tag{B.12}$$

When $V(1)$ is small, Δt can become large, which could lead to instabilities. We let Δt equal the right-hand side multiplied by 0.8, but limit its size to a maximum value of 0.001.

In order to find the contractile force, by solving the Huxley-Hai-Murphy model, the sum of the attached crossbridges over the region $-\infty < x < \infty$ must be found (c.f. (2.3.17)). However, the crossbridges can only attach in the region $0 \leq x \leq 1$, out of which they may then move if $v \neq 0$. For larger stretches or contractions they will move further out, although they are then also more likely to detach. Nevertheless it is unnecessary and also impossible to consider numerically the full region $-\infty < x < \infty$. Instead a region is selected, suitable for the simulation, such that attached crossbridges do not leave the region. Assuming that $v \neq 0$, at one edge, points will leave the region, while at the opposite edge, new points will enter the region. Now far from $0 \leq x \leq 1$, where there are no attached crossbridges, $\mathbf{n}$ is independent of x, with $n_A + n_B = 1$ and $n_C = n_D = 0$. Here the phosphorylated and unphosphorylated unattached crossbridges tend to a equilibrium solution. Due to the condition (B.12) there can be at most one point entering the chosen region at each timestep. As the Godunov scheme is carried out, we set $n_i^{j+1/2}$ and n_i^{j+1} at the end points, in the region considered, to equal the values of the point next to them. After each step checks are made that $n_C < eps$, $n_D < eps$ and $n_A + n_B - 1 < tol$ at the two edges, where tol is some small tolerance. If these conditions are broken, the code is programed to stop and display an error message. Checks can be made that these tests are functioning properly by running simulations, for which it is known that the range of values of x, that the crossbridge populations is calculated for, is unreasonably small or by using an unrealistically large value of tol.

B.2 Comments on using a viscoelastic parenchyma

Assuming that the parenchyma is elastic, $\mathbf{n}$ can be updated and then r_b and $\mathrm{d}r_b/\mathrm{d}t$ can be found using (4.2.12) and (4.2.13) or (4.2.15) and (4.2.16) depending on the boundary conditions. However, if the parenchyma is viscoelastic, it is not possible to simply find r_b at the end of each timestep, since the airway is no longer quasi-static. Instead (4.2.7) or (4.2.10) is used. Here it is noted that $\mathrm{d}r_b/\mathrm{d}t$ depends on a number of time-dependent quantities so for case (i), where $\tau_a(t)$ and $\tau_p(t)$ are prescribed, there is a function of the following form:

$$\frac{\mathrm{d}r_b}{\mathrm{d}t} = f\left(r_b, \tau_a, \frac{\mathrm{d}\tau_a}{\mathrm{d}t}, \tau_p, \frac{\mathrm{d}\tau_p}{\mathrm{d}t}, A(\mathbf{n}), \mathcal{H}_1(\mathbf{n}), \mathcal{H}_2(\mathbf{n})\right). \tag{B.1}$$

r_b is updated by discretising time and using a midpoint method. Firstly a half-timestep is taken using the old values so that

$$\begin{aligned} r_b(t^{j+1/2}) = r_b(t^j) + \frac{\Delta t}{2} f\Big(& r_b(t^j), \tau_a(t^j), \frac{\mathrm{d}\tau_a}{\mathrm{d}t}(t^j), \tau_p(t^j), \frac{\mathrm{d}\tau_p}{\mathrm{d}t}(t^j), \\ & A(\mathbf{n}(t^j)), \mathcal{H}_1(\mathbf{n}(t^j)), \mathcal{H}_2(\mathbf{n}(t^j))\Big). \end{aligned} \tag{B.2}$$

The values of $\mathbf{n}$ and r_b at $t^{j+1/2}$ are then used to update the function and then $r_b(t^{j+1})$ is found by solving

$$\begin{aligned} r_b(t^{j+1}) = r_b(t^j) + \Delta t\, f\Big(& r_b(t^{j+1/2}), \tau_a(t^{j+1/2}), \frac{\mathrm{d}\tau_a}{\mathrm{d}t}(t^{j+1/2}), \tau_p(t^{j+1/2}), \frac{\mathrm{d}\tau_p}{\mathrm{d}t}(t^{j+1/2}), \\ & A(\mathbf{n}(t^{j+1/2})), \mathcal{H}_1(\mathbf{n}(t^{j+1/2})), \mathcal{H}_2(\mathbf{n}(t^{j+1/2}))\Big). \end{aligned} \tag{B.3}$$

Finally the values of $\mathbf{n}$ and r_b at t^{j+1} are used in (4.2.7) to find $\mathrm{d}r_b/\mathrm{d}t(t^{j+1})$. There is a similar method for case (ii), where $r_p(t)$ is prescribed instead of $\tau_p(t)$.

B.3 Choice of discretisation

In order to set up the numerical methods it is necessary to select values for Δx and ΔR. The smaller the value of Δx the more points that must be calculated for and the timesteps will also become smaller. This can result in more accuracy, but at the cost of calculation time. Likewise reducing ΔR will increase the number of points to calculate for, thus increasing the accuracy and the time taken. We therefore want a balance of a reasonable accuracy and calculation time. In order to test our choice of discretisation, we run some simulations for different values of Δx and ΔR. In order to ensure that the tests are relevent to the simulations shown in Sec. 4.4 we consider both the contraction of an airway and the application of oscillations to the pleural position, having started from the contracted equilibrium state. Tests are carried out for the largest amplitude oscillations that are used ($a = 1$), since the most error is expected with this example. We consider the airway when the parenchyma is elastic with no displacement at its outer boundary, so that $r_p = R_p$.

In Fig. B.1 the effect of varying Δx is shown. When solving the HHM model Mijailovich *et al.* [116] let $\Delta x = 1/800$, while Wang *et al.* [173] let $\Delta x = 1/20$. Comparisons are shown for $\Delta x = 1/400$, $1/800$ and $1/1200$. For the contracting airway (a), the level of contraction increases a very small amount when Δx decreases from $1/400$ to $1/800$, while the increase in contraction is even less when Δx reduces further to $1/1200$. Applying tidal oscillations to the contracted airway (b), the results are similar. This gave us sufficient confidence to use $\Delta x = 1/800$.

In Fig. B.2 the effect of varying ΔR is shown, with $\Delta R = 0.1$, 0.01 or 0.001. For the contracting airway (a), the level of contraction increases slightly when ΔR decreases from 0.1 to 0.01, while the contraction increases even less when ΔR reduces to 0.001. Applying tidal oscillations to the contracted airway (b), the airway is contracted slightly less when $\Delta R = 0.01$ to when $\Delta R = 0.1$. The difference is even smaller when ΔR is decreased further to 0.001. Due to the tiny difference between when ΔR is $1/100$ or $1/1000$, and taking into account the differences in computation time, we chose $\Delta R = 1/100$.

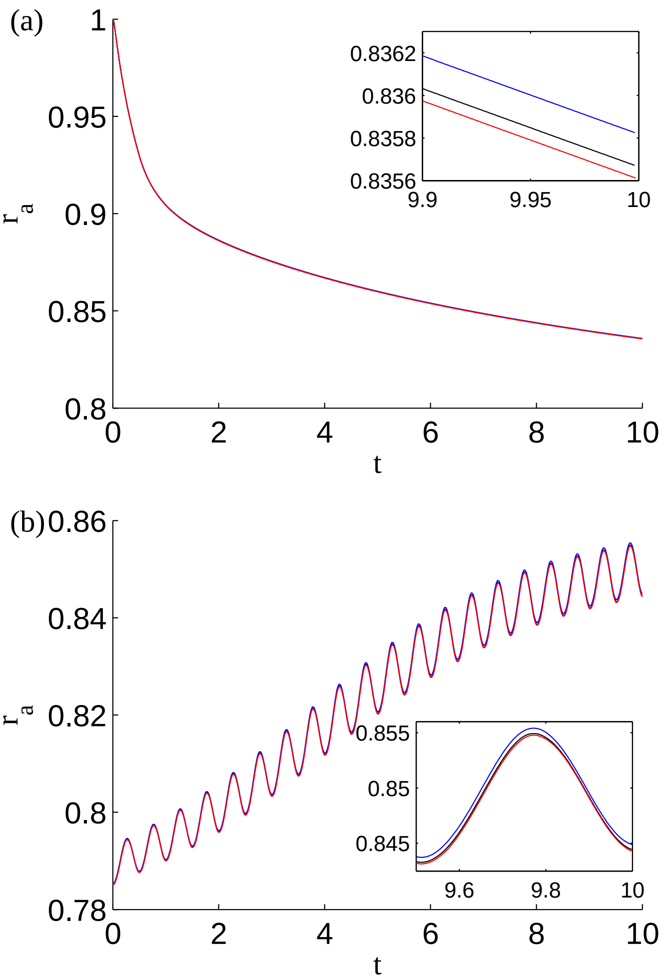

Figure B.1: Plots for (a) the contracting airway (Sec. 4.4) or (b) when tidal oscillations are applied to the contracted airway (Sec. 4.4.1) with $\Delta x = 1/400$ (blue), $1/800$ (black) or $1/1200$ (red). $\Delta R = 0.01$. The other parameter values are given in Table 4.3, while the HHM rates are given in Table 4.2.

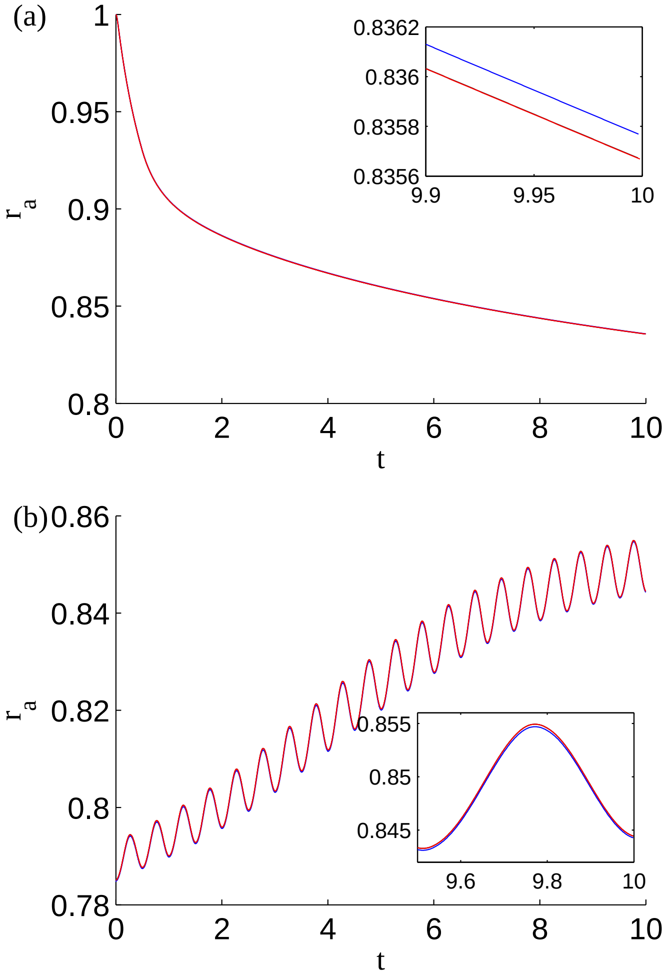

Figure B.2: Plots for (a) the contracting airway (Sec. 4.4) or (b) when tidal oscillations are applied to the contracted airway (Sec. 4.4.1) with $\Delta R = 0.1$ (blue), 0.01 (black) or 0.01 (red). (The red and black lines overlap.) $\Delta x = 1/800$. The other parameter values are given in Table 4.3, while the HHM rates are given in Table 4.2.

References

[1] A. Adler, E.A. Cowley, J.H.T. Bates, and D.H. Eidelman. Airway-parenchymal interdependence after airway contraction in rat lung explants. *Journal of Applied Physiology*, 85(1):231–237, 1998.

[2] D.A. Affonce and K.R. Lutchen. New perspectives on the mechanical basis for airway hyperreactivity and airway hypersensitivity in asthma. *Journal of Applied Physiology*, 101(6):1710–1719, 2006.

[3] D. Ambrosi and S. Pezzuto. Active stress vs. active strain in mechanobiology: Constitutive issues. *Journal of Elasticity*, 107:199–212, 2012.

[4] J.R. Barber. *Elasticity*. Solid Mechanics and its Applications. Kluwer academic publishers, second edition, 2002.

[5] P.J. Barnes, K.F. Chung, and C.P. Page. Inflammatory mediators of asthma: An update. *Pharmacological Reviews*, 50(4):515–596, 1998.

[6] P.J. Barnes, B. Jonsson, and J.B. Klim. The costs of asthma. *European Respiratory Journal*, 9(4):636–642, 1996.

[7] N.A. Barrett and K.F. Austen. Innate Cells and T Helper 2 Cell Immunity in Airway Inflammation. *Immunity*, 31(3):425–437, 2009.

[8] J.H.T. Bates, S.R. Bullimore, A.Z. Politi, J. Sneyd, R.C. Anafi, and A.M. Lauzon. Transient oscillatory force-length behavior of activated airway smooth muscle. *American Journal of Physiology. Lung Cellular and Molecular Physiology*, 297(2):L362–L372, 2009.

[9] E.H. Bel. Bronchial thermoplasty: Has the promise been met? *American Journal of Respiratory and Critical Care Medicine*, 181(2):101–102, 2010.

[10] R. Berair, R. Saunders, and C.E. Brightling. Origins of increased airway smooth muscle mass in asthma. *BMC Medicine*, 11:145, 2013.

[11] C. Bergeron, W. Al-Ramli, and Q. Hamid. Remodeling in asthma. *Proceedings of the American Thoracic Society*, 6(3):301–305, 2009.

[12] A. Bergner and M.J. Sanderson. Acetylcholine-induced calcium signaling and contraction of airway smooth muscle cells in lung slices. *The Journal of General Physiology*, 119:187–198, 2002.

[13] M.J. Berridge, P. Lipp, and M.D. Bootman. The versatility and universality of calcium signalling. *Nature Reviews Molecular Cell Biology*, 1(1):11–21, 2000.

[14] J. Bousquet, P.K. Jeffery, W.W. Busse, M. Johnson, and A.M. Vignola. Asthma - From bronchoconstriction to airways inflammation and remodeling. *American Journal of Respiratory and Critical Care Medicine*, 161(5), 2000.

[15] J. Bousquet, E. Mantzouranis, A.A. Cruz, C.E. Aït-Khaled, N.and Baena-Cagnani, E.R. Bleecker, C.E. Brightling, P. Burney, A. Bush, W.W. Busse, T.B. Casale, M. Chan-Yeung, R. Chen, B. Chowdhury, K.F. Chung, R. Dahl, J.M. Drazen, L.M. Fabbri, S.T. Holgate, F. Kauffmann, T. Haahtela, N. Khaltaev, J.P. Kiley, M.R. Masjedi, Y. Mohammad, P. O'Byrne, M.R. Partridge, K.F. Rabe, A. Togias, C. van Weel, S. Wenzel, N. Zhong, and T. Zuberbier. Uniform definition of asthma severity, control, and exacerbations: Document presented for the world health organization consultation on severe asthma. *Journal of Allergy and Clinical Immunology*, 126(5):926 – 938, 2010.

[16] R.N. Bracewell. *The Fourier Transform and its Applications*. McGraw-Hill Kogakusha, Ltd., Tokyo, second edition, 1978.

[17] C.E. Brightling, S. Gupta, S. Gonem, and S. Siddiqui. Lung damage and airway remodelling in severe asthma. *Clinical & Experimental Allergy*, 42(5):638–649, 2012.

[18] British Thoracic Society. British guideline on the management of asthma: A national clinical guideline, 2009.

[19] British Thoracic Society COPD Consortium. Spirometry in practice: A practical guide to using spirometry in primary care second edition, 2005.

[20] B.S. Brook, S.A.E.G. Falle, and T.J. Pedley. Numerical solutions for unsteady gravity-driven flows in collapsible tubes: evolution and roll-wave instability of a steady state. *Journal of Fluid Mechanics*, 396:223–256, 1999.

[21] B.S. Brook and O.E. Jensen. The role of contractile unit reorganization in force generation in airway smooth muscle. *Mathematical Medicine and Biology*, 2013.

[22] B.S. Brook, S.E. Peel, I.P. Hall, A.Z. Politi, J. Sneyd, Y. Bai, M.J. Sanderson, and O.E. Jensen. A biomechanical model of agonist-initiated contraction in the asthmatic airway. *Respiratory Physiology & Neurobiology*, 170(1):44 – 58, 2010.

[23] D. Bumbacea, D. Campbell, L. Nguyen, D. Carr, P.J. Barnes, D. Robinson, and K.F. Chung. Parameters associated with persistent airflow obstruction in chronic severe asthma. *European Respiratory Journal*, 24(1):122–128, 2004.

[24] J.P. Butler, I.M. Tolić-Nørrelykke, B. Fabry, and J.J. Fredberg. Traction fields, moments, and strain energy that cells exert on their surroundings. *American Journal of Physiology - Cell Physiology*, 282(3):C595–C605, 2002.

[25] C. Calogero and P.D. Sly. Developmental physiology: Lung function during growth and development from birth to old age. *European Respiratory Society Monograph*, 47:1–15, 2010.

[26] P.G. Ciarlet and G. Geymonat. Sur les lois de comportement en élasticité non linéaire compressible. *Comptes-rendus de l'Académie des Sciences de Paris Série II*, 295:423–426, 1982.

[27] S.L. Codd, R.K. Lambert, M.R. Alley, and R.J. Pack. Tensile stiffness of ovine tracheal wall. *Journal of Applied Physiology*, 76(6):2627–2635, 1994.

[28] M.F. Coughlin, B. Suki, and D. Stamenovic. Dynamic behavior of lung parenchyma in shear. *Journal of Applied Physiology*, 80(6):1880–1890, 1996.

[29] R. Courant, E. Isaacson, and M. Rees. On the solution of nonlinear hyperbolic differential equations by finite differences. *Communications on Pure and Applied Mathematics*, 5(3):243–255, 1952.

[30] G. Cox, J.D. Miller, A. McWilliams, J.M. FitzGerald, and S. Lam. Bronchial thermoplasty for asthma. *American Journal of Respiratory and Critical Care Medicine*, 173(9):965–969, 2006.

[31] R.G. Crystal, J.B. West, P.J. Barnes, and E.R. Weibel, editors. *The Lung: Scientific Foundations*. Raven Press Ltd., New York, 1991.

[32] D.E. Davies, J. Wicks, R.M. Powell, S.M. Puddicombe, and S.T. Holgate. Airway remodeling in asthma: New insights. *Journal of Allergy and Clinical Immunology*, 111(2):215–225, 2003.

[33] J.C. de Jongste, R. van Strik, I.L. Bonta, and K.F. Kerrebijn. Measurement of human small airway smooth muscle function in vitro with the bronchiolar strip preparation. *Journal of Pharmacological Methods*, 14(2):111 – 118, 1985.

[34] J.G.R. Demonchy, H.F. Kauffman, P. Venge, G.H. Koeter, H.M. Jansen, H.J. Sluiter, and K. Devries. Bronchoalveolar eosinophilia during allergen-induced late asthmatic reactions. *American Review of Respiratory Disease*, 131(3):373–376, 1985.

[35] A. Dietrich, V. Chubanov, H. Kalwa, B.R. Rost, and T. Gudermann. Cation channels of the transient receptor potential superfamily: Their role in physiological and pathophysiological processes of smooth muscle cells. *Pharmacology & Therapeutics*, 112(3):744–760, 2006.

[36] E.H. Dill. *Continuum mechanics: elasticity, plasticity, viscoelasticity*. CRC Press, Boca Raton, Fl, 2007.

[37] P.F. Dillon, M.O. Aksoy, S.P. Driska, and R.A. Murphy. Myosin phosphorylation and the cross-bridge cycle in arterial smooth-muscle. *Science*, 211(4481):495–497, 1981.

[38] G.M. Donovan and M.H. Tawhai. A simplified model of airway narrowing due to bronchial mucosal folding. *Respiratory Physiology & Neurobiology*, 171(2):144–150, 2010.

[39] M. Ebina, H. Yaegashi, T. Takahashi, M. Motomiya, and M. Tanemura. Distribution of smooth muscles along the bronchial tree: A morphometric study of ordinary autopsy lungs. *American Journal of Respiratory and Critical Care Medicine*, 141(5 Pt 1):1322–1326, 1990.

[40] B. Fabry and J.J. Fredberg. Remodeling of the airway smooth muscle cell: are we built of glass? *Respiratory Physiology & Neurobiology*, 137(2-3):109–124, 2003.

[41] G. Farnebäck. Two-frame motion estimation based on polynomial expansion. In J. Bigun and T. Gustavsson, editors, *Image Analysis*, volume 2749 of *Lecture Notes in Computer Science*, pages 363–370. Springer Berlin Heidelberg, 2003.

[42] J. Fox. *Utility of the precision cut lung slice model to investigate airway smooth muscle contraction*. PhD thesis, University of Nottingham, UK, 2011.

[43] J.J. Fredberg, D. Inouye, B. Miller, M. Nathan, S. Jafari, S.H. Raboudi, J.P. Butler, and S.A. Shore. Airway smooth muscle, tidal stretches, and dynamically determined contractile states. *American Journal of Respiratory and Critical Care Medicine*, 156(6):1752–1759, 1997.

[44] J.J. Fredberg, D.S. Inouye, S.M. Mijailovich, and J.P. Butler. Perturbed equilibrium of myosin binding in airway smooth muscle and its implications in bron-

chospasm. *American Journal of Respiratory and Critical Care Medicine*, 159(3):959–967, 1999.

[45] Y.C. Fung. A theory of elasticity of the lung. *Journal of Applied Mechanics*, 41(1):8–14, 1974.

[46] Y.C. Fung. *Biomechanics, Mechanical Properties of Living Tissues*. Springer-Verlag, New York, second edition, 1993.

[47] T.C. Gasser, R.W. Ogden, and G.A. Holzapfel. Hyperelastic modelling of arterial layers with distributed collagen fibre orientations. *Journal of the Royal Society Interface*, 3(6):15–35, 2006.

[48] Global Initiative For Asthma. Pocket guide to asthma management and prevention, 2010.

[49] J.B. Grotberg and S.H. Davis. Fluid-dynamical flapping of a collapsible channel: sound generation and flow limitation. *Journal of Biomechanics*, 13:219–230, 1980.

[50] S. J. Gunst, J.Q. Stropp, and J. Service. Mechanical modulation of pressure-volume characteristics of contracted canine airways in vitro. *Journal of Applied Physiology*, 68:2223–2229, 1990.

[51] S.J. Gunst and D.D. Tang. The contractile apparatus and mechanical properties of airway smooth muscle. *European Respiratory Journal*, 15(3):600–616, 2000.

[52] C.M. Hai and R.A. Murphy. Cross-bridge phosphorylation and regulation of latch state in smooth-muscle. *American Journal of Physiology*, 254(1 Pt 1):C99–C106, 1988.

[53] C.M. Hai and R.A. Murphy. Regulation of shortening velocity by cross-bridge phosphorylation in smooth muscle. *American Journal of Physiology - Cell Physiology*, 255(1):C86–C94, 1988.

[54] H. Hammad and B.N. Lambrecht. Dendritic cells and epithelial cells: linking innate and adaptive immunity in asthma. *Nature Reviews Immunology*, 8(3):193–204, 2008.

[55] A. Harten, P. Lax, and B. Leer. On upstream differencing and godunov-type schemes for hyperbolic conservation laws. *SIAM Review*, 25(1):35–61, 1983.

[56] M. Heil, A.L. Hazel, and J.A. Smith. The mechanics of airway closure. *Respiratory Physiology & Neurobiology*, 163(1-3):214 – 221, 2008.

[57] A.M. Herrera, B.E. McParland, A. Bienkowska, R. Tait, P.D. Paré, and C.Y. Seow. 'Sarcomeres' of smooth muscle: functional characteristics and ultrastructural evidence. *Journal of Cell Science*, 118(11):2381–2392, 2005.

[58] S.J. Hirst. Airway smooth muscle as a target in asthma. *Clinical and Experimental Allergy*, 30:54–59, 2000.

[59] S.T Holgate. The airway epithelium is central to the pathogenesis of asthma. *Allergology International : official journal of the Japanese Society of Allergology*, 57(1):1–10, 2008.

[60] S.T. Holgate and R. Polosa. Treatment strategies for allergy and asthma. *Nature Reviews Immunology*, 8(3):218–230, 2008.

[61] G. Holzapfel, T. Gasser, and R. Ogden. A new constitutive framework for arterial wall mechanics and a comparative study of material models. *Journal of Elasticity*, 61(1):1–48, 2000.

[62] G.A. Holzapfel. *Nonlinear solid mechanics : a continuum approach for engineering*. Wiley, Chichester, 2000.

[63] G.A. Holzapfel and R.W. Ogden. Constitutive modelling of arteries. *Proceedings of the Royal Society A-Mathematical physical and engineering sciences*, 466:1551–1597, 2010.

[64] F.G. Hoppin. Parenchymal mechanics and asthma. *Chest*, 107(3 Suppl):S140–S144, 1995.

[65] F.G. Hoppin, G.C. Lee, and S.V. Dawson. Properties of lung parenchyma in distortion. *Journal of Applied Physiology*, 39(5):742–751, 1975.

[66] P. Howell, G. Kozyreff, and J. Ockendon. *Applied Solid Mechanics*. Cambridge University Press, Cambridge, 2009.

[67] J.D. Humphrey and S.L. Delange. *An Introduction to Biomechanics: Solids and Fluids, Analysis and Design*. Springer, 2004.

[68] A.F. Huxley. Muscle structure and theories of contraction. *Progress in Biophysics & Molecular Biology*, 7:255–&, 1957.

[69] R.E. Hyatt, T.A. Wilson, and E. Bar-Yishay. Prediction of maximal expiratory flow in excised human lungs. *Journal of Applied Physiology*, 48(6):991–998, 1980.

[70] H. Itoh, M. Nishino, and H. Hatabu. Architecture of the lung - Morphology and function. *Journal of Thoracic Imaging*, 19(4):221–227, 2004.

[71] L.J. Janssen and K. Killian. Airway smooth muscle as a target of asthma therapy: history and new directions. *Respiratory Research*, 7(123), 2006.

[72] P.K. Jeffery. Remodeling in asthma and chronic obstructive lung disease. *American Journal of Respiratory and Critical Care Medicine*, 164(10, S):S28–S38, 2001.

[73] B. Jonson and C. Svantesson. Elastic pressure-volume curves: what information do they convey? *Thorax*, 54(1):82–87, 1999.

[74] J.A. Jude, M.E. Wylam, T.F. Walseth, and M.S. Kannan. Calcium signaling in airway smooth muscle. *Proceedings of the American Thoracic Society*, 5(1):15–22, 2008.

[75] K.E. Kadler, D.F. Holmes, J.A. Trotter, and J.A. Chapman. Collagen fibril formation. *Biomedical Journal*, 316(Pt 1):1–11, 1996.

[76] M. Kaliske and H. Rothert. Formulation and implementation of three-dimensional viscoelasticity at small and finite strains. *Computational Mechanics*, 19(3):228–239, 1997.

[77] K.E. Kamm and J.T. Stull. Activation of smooth-muscle contraction - relation between myosin phosphorylation and stiffness. *Science*, 232:80–82, 1986.

[78] R.D. Kamm. Airway wall mechanics. *Annual Review of Biomedical Engineering*, 1:47–72, 1999.

[79] R.D. Kamm and T.J. Pedley. Flow in collapsible tubes: a brief review. *Journal of Biomechanical Engineering*, 111:177–179, 1989.

[80] J. Keener and J. Sneyd. *Mathematical Physiology II: Systems Physiology 2nd ed.* Springer, New York, 2009.

[81] H.Y. Kim, R.H. DeKruyff, and D.T. Umetsu. The many paths to asthma: phenotype shaped by innate and adaptive immunity. *Nature Immunology*, 11(7):577–584, 2010.

[82] G.G. King, P.D. Paré, and C.Y. Seow. The mechanics of exageratted airway narrowing in asthma: the role of smooth muscle. *Respiration Physiology*, 118:1–13, 1999.

[83] M. Kroon. A constitutive model for smooth muscle including active tone and passive viscoelastic behaviour. *Mathematical Medicine and Biology-A Journal of the IMA*, 27(2):129–155, 2010.

[84] M. Kroon. Influence of dispersion in myosin filament orientation and anisotropic filament contractions in smooth muscle. *Journal of Theoretical Biology*, 272(1):72 – 82, 2011.

[85] M. Kroon. Optimal length of smooth muscle assessed by a microstructurally and statistically based constitutive model. *Computer Methods in Biomedical Engineering*, 14(1):43–52, 2011.

[86] K.-H. Kuo, A.M. Herrera, and C.Y. Seow. Ultrastructure of airway smooth muscle. *Respiratory Physiology & Neurobiology*, 137(2-3):197–208, 2003.

[87] K.-H. Kuo and C.Y. Seow. Contractile filament architecture and force transmission in swine airway smooth muscle. *Journal of Cell Science*, 117(8):1503–1511, 2004.

[88] K.-H. Kuo, L. Wang, P.D. Paré, L.E. Ford, and C.Y. Seow. Myosin thick filament lability induced by mechanical strain in airway smooth muscle. *Journal of Applied Physiology*, 90(5):1811–1816, 2001.

[89] K. Kuwano, C.H. Bosken, P.D. Paré, T.R. Bai, B.R. Wiggs, and J.C. Hogg. Small airways dimensions in asthma and in chronic obstructive pulmonary disease. *American Journal of Respiratory and Critical Care Medicine*, 148(5):1220–1225, 1993.

[90] S.J. Lai-Fook. Lung parenchyma described as a prestressed compressible material. *Journal of Biomechanics*, 10:357–365, 1977.

[91] S.J. Lai-Fook, R.E. Hyatt, J.R. Rodarte, and T.A. Wilson. Behavior of artificially produced holes in lung parenchyma. *Journal of Applied Physiology*, 43(4):648–655, 1977.

[92] S.J. Lai-Fook, T.A. Wilson, R.E. Hyatt, and J.R. Rodarte. Elastic constants of inflated lobes of dog lungs. *Journal of Applied Physiology*, 40(4):508–513, 1976.

[93] R. Lakes. *Viscoelastic Materials*. Cambridge University Press, Cambridge, 2009.

[94] R.K. Lambert. Sensitivity and specificity of the computational model for maximal expiratory flow. *Journal of Applied Physiology*, 57(4):958–970, 1984.

[95] R.K. Lambert, R.G. Castile, and R.S. Tepper. Model of forced expiratory flows and airway geometry in infants. *Journal of Applied Physiology*, 96(2):688–692, 2004.

[96] R.K. Lambert and T.A. Wilson. A model for the elastic properties of the lung and their effect on expiratory flow. *Journal of Applied Physiology*, 34:34–48, 1973.

[97] R.K. Lambert and T.A. Wilson. Smooth muscle dynamics and maximal expiratory flow in asthma. *Journal of Applied Physiology*, 99(5):1885–1890, 2005.

[98] R.K. Lambert, T.A. Wilson, R.E. Hyatt, and J.R. Rodarte. A computational model for expiratory flow. *Journal of Applied Physiology*, 52(1):44–56, 1982.

[99] B. Lande and W. Mitzner. Analysis of lung parenchyma as a parametric porous medium. *Journal of Applied Physiology*, 101:926–933, 2006.

[100] A.S. LaPrad and K.R. Lutchen. The dissolution of intact airway responsiveness from breathing fluctuations: what went wrong? *Journal of Applied Physiology*, 110(6):1506–1507, 2011.

[101] A.S. LaPrad, K.R. Lutchen, and B. Suki. A mechanical design principle for tissue structure and function in the airway tree. *PLoS Computational Biology*, 9(5), 2013.

[102] A.S. LaPrad, T.L. Szabo, B. Suki, and K.R. Lutchen. Reply to noble, hernandez, mitchell, and janssen. *Journal of Applied Physiology*, 109(3):940–941, 2010.

[103] A.S. LaPrad, T.L. Szabo, B. Suki, and K.R. Lutchen. Tidal stretches do not modulate responsiveness of intact airways in vitro. *Journal of Applied Physiology*, 109(2):295–304, 2010.

[104] J. Latourelle, Fabry B., and J.J. Fredberg. Dynamic equilibration of airway smooth muscle contraction during physiological loading. *Journal of Applied Physiology*, 92(2):771–779, 2002.

[105] T.L. Lavoie, R. Krishnan, H.R. Siegel, E.D. Maston, J.J. Fredberg, J. Solway, and M.L. Dowell. Dilatation of the constricted human airway by tidal expansion of lung parenchyma. *American Journal of Respiratory and Critical Care Medicine*, 186(3):225–232, 2012.

[106] M. Lei, H. Ghezzo, M.F. Chen, and D.H. Eidelman. Airway smooth muscle orientation in intraparenchymal airways. *Journal of Applied Physiology*, 82(1):70–77, 1997.

[107] T.K. Lim, N.B. Pride, and J.R.J. Inram. Effects of volume history during spontaneous and acutely induced air-flow obstruction in asthma. *The American Review of Respiratory Disease*, 135:591–596, 1987.

[108] B. Ma and J.H.T. Bates. Continuum vs. spring network models of airway-parenchymal interdependence. *Journal of Applied Physiology*, 113(1):124–129, 2012.

[109] B. Ma, M. Sanderson, and J.H.T. Bates. Airway-parenchymal interdependence in the lung slice. *Respiratory Physiology & Neurobiology*, 185(2):211 – 216, 2013.

[110] L. Marcucci and L. Truskinovsky. Mechanics of the power stroke in myosin II. *Physical Review E*, 81(051915), 2010.

[111] L. Marcucci and L. Truskinovsky. Muscle contraction: A mechanical perspective. *The European Physical Journal E*, 32:411–418, 2010.

[112] R. Marshall and J.G. Widdicombe. Stress relaxation of human lung. *Clinical Science*, 20(1):19–31, 1961.

[113] J. Mead, T. Takishima, and D. Leith. Stress distribution in lungs: a model of pulmonary elasticity. *Journal of Applied Physiology*, 28(5):596–608, 1970.

[114] D. Mehta and S.J. Gunst. Actin polymerization stimulated by contractile activation regulates force development in canine tracheal smooth muscle. *The Journal of Physiology*, 519(3):829–840, 1999.

[115] R.R. Mercer and J.D. Crapo. Spatial distribution of collagen and elastin fibers in the lungs. *Journal of Applied Physiology*, 69(2):756–765, 1990.

[116] S.M. Mijailovich, J.P. Butler, and J.J. Fredberg. Perturbed equilibria of myosin binding in airway smooth muscle: Bond-length distributions, mechanics, and atp metabolism. *Biophysical Journal*, 79(5):2667 – 2681, 2000.

[117] K.L. Moore and T.V.N. Persaud. *The developing human : clinically oriented embryology*. Elsevier Mosby, Philadelphia, eighth edition, 2008.

[118] H. Motulsky and A. Christopoulos. *Fitting models to biological data using linear and nonlinear regression: a practical guide to curve fitting*. Oxford University Press, Oxford, 2004.

[119] D.E. Moulton and A. Goriely. Possible role of differential growth in airway wall remodeling in asthma. *Journal of Applied Physiology*, 110(4):1003–1012, 2011.

[120] S.-I. Murtada, M. Kroon, and G.A. Holzapfel. A calcium-driven mechanochemical model for prediction of force generation in smooth muscle. *Biomechanics and Modeling in Mechanobiology*, 9(6):749–762, 2010.

[121] S.-I. Murtada, M. Kroon, and G.A. Holzapfel. Modeling the dispersion effects of contractile fibers in smooth muscles. *Journal of the Mechanics and Physics of Solids*, 58(12):2065 – 2082, 2010.

[122] J.A. Nadel and D.F. Tierney. Effect of a previous deep inspiration on airway resistance in man. *Journal of Applied Physiology*, 16:717–719, 1966.

[123] P. Nardinocchi and L. Teresi. On the active response of soft living tissues. *Journal of Elasticity*, 88(1):27–39, 2007.

[124] P.B. Noble, J.M. Hernandez, H.W. Mitchell, and L.J. Janssen. Deep inspiration and airway physiology: human, canine, porcine, or bovine? *Journal of Applied Physiology*, 109(3):938–939, 2010.

[125] P.B. Noble, R.L. Jones, E.T. Needi, A. Cairncross, H.W. Mitchell, A.L. James, and P.K. McFawn. Responsiveness of the human airway in vitro during deep inspiration and tidal oscillation. *Journal of Applied Physiology*, 110(6):1510–1518, 2011.

[126] P.M. O'Byrne and M.D. Inman. Airway hyperresponsiveness. *Chest*, 123(3 Suppl):S411–S416.

[127] R.W. Ogden. Large deformation isotropic elasticity - on the correlation of theory and experiment for incompressible rubberlike solids. *Proceedings of the Royal Society of London. A. Mathematical and Physical Sciences*, 326(1567):565–584, 1972.

[128] R.W. Ogden. Nonlinear elasticity, anisotropy, material stability and residual stresses in soft tissue. In G. Holzapfel and R.W. Ogden, editors, *Biomechanics of Soft Tissue in Cardiovascular Systems*, number 441 in CISM Courses and Lectures, pages 65–108. Springer-Verlag, 2003.

[129] M.N. Oliver, B. Fabry, A. Marinkovic, S.M. Mijailovich, J.P. Butler, and J.J. Fredberg. Airway hyperresponsiveness, remodeling, and smooth muscle mass right answer, wrong reason? *American Journal of Respiratory Cell and Molecular Biology*, 37(3):264–272, 2007.

[130] M.R. Owen and M.A. Lewis. The mechanics of lung tissue under high-frequency ventilation. *SIAM Journal on Applied Mathematics*, 61:2001, 2001.

[131] M. Palmqvist, G. Persson, L. Lazer, J. Rosenborg, P. Larsson, and J. Lotvall. Inhaled dry-powder formoterol and salmeterol in asthmatic patients: onset of action, duration of effect and potency. *European Respiratory Journal*, 10(11):2484–2489, 1997.

[132] A. Papi, S. Amadesi, P. Chitano, P. Boschetto, A. Ciaccia, P. Geppetti, L.M. Fabbri, and C.E. Mapp. Bronchopulmonary inflammation and airway smooth muscle hyperresponsiveness induced by nitrogen dioxide in guinea pigs. *European Journal of Pharmacology*, 374(2):241 – 247, 1999.

[133] R.M. Pascual and S.P. Peters. Airway remodeling contributes to the progressive loss of lung function in asthma: An overview. *Journal of Allergy and Clinical Immunology*, 116(3):477–486, 2005.

[134] T.J. Pedley and X.Y. Luo. Modelling flow and oscillations in collapsible tubes. *Theoretical and Computational Fluid Dynamics*, 10:277–294, 1998.

[135] J.J. Perez Fontan, A.O. Ray, and T.R. Oxland. Stress relaxation of the respiratory system in developing piglets. *Journal of Applied Physiology*, 73(4):1297–1309, 1992.

[136] P.D. Phelan, C.F. Robertson, and A. Olinsky. The Melbourne asthma study: 1964-1999. *Journal of Allergy and Clinical Immunology*, 109(2):189–194, 2002.

[137] S. Phipps, F. Benyahia, T.T. Ou, J. Barkans, D.S. Robinson, and A.B. Kay. Acute allergen-induced airway remodeling in atopic asthma. *American Journal of Respiratory Cell and Molecular Biology*, 31(6):626–632, 2004.

[138] A.C. Pipkin. *Lectures on Viscoelasticity Theory*. Springer-Verlag, New York, second edition, 1986.

[139] G. Pocock and C.D. Richards. *Human Physiology-The Basis of Medicine third edition*. Oxford University Press, Oxford, 2006.

[140] A.Z. Politi, G.M. Donovan, M.H. Tawhai, M.J. Sanderson, A.-M. Lauzon, J.H.T. Bates, and J. Sneyd. A multiscale, spatially distributed model of asthmatic airway hyper-responsiveness. *Journal of Theoretical Biology*, 266(4):614 – 624, 2010.

[141] A. Rachev and K. Hayashi. Theoretical study of the effects of vascular smooth muscle contraction on strain and stress distributions in arteries. *Annals of Biomedical Engineering*, 27(4):459–468, 1999.

[142] F. Rasmussen, D.R. Taylor, E.M. Flannery, J.O. Cowan, J.M. Greene, G.P. Herbison, and M.R. Sears. Risk factors for airway remodeling in asthma manifested by a low postbronchohator FEV1/vital capacity ratio - A longitudinal population study from childhood to adulthood. *American Journal of Respiratory and Critical Care Medicine*, 165(11):1480–1488, 2002.

[143] S.I. Rennard. Repair mechanisms in asthma. *Journal of Allergy and Clinical Immunology*, 98(6 Pt 2), 1996.

[144] H.Y. Reynolds. Lung inflammation - normal host defense or a complication of some diseases. *Annual Review of Medicine*, 38:295–323, 1987.

[145] W.R. Roche, R. Beasley, J.H. Williams, and S.T. Holgate. Subepithelial fibrosis in the bronchi of asthmatics. *Lancet*, 1(8637):520–524, 1989.

[146] P.L. Roe. Characteristic-based schemes for the euler equations. *Annual Review of Fluid Mechanics*, 18(1):337–365, 1986.

[147] D.F. Rogers. The airway goblet cell. *International Journal of Biochemistry & Cell Biology*, 35(1):1–6, 2003.

[148] D.F. Rogers. Airway mucus hypersecretion in asthma: an undervalued pathology? *Current Opinion in Pharmacology*, 4(3):241–250, 2004.

[149] J. Roig, R. Hernando, and R. Mora. Indacaterol, a novel once daily inhaled $\beta 2$-adrenoreceptor agonist. *The Open Respiratory Medicine Journal*, 3:27–30, 2009.

[150] A. Schmitz and M. Böl. On a phenomenological model for active smooth muscle contraction. *Journal of Biomechanics*, 44(11):2090–2095, 2011.

[151] M.R. Sears. Lung function decline in asthma. *European Respiratory Journal*, 30(3):411–413, 2007.

[152] C.Y. Seow, V.R. Pratusevich, and L.E. Ford. Series-to-parallel transition in the filament lattice of airway smooth muscle. *Journal of Applied Physiology*, 89(3):869–876, 2000.

[153] M. Siklosi, O.E. Jensen, R.H. Tew, and A. Logg. Multiscale modeling of the acoustic properties of lung parenchyma. *ESAIM: Proceedings*, 23:78–97, 2008.

[154] S.M. Smiley-Jewell, M.U. Tran, A.J. Weir, Z.A. Johnson, L.S. Van Winkle, and C.G. Plopper. Three-dimensional mapping of smooth muscle in the distal conducting airways of mouse, rabbit, and monkey. *Journal of Applied Physiology*, 93(4):1506–1514, 2002.

[155] I.S. Sokolnikoff. *Mathematical theory of elasticity*. McGraw-Hill, New York, second edition, 1956.

[156] M.P. Sparrow, M. Weichselbaum, and P.B. McCray. Development of the innervation and airway smooth muscle in human fetal lung. *American journal of respiratory cell and molecular biology*, 20(4):550–560, 1999.

[157] A.J.M. Spencer. Constitutive theory for strongly anisotropic solids. In A.J.M. Spencer, editor, *Continuum Theory of the Mechanics of Fibre-Reinforced Composites*, CISM Courses and Lectures No. 282, International Centre for Mechanical Sciences, pages 1–32. Springer-Verlag, Wien, 1984.

[158] J. Stålhand, A. Klarbring, and G.A. Holzapfel. Smooth muscle contraction: Mechanochemical formulation for homogeneous finite strains. *Progress in Biophysics & Molecular Biology*, 96(1-3):465–481, 2008.

[159] D. Stamenovic and T.A. Wilson. A strain energy function for lung parenchyma. *Journal of Biomechanical Engineering*, 107(1):81–86, 1985.

[160] D. Stamenovic and D. Yager. Elastic properties of air- and liquid-filled lung parenchyma. *Journal of Applied Physiology*, 65:2565–2570, 1988.

[161] S. Stanojevic, A. Wade, J. Stocks, J. Hankinson, A.L. Coates, H. Pan, M. Rosenthal, M. Corey, P. Lebecque, and T.J. Cole. Reference ranges for spirometry across all ages - A new approach. *American Journal of Respiratory and Critical Care Medicine*, 177(3):253–260, 2008.

[162] B.C. Starcher. Elastin and the lung. *Thorax*, 41(8):577–585, 1986.

[163] A. Stevens and J. Lowe. *Human Histology*. Elsevier Mosby, Philadelphia, third edition, 2005.

[164] M.E. Strek. Difficult asthma. *Proceedings of the American Thoracic Society*, 3(1):116–123, 2006.

[165] Y. Sumi and Q. Hamid. Airway remodeling in asthma. *Allergology international : official journal of the Japanese Society of Allergology*, 56(4):341–348, 2007.

[166] L.A. Taber and R. Perucchio. Modeling heart development. *Journal of Elasticity*, 61(1-3):165–197, 2000.

[167] T. Takishima and J. Mead. Tests of a model of pulmonary elasticity. *Journal of Applied Physiology*, 33:576–581, 1972.

[168] H. Tavana, D. Huh, J.B. Groberg, and S. Takayama. Microfluidics, lung surfactant, and respiratory disorders. *Labmedicine*, 40(4):203–209, 2009.

[169] K.J. Taylor and A.R. Luksza. Peripheral-blood eosinophil counts and bronchial responsiveness. *Thorax*, 42(6):452–456, 1987.

[170] The National Centre for the Replacement, Refinement and and Reduction of Animals in Research. The challenge of animal research. http://www.nc3rs.org.uk/landing.asp?id=2, 2009.

[171] P. Tonino, M. Simon, and R. Craig. Mass determination of native smooth muscle myosin filaments by scanning transmission electron microscopy. *Journal of Molecular Biology*, 318(4):999 – 1007, 2002.

[172] P. Tracqui and J. Ohayon. An integrated formulation of anisotropic force-calcium relations driving spatio-temporal contractions of cardiac myocytes. *Philosophical Transactions of the Royal Society A-Mathematical Physical and Engineering Sciences*, 367(1908):4887–4905, 2009.

[173] I. Wang, A.Z. Politi, N. Tania, Y. Bai, M.J. Sanderson, and J. Sneyd. A mathematical model of airway and pulmonary arteriole smooth muscle. *Biophysical Journal*, 94(6):2053–2064, 2008.

[174] L. Wang, P.D. Paré, and C.Y. Seow. Effects of length oscillation on the subsequent force development in swine tracheal smooth muscle. *Journal of Applied Physiology*, 88(6):2246–2250, 2000.

[175] H.M. Warrick and J.A. Spudich. Myosin structure and function in cell motility. *Annual Review of Cell Biology*, 3:379–422, 1987.

[176] E.R. Weibel. *Morphometry of the human lung*. Springer Verlag and Academic Press, New York, 1963.

[177] S.E. Wenzel. Asthma: defining of the persistent adult phenotypes. *Lancet*, 368(9537):804–813, 2006.

[178] A.R. West, H.T. Syyong, S. Siddiqui, C.D. Pascoe, T.M. Murphy, H. Maarsingh, L. Deng, G.N. Maksym, and Y. Bossé. Airway contractility and remodeling: Links to asthma symptoms. *Pulmonary Pharmacology & Therapeutics*, 26(1):3 – 12, 2013.

[179] B.R. Wiggs, C.A. Hrousis, J.M. Drazen, and R.D. Kamm. On the mechanism of mucosal folding in normal and asthmatic airways. *Journal of Applied Physiology*, 83(6):1814–1821, 1997.

[180] M.W. Wong. *Discrete fourier analysis*. Pseudo-differential operators: theory and applications Vol.5. Birkhäuser, Basel, 2011.

[181] World Health Organisation. Asthma: fact sheet 307. http://www.who.int/mediacentre/factsheets/fs307/en/index.html, May 2011.

[182] Z.-X. Wu, J.S. Barker, T.P. Batchelor, and R.D. Dey. Interleukin (IL)-1 regulates ozone-enhanced tracheal smooth muscle responsiveness by increasing substance P (SP) production in intrinsic airway neurons of ferret. *Respiratory Physiology & Neurobiology* , 164(3):300 – 311, 2008.

[183] J. Yang, J.W. Clark Jr., R.M. Bryan, and C. Robertson. The myogenic response in isolated rat cerebrovascular arteries: smooth muscle cell model. *Medical Engineering & Physics*, 25(8):691 – 709, 2003.

[184] J. Yang, J.W. Clark Jr., R.M. Bryan, and C.S. Robertson. The myogenic response in isolated rat cerebrovascular arteries: vessel model. *Medical Engineering & Physics*, 25(8):711 – 717, 2003.

[185] M.A. Zulliger, A. Rachev, and N. Stergiopulos. A constitutive formulation of arterial mechanics including vascular smooth muscle tone. *American Journal of Physiology-Heart and Circulatory Physiology*, 287(3):H1335–H1343, 2004.